Dissertation
zur Erlangung des akademischen Grades
Dr. rer. nat.

Flavorful Models for Asymptotic Safety

Clara Hormigos Feliu

Fakultät Physik,
Technische Universität Dortmund

Dortmund, Januar 2021

technische universität
dortmund

Gutachter dieser Arbeit:
Prof. Dr. Gudrun Hiller und Prof. Dr. Joachim Brod

Vorsitzender des Promotionsausschusses:
Prof. Dr. Johannes Albrecht

Datum der mündlichen Promotionsprüfung:
23. Februar 2021

This thesis contains the following work published by the author:

- S. Bißmann, G. Hiller, C. Hormigos-Feliu and D. F. Litim. *Multi-lepton signatures of vector-like leptons with flavor*, Eur. Phys. J. C 81 (2021) 101, arXiv:2011.12964.
- G. Hiller, C. Hormigos-Feliu, D. F. Litim and T. Steudtner, *Model Building from Asymptotic Safety with Higgs and Flavor Portals*, Phys. Rev. D 102 (2020) 095023, arXiv:2008.08606.
- G. Hiller, C. Hormigos-Feliu, D. F. Litim and T. Steudtner, *Anomalous magnetic moments from asymptotic safety*, Phys. Rev. D 102 (2020) 071901, arXiv:1910.14062.
- G. Hiller, C. Hormigos-Feliu, D. F. Litim, and T. Steudtner, *Asymptotically safe extensions of the Standard Model with flavour phenomenology*, in *54th Rencontres de Moriond on Electroweak Interactions and Unified Theories (Moriond EW 2019) La Thuile, Italy, March 16-23, 2019,* 2019. arXiv:1905.11020.

And the following work in preparation:

- G. Hiller and C. Hormigos-Feliu. *Flavor from running in $U(1)_X$ models.*

Abstract

In this thesis we study asymptotically safe models with implications for flavor physics. We show that the Yukawa couplings necessary to generate ultraviolet fixed points could link a new sector to the Standard Model, generating a rich phenomenology. Most prominently, we find that for theories with heavy vector-like leptons and singlet scalars the discrepancies in the anomalous magnetic moments of the electron and the muon can be simultaneously explained without explicitly breaking lepton flavor universality. We study implications for the models at colliders, and propose targeted observables and null tests which exploit the flavor structure of the new sector. We finally show that, in asymptotically safe theories where the Standard Model is extended with an additional $U(1)$ gauge symmetry, large hierarchies in the Yukawa sector can be generated through renormalization group running. Employing non-universal charge assignments, we find that the observed fermion masses and quark mixing patterns can be reproduced to the order of magnitude.

Zusammenfassung

In dieser Arbeit untersuchen wir asymptotisch sichere Modelle mit Implikationen für Flavorphysik. Wir zeigen, dass die Yukawa-Kopplungen, die zur Erzeugung ultravioletter Fixpunkte notwendig sind, einen neuen Sektor mit dem Standardmodell verknüpfen können, wodurch eine reichhaltige Phänomenologie entsteht. Vor allem finden wir heraus, dass für Theorien mit schweren vector-like Leptonen und Singulett-Skalaren die Diskrepanzen in den anomalen magnetischen Momenten des Elektrons und des Myons gleichzeitig erklärt werden können, ohne die Leptonflavoruniversalität explizit zu brechen. Wir untersuchen Implikationen für die Modelle an Collidern und schlagen gezielte Observablen und Nulltests vor, die die Flavorstruktur des neuen Sektors ausnutzen. Schließlich zeigen wir, dass in asymptotisch sicheren Theorien, in denen das Standardmodell um eine zusätzliche $U(1)$-Eichsymmetrie erweitert wird, durch Renormierungsgruppenlaufen große Hierarchien im Yukawa-Sektor erzeugt werden können. Unter Verwendung von nicht-universellen Ladungen finden wir, dass die beobachteten Fermionenmassen und Quark-Mischungsmuster in der Größenordnung reproduziert werden können.

Acknowledgements

First of all I would like to thank my advisor, Gudrun Hiller, for giving me the opportunity to work in Dortmund during the past three years, for sharing her ideas and insights and for always conveying a contagious enthusiasm which has been both an inspiration and a source of motivation. I would also like to thank Daniel Litim for a fruitful collaboration and for his valuable support, and Joachim Brod for kindly agreeing to be the second referee of this work.

The members of T3 and T4 deserve my warmest thanks, for all the coffee breaks, movie nights, roof beers and climbing sessions which I came to miss very much once they had to stop. I especially want to thank Peter, for countless, endless and always fun discussions in the office; Dennis, for showing me how to diagonalize 2x2 matrices and other high-level problems, and for suffering through many pages of this work; Mathias, who made life in physics much more fun; Fagner, for always including me in his inspiring views of life and physics; Tom, for sharing the pains and joys of our joint projects as well as his weird sense of humor, and Tim and Innes, for reading through some of these pages. A very exceptional thanks must go to Stefan, who has been a bottomless source of support and with whom it has been a pleasure to work. My time in Dortmund would not have been the same without Johanna and Tabea, who made me feel at home away from home. To Hedi, I could not be more grateful for all the balcony (and non-balcony) time we shared.

També vull donar les gràcies a l'Arnau, per tot els suport que m'has donat i per unes trobades increïbles durant aquests anys. A l'Álvaro, gràcies per tots els escaips, que sempre m'han fet sentir com si mai hagués marxat. A l'Andreu, moltes gràcies per recolzar-me durant tot aquest temps. A la Gemma, per fer que m'oblidés de la distància a cada trucada random. Finalment, vull donar les gràcies a la meva mare, la Dolors, i el meu pare, l'Antonio, que m'han donat tot el suport en cada aventura i m'han ajudat en tot moment. I una mica per tot, i una mica per res, moltes gràcies Pau.

Contents

Acronyms

4L	4 Light leptons
AMM	Anomalous Magnetic Moment
BSM	Beyond the Standard Model
CKM	Cabibbo-Kobayashi-Maskawa
CR	Conversion Rate
EDM	Electric Dipole Moment
EWSB	Electroweak Symmetry Breaking
FCNC	Flavor-Changing Neutral Current
HL-LHC	High Luminosity Large Hadron Collider
IR	Infrared
LFU	Lepton Flavor Universality
(c)LFV	(charged) Lepton Flavor Violation
LHC	Large Hadron Collider
MFV	Minimal Flavor Violation
MS	Minimal Subtraction
OCDF	Opposite Charge, Different Flavor
OCSF	Opposite Charge, Same Flavor
PDF	Parton Distribution Function
RG	Renormalization Group
RGE	Renormalization Group Equation
SM	Standard Model
UV	Ultraviolet
VEV	Vacuum Expectation Value
VLL	Vector-Like Lepton

1 Introduction

In 2020, the Nobel Prize in physics was awarded to groundbreaking theoretical and experimental findings which instituted black holes as physical phenomena occurring in nature. In particular, Roger Penrose was awarded the prize for establishing that black holes are a solid prediction of Einstein's theory of general relativity, while Andrea Ghez and Reinhard Genzel were recognized for leading the discovery that a supermassive black hole resides at the center of our galaxy. Therefore, this year's prize exemplifies how both theoretical and experimental developments are crucial and necessary to advance our knowledge of nature, and showcases the importance of addressing fundamental questions about our universe.

Within the realm of particle physics, the Standard Model (SM) has been well established as the current paradigm after exhibiting great success, manifest through accurate predictions in agreement with numerous experimental measurements. In particular, the discovery of the Higgs boson at the LHC in the beginning of the last decade [1, 2] corroborated the existence of the last missing piece of the SM. However, theoretical shortcomings as well as unexplained observations remain which make the need for physics beyond the Standard Model (BSM) seem imperative. This holds especially true for the flavor sector of the SM: the existence of three generations of quarks and leptons with order-of-magnitude disparities between their masses and the hierarchical structure of the quark-mixing matrix remain unexplained features of the SM. Even though these phenomena are allowed from a theoretical point of view, the lack of a fundamental explanation as to why the flavor structure is such as we observe is striking, and often referred to as the *Standard Model flavor puzzle* [3]. Moreover, measurements of neutrino oscillations [4, 5] confirming that neutrinos carry a mass have deepened the SM flavor puzzle even further. Indeed, a mechanism giving rise to neutrino masses and their mixing, which appears to display an anarchical pattern rather than a marked hierarchy, is still absent within the SM.

Theoretical efforts towards elucidating the origin of flavor include models with extra dimensions [6–8], RG-induced hierarchies [9–11] and global symmetries, such as in the Froggatt-Nielsen mechanism [12]. If one insists that flavorful new physics arise at the TeV scale, as is motivated by the hierarchy problem or certain dark matter scenarios, further questions arise regarding the flavor structure of theories beyond the SM. These should present some mechanism to suppress contributions to flavor-changing observables, which are mostly seen to be in great agreement with the SM. The question of how TeV-scale new physics is not appearing in such observables constitutes the *New Physics flavor problem*. As an example, one option to circumvent the issue of sizable flavor-changing interactions is to parametrize all new physics using the criteria of Minimal Flavor Violation (MFV), which assumes that the only source of flavor violation beyond the SM resides in the SM Yukawas themselves [13].

Furthermore, from the experimental side certain observables within the flavor sector have reported discrepancies with respect to their SM predictions, in what could be signals of the presence of new physics. This is the case for the anomalous magnetic moments of the electron and the muon, which presently deviate from their SM values by -2.4σ and 3.5σ, respectively [14–16]. Additionally, several b physics observables present as well deviations from theory values. For instance, $b \to s\ell\ell$ processes show hints of $\mu - e$ non-universality [17–19], as well as anomalies in angular observables [20, 21]. Therefore, both from a theoretical and experimental point of view the flavor sector constitutes a natural area to expect physics beyond the Standard Model.

Going beyond flavor physics, further theoretical issues of the SM include the presence of a transplanckian *Landau pole* in the case of the hypercharge coupling, which destabilizes the renormalization group evolution of the SM. The $U(1)_Y$ divergence signals a loss of predictivity at high scales, which entails that the SM is not ultraviolet (UV) complete in the sense of perturbation theory. The influence of new physics in the running of α_1, either through quantum gravity effects kicking in at the Planck scale [22, 23] or lighter new physics [24–26] may help resolve this issue. Additional shortcomings of the SM comprise the *strong $\mathcal{CP}$ problem*, which questions why the $\mathcal{CP}$-violating parameter θ_{QCD} of the QCD Lagrangian should be so small, the strong evidence for the existence of *dark matter* and *dark energy* and the observed *matter-antimatter asymmetry* of the universe, all of which find no explanation within the SM. Lastly, the SM does not provide a framework to describe gravity. Even though at the scales currently probed by the SM gravity effects are negligible, these could become important at planckian energies. Altogether, both from the theoretical and experimental side it is clear that the SM cannot be the ultimate theory of nature, and therefore physics beyond it must be present at some scale.

In this thesis, we explore the possibility that flavorful new physics exists which has a certain impact on a fundamental property of the SM as a renormalizable quantum field theory: the evolution of couplings with the energy scale. In particular, we focus on UV completions of the SM which have the ability to render it scale invariant at high energies. A key ingredient is the presence of fixed points of the renormalization group equations, which drive the couplings towards constant, non-zero values. Such *asymptotically safe* models not only avoid Landau poles throughout the running of couplings and maintain predictivity at all scales, but also allow to constrain the parameter space of new physics by demanding that renormalization group (RG) trajectories be matched onto the SM. Here, we employ model building tools from asymptotically safe SM extensions [27–29] to address both fundamental and data-driven problems of the flavor sector. In order to study the testability of the proposed models at current experiments, we explore in detail their phenomenology and implications at colliders. This allows us to ascertain whether new physics necessary to render the SM asymptotically safe could reside at the TeV scale, and potentially be probed with present or near-future data.

The thesis is structured as follows: in the remainder of this chapter we review the building

blocks of the SM, with a special focus on its flavor and renormalization group properties. In Chapter 2 we present general formulae for asymptotically safe SM extensions and the different new physics models discussed in this thesis. The subsequent chapters contain the following work:

- Chapter 3 explores models where a new sector is connected to the SM both through mixed Yukawa terms, which mediate interactions between leptons and new vector-like fermions, and through a scalar portal coupling linking the Higgs to heavy singlet scalars. We exploit flavor symmetries to parametrize new physics couplings, and then show that the models can constitute asymptotically safe extensions of the SM. We provide a thorough discussion of their phenomenology, and detail how the subset corresponding to models of vector-like leptons is able to simultaneously explain the discrepancies in the anomalous magnetic moment (AMM) of the electron and the muon without requiring an explicit breaking of lepton flavor universality.

- In Chapter 4 we analyze implications of vector-like lepton models at the LHC, focusing on the parameter space of Yukawa couplings which can accommodate both AMM anomalies. We identify lepton-flavor-violating-like signatures which arise from the flavor structure of the scalar sector, and use these to build new observables which can serve as null tests of the SM and help discern the mass hierarchy of the BSM states.

- Chapter 5 deals with asymptotically safe SM extensions featuring an additional local $U(1)$ symmetry, with an associated massive and electrically neutral Z' boson. We show how assigning non-universal new charges to SM fermions allows the renormalization group flow to generate large hierarchies between Yukawa couplings, which in certain scenarios can approximately reproduce the mass patterns of the SM. Phenomenological consequences such as Z'-mediated flavor-changing neutral currents and implications for B anomalies are discussed.

At the end of each chapter we briefly outline our findings, while a general summary and conclusions are provided in Chapter 6.

1.1 Flavor and the Standard Model

The Standard Model of particle physics employs quantum fields and their symmetries to describe matter and its interactions at the most fundamental level. In this section we present the building blocks of the SM, starting from the full gauge theory and then examining the consequences of electroweak symmetry breaking (EWSB) and its implications for the flavor sector.

1.1.1 Fields and Symmetries

In the SM, matter fields are diversely charged under the gauge group

$$\mathcal{G}_{\rm SM} = SU(3)_C \times SU(2)_L \times U(1)_Y \,, \tag{1.1.1}$$

which determines their interactions. The electric charge Q_e of a particle is given by the Gell-Mann–Nishijima relation

$$Q_e = T_3 + Y \,, \tag{1.1.2}$$

where T_3 is the weak isospin component of a given particle and Y its hypercharge. In Tab. 1.1 we summarize the full particle content of the SM together with its charges. The fermionic fields consist of quark $SU(2)_L$ doublets Q and singlets U and D, as well as lepton doublets L and singlets E. For each fermion three different flavors exist, which in the SM are distinguished only by their masses, and additionally their charged weak interactions in the case of the quarks. Furthermore, the gauge eigenstates Q, U, D, L, E present a definite chirality: while $SU(2)_L$ doublets are left-handed, singlets are right-handed. It is a salient feature of the SM that right- and left-handed fermions carry different charges under $\mathcal{G}_{\rm SM}$, yielding it a chiral theory where only left-handed fields are charged under $SU(2)_L$. There is, however, no given reason why right-handed fields beyond those in the SM could not be charged under $SU(2)_L$. For any Dirac fermion f, we define its left-handed (right-handed) part as $f_L = P_L f$ ($f_R = P_R f$) in terms of the projectors

$$P_L = \frac{1}{2}\left(1 - \gamma^5\right) \,, \qquad P_R = \frac{1}{2}\left(1 + \gamma^5\right) \,, \tag{1.1.3}$$

where $\gamma^5 \equiv i\gamma^0\gamma^1\gamma^2\gamma^3$ corresponds to the fifth Dirac gamma matrix [30, 31]. The gauge interactions of the SM fermions are described by the Lagrangian

$$\mathcal{L}_{\rm kin} = \overline{Q} i\not{D} Q + \overline{U} i\not{D} U + \overline{D} i\not{D} D + \overline{L} i\not{D} L + \overline{E} i\not{D} E \,, \tag{1.1.4}$$

with $\not{D} = \gamma^\mu D_\mu$. The covariant derivative D_μ can be expressed as

$$D_\mu = \partial_\mu + ig' Y B_\mu + igT^a W^a_\mu + ig_3 \lambda^b G^b_\mu \,, \tag{1.1.5}$$

where all flavor and gauge indices are implicitly contracted. In any $SU(N)$ group the number of generators equals $N^2 - 1$, which yields 3 generators T^a for $SU(2)_L$, with $a = 1, 2, 3$, and 8 generators λ^b for $SU(3)_C$, with $b = 1, 2, ..., 8$. The fields B_μ, W^a_μ and G^b_μ correspond to the gauge bosons of $U(1)_Y$, $SU(2)_L$ and $SU(3)_C$ respectively, with g', g and g_3 their respective couplings. All terms in the kinetic Lagrangian (1.1.4) are diagonal in

Field	Flavors	$SU(3)_C \times SU(2)_L \times U(1)_Y$	Q_e
Q	$\begin{pmatrix} u_L \\ d_L \end{pmatrix}, \begin{pmatrix} c_L \\ s_L \end{pmatrix}, \begin{pmatrix} t_L \\ b_L \end{pmatrix}$	$(3, 2, 1/6)$	$2/3$ $-1/3$
U	u_R, c_R, t_R	$(3, 1, 2/3)$	$2/3$
D	d_R, s_R, b_R	$(3, 1, -1/3)$	$-1/3$
L	$\begin{pmatrix} \nu_L^e \\ e_L \end{pmatrix}, \begin{pmatrix} \nu_L^\mu \\ \mu_L \end{pmatrix}, \begin{pmatrix} \nu_L^\tau \\ \tau_L \end{pmatrix}$	$(1, 2, -1/2)$	0 -1
E	e_R, μ_R, τ_R	$(1, 1, -1)$	-1
H	$\begin{pmatrix} \varphi^+ \\ \varphi^0 \end{pmatrix}$	$(1, 2, 1/2)$	1 0

Table 1.1. Fields and charges in the Standard Model. The second column shows the different flavors in terms of their $SU(2)_L$ components.

flavor space, since any hermitian matrix mixing the generations could be reduced to one parameter after performing unitary transformations.[1] Thus, $\mathcal{L}_{\rm kin}$ presents a global $U(3)^5$ flavor symmetry, where each of the five fermion fields accept an independent $U(3)$ rotation [13, 32]. This symmetry can be further decomposed as

$$\mathcal{G}_{\rm flav} = SU(3)_q^3 \times SU(3)_\ell^2 \times U(1)_B \times U(1)_L \times U(1)_Y \times U(1)_{\rm PQ} \times U(1)_E \,, \tag{1.1.6}$$

where

$$SU(3)_q^3 = SU(3)_Q \times SU(3)_U \times SU(3)_D \,, \quad SU(3)_\ell^2 = SU(3)_L \times SU(3)_E \,. \tag{1.1.7}$$

We identify the $U(1)$ rotations in Eq. (1.1.6) with baryon number (B), lepton number (L), global hypercharge (Y), Peccei-Quinn symmetry, [33], and finally a rotation of the E field only.

In addition, the SM contains the Higgs doublet field H. It will prove useful to define as well its charge conjugate

$$\tilde{H} = i\sigma_2 H^* = \begin{pmatrix} \varphi^{0*} \\ -\varphi^- \end{pmatrix} , \tag{1.1.8}$$

where σ_2 is the second Pauli matrix and $\varphi^- = (\varphi^+)^*$. Note that $\tilde{H}$ is an $SU(2)_L$ doublet with hypercharge $-1/2$. The Higgs couples to fermions through renormalizable Yukawa

[1] More explicitly, such an an hermitian matrix would break the $U(3)$ symmetry of a given fermion kinetic term to a $U(1)$, yielding 8 broken symmetries. Then, from the 9 general parameters of the hermitian matrix, only $9 - 8 = 1$ is physical, see Eq. (1.1.11).

interactions, which can be written as

$$-\mathcal{L}_{\text{Yuk}} = \overline{Q} Y_d H D + \overline{Q} Y_u \tilde{H} U + \overline{L} Y_\ell H E + \text{h.c.}\,. \tag{1.1.9}$$

Therefore, the Yukawa sector partially breaks the flavor symmetry (1.1.6), yielding

$$\mathcal{G}_{\text{flav}} \to U(1)_B \times U(1)_e \times U(1)_\mu \times U(1)_\tau\,, \tag{1.1.10}$$

where the $U(1)_\ell$ correspond to the individual lepton numbers[2]. In order to count the number of physical parameters, we must subtract the number of broken generators from the total number of parameters in the Lagrangian [32], following

$$N_{\text{phys}} = N_{\text{tot}} - N_{\text{broken}}\,. \tag{1.1.11}$$

In the lepton sector, N_{tot} corresponds to the 18 independent entries of the Yukawa matrix Y_ℓ, while from the $2 \times 9 = 18$ symmetries of $U(3)_\ell \times U(3)_E$ only 3 are conserved (the individual lepton numbers), while 15 are broken. Thus, we obtain $N_{\text{phys}} = 18 - 15 = 3$ physical parameters, which correspond to the three charged lepton masses. In the quark sector, we start out with the $2 \times 18 = 36$ parameters of the Y_u and Y_d matrices, and from the $3 \times 9 = 27$ symmetries of the three $U(3)$ quark rotations only one is conserved, corresponding to baryon number. Thus, we are left with 26 broken symmetries. Using again Eq. (1.1.11), this yields $N_{\text{phys}} = 36 - 26 = 10$ physical parameters, which correspond to the six quark masses and a unitary rotation matrix with three angles and one phase.

1.1.2 Electroweak Symmetry Breaking

Through spontaneous symmetry breaking in the Higgs sector, the electroweak $SU(2)_L \times U(1)_Y$ symmetry of the SM is broken to the electromagnetic $U(1)_{\text{em}}$ symmetry, yielding a breaking pattern $\mathcal{G}_{\text{SM}} \to SU(3)_C \times U(1)_{\text{em}}$. Additionally, the Higgs mechanism allows fermions and weak gauge bosons to acquire masses without the need of adding them by hand, which would break gauge invariance and endanger the renormalizability of the theory. Thus, the full SM gauge symmetry is preserved at high energies, and the full theory remains renormalizable. In what follows, we describe electroweak symmetry breaking and the generation of the fermion and Z, W masses in the SM.

The Higgs potential

Let us start by studying the gauge and self-interactions of the Higgs, which can be expressed as the Lagrangian

$$\mathcal{L}_{\text{Higgs}} = (D_\mu H)(D^\mu H^\dagger) - V(H)\,, \tag{1.1.12}$$

where the Higgs potential at tree level reads

$$V(H) = -\mu^2 H^\dagger H + \frac{\lambda}{2}(H^\dagger H)^2\,. \tag{1.1.13}$$

[2]The global $U(1)_Y$ is also a conserved symmetry of the Yukawa sector. However, it is only preserved due to the presence of the Higgs, which has non-vanishing hypercharge, and thus we must not count it among the symmetries strictly preserved by fermionic flavor rotations.

If the parameters of the potential fulfill both $\mu^2 > 0$ and $\lambda > 0$, V presents a local maximum at $|H| = 0$ and a global minimum at

$$|H|^2 = \frac{\mu^2}{\lambda} = \frac{v_h^2}{2}\,, \tag{1.1.14}$$

where $v_h = 246$ GeV is the vacuum expectation value (VEV) of the Higgs field. The extrema structure of V is modified when including further terms of the effective potential. Then, renormalization group running of the Higgs quartic can lead to the vacuum becoming metastable or unstable [34–36], as we shall discuss further in Sec. 1.2. Here we focus on the tree level relations arising from spontaneous symmetry breaking. To this end, the Higgs field can be written in terms of its $SU(2)_L$ components as

$$H(x) = \frac{1}{\sqrt{2}} \begin{pmatrix} \varphi_1(x) + i\varphi_2(x) \\ \varphi_3(x) + i\varphi_4(x) \end{pmatrix}\,, \tag{1.1.15}$$

which contains four degrees of freedom corresponding to real scalar fields φ_i. Using Eq. (1.1.15) one obtains $|H|^2 = (\varphi_1^2 + \varphi_2^2 + \varphi_3^2 + \varphi_4^2)/2$, so that we may choose the minimum H_0 to be at

$$\varphi_1 = \varphi_2 = \varphi_4 = 0\,, \qquad \varphi_3^2 = v_h^2 = \frac{2\mu^2}{\lambda}\,, \qquad H_0 = \frac{1}{\sqrt{2}} \begin{pmatrix} 0 \\ v_h \end{pmatrix}\,, \tag{1.1.16}$$

see for instance [31]. In the unitary gauge, expanding H around H_0 yields

$$H(x) = \frac{1}{\sqrt{2}} \begin{pmatrix} 0 \\ v_h + h(x) \end{pmatrix}\,, \tag{1.1.17}$$

where h is the Higgs boson with mass $m_h \simeq 125$ GeV [37], fulfilling $m_h = v_h\sqrt{\lambda}$ with $\lambda(m_h) \simeq 0.26$. The reason why H can be expressed as in Eq. (1.1.17) is rooted in the $SU(2)_L$ invariance of $\mathcal{L}_{\text{Higgs}}$, and the fact that we can use an $SU(2)_L$ rotation to remove three of the field perturbations around the ground state. In order to see this more explicitly, we apply such an $SU(2)_L$ transformation to (1.1.17), with finite parameters $w_a(x)/v_h$. This yields

$$H(x) \to\ e^{i\sigma^a w_a(x)/v_h}\, H(x) = \frac{1}{\sqrt{2}} \begin{pmatrix} w_2(x) + iw_1(x) \\ v_h + h(x) - iw_3(x) \end{pmatrix} + \mathcal{O}\left(\frac{w(x)h(x)}{v_h}\right)\,, \tag{1.1.18}$$

where σ^a are the Pauli matrices, see Appendix A.1. Hence, three of the degrees of freedom of a perturbation around the minimum can be adjusted at will by fixing the parameters w_a of the $SU(2)_L$ transformations; in other words, they can be removed by fixing the gauge[3] Eq. (1.1.17) corresponds to the unitary gauge, where the Higgs scalar $h(x)$ constitutes the only perturbation around the ground state. Note as well that H_0 is invariant under a gauge transformation with generator $Q_e = T_3 + Y$, yielding

$$H_0 \to\ e^{iQ_e\alpha(x)}\, H_0 = H_0\,, \tag{1.1.19}$$

[3]In our notation, the $SU(2)_L$ gauge bosons transform as $W_\mu^a(x) \to W_\mu^a(x) + \frac{1}{g v_h}\partial_\mu w_a(x)$. In choosing the ground state in Eq. (1.1.17), the unitary gauge corresponds to setting $w_a(x) = 0$.

which entails that the ground state preserves electric charge. Hence, out of the four generators of $SU(2)_L \times U(1)_Y$ only one particular combination is preserved after EWSB, the electric charge of $U(1)_{\rm em}$. According to Goldstone's theorem, there exists one massless Goldstone boson for each broken generator; in this case, the perturbations w_a represent the Goldstone bosons of the Higgs mechanism. In any arbitrary gauge these appear in the Lagrangian as unphysical massless modes, while they are completely absent in the unitary gauge, which we shall use throughout this work.

Masses and mixing

Having reviewed EWSB in the Higgs potential, we are ready to discuss its effects in other sectors of the SM: the Higgs boson kinetic term yields the masses of the Z and W bosons, while the Yukawa sector generates mass terms for the fermions. Let us start with the $SU(2)_L \times U(1)_Y$ interactions of the Higgs, which after EWSB yield

$$\begin{aligned} |D_\mu H_0|^2 &= \left| \left(i g' Y B_\mu + i g T^a W_\mu^a \right) \frac{1}{\sqrt{2}} \begin{pmatrix} 0 \\ v_h \end{pmatrix} \right|^2 = \left| i \frac{v_h}{2\sqrt{2}} \begin{pmatrix} (W_\mu^1 - i W_\mu^2) g \\ W_\mu^3 g + B_\mu g' \end{pmatrix} \right|^2 \\ &= \frac{v_h^2}{4} g^2 W_\mu^+ W^{\mu -} + \frac{v_h^2}{8} (W_\mu^3,\ B_\mu) \begin{pmatrix} g^2 & -g g' \\ -g g' & g'^2 \end{pmatrix} \begin{pmatrix} W^{3\mu} \\ B^\mu \end{pmatrix} , \end{aligned} \tag{1.1.20}$$

according to the covariant derivative in Eq. (1.1.5), and we used $W_\mu^\pm = (W_\mu^1 \mp i W_\mu^2)/\sqrt{2}$ as well as the generators $T^a = \sigma^a/2$ in the doublet representation. Then, the mass of the $W^\pm$ bosons can be automatically read off Eq. (1.1.20), and obeys

$$M_W = \frac{1}{2} v_h g \, . \tag{1.1.21}$$

Furthermore, the matrix mixing the neutral bosons B and W_3 can be diagonalized yielding two eigenstates

$$A_\mu = \cos\theta_w B_\mu + \sin\theta_w W_\mu^3 \, , \qquad Z_\mu = \cos\theta_w W_\mu^3 - \sin\theta_w B_\mu \, , \tag{1.1.22}$$

corresponding to the photon and the Z boson respectively, with θ_w the weak mixing angle defined by

$$\cos\theta_w = \frac{g}{\sqrt{g^2 + g'^2}} \, . \tag{1.1.23}$$

The masses of the A_μ and Z_μ bosons can be then computed from Eq. (1.1.20), which gives

$$M_A = 0 \, , \qquad M_Z = \frac{1}{2} v_h \sqrt{g^2 + g'^2} = \frac{1}{2} \frac{v_h g}{\cos\theta_w} \, . \tag{1.1.24}$$

We are now in position to define the ρ-parameter, which involves the ratio of the Z and W boson masses, and provides an important test of the SM. In the Weinberg-Salam model with the Higgs mechanism, one obtains at tree level

$$\rho = \frac{M_W^2}{M_Z^2 \cos^2\theta_w} = 1 \, , \tag{1.1.25}$$

and measurements require $\rho = 1$ within a small error. Indeed, global fits currently yield [16]

$$\rho_0 = 1.00038 \pm 0.00020\,. \tag{1.1.26}$$

The result $\rho = 1$ at tree level in the SM reflects the remnant *custodial* symmetry of the Higgs Lagrangian after EWSB. Before spontaneous symmetry breaking, $\mathcal{L}_{\text{Higgs}}$ presents an $SO(4)$ (or analogously an $SU(2)_L \times SU(2)_R$) global symmetry, which corresponds to rotations of the four real components of H. After the electrically neutral component acquires a VEV, the symmetry is broken to $SO(3)$, and can also be described as the vectorial part $SU(2)_V$ of $SU(2)_L \times SU(2)_R$, known as *custodial isospin* or *custodial* $SU(2)$ [38]. This pattern of global symmetries can be altered in extensions of the SM with additional scalar content, leading to modifications of the ρ-parameter.

Focusing now on the fermion sector, after EWSB the interactions of any chiral (either right- or left-handed) fermion ψ with the neutral gauge bosons become

$$\overline{\psi}\left(-gT^3W_\mu^3 - g'YB_\mu\right)\gamma^\mu\psi = -\overline{\psi}\left(Z_\mu\frac{g}{\cos\theta_w}(T^3 - \sin^2\theta_w Q_e) + e\,Q_e A_\mu\right)\gamma^\mu\psi\,, \tag{1.1.27}$$

where we have used Eqs. (1.1.22), (1.1.28) and (1.1.2), and the couplings obey

$$e = g\sin\theta_w = g'\cos\theta_w\,, \qquad \frac{1}{2v_h^2} = \frac{g^2}{8M_W^2} = \frac{G_F}{\sqrt{2}}\,, \tag{1.1.28}$$

with e the electromagnetic coupling and G_F the Fermi constant. The fine structure constant is then given by

$$\alpha_e = \frac{e^2}{4\pi}\,, \tag{1.1.29}$$

with $\alpha_e \simeq 1/137$ when measured at the electron mass scale.

From Eq. (1.1.27) we can now see that the electromagnetic interaction affects right- and left-handed fields in the same way, since in the SM they carry the same electric charge. Thus, for any Dirac fermion f its QED interactions can be written as

$$\mathcal{L}_{\text{QED}} = -e\,\overline{f}\gamma^\mu Q_e f A_\mu\,. \tag{1.1.30}$$

However, as T^3 components are different for fermions of opposite chirality, the Z current is intrinsically chiral. For a Dirac fermion f it can be expressed in a general way as

$$\mathcal{L}_Z = -\frac{g}{2\cos\theta_w}\overline{f}\,\gamma^\mu(g_V - g_A\gamma^5)f\,Z_\mu = -\frac{g}{2\cos\theta_w}\overline{f}\,\gamma^\mu(c_L P_L + c_R P_R)f\,Z_\mu\,. \tag{1.1.31}$$

Using $s_w^2 = \sin^2\theta_w$, the coefficients of the Z couplings obey

$$\begin{aligned} g_V &= T_L^3 + T_R^3 - 2Q_e s_w^2, & g_A &= T_L^3 - T_R^3\,, \\ c_L &= 2(T_L^3 - Q_e s_w^2), & c_R &= 2(T_R^3 - Q_e s_w^2)\,, \end{aligned} \tag{1.1.32}$$

where T_L^3 (T_R^3) denotes the third isospin component of the left- (right-) handed chirality of each fermion, with all SM fields fulfilling $T_R^3 = 0$. The g_V, g_A couplings in the SM can

Fermion	g_A $\left(g_A^{1,\exp}\right)$	g_V $\left(g_V^{1,\exp}\right)$
u, c, t	$1/2$ $(0.519^{+0.028}_{-0.033})$	$1/2 - 4/3 \sin^2\theta_w \simeq 0.19$ (0.266 ± 0.034)
d, s, b	$1/2$ $(-0.527^{+0.040}_{-0.028})$	$-1/2 + 2/3 \sin^2\theta_w \simeq -0.35$ $(-0.38^{+0.04}_{-0.05})$
e, μ, τ	$-1/2$ (-0.50111 ± 0.00035)	$-1/2 + 2\sin^2\theta_w \simeq -0.038$ (-0.03817 ± 0.00047)
ν_e, ν_μ, ν_τ	$1/2$	$1/2$ $(0.5008 \pm 0.0008)^\dagger$

Table 1.2. Couplings of the Z boson to SM fermions, see Eqs. (1.1.31) and (1.1.32). Numerical values are computed using the $\overline{\text{MS}}$ scheme value $\sin^2\theta_w(M_Z) \simeq 0.231$. Between parentheses we show experimental values for the couplings of the first generation [16]. †The neutrino measurement corresponds to the average over neutrino species of the purely left-handed coupling $g^\nu = g_A^\nu = g_V^\nu$.

be found in Tab. 1.2 together with their measured values, which provide stringent tests on BSM models modifying Z interactions.

In the case of charged currents, for any $SU(2)_L$ doublet $\psi = (\psi_1, \psi_2)^T$, where ψ is again a chiral spinor, these can be written as

$$-\overline{\psi}(gT_1 W_\mu^1 + gT_2 W_\mu^2)\gamma^\mu\psi = -\frac{g}{\sqrt{2}}\left(\overline{\psi}_1\gamma^\mu\psi_2 W_\mu^+ + \overline{\psi}_2\gamma^\mu\psi_1 W_\mu^-\right) . \tag{1.1.33}$$

In the SM, only left-handed fields present charged-current interactions, so that the couplings of a Dirac fermion f to the W boson become

$$-\frac{g}{\sqrt{2}}\overline{f}_1\gamma^\mu P_L f_2\, W_\mu^+ + \text{h.c.}\,. \tag{1.1.34}$$

However, before explicitly writing down charged weak interactions after EWSB, it is paramount that we inspect first the Yukawa sector, as rotations to the mass basis affect W interactions of the quarks. The Yukawa interactions of Eq. (1.1.9) after EWSB become

$$-\mathcal{L}_{\text{Yuk, EWSB}} = \frac{1}{\sqrt{2}}(v_h + h)\left[\overline{d}_L\, y_d\, d_R + \overline{u}_L\, y_u\, u_R + \overline{\ell}_L\, y_\ell\, \ell_R\right] + \text{h.c.}\,, \tag{1.1.35}$$

where $\ell = e, \mu, \tau$, $d = d, s, b$ and $u = u, c, t$ and the y_f are diagonal matrices. In order to arrive at (1.1.35), one must first diagonalize the general complex matrices Y_f appearing in Eq. (1.1.9). To this end, we employ a singular value decomposition, where two different unitary matrices L_f, R_f allow to write

$$Y_f = L_f y_f R_f^\dagger\,. \tag{1.1.36}$$

Then, by performing the field redefinitions

$$f_L \to L_f f_L, \qquad f_R \to R_f f_R\,, \tag{1.1.37}$$

the Yukawa sector is successfully diagonalized, yielding the result (1.1.35). The terms proportional to v_h generate masses for the quarks and charged leptons, which fulfill

$$m_f = \frac{v_h}{\sqrt{2}}\, y_f\,. \tag{1.1.38}$$

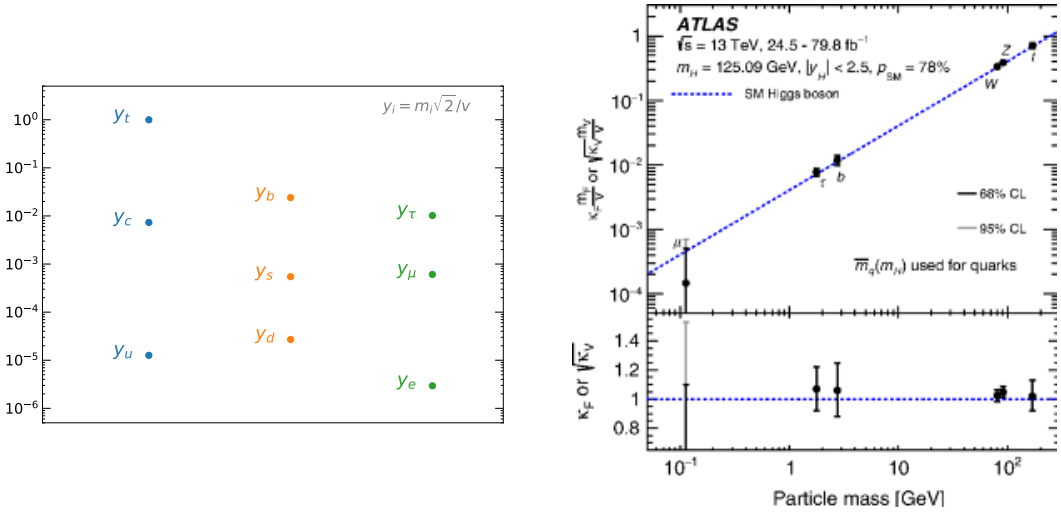

Figure 1.1. Left: values of the diagonal Yukawa couplings in the SM, as computed from the fermion masses in (1.1.39). Right: experimental measurements of the diagonal Yukawa couplings [39], with $\kappa_f = 1$ in the SM. Third-generation Yukawas present the greater experimental accuracy.

within the SM. Measurements of the fermion masses indicate values[4] [16]

$$\begin{aligned} m_u &\simeq 2.2 \text{ MeV}\,, & m_c &\simeq 1.27 \text{ GeV}\,, & m_t &\simeq 172.8 \text{ GeV}\,, \\ m_d &\simeq 4.7 \text{ MeV}\,, & m_s &\simeq 93 \text{ MeV}\,, & m_b &\simeq 4.18 \text{ GeV}\,, \\ m_e &\simeq 0.511 \text{ MeV}\,, & m_\mu &\simeq 105 \text{ MeV}\,, & m_\tau &\simeq 1.78 \text{ GeV}\,. \end{aligned} \tag{1.1.39}$$

Then, in the SM the values of the diagonal Yukawa couplings y_f can be computed from the masses (1.1.39) and the relation (1.1.38), given by spontaneous symmetry breaking through the Higgs mechanism. The resulting values of the Yukawas in the SM are shown schematically in Fig. 1.1 (left). The fact that the y_f differ by several orders of magnitude, from $y_t \sim 1$ to $y_e \sim 10^{-6}$, remains an unexplained feature of the SM. Performing precise, independent measurements of Yukawa couplings represents an important, yet experimentally challenging, test of the theory. Indeed, the Higgs decay rates to fermions are proportional to the Yukawa couplings squared (or, equivalently, proportional to m_f^2/v_h^2), and therefore generally very small. Third-generation Yukawas present the best opportunities to be determined experimentally, and are measured to a far greater accuracy than any other generation [39], as seen in Fig. 1.1 (right). In the case of the lighter flavors, measurements still allow for considerable room for new physics [40].

Regarding the kinetic terms, the unitary rotations (1.1.37) cancel everywhere in Eq. (1.1.4) except for the charged weak currents. Mixing matrices do not appear in Higgs-fermion interactions, as a consequence of each fermion species acquiring mass from the vacuum expectation value of a single scalar. This result is also known as the Paschos-Weinberg

[4]The light quark masses m_u, m_d, m_s are computed in the $\overline{\text{MS}}$ scheme at the scale $\mu = 2$ GeV. The charm and bottom mass correspond to $m_c(\mu = m_c)$ and $m_b(\mu = m_b)$ as well in the $\overline{\text{MS}}$ scheme. The value m_t in Eq. (1.1.39) stems from direct measurements, and can be interpreted as the pole mass [16].

theorem [41, 42], and entails that in the SM there are no scalar-mediated flavor-changing currents. As already mentioned, rotations to the mass basis do have an effect on W-mediated currents. Indeed, using Eq. (1.1.34) and performing the rotations (1.1.37) one obtains

$$\mathcal{L}_W = -\frac{g}{\sqrt{2}} \left(\overline{u}\, V_{\rm CKM}\, \gamma^\mu P_L d + \overline{\nu} \gamma^\mu P_L \ell\right) W_\mu^+ + \text{h.c.}\,. \tag{1.1.40}$$

where $\nu = \nu_e, \nu_\mu, \nu_\tau$ and $V_{\rm CKM}$ is the Cabibbo–Kobayashi–Maskawa (CKM) quark-mixing matrix, which corresponds to the combination of left-handed quark rotations

$$V_{\rm CKM} = L_u^\dagger L_d = \begin{pmatrix} V_{ud} & V_{us} & V_{ub} \\ V_{cd} & V_{cs} & V_{cb} \\ V_{td} & V_{ts} & V_{tb} \end{pmatrix} . \tag{1.1.41}$$

In the SM, the CKM matrix is strictly unitary, and contains three angles and one phase, which is responsible for $\mathcal{CP}$ violation in the quark sector. The Wolfenstein parametrization allows to write the CKM matrix as an expansion in a small parameter λ, which can be approximately identified with the Cabbibo angle. The CKM matrix then takes the form

$$V_{\rm CKM} = \begin{pmatrix} 1 - \frac{1}{2}\lambda^2 & \lambda & A\lambda^3(\overline{\rho} - i\overline{\eta}) \\ -\lambda & 1 - \frac{1}{2}\lambda^2 & A\lambda^2 \\ A\lambda^3(1 - \overline{\rho} - i\overline{\eta}) & -A\lambda^2 & 1 \end{pmatrix} + \mathcal{O}(\lambda^4)\,. \tag{1.1.42}$$

Fits indicate $\lambda = 0.22453 \pm 0.00044$, $A = 0.836 \pm 0.015$, $\overline{\rho} = 0.122^{+0.018}_{-0.017}$ and $\overline{\eta} = 0.355^{+0.012}_{-0.011}$ [37]. At order λ^3, the $\mathcal{CP}$-violating phase only enters the CKM elements V_{td} and V_{ub}, and is absent elsewhere. Furthermore, the CKM matrix presents a highly hierarchical nature, with diagonal entries close to 1. Together with the unknown origin of the order-of-magnitude disparity of the Yukawa couplings, the lack of an established explanation for the observed pattern of quark mixing is often referred to as the *SM flavor puzzle*. Simply put, it consists in the question of why all fermions exist in three generations which only differ in their masses, while exhibiting a very specific mixing pattern in the quark sector.

After studying mixing in the quark sector, it is worth reflecting on why rotations to the mass basis do not affect leptons. This is due to the fact that in the SM neutrinos are strictly massless and left-handed, which permits us to freely perform any rotations on the ν_L. More explicitly, the rotation of the ℓ_L field in the W currents can be canceled by an analogous rotation of the ν_L. This entails that, in the SM, lepton flavor is strictly conserved. Nevertheless, it is now established that neutrinos are not massless [4, 5], and therefore lepton flavor must be violated at some scale.

Finally, putting together all the pieces of the SM leads us to the full Lagrangian

$$\mathcal{L}_{\rm SM} = \mathcal{L}_{\rm gauge} + \mathcal{L}_{\rm kin} + \mathcal{L}_{\rm Yuk} + \mathcal{L}_{\rm Higgs}\,, \tag{1.1.43}$$

as written in Eqs. (1.1.4), (1.1.9) and (1.1.12) before EWSB, and where $\mathcal{L}_{\rm gauge}$ contains the kinetic terms of the gauge bosons. After EWSB, it can prove useful to use $\mathcal{L}_{\rm QED}$, $\mathcal{L}_Z$

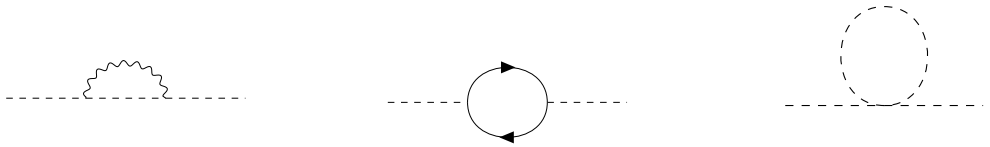

$\sim g^2/(4\pi)^2$ $\sim y^2/(4\pi)^2$ $\sim \lambda/(4\pi)^2$

Figure 1.2. Schematic scaling of 1-loop diagrams of gauge (left), Yukawa (center) and scalar quartic (right) couplings.

and $\mathcal{L}_W$ (Eqs. (1.1.30), (1.1.31) and (1.1.40), respectively) for electroweak interactions, and Eq. (1.1.35) for the Yukawa interactions. At this point, we are equipped to count the parameters of the SM. These consist of 6 quark masses, 3 charged-lepton masses, 4 CKM parameters, 3 gauge couplings, the Higgs quartic coupling and the Higgs mass, which add up to 18 independent parameters. There is, however, an additional interaction which we have not considered so far. This corresponds to the strong $\mathcal{CP}$ phase $\theta_{\rm QCD}$, which enters the SM Lagrangian in the form

$$\mathcal{L}_\theta = \theta_{\rm QCD}\frac{g_3^2}{32\pi^2}\epsilon^{\mu\nu\alpha\beta}G^a_{\mu\nu}G^a_{\alpha\beta}\,, \tag{1.1.44}$$

and stems from anomalous chiral rotations [38]. Neutron electric dipole moment (EDM) measurements indicate the strong $\mathcal{CP}$ phase to be very suppressed, at order $\theta_{\rm QCD} \lesssim 10^{-13}$ [43]. The absence of an established explanation for the smallness of this parameter leads to a fine-tuning problem, referred to as the strong $\mathcal{CP}$ problem, which remains an open question in the SM. Terms analogous to Eq. (1.1.44) but for the $SU(2)_L$ and $U(1)_Y$ tensors are also allowed. Such interactions, however, can be removed by performing chiral rotations, which is not the case for $\theta_{\rm QCD}$ [38]. This completes our parameter counting of the SM, yielding a theory with 19 free parameters. Although at first glance this might seem a theory with low predictivity, the astounding success of the SM relies exactly on the fact that hundreds of measured observables can be explained with the same values of the parameters.

1.2 Running of Couplings in the Standard Model

An important feature of quantum field theories such as the Standard Model consists in the energy dependence of the physical couplings of the theory, a behavior known as running, which arises due to quantum fluctuations. In this work, the running of couplings will play a crucial role, serving as a guiding tool to look for new physics. In this section we review the main features of the evolution of gauge, Yukawa and scalar quartic couplings, with a focus on the interactions of the SM.

The evolution of couplings with the energy scale is encoded in their β-functions or renormalization group equations (RGEs), which in turn depend on the interactions and particle content of a model. RGEs can be computed in perturbation theory, with each successive

term being proportional to higher powers of the coupling constants and additional loop factors $1/(4\pi)^2$. In order simplify expressions, it will prove useful to normalize couplings so that factors $1/(4\pi)^2$ no longer appear in the β-functions. Here we shall use

$$\alpha_g \equiv \frac{g^2}{(4\pi)^2}\,, \quad \alpha_y \equiv \frac{y^2}{(4\pi)^2}\,, \qquad \alpha_\lambda \equiv \frac{\lambda}{(4\pi)^2}\,, \tag{1.2.1}$$

where g, y, λ are gauge, Yukawa and scalar quartic couplings appearing in the Lagrangian, respectively. The different normalization for each type of interaction can be understood by looking at its 1-loop contribution to the propagator of a scalar particle: as seen in Fig. 1.2, to close a loop one requires either two gauge or two Yukawa vertices, but only one scalar quartic. Throughout this work, we employ β-functions computed in the modified minimal subtraction ($\overline{\text{MS}}$) scheme [44]. Using the definitions (1.2.1), we define the β-function β_i of any coupling α_i as

$$\beta_i \equiv \frac{d\alpha_i}{d\ln\mu}\,, \tag{1.2.2}$$

where μ is the renormalization scale. A useful way to make sense of the orders in perturbation theory at which one should study β-functions are the Weyl consistency conditions, which relate different β-functions through partial derivatives [27]. Following Weyl consistency, the lowest ordering that is non-trivial in Yukawa couplings includes their β-functions at 1-loop, while the RGEs of gauge couplings should be taken at 2-loop. The scalar sector, which does not enter neither 1-loop Yukawa nor 2-loop gauge β-functions, is not considered. In this approximation, known as `210`, the β-functions of a simple system of one gauge and one Yukawa coupling can be written in a general way as

$$\begin{aligned} \beta_g &= \frac{d\alpha_g}{d\ln\mu} = \alpha_g^2\left(-B + C\alpha_g - D\,\alpha_y\right)\,, \\ \beta_y &= \frac{d\alpha_y}{d\ln\mu} = \alpha_y\left(E\,\alpha_y - F\,\alpha_g\right)\,, \end{aligned} \tag{1.2.3}$$

for gauge and Yukawa couplings respectively, following the notation of [27, 28] and subsequent works. The coefficients B, C, D, E and F are functions of the particle content and charges of the theory, and their signs play an important role in the analysis of β-functions. In any quantum field theory, the 1-loop coefficients E, F of the Yukawa β-functions as well as the two-loop coefficient D in a gauge β-function are always positive, while B and C can take either sign [28, 29]. From inspection of Eq. (1.2.3) one can already expect the signs of the β-function coefficients to play an important role in the evolution of couplings.

1.2.1 Gauge Couplings

Let us first examine the β-functions of gauge couplings at 1-loop. In an $SU(N)$ gauge theory with N_F Weyl fermions transforming in a representation R_F and N_S complex scalars with representation R_S, the 1-loop coefficient B is given by [46]

$$B = \frac{22}{3}N - \frac{4}{3}N_F\,S_2(R_F) - \frac{2}{3}N_S\,S_2(R_S)\,, \tag{1.2.4}$$

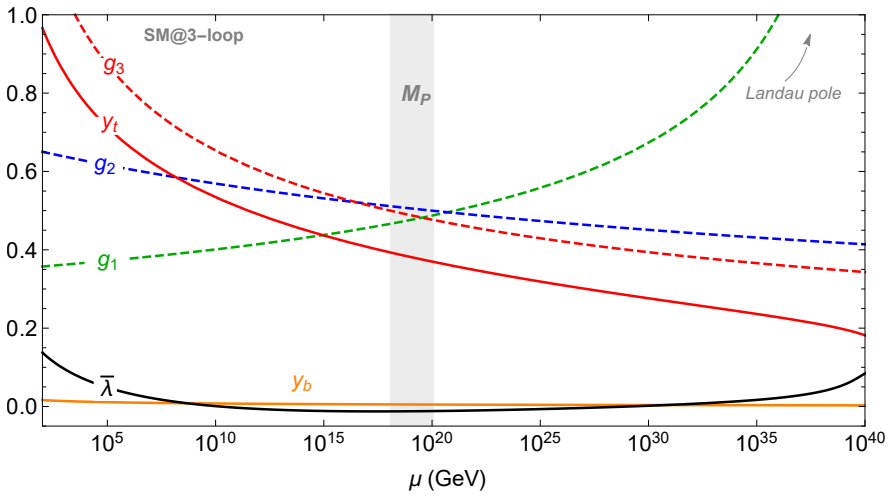

Figure 1.3. Running of the SM couplings at 3-loop. Dotted lines denote gauge couplings, while the top and bottom Yukawas together with the Higgs quartic $\overline{\lambda} = \lambda/2$ (see Eq. (1.1.13)) are shown in full lines. The gray band indicates the Planck scale, while the onset of the $U(1)_Y$ Landau pole can be seen towards the deep UV. RGEs are computed in the $\overline{\text{MS}}$ scheme using `ARGES` [45], and initial conditions extracted from [34].

where S_2 is the Dynkin index, see Appendix B for details. Hence, gauge fields contribute positively to B while charged matter yields negative contributions, so that the 1-loop coefficient can take either sign. For instance, for $SU(3)$ with 12 Weyl fermions transforming as triplets (with $S_2(3) = 1/2$ in $SU(3)$) and no charged scalars, one obtains $B = 22 - 6 = 14$, as is the case for $SU(3)_C$ in the SM. On the other hand, for a $U(1)$ symmetry the 1-loop coefficient is obtained by setting $N = 0$ in Eq. (1.2.4), so that one invariably finds $B < 0$. With this in mind, we can understand the form of the β-functions of the SM gauge couplings at 1-loop, which read

$$\beta^{(1)}_{1,\text{SM}} = \frac{41}{3}\alpha_1^2\,, \quad \beta^{(1)}_{2,\text{SM}} = -\frac{19}{3}\alpha_2^2\,, \qquad \beta^{(1)}_{3,\text{SM}} = -14\,\alpha_3^2\,, \tag{1.2.5}$$

Here, we have used normalized the couplings according to Eq. (1.2.1) and employed

$$g' = g_1, \qquad\qquad g = g_2\,, \tag{1.2.6}$$

for the $U(1)_Y$ and $SU(2)_L$ interactions, in order to align with literature conventions in RGE studies [24–26, 29]. From (1.2.5) we observe that $\beta_{2,\text{SM}}, \beta_{3,\text{SM}} < 0$ and $\beta_{1,\text{SM}} > 0$ at leading order. The 1-loop RGEs can be solved analytically, yielding

$$\alpha_i(\mu) = \frac{\alpha_{i,0}}{1 + \alpha_{i,0}\, B_i \ln \frac{\mu}{\mu_0}}\,, \tag{1.2.7}$$

where $\alpha_{i,0} = \alpha_i(\mu_0)$, and B_i are the 1-loop coefficients of the β_i. Assuming that including higher loop orders does not lead to large deviations from the running of Eq. (1.2.7), we can now infer the fate of the SM gauge couplings at high energies: α_2 and α_3 will decrease towards zero, following the behavior called *asymptotic freedom*, while α_1 will grow with

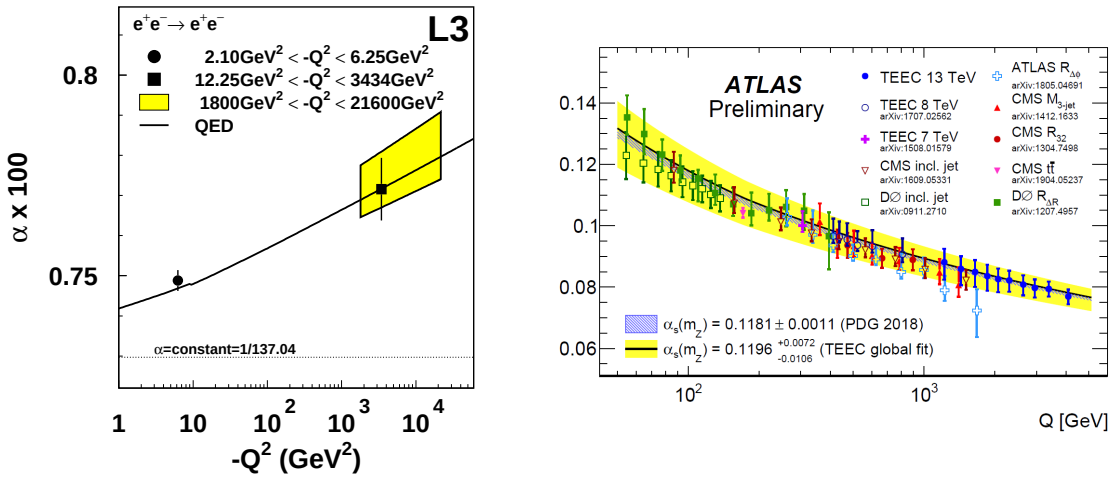

Figure 1.4. Experimental measurements of the electromagnetic coupling [48] with $\alpha_{\rm e} = e^2/(4\pi)$ (left), and the strong coupling [49], with $\alpha_s = g_3^2/(4\pi)$ (right).

energy and eventually diverge, presenting a *Landau pole*. This is indeed the case, as can be seen in Fig. 1.3, where the full 3-loop running of the SM couplings is depicted. For the computation of 3-loop RGEs we have used `ARGES` [45]; results are in agreement with the literature [34, 47]. In Fig. 1.3 the onset of the $U(1)_Y$ divergence can be seen at trans-planckian energies of about $\sim 10^{40}$ GeV. Gravitational interactions kicking in at $M_{\rm Pl}$ could potentially modify the running of α_1 so that the Landau pole is avoided, a possibility that has been explored in the literature [22, 23]. In the absence of such interactions, demanding that the $U(1)_Y$ coupling vanish in the UV within the SM running would require setting $\alpha_1 = 0$ at all scales, which poses a *triviality problem*. Nonetheless, it must be noted that the issues in the running of the hypercharge hinge on the fact that the theory becomes non-perturbative, and therefore we loose our ability to make predictions. In a sense, it may not be very different from the divergence of the strong coupling at low scales: it is not unphysical, but our understanding of physics is hindered past a certain scale. Regardless, if solutions to this problem exist which involve new physics below $M_{\rm Pl}$ (and ideally not far from the TeV scale), these are worth exploring.

Finally, for this work it will prove necessary to study β-functions beyond 1-loop, most importantly in the case of gauge couplings. In a general case of an $SU(N)$ interaction, the 2-loop coefficient C associated to α_g^3 terms reads [46]

$$C = -\frac{68}{3}N^2 + N_F S_2(R_F)\left(4C_2(R_F) + \frac{20}{3}N\right) + N_S S_2(R_S)\left(8C_2(R_S) + \frac{4}{3}N\right), \quad (1.2.8)$$

where R_F, R_S and N_F, N_S are the representations and multiplicities of Weyl fermions and scalars in the theory, respectively. Similarly to the 1-loop coefficients, C can be either negative or positive, depending on the balance between gauge and matter fields. In the

SM, the 2-loop β-functions of the gauge sector read

$$\begin{aligned}
\beta^{(2)}_{1,\mathrm{SM}} &= \alpha_1^2 \left(\frac{41}{3} + \frac{199}{9}\alpha_1 + 9\alpha_2 + \frac{88}{3}\alpha_3 - \frac{17}{3}\alpha_t \right) , \\
\beta^{(2)}_{2,\mathrm{SM}} &= \alpha_2^2 \left(-\frac{19}{3} + \frac{35}{3}\alpha_2 + 3\alpha_1 + 24\alpha_3 - 3\alpha_t \right) , \\
\beta^{(2)}_{3,\mathrm{SM}} &= \alpha_3^2 \left(-14 - 52\alpha_3 + 11\alpha_1 + 9\alpha_2 - 4\alpha_t \right) ,
\end{aligned} \tag{1.2.9}$$

where we have included effects of the top Yukawa, which enter, as expected, with a negative sign. Note that only in the case of $SU(3)_C$ one obtains $C < 0$.

1.2.2 Yukawa Couplings

For Yukawa couplings, β-functions depend both on Yukawa and gauge couplings already at 1-loop. For instance, in the SM the top and bottom Yukawas present 1-loop RGEs

$$\begin{aligned}
\beta^{(1)}_{t,\mathrm{SM}} &= \alpha_t \left(9\alpha_t + 3\alpha_b - \frac{17}{6}\alpha_1 - \frac{9}{2}\alpha_2 - 16\,\alpha_3 \right) , \\
\beta^{(1)}_{b,\mathrm{SM}} &= \alpha_t \left(9\alpha_b + 3\alpha_t \; - \frac{5}{6}\alpha_1 \; - \frac{9}{2}\alpha_2 - 16\,\alpha_3 \right) ,
\end{aligned} \tag{1.2.10}$$

in the approximation where all other Yukawas are negligible, which holds for the β-functions of the SM. Hence, it is not so straightforward to guess the RGE behavior of Yukawa couplings without explicitly evaluating their β-functions at a given scale. In the case of the top, contributions from gauge couplings in Eq. (1.2.10) are always subleading with respect to the α_t^2 term, so that one obtains $\beta_t > 0$ throughout the running. As a consequence, the top Yukawa decreases towards high energies, as seen in Fig. 1.3. There we also show the evolution of the bottom Yukawa, which follows the same behavior, while all other Yukawas are smaller in size and not shown. It is noteworthy that, neglecting the contribution from other Yukawas and the electroweak gauge couplings, the top β-function presents an approximate zero which acts as an infrared (IR) attractor, driving the top Yukawa to a constant value at low energies [28, 50–52]. This allows to parametrize the evolution of y_t in terms of the strong coupling. Then, demanding that the couplings remain perturbative at the Planck scale yields the bound $m_t \gtrsim 210$ GeV [53], obtained before any measurement of the top mass was available. Remarkably, the result stands after experiments have shown $m_t \simeq 173$ GeV.

1.2.3 Higgs Quartic

The RG behavior of scalar quartics can differ substantially from that of gauge or Yukawa couplings. This is due to the fact that, opposed to the latter, the β-functions of a scalar quartic can contain terms which are not proportional to the coupling itself. Thus, their behavior can never be expected to be tamed by small values of the coupling. In the SM, the β-function of the Higgs quartic at 1-loop obeys

$$\beta^{(1)}_{\lambda,\mathrm{SM}} = 12\alpha_\lambda^2 + \frac{3}{4}\alpha_1^2 + \frac{9}{4}\alpha_2^2 + \frac{3}{2}\alpha_1\alpha_2 - 12\alpha_t^2 - \alpha_\lambda(3\alpha_1 + 9\alpha_2 - 12\alpha_t) , \tag{1.2.11}$$

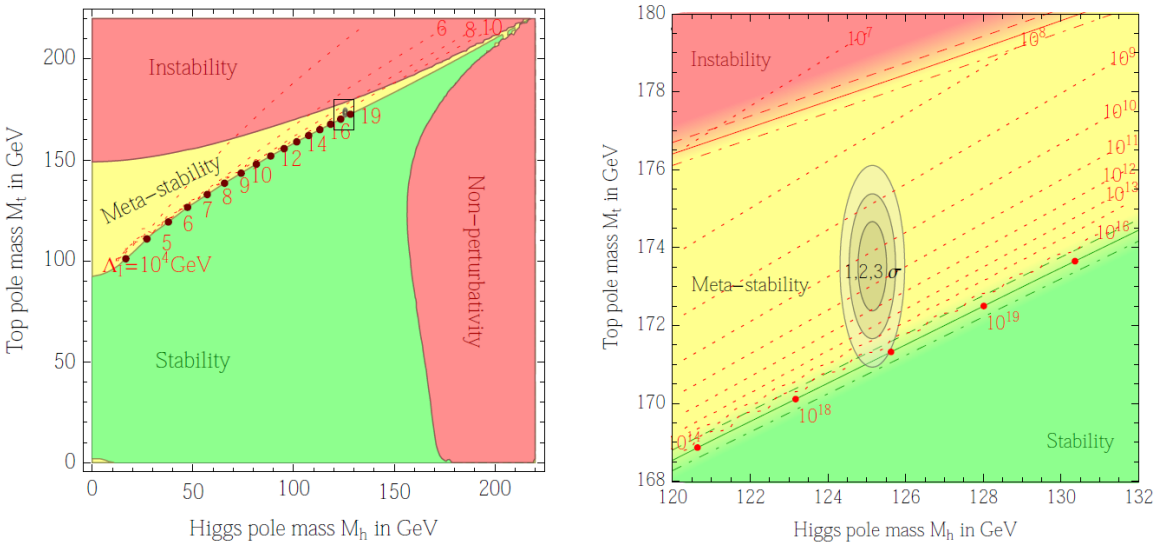

Figure 1.5. Right: phase diagrams depicting the stability of the SM electroweak vacuum in terms of the Higgs and the top pole mass, from [34]. The SM lies in the metastability region, close to the absolute stability limit. Left: zoom in around the experimentally favored region of the top and Higgs mass.

where we have neglected all Yukawas except for the top. As expected, several terms are not proportional to α_λ and can greatly influence the running. For instance, in the vicinity of the electroweak scale β_λ is dominated by the top Yukawa contribution, which yields $\beta_\lambda < 0$. Assuming a constant α_t one can approximate

$$\lambda \simeq \lambda_0 - \frac{3}{4\pi^2}\, y_t^2\, \ln\frac{\mu}{\mu_0}\,. \tag{1.2.12}$$

Indeed, as seen in Fig. 1.3, λ first decreases with energy, switching sign around $\mu \sim 10^{10}$ GeV, and then grows to become positive again beyond $M_{\rm Pl}$. Due to the strong dependence of β_λ on the top Yukawa, the determination of the top mass has crucial implications for the stability of the electroweak vacuum [34–36] at the Planck scale. As as seen in Fig. 1.5, absolute stability ($\lambda > 0$) does not hold at all energies. Instead, the Standard Model electroweak vacuum remains metastable up to the Planck scale, in a region of near-criticality close to the absolute stability boundary.

This concludes our description of the RG behavior of different types of couplings, and their evolution in the case of the SM. We have seen that the SM running is well behaved up to the Planck scale, with the $U(1)_Y$ coupling diverging at higher energies and destabilizing the flow. Moreover, the Higgs potential looses absolute stability below $M_{\rm Pl}$, placing the SM in a region of metastability. These issues can potentially be addressed by new physics, which should present some portal interaction to the SM in order to enter the β-functions of the problematic couplings. In Chapters 3 and 5, we discuss such possibilities in the context of asymptotically safe extensions of the SM.

2 UV-safe Model Building

In Sec. 1.2 we studied the running of SM couplings and in particular their UV behavior. In the case of gauge interactions, we saw that g_2 and g_3 are asymptotically free, evolving towards zero at high energies, while g_1 runs into a transplanckian Landau pole. However, an alternative UV fate of RG flows, termed *asymptotic safety*, is also possible. First conjectured in the context of quantum gravity [54], asymptotic safety proposes that the couplings of a theory run into an interacting fixed point of the renormalization group equations in the UV. The importance of fixed points of the RGEs has been long well established [55, 56]. In fact, asymptotically free couplings tend to zero at high energies driven by the presence of a UV fixed point where they vanish. In this sense, asymptotic safety is a generalization of asymptotic freedom: in the UV couplings run towards constant values, which need not be zero, and enter a nearly-conformal regime.

The discovery that quantum field theories can display asymptotic safety under rigorous perturbative control thanks to the presence of *interacting* UV fixed points is, however, a recent one [27, 28, 57–60], and it has drawn attention for several reasons. In the first place, if one ensures that the fixed points be perturbative, and if an RG trajectory connecting low-energy physics with a UV fixed point exists, theories are well behaved and predictive at all scales. In an extension of the SM presenting such features, the $U(1)_Y$ triviality problem could be resolved, removing UV divergences. Moreover, the limited number of RG trajectories connecting a fixed point with consistent IR physics often leads to a significant reduction of the parameter space of a theory. In model building beyond the SM this results in an enhancement of predictivity, since the requirement that an RG flow from a UV fixed point match measured values of the SM couplings around the electroweak scale constrains BSM parameters. Because of these features, asymptotic safety has begun to be used both as a template to look for extensions of the SM [25, 29, 61] and as a tool reduce the parameter space of known BSM models [62]. Progress in asymptotically safe theories has also been made in the context of supersymmetric models [63, 64], conformal windows of parameters [65], and theories with large particle multiplicities [27, 66–72].

Recently, proposals have been put forward which connect asymptotically safety with flavor physics within and beyond the SM. Indeed, it has been shown that asymptotically safe models may be able to explain measurements in the flavor sector in discrepancy with the SM [24, 25, 73]. Such a scenario is explored in Chapter 3, where we connect asymptotically safe models with data on anomalous magnetic moments. Moreover, asymptotically safe SM extensions may lead to RG-driven flavor structures which can explain or at least alleviate the striking flavor pattern of the SM, both with and without taking into account quantum gravity effects [11, 23, 73, 74]. This is the focus of Chapter 5, which is devoted to asymptotically safe $U(1)$ extensions where flavor hierarchies arise from RG running. Altogether,

asymptotically safe UV completions of the SM can present strong implications for flavor physics.

In the remainder of this chapter we outline the main concepts behind asymptotically safe model building, and provide general formulae. In Sec. 2.1 we review the mechanisms leading to UV fixed points in gauge-Yukawa theories, and in Sec. 2.2 we discuss models where such fixed points arise under perturbative control. In Sec. 2.3, we work out expressions for models containing vector-like fermions, which represent key ingredients in asymptotically safe theories [27, 28]. Finally, Sec. 2.4 is devoted to studying the extended scalar sector typically present in asymptotically safe extensions of the SM.

2.1 Asymptotic Safety in Gauge-Yukawa Theories

As a starting point, asymptotic safety requires that the β-functions of a theory present a fixed point, i.e. some set of coupling values α^* for which all β-functions vanish. This condition can be expressed as

$$\beta_i(\alpha)\big|_{\alpha=\alpha^*} \equiv \frac{d\alpha_i}{d\ln\mu}\bigg|_{\alpha=\alpha^*} = 0\,. \tag{2.1.1}$$

In general, when looking for fixed points we shall demand the following:

i) The coordinates must be physical, fulfilling $\alpha_i^* \geq 0$

ii) Couplings must be perturbative, which requires $\alpha_i^* \leq 1$

with the couplings α_i normalized according to Eq. (1.2.1). Condition *ii*) allows to choose weakly interacting fixed points, which can potentially render the theory predictive at all scales. In order to illustrate the instances in which a model can present such fixed points we now study a simple gauge theory containing one gauge coupling g and one Yukawa coupling y. Following [27–29] and related works, in the `210` approximation we can express the β-functions of such a theory as

$$\begin{aligned} \beta_g &= \alpha_g^2\left(-B + C\alpha_g - D\,\alpha_y\right)\,, \\ \beta_y &= \alpha_y\left(E\,\alpha_y - F\,\alpha_g\right)\,, \end{aligned} \tag{2.1.2}$$

as already discussed in Sec. 1.2. Several types of fixed points exist for the system (2.1.2). Firstly, the *gaussian fixed point* is given by

$$\alpha_g^* = \alpha_y^* = 0\,, \tag{2.1.3}$$

and may present itself in different energy regimes depending on the specific particle content and symmetries of a theory. The sign of the 1-loop coefficient is in this case key: for $B > 0$ the gaussian fixed point is reached in the IR in the direction of the gauge coupling, while for $B < 0$ it is reached in the UV. In the SM, the gaussian fixed point is responsible for the

asymptotically free behavior of α_2 and α_3. Next, Eq. (2.1.2) admits a fixed point where α_y is asymptotically free but α_g is interacting, given by

$$\alpha_g^* = \frac{B}{C}\,, \qquad \alpha_y^* = 0\,. \tag{2.1.4}$$

The above solution is known as the *Caswell-Banks-Zaks fixed point* [75, 76], and it requires $B/C > 0$ in order to be physical and $B/C < 1$ to ensure perturbativity. As we shall detail shortly, the Caswell-Banks-Zaks fixed point (2.1.4) can only be reached in the infrared along the direction of the gauge coupling. Therefore, it is not a suitable solution if we are attempting to find gauge-Yukawa theories with asymptotic safety in the UV. Finally, the system in study permits another type of fixed point, where both couplings are non-vanishing. This is the case of the *gauge-Yukawa fixed point*, which presents coordinates

$$\alpha_g^* = \frac{B}{C'}\,, \qquad \alpha_y^* = \frac{BF}{C'E}\,, \tag{2.1.5}$$

with

$$C' = C - \frac{DF}{E}\,, \tag{2.1.6}$$

where the coefficient C' can take either sign, so that the fixed point can be physical for both $B < 0$ and $B > 0$. Gauge-Yukawa fixed points have the particularity that, unlike Caswell-Banks-Zaks fixed points, they can be reached the UV [28] and, opposed to the gaussian, the gauge coupling is interacting at the fixed point. Thus, they can potentially describe a UV behavior which differs from asymptotic freedom and at the same time provide a controlled RG evolution at all energies. These are, in fact, the fixed points of asymptotic safety, which we focus on in this work.

2.1.1 Stability Analysis

A crucial question when studying fixed points of the RGEs is whether they can be reached in the UV or the IR, and in which particular directions in coupling space this is possible. Here we aim to address this question in more detail by studying the RG flow around the fixed points of the simplified system described in the previous section. In what follows, we designate directions in coupling space as *relevant* if they allow to reach the fixed point in the UV, and as *irrelevant* if they draw couplings away from it. Thus, the notion of relevant or irrelevant we employ refers to the orientation of a direction with respect to a particular fixed point. In some cases a direction in coupling space might correspond to a good approximation to variations of a single coupling. In these cases, we shall speak of relevant or irrelevant couplings for simplicity.

In order to see how the couplings flow around a given fixed point, we begin by expanding the β-functions in its vicinity, which results in the linearized flow

$$\beta_i = \sum_j M_{ij}\delta_j + \mathcal{O}(\delta^2)\,, \tag{2.1.7}$$

where $\delta_i = \alpha_i - \alpha_i^*$. The *stability matrix* M_{ij} is given by the first derivatives of the β-function, and obeys

$$M_{ij} = \left.\frac{\partial \beta_i}{\partial \alpha_j}\right|_{\alpha=\alpha^*} . \tag{2.1.8}$$

An analytical first order solution for the evolution of the couplings around the fixed point can be obtained by solving the linearized set of β-functions, which must first be decoupled. To that end, we first rewrite Eq. (2.1.7) as

$$\frac{d\delta_i}{d\ln\mu} \simeq \sum_j M_{ij}\delta_j = \sum_j (V\theta V^{-1})_{ij}\delta_j \,, \tag{2.1.9}$$

where we decomposed M in terms of a matrix V containing its eigenvectors as columns and the diagonal matrix θ composed of its eigenvalues. Using the redefinition of couplings $\sigma_i = (V^{-1})_{ij}\delta_j$ the system of RGEs decouples, yielding

$$\frac{d\sigma_i}{d\ln\mu} \simeq \theta_i \sigma_i \,, \tag{2.1.10}$$

where there is no implicit sum over i. Solving the above readily gives

$$\sigma_i - \sigma_i^0 \simeq c_i \ln\left(\frac{\mu}{\mu_0}\right)^{\theta_i} , \tag{2.1.11}$$

with c_i the integration coefficients associated to each eigenvector, and $\sigma_i^0 = \sigma_i(\mu_0)$. Then, after undoing both variable changes one obtains

$$\alpha_i \simeq \alpha_i^* + \sum_j c_j V_{ji} \left(\frac{\mu}{\mu_0}\right)^{\theta_j} , \tag{2.1.12}$$

where μ_0 is a scale sufficiently close to the fixed point so that $\delta_i^0 \simeq 0$. Eq. (2.1.12) encapsulates the features of the flow around a fixed point. Firstly, the eigenvalues θ_j act as *critical exponents* of the RG flow, and their sign determines whether the corresponding eigendirection drives α_i away from or closer to the fixed point. More explicitly, if μ_0 is a high scale the fixed point can only be reached in the UV if at least one of the eigenvalues is negative. Thus, the eigenvectors associated to negative (positive) eigenvalues correspond to relevant (irrelevant) directions. Lastly, one might encounter eigenvalues which exactly vanish. Their associated directions are called *marginal*, and do not alter the flow from the fixed point at first order. At higher orders, however, they might drive couplings towards the UV fixed point, in which case they are *marginally relevant*, or away from it when they are *marginally irrelevant*.

We now take the Caswell-Banks-Zaks fixed point of the system in Eq. (2.1.2), given by the coordinates (2.1.4). The critical exponents that follow from diagonalizing the stability matrix obey

$$\theta_1 = -\frac{BF}{C} \,, \qquad \theta_2 = \frac{B^2}{C} \,, \tag{2.1.13}$$

with $\theta_1 < 0 < \theta_2$. The sign of the scaling exponents can be deduced from the fact that, for a gauge theory with $B \leq 0$ one immediately obtains $C > 0$. This entails that Caswell-Banks-Zaks points, which require $B \cdot C > 0$ to be physical, only appear in theories with $B, C > 0$ [28]. Then, from Eq. (2.1.13) one obtains $\theta_2 > 0$ and the general result $F > 0$ gives $\theta_1 > 0$. The corresponding eigenvectors in the (α_g, α_y) basis obey

$$v_1 = \left(\frac{BD}{C(B+F)}, 1 \right) , \qquad v_2 = (1, 0) . \tag{2.1.14}$$

Then, and according to Eq. (2.1.12), v_2 is an irrelevant direction which at first order is strictly in the direction of gauge coupling, while v_1 is UV-attractive and runs mostly along the direction of the Yukawa coupling. Therefore, in the absence of Yukawa interactions, Caswell-Banks-Zaks fixed points are invariably IR. In the case of gauge-Yukawa fixed points, the scaling exponents are given by

$$\theta_1 \simeq \frac{B^2}{C'} , \qquad \theta_2 \simeq \frac{BF}{C'} , \tag{2.1.15}$$

at leading order in $B/C' \ll 1$. With $B/C' > 0$, and since F is always positive, one always finds $\theta_2 > 0$. However, for a negative shifted coefficient C' (see Eq. (2.1.6)) one obtains $\theta_1 < 0$. This is only possible for theories with $B < 0$. Then, the eigenvector of the relevant direction again in the $B/C' \ll 1$ limit reads

$$v_1 = \left(\frac{E}{F} \left(1 - \frac{B}{F} \right) , 1 \right) , \tag{2.1.16}$$

for which both components fulfill $v_1^i > 0$. Thus, the theory presents an asymptotically safe fixed point which can be reached in the UV along a direction involving the gauge and the Yukawa couplings. This relevant direction corresponds to the 1-dimensional UV-critical surface of the flow, known as the *separatrix* [28]. The significance of this trajectory relies on the fact that all UV theories which lie close to the gauge-Yukawa fixed point will flow into the IR approximating the separatrix, and therefore will present the same IR physics. A useful way to study the evolution of the gauge coupling along the separatrix is to fix the Yukawa coupling by the *nullcline condition* $\beta_y = 0$, which yields $\alpha_y = (F/E)\alpha_g$. Then, the gauge coupling runs according to

$$\beta_g = \alpha_g^2 (-B + C' \alpha_g) . \tag{2.1.17}$$

Solutions of the above yield good approximations of the separatrix, coinciding both in the vicinity of the gaussian and close to the UV fixed point [29].

To summarize, we have now studied the linearized flow (2.1.12) of the gauge-Yukawa system, and explicitly given its coefficients around the Caswell-Banks-Zaks and gauge-Yukawa fixed points. The former can only be reached in the IR if Yukawa couplings are absent, whereas the gauge-Yukawa fixed point can present relevant directions which allow to reach it in the UV. Therefore, we can now ascertain that *Yukawa couplings are essential for a theory to present asymptotic safety*, an idea which will guide model-building efforts throughout this work.

2.1.2 Asymptotically Free Couplings

We would now like to study in more detail how asymptotically free couplings behave around fixed points. The linearized flow (2.1.12) constitutes a good approximation when at least one of the first order derivatives M_{ij} does not vanish at the fixed point, which is sometimes not the case when some couplings are asymptotically free. For instance, at the gaussian fixed point (2.1.3) the β-function of a gauge coupling α_i fulfills $\partial\beta_i/\partial\alpha_j|_{\alpha=\alpha^*} = 0$, so that $M_{ij} = 0$. In such cases, we must resort to the second order expansion of the β-functions, which can be written down as

$$\beta_i = \sum_j M_{ij}\delta_j + \frac{1}{2}\sum_{j,k} P_{ijk}\delta_j\delta_k + \mathcal{O}(\delta^3)\,, \tag{2.1.18}$$

where we used again $\delta_i = \alpha_i - \alpha_i^*$, and the P_{ijk} encode the second derivatives evaluated at the fixed point, obeying

$$P_{ijk} = \left.\frac{\partial^2\beta_i}{\partial\alpha_j\partial\alpha_k}\right|_{\alpha=\alpha^*}. \tag{2.1.19}$$

Let us now focus on the cause where a gauge coupling α_i is asymptotically free. As one always finds $\beta_i \propto \alpha_i^2$, the only non-vanishing coefficient of the second-order expansion reads $P_{iii} = \partial^2\beta_i/\partial\alpha_i^2|_{\alpha=\alpha^*}$. In the case of the simple system of Eq. (2.1.2), one finds $P_{iii} = 2(-B + C\alpha_y^*)$. In order to obtain expressions for the second derivatives in a general case, we first write the 2-loop β-function of a gauge coupling in any model as

$$\beta_i = -\alpha_i^2\left(B_i - \sum_{j=\text{gauge}} C_{ij}\,\alpha_j + \sum_{n=\text{Yukawa}} D_{in}\,\alpha_n\right) + \mathcal{O}\left(\alpha^4\right)\,, \tag{2.1.20}$$

where the indices now include all possible gauge and Yukawa interactions in the theory. Then, at a fixed point where $\alpha_i^* = 0$ one finds

$$P_{iii} = -2\left(B_i - \sum_j C_{ij}\alpha_j^* + \sum_n D_{in}\alpha_n^*\right) = -2B_i^{\text{eff}}\,, \tag{2.1.21}$$

where B_i^{eff} acts as an effective 1-loop coefficient, which allows to write Eq. (2.1.18) as

$$\beta_i \simeq -\alpha_i^2 B_i^{\text{eff}}\,. \tag{2.1.22}$$

At the gaussian fixed point, with all gauge and Yukawa couplings vanishing, one finds $B_i^{\text{eff}} = B_i$ and recovers the 1-loop β-function. In the case where the gauge coupling α_i is asymptotically free, but other couplings can take any value at the fixed point, solving Eq. (2.1.22) describes the flow of α_i to a good approximation. The result is equivalent to solutions of the 1-loop running (given in Eq. (1.2.7)) after substituting B_i for B_i^{eff}. Thus, a gauge coupling vanishing at a fixed point follows a logarithmic evolution where the UV fate of the coupling is determined by the sign of the effective 1-loop coefficient: for $B_i^{\text{eff}} > 0$, the gauge coupling grows as it flows to the IR, while for $B_i^{\text{eff}} < 0$ the coupling must remain zero at all scales if one insists that the fixed point be UV. Therefore, when looking at

asymptotically safe trajectories of a model, if a gauge coupling fulfills $\alpha_i^* = 0$ it will only display non-trivial IR physics if $B_i^{\text{eff}} > 0$.

Conversely, asymptotically free Yukawa couplings present a rather different behavior. Let us also write their general β-function, which can be expressed as

$$\beta_n = \alpha_n \left(\sum_{m=\text{Yukawa}} E_{nm}\, \alpha_m - \sum_{i=\text{gauge}} F_{ni}\, \alpha_i \right) + \mathcal{O}\left(\alpha^3\right), \tag{2.1.23}$$

for a Yukawa coupling α_n. In this case, $M_{nn} = \partial\beta_n/\partial\alpha_n|_{\alpha=\alpha^*}$ does not vanish if at least some gauge or Yukawa coupling in the theory is interacting at the fixed point. For $\alpha_n^* = 0$, the only non-vanishing first derivative obeys

$$M_{nn} = \sum_{m=\text{Yukawa}} E_{nm}\, \alpha_m^* - \sum_{i=\text{gauge}} F_{ni}\, \alpha_i^*. \tag{2.1.24}$$

Therefore, the running of α_n can be approximated at first order, and it takes the form of the exponential evolution in Eq. (2.1.12). To obtain a more explicit result for the running, we rewrite β_n as

$$\beta_n \simeq \alpha_n\, M_{nn}\,, \tag{2.1.25}$$

which leads to the solution

$$\alpha_n(\mu) \simeq \alpha_{n,0} \left(\frac{\mu}{\mu_0}\right)^{M_{nn}}, \tag{2.1.26}$$

where $\alpha_{n,0} = \alpha_n(\mu_0)$ and we assume μ_0 is a high scale. In Eq. (2.1.26) M_{nn} acts as the critical exponent of the flow, and only if $M_{nn} < 0$ the coupling corresponds to a relevant direction of the UV fixed point. In that case, the Yukawa coupling α_n presents an exponential growth towards the IR, a behavior which is radically different to that of asymptotically free gauge couplings, which run out of the fixed point only logarithmically. A case of special interest arises when some of the gauge couplings present $\alpha_i^* \neq 0$, while all the terms corresponding to Yukawa interactions in the right-hand side of Eq. (2.1.24) vanish. Note that this does not require that all Yukawa couplings α_m vanish at the fixed point; it suffices that for the nonzero α_m^* the respective coefficients E_{nm} in the β-function of α_n vanish. Then, given that the F_{ni} are always positive, one invariably obtains $M_{nn} < 0$ and the asymptotically free Yukawa is relevant. In Chapter 5 we explore this possibility within an extension of the SM with non-universal interactions. The non-trivial flavor structure of the studied model allows the coefficients M_{nn} to be substantially different for each asymptotically free Yukawa coupling, leading to significant RG-induced deviations in their numerical values.

In conclusion, in this section we studied how asymptotically free couplings behave near the fixed point. We found that, for gauge couplings, one needs to resort to second-order derivatives to approximate their flow, which turns out to be logarithmic and governed by the effective coefficient B_i^{eff} in Eq. (2.1.21). For $B_i^{\text{eff}} > 0$, the gauge coupling corresponds to a relevant direction of the UV fixed point. In the case of asymptotically free Yukawa couplings, we found that they present an exponential evolution around the fixed point, and grow towards the IR if the relevant first derivative fulfills $M_{nn} < 0$.

2.2 A Template Model towards Asymptotic Safety

In [27] and subsequent works, asymptotic safety in gauge-Yukawa theories was shown to be realized under rigorous perturbative control in models of vector-like fermions, singlet scalars and non-abelian gauge fields. In this section we describe this setup and its features, and go on to motivate its role as an extension of the SM. As the starting point, we consider a theory with an $SU(N)$ gauge symmetry and N_F generations of vector-like fermions ψ_i, transforming in the fundamental representation under $SU(N)$. Given that vector-like fermions do not introduce triangle anomalies, their representations under the gauge group can be chosen freely. We also include $N_F \times N_F$ complex scalars S_{ij}, which are assumed to be singlets under the gauge symmetry. The scalars are meson-like, in the sense that they carry two flavor indices. This model presents renormalizable interactions [27, 28, 60]

$$\mathcal{L}_{\rm AS} = \mathrm{Tr}\left[\overline{\psi} \not{D} \psi\right] + \mathrm{Tr}\left[(\partial_\mu S)^\dagger (\partial^\mu S)\right] - y\,\mathrm{Tr}\left[\overline{\psi}_L S \psi_R + h.c.\right] - V(S)\,, \tag{2.2.1}$$

where the traces run over gauge and flavor indices, and the scalar potential is given by

$$V(S) = -\mu_s^2\,\mathrm{Tr}\Big[S^\dagger S\Big] + u\,\mathrm{Tr}\left[S^\dagger S S^\dagger S\right] + v\,\left(\mathrm{Tr}\left[S^\dagger S\right]\right)^2\,. \tag{2.2.2}$$

A mass term $M_F\,\overline{\psi}_L \psi_R$ for the vector-like fermions is also allowed, as well as trilinear terms in $V(S)$ in the case $N_F = 3$. The key feature of the Lagrangian (2.2.1) in the context of asymptotic safety relies on the presence of the Yukawa coupling y, essential to negotiate interacting UV fixed points. It must be noted, however, that the Yukawa y in Eq. (2.2.1) does not describe the most general form of the interaction. Indeed, the flavor structure of the model allows to write

$$y_{ijkl}\,\overline{\psi}_{Li} S_{jk} \psi_{Rl}\,, \tag{2.2.3}$$

where the indices of the tensor coupling can each take values $i, j, k, l = 1, .., N_F$. However, the number of parameters can be drastically reduced by the use of flavor symmetries. In the absence of the Yukawa interaction (2.2.3), the Lagrangian $\mathcal{L}_{\rm AS}$ presents global flavor symmetry

$$\begin{aligned} U(N_F)^2_\psi &= U(N_F)_{\psi_L} \otimes U(N_F)_{\psi_R}\,, \\ U(N_F)^2_S &= U(N_F)_{S_L} \otimes U(N_F)_{S_R}\,, \end{aligned} \tag{2.2.4}$$

where the $\psi_{L,R}$ transform as triplets under $U(N_F)_{\psi_{L,R}}$, and the scalars transform in the representation $(\mathbf{N_F}, \overline{\mathbf{N}}_\mathbf{F})$ under $U(N_F)_{S_L} \otimes U(N_F)_{S_R}$. Identifying $U(N_F)^2_S$ with $U(N_F)^2_\psi$ in Eq. (2.2.4) and imposing that the flavor symmetry be conserved by the full Lagrangian only allows for the single-parameter Yukawa interaction $y\,\mathrm{Tr}\left[\overline{\psi}_L S \psi_R + h.c.\right]$, as written in Eq. (2.2.1).

In terms of RGEs, the model is described by the gauge and Yukawa β-functions in the `210` approximation given in Eq. (2.1.2), in this case with coefficients

$$\begin{aligned} &B = \frac{22}{3}N - \frac{8}{3}N_F S_2(R)\,, \qquad C = 4N_F S_2(R)\left(2C_2(R) + \frac{10}{3}N\right) - \frac{68}{3}N^2\,, \\ &D = 4N_F^2 S_2(R)\,, \qquad E = 2\left(N_F + d(R)\right)\,, \qquad F = 12 C_2(R)\,, \end{aligned} \tag{2.2.5}$$

in terms of the representation R of the vector-like fermions under $SU(N)$. An important feature of the coefficients (2.2.5) is the N_F^2 dependence of the D coefficient, which enters the β-function of the gauge coupling as $\beta_g \propto -D\alpha_y$. For large N_F the coefficient is enhanced with respect to B and C, and can therefore be sizable enough to compensate their effects and deliver $\beta_g = 0$ solutions. The N_F^2 dependence in D stems directly from the flavor structure of the model, in particular from the fact that the scalars S_{ij} carry two flavor indices.

The crucial feature of the model (2.2.1) is that its β-functions present a gauge-Yukawa fixed point the perturbativity of which can be controlled in the *Veneziano limit* [77], which consists in simultaneously taking $N_F \to \infty$, $N \to \infty$ while maintaining the ratio N_F/N fixed. To see the effect of this limit on the β-functions, one rewrites them in terms of the infinitesimal parameter

$$\epsilon = \frac{N_F}{N} - \frac{11}{2}\,. \tag{2.2.6}$$

Assuming the ψ belong to the fundamental representation of $SU(N)$, an expansion in powers of ϵ shows that the gauge-Yukawa fixed point and its critical exponents are perturbative as long as ϵ remains small, see [27] for details. A more detailed analysis of the Veneziano limit is beyond the scope of this work. Here it is sufficient to note that, in theories containing non-abelian gauge interactions together with fermionic and scalar matter, large-N techniques corroborate the viability of UV gauge-Yukawa fixed points. One may also wonder about the dependence of the fixed point on the renormalization scheme, as β-functions at any arbitrary order are generally scheme-dependent. However, the 1-loop coefficients of a gauge β-function β_g are scheme-independent, and the 2-loop gauge contributions to β_g are universal in mass-independent schemes such as $\overline{\text{MS}}$. These features can be used to show that, in the Veneziano limit, the gauge-Yukawa fixed point is invariant under reparameterizations of the gauge coupling at order ϵ, indicating independence of the renormalization scheme [27]. Away from the Veneziano limit, or in systems of β-functions at general loop orders, this invariance cannot be a priori guaranteed. However, we may argue that, if a fixed point is physical, it will lead to measurable effects in observable quantities. Therefore, even though the coordinates α^* may differ in different schemes, the presence of the fixed point may be regarded as a scheme-independent statement.

Next, one might note that the SM itself shares many features with the models of Eq. (2.2.1): it is a gauge theory, with some of the gauge groups being non-abelian, and it contains fermionic and scalar fields with abundant Yukawa interactions. Therefore, it is natural to wonder whether the SM contains UV fixed points which can render it asymptotically safe. Large-N studies, however, are not directly applicable in the SM, for which the number of flavors is fixed to $N_F = 3$ and the gauge groups determined. $1/N$ expansions may in this case prove useful; these are nevertheless beyond this work.

Despite its promising structure, the SM does not, however, display asymptotic safety in the UV. As we already saw in Sec. 1.2, the $U(1)_Y$ coupling suffers from a Landau pole, and the Higgs quartic faces stability issues. Thus, in the SM the Yukawas are not capable of driving

the gauge couplings into a fixed point. This can also be understood by inspection of the 2-loop gauge RGEs shown in Eq. (1.2.9). Take for instance the $U(1)_Y$ β-function: in order to obtain $\beta_{1,\mathrm{SM}} = 0$ the top Yukawa should acquire non-perturbative values, since the 1-loop coefficient B_1 is negative and quite sizable. Furthermore, even if one allowed for $\alpha_t^* > 1$ solutions, these are not accessible in the SM: although the top Yukawa is considerably large at the electroweak scale, it only decreases towards the UV. Hence, we are left with the conclusion that the SM alone cannot display asymptotic safety. Nonetheless, it is possible that in extending the SM it can be rendered asymptotically safe. To this end, one must attempt to include new Yukawa interactions which can deliver UV fixed points for the SM gauge couplings, at least in the case of α_1. For α_2 and α_3 it is in principle sufficient that they remain asymptotically free, but they may also acquire non-vanishing fixed point values. At 2-loop, BSM physics will modify the RGEs of the gauge couplings only if the new states are coupled to the SM through either gauge or Yukawa interactions. Thus, a minimal possibility consists in extending the SM by the model discussed in this section and assume that the vector-like fermions are charged under the symmetries of the SM, as explored in [29] and subsequent works [24, 25, 61]. The Lagrangian of the full theory then reads

$$\mathcal{L}_{\mathrm{SM,\,AS}} = \mathcal{L}_{\mathrm{SM}} + \mathcal{L}_{\mathrm{AS}} + \mathcal{L}_{\mathrm{Y}} - V(H,S)\,, \tag{2.2.7}$$

where the scalar potential fulfills

$$V(H,S) = V(H) + V(S) + \delta\,\mathrm{Tr}\left[S^\dagger S\right] H^\dagger H\,, \tag{2.2.8}$$

and $\mathcal{L}_{\mathrm{Y}}$ contains further BSM Yukawa interactions which may or may not arise depending on the charges of the vector-like fermions. The full theory (2.2.7) includes at least one additional Yukawa coupling, y, which enters the β-functions of the gauge couplings of the symmetries under which the ψ are charged. Hence, it can potentially lead to asymptotically safe solutions involving the SM. Furthermore, the vector-like nature of the new fermionic matter avoids any constraints on its charges arising from triangle anomalies.

2.3 Colorless Vector-like Fermions

As argued in Sec. 2.2, vector-like fermions play an important role in asymptotically safe extensions of the SM. Here, we provide general formulae for color-singlet vector-like fermions, which will prove useful in Chapters 3 and 4. In particular, we focus on vector-like fermions ψ in the singlet, doublet and triplet representation of $SU(2)_L$, and describe their weak interactions including effects from mixing with SM leptons. Let us start by writing the kinetic terms of the ψ in the interaction basis, which read

$$\mathcal{L}_{\psi,\,\mathrm{kin}} = \overline{\psi}_L i\not{D}\psi_L + \overline{\psi}_R i\not{D}\psi_R = \overline{\psi} i\not{D}\psi\,. \tag{2.3.1}$$

Since the left- and right-handed components of the ψ carry the same charges, in the gauge basis they present vanishing axial couplings. The coefficients of the interactions of the Z boson with the ψ then fulfill

$$g_V = c_L = c_R = 2(T^3 - Q_e s_w^2), \qquad g_A = 0\,, \tag{2.3.2}$$

in the conventions of Eq. (1.1.32), where T^3 is the third isospin component of the vector-like fermion. Furthermore, for $SU(2)_L$-charged vector-like fermions both the right- and left-handed components acquire W boson interactions, with numerical factors depending on the particular representation through Clebsch-Gordon coefficients. In the case of $SU(2)_L$ doublets and triplets, the T^3 eigenstates can be expressed as

$$\psi_d = \begin{pmatrix} \psi^{+1/2} \\ \psi^{-1/2} \end{pmatrix} , \qquad \psi_t = \begin{pmatrix} \psi^{+1} \\ \psi^{0} \\ \psi^{-1} \end{pmatrix} , \tag{2.3.3}$$

respectively, where the superscript indicates the T^3 value of each component. Then, their W interactions in the gauge basis obey

$$\begin{aligned} -\overline{\psi}_d \left(g\frac{\sigma^1}{2} W_\mu^1 + g\frac{\sigma^2}{2} W_\mu^2 \right) \gamma^\mu \psi_d &= -\frac{g}{\sqrt{2}}\, \overline{\psi}^{+1/2} \gamma^\mu \psi^{-1/2}\, W_\mu^+ + \text{h.c.}\,. \\ -\overline{\psi}_t \left(g\, t_1 W_\mu^1 + g\, t_2 W_\mu^2 \right) \gamma^\mu \psi_t &= -g \left(\overline{\psi}^{+1} \gamma^\mu \psi^0 - \overline{\psi}^0 \psi^{-1} \right) W_\mu^+ + \text{h.c.}\,, \end{aligned} \tag{2.3.4}$$

where σ^a and t^a correspond to the $SU(2)$ generators in the doublet and triplet representation, respectively, as shown in Appendix A.1. For the triplets, as well as for higher representations, it can be advantageous to employ tensor notation, especially when index contractions are non-trivial. An $SU(2)$ triplet can be written in terms of vectors u^i in the $\mathbf{2}$ and v_j in the $\overline{\mathbf{2}}$ representation as the traceless tensor

$$\mathcal{T}_j^i = u^i v_j - \frac{1}{2} \delta_j^i u^k v_k \,, \tag{2.3.5}$$

see for instance [78, 79]. Then, equating tensor and $SU(2)_L$ components one obtains

$$\psi_2^1 = \psi^{+1} \,, \qquad \psi_1^2 = \psi^{-1} \,, \qquad \psi_1^1 = -\psi_2^2 = \frac{\psi^0}{\sqrt{2}} \,, \tag{2.3.6}$$

so that the triplet can be written in matrix form as

$$\psi_j^i = \begin{pmatrix} \psi^0/\sqrt{2} & \psi^{1+} \\ \psi^{-1} & -\psi^0/\sqrt{2} \end{pmatrix} . \tag{2.3.7}$$

The above is a familiar result, used in the SM to express the W boson triplet as a matrix, allowing us to describe its interactions with doublets in a straightforward way.

Furthermore, vector-like fermions with electric charge $Q_e = +1$ or $Q_e = 0$ can acquire mixing with SM charged leptons or neutrinos, provided they present mixed Yukawa interactions with scalars undergoing spontaneous symmetry breaking. Let us assume that rotations to the mass basis are described through mixing angles θ_L^0 and $\theta_{L,R}$ as

$$\begin{aligned} \psi_X^{-1} &= c_{\theta_X} \psi_X^{-1,\,m} - s_{\theta_X} \ell_X^m \,, \quad \ell_X = c_{\theta_X} \ell_X^m + s_{\theta_X} \psi_X^{-1,\,m} \,, \\ \psi_L^0 &= c_{\theta_L^0} \psi_L^{0,\,m} - s_{\theta_L^0} \nu_L^m \,, \qquad \nu_L = c_{\theta_L^0} \nu_L^m + s_{\theta_L^0} \psi_L^{0,\,m} \,, \end{aligned} \tag{2.3.8}$$

$\overline{f}^{-1}, f'^{-1}$	g_V	g_A
$\bar{\ell}$, ℓ	$-1/2 + 2s_w^2 + \Delta g_V^\ell$	$-1/2 + \Delta g_A^\ell$
$\overline{\psi}^{-1}$, ψ^{-1}	$2\left(T^3_{\psi^{-1}} + s_w^2\right) - \Delta g_V^\ell$	$-\Delta g_A^\ell$
$\overline{\psi}^{-1}$, ℓ	$-\frac{1}{2}\left[s_{2\theta_L}(T^3_{\psi^{-1}} + 1/2) + s_{2\theta_R} T^3_{\psi^{-1}}\right]$	$-\frac{1}{2}\left[s_{2\theta_L}(T^3_{\psi^{-1}} + 1/2) - s_{2\theta_R} T^3_{\psi^{-1}}\right]$

Table 2.1. Coefficients of the Z boson interactions with $Q_e = -1$ fermions in the mass basis (see Eq. (2.3.8) and Eq. (2.3.9)), with $\Delta g^\ell_{\substack{V\\A}} = s^2_{\theta_L}(T^3_{\psi^{-1}} + 1/2) \pm s^2_{\theta_R} T^3_{\psi^{-1}}$.

$\overline{f}^{0}, f'^{0}$	g_V	g_A
$\overline{\nu}$, ν	$1/2 + \Delta g^\nu$	$1/2 + \Delta g^\nu$
$\overline{\psi}^0$, ψ^0	$2T^3_{\psi^0} - \Delta g^\nu$	$-\Delta g^\nu$
$\overline{\psi}^0$, ν	$-\frac{1}{2} s_{2\theta^0_L}(T^3_{\psi^0} - 1/2)$	$-\frac{1}{2} s_{2\theta^0_L}(T^3_{\psi^0} - 1/2)$

Table 2.2. Coefficients of the Z boson interactions with $Q_e = 0$ fermions in the mass basis (see Eq. (2.3.8) and Eq. (2.3.9)), with $\Delta g^\nu = s^2_{\theta^0_L}\left[T^3_{\psi^0} - 1/2\right]$.

where $X = L, R$.[1] The superscripts in Eq. (2.3.8) indicate the electric charge of the vector-like fermions, and m denotes the mass basis. Due to these rotations, chiral interactions are affected, while QED vertices are left invariant. The modified Z couplings to two fermions f and f' in the mass basis are collected in Tabs. 2.1 and 2.2 for the case where both fermions carry electric charge $Q_e = -1$ and $Q_e = 0$, respectively. The couplings are entirely determined by the rotation angles and the T^3 component of the vector-like fermions, and normalized following

$$\mathcal{L}_Z = -\frac{g}{2\cos\theta_w} \overline{f}^{\,Q_e} \gamma^\mu (g_V - g_A\gamma^5) f'^{Q_e} Z_\mu \,. \tag{2.3.9}$$

Note that the charged-lepton couplings are modified by the quantities $\Delta g^\ell_{V,A}$ (see Tab. 2.1). However, measurements of the Z couplings agree with the SM at permille accuracy, as shown in Tab. 1.2, strongly constraining the rotation angles of a BSM model. Moreover, mixing gives rise to Z couplings to an SM lepton and a vector-like fermion. Therefore, it enables electroweak decays of vector-like fermions to Z plus lepton, which can be extremely relevant phenomenologically.

Next, we consider implications of mixing for charged-current interactions, which affect $Q_e = +1, 0, -1, -2$ states. Without specifying the particular $U(1)_Y \times SU(2)_L$ representation of the vector-like fermions, their W interactions can be written as

$$\mathcal{L}_{W,\psi} = -\frac{g}{\sqrt{2}} C_{Q_e} \overline{\psi}^{\,Q_e} \gamma^\mu \psi^{Q_e - 1} W^+_\mu + \text{h.c.}\,. \tag{2.3.10}$$

[1] These rotations correspond to the limit of no flavor mixing, in which each lepton mixes exclusively with one generation of vector-like fermions.

$\overline{f}^{Q_e}, f'^{Q_e-1}$	c_L	c_R	$\overline{f}^{Q_e}, f'^{Q_e-1}$	c_L	c_R
$\overline{\nu}$, ℓ	$c_{\theta_L}c_{\theta_L^0} + C_0 s_{\theta_L}s_{\theta_L^0}$	0	$\overline{\psi}^{+1}$, ψ^0	$C_1 c_{\theta_L^0}$	C_1
$\overline{\psi}^0$, ψ^{-1}	$s_{\theta_L}s_{\theta_L^0} + C_0 c_{\theta_L}c_{\theta_L^0}$	$C_0 c_{\theta_R}$	$\overline{\psi}^{+1}$, ν	$-C_1 s_{\theta_L^0}$	0
$\overline{\psi}^0$, ℓ	$c_{\theta_L}s_{\theta_L^0} - C_0 s_{\theta_L}c_{\theta_L^0}$	$-C_0 s_{\theta_R}$	$\overline{\psi}^{-1}$, ψ^{-2}	$C_{-1}c_{\theta_L}$	$C_{-1}c_{\theta_R}$
$\overline{\nu}$, ψ^{-1}	$s_{\theta_L}c_{\theta_L^0} - C_0 c_{\theta_L}s_{\theta_L^0}$	0	$\overline{\ell}$, ψ^{-2}	$-C_{-1}s_{\theta_L}$	$-C_{-1}s_{\theta_R}$

Table 2.3. Coefficients of the W boson interactions with fermions of electric charge $Q_e = -1, 0, -1, -2$ in the mass basis (see Eq. (2.3.8) and Eq. (2.3.11)).

where C_{Q_e} are Clebsch-Gordan coefficients depending on the $SU(2)_L$ representation of the ψ. After rotations to the mass basis, interactions of vector-like fermions and leptons take the form

$$\mathcal{L}_{W,\text{mix}} = -\frac{g}{\sqrt{2}}\overline{f}^{Q_e}\gamma^\mu(c_L P_L + c_R P_R) f'^{Q_e-1} W_\mu^+ + \text{h.c.}\,, \tag{2.3.11}$$

where the coefficients c_L, c_R are given in Tab. 2.3. There, one observes two effects arising from mixing: on the one hand, vector-like fermions acquire axial couplings at order $s^2_{\theta_{L,R}}$ and, on the other hand, charged leptons pick up $s_{\theta_{L,R}}$-suppressed right-handed couplings to the W boson and a vector-like fermion. Again, this opens up new decay channels of the ψ.

Lastly, let us comment on the representations known as *vector-like leptons*, which carry $SU(3)_C \times SU(2)_L \times U(1)_Y$ charges

$$(1, 1, -1)\,, \qquad \text{or} \qquad (1, 2, -1/2)\,, \tag{2.3.12}$$

coinciding with those of the SM lepton singlet and doublet, respectively. The charged components of the vector-like leptons fulfill $T^3_{\psi^{-1}} = 0$ ($T^3_{\psi^{-1}} = -1/2$) in the singlet (doublet) case, while the neutral component of the doublet representation presents $T^3_{\psi^0} = 1/2$. This leads to certain cancellations in the expressions of Z couplings after mixing, as can be seen from inspection of Tabs. 2.1 and 2.2. In particular, the quantity Δg^ℓ depends only on the rotation angle θ_L (θ_R) for the singlet (doublet) representation, while Δg^ν vanishes.

2.4 Singlet Scalars with a Higgs Portal

In this section we study the vacuum stability and mass spectrum of the scalar sector involving the SM Higgs doublet together with the scalars S_{ij}, with $i, j = 1, ..., N_F$, of the model described in Sec. 2.2. The results describe the scalar sector of general asymptotically safe extensions of the SM based on this model, as studied for instance in [24, 25]. In what follows, we keep N_F as a free parameter while providing in some cases explicit results for $N_F = 3$, as they will prove useful for the models studied in Chapter 3.

The full potential of the scalar sector of study can be written as

$$\begin{aligned} V(H,S) = &- \mu^2 H^\dagger H - \mu_s^2 \operatorname{Tr}\Big[S^\dagger S\Big] + \lambda (H^\dagger H)^2 + \delta H^\dagger H \operatorname{Tr}\Big[S^\dagger S\Big] \\ &+ u \operatorname{Tr}\Big[S^\dagger S S^\dagger S\Big] + v \left(\operatorname{Tr}\Big[S^\dagger S\Big]\right)^2 , \end{aligned} \tag{2.4.1}$$

which follows the notation of the Higgs and S potentials of Eqs. (1.1.13) and (2.2.2), respectively,[2] with the addition of a portal coupling δ. This potential exhibits the BSM flavor symmetry (2.2.4), as well as the SM gauge and flavor symmetries. In particular, for $N_F = 3$ the potential is invariant under $U(3)_{\psi_L} \times U(3)_{\psi_R}$ rotations of the S. Furthermore, the case $N_F = 3$ allows for the trilinear term

$$- \mu_{\det} \left(\det S + \det S^\dagger\right) , \tag{2.4.2}$$

which presents $SU(3)_{\psi_L} \times SU(3)_{\psi_R}$ symmetry. Therefore, $U(3)$ rotations will yield a phase in (2.4.2) which must not necessarily vanish. However, one can then perform an additional $U(1)$ rotation of the S fields in order to cancel such a phase while keeping the potential invariant (see for instance [80] for the study of a scalar model involving trilinear terms).

2.4.1 Vacuum Stability

In order to study the stability of the vacuum, we want to look for directions along which the potential (2.4.1) presents infinite degenerate minima. This set of directions can be studied in terms of classical fields, and is then termed the *classical moduli space* [60, 81]. The idea behind this analysis is to diagonalize the classical field S_c in order to obtain a potential which depends only on its real eigenvalues s_i. Thanks to the flavor symmetry of the potential, all dependence on rotation matrices after diagonalization vanishes and it can be written entirely in terms of the s_i. Then, directions with constant moduli can be defined as those fulfilling $\sum_i s_i^2 = R^2$, where R is a constant. This condition can be enforced by use of a Lagrange multiplier η, which we take to enter the potential as $-2\eta(\sum_i s_i^2 - R^2)$. This will allow us to search for flat directions. The potential to be minimized then becomes

$$\begin{aligned} V(H,s) = &- \mu^2 H^2 - \mu_s^2 \sum_i s_i^2 + \lambda H^4 + \delta H^2 \sum_i s_i^2 \\ &+ u \sum_i s_i^4 + v \left(\sum_i s_i^2\right)^2 - 2\eta \left(\sum_i s_i^2 - R^2\right) , \end{aligned} \tag{2.4.3}$$

where we have substituted $H^\dagger H = H^2$ for simplicity. The first derivatives of the potential now obey

$$\begin{aligned} \frac{\partial V}{\partial s_i} &= 2 s_i \left(-\mu_s^2 + \delta H^2 + 2 u s_i^2 + 2 v R^2 - 2\eta\right) , \\ \frac{\partial V}{\partial H} &= -2 \left(-\mu^2 + 2\lambda H^2 + \delta R^2\right) , \\ \frac{\partial V}{\partial \eta} &= -2 \left(\sum_i s_i^2 - R^2\right) . \end{aligned} \tag{2.4.4}$$

[2] Up to a factor 2 in the Higgs quartic λ.

To find the minima of V we require that all the derivatives in (2.4.4) vanish, with the values $|H|, |s_i|$ of the fields at the minimum constituting their VEVs. From $\partial V/\partial s_i$ in Eq. (2.4.4) one can see that if either one or several of the s_i acquire nonzero VEVs these must all take the same value, which we define as

$$|s_i| = \frac{v_s}{\sqrt{2}} = \frac{R^2}{n}\,, \tag{2.4.5}$$

where n is the number of fields s_i which do acquire a VEV, with possible values $n = 1, ..., N_F$. Then, the potential at the minimum is given by

$$V_{\rm min} = -\,\mu^2\,|H|^2 - \mu_s^2 R^2 + \lambda\,|H|^4 + \delta\,|H|^2\,R^2 + \frac{u}{n}R^4 + vR^4\,. \tag{2.4.6}$$

This result allows to identify two vacuum configurations in terms of the sign of the quartic coupling u. Firstly, for $u < 0$ the potential is minimized for the lowest value of n, which corresponds to $n = 1$. Hence, only one of the diagonal components of the S acquires a VEV. We shall refer to this configuration as V^-. On the other hand, if $u > 0$ the lowest value of $V_{\rm min}$ is given by taking the maximum value of n. This corresponds to $n = N_F$, which entails that all the s_i acquire a VEV. We denote this ground state as V^+. Furthermore, imposing that the potential be bounded from below in the limit $R \to \infty$ leads to the constraint

$$u + nv > 0\,, \tag{2.4.7}$$

which holds for both vacuum structures. In addition, in the limit of large Higgs field one obtains

$$\lambda > 0\,. \tag{2.4.8}$$

Let us study now another flat direction, in which the VEVs of the Higgs and the S fulfill

$$|H|^2 = R\cos\theta\,, \qquad \sum_i |s_i|^2 = R\sin\theta\,, \tag{2.4.9}$$

where the angle θ must belong to the first quadrant so that both vacuum expectation values as well as R remain positive definite. In this direction the potential takes the form

$$V(\theta) = -\,R^2(\mu^2\cos^2\theta + \mu_s^2\sin^2\theta) + R^4\cos^2\theta\left[\lambda + \left(\frac{u}{n} + v\right)\tan^2\theta + \delta\tan\theta\right]\,. \tag{2.4.10}$$

Thus, in the large-R limit V is unbounded from below as soon as the second term in the right-hand side of (2.4.10) becomes negative. Taking into account the conditions (2.4.7) and (2.4.8), one finds that this is only possible for $\delta < 0$. If that is the case, one can show that the minimum value of the potential (2.4.10) is obtained for $\tan\theta_{\rm min} = -\delta/2(u/n + v)$. Imposing that $V(\theta)$ be positive at the minimum for large R we find

$$\delta > -2\sqrt{\lambda(u/n + v)}\,. \tag{2.4.11}$$

This result completes the conditions for absolute stability of the potential (2.4.1). Collecting them for each type of vacua we obtain

$$\begin{aligned} V^+:&\quad \begin{cases} \lambda > 0, \quad u > 0, \quad u + N_F\,v > 0, \\ \delta > -2\sqrt{\lambda\,(u/N_F + v)}\,, \end{cases} \\ V^-:&\quad \begin{cases} \lambda > 0, \quad u < 0, \quad u + v > 0, \\ \delta > -2\sqrt{\lambda\,(u + v)}\,. \end{cases} \end{aligned} \tag{2.4.12}$$

Hence, we have encountered two vacuum structures with distinct stability conditions as well as different implications for flavor. In V^-, where only one of the components s_k acquires a VEV, the flavor k is singled out and after spontaneous symmetry breaking the $U(3)_{\psi_L} \times U(3)_{\psi_R}$ flavor symmetry is broken into $U(2)_{\psi_L} \times U(2)_{\psi_R} \times U(1)$. According to the parameter counting in Eq. (1.1.11), this yields $2 \cdot 9 - 2 \cdot 4 - 1 = 9$ massless modes in S. Conversely, the V^+ vacuum is flavor-symmetric, with the universal VEVs breaking the flavor symmetry into a $U(3)_{diag}$, which yields 9 Goldstone modes as well. The presence of massless modes can be avoided by adding to the potential terms of the type $M_{ij}^2 s_{ij} s_{ij}^*$, which provide masses for the would-be Goldstone bosons at the cost of breaking the global $U(3)_{\psi_L} \times U(3)_{\psi_R}$ symmetry. The symmetries involving the Higgs are the same as in the SM, rendering 3 massless states which in the unitary gauge are absorbed by the W and Z bosons, as described in Sec. 1.1.

Analytical expressions for the vacuum expectation values of the S and the Higgs can be obtained by imposing that the first derivatives in Eq. (2.4.4) vanish at the minimum. Using $|H| = v_h/\sqrt{2}$, we obtain

$$\begin{aligned} v_s^2 &= \frac{\mu_s^2 - \frac{\delta}{2\lambda}\,\mu^2}{u + nv - n\frac{\delta^2}{4\lambda}}\,, \\ v_h^2 &= \frac{\mu^2 - \frac{\delta n}{2(u+nv)}\mu_s^2}{\lambda - n\frac{\delta^2}{4(u+nv)}} = \frac{1}{\lambda}\left(\mu^2 - n\delta\frac{v_s^2}{2}\right). \end{aligned} \tag{2.4.13}$$

Note that only for V^+ including the determinant term (2.4.2) in the Lagrangian affects the expressions of the VEVs. These can be obtained by replacing $\mu_s^2 \to \mu_s^2 + \mu_{\rm det} v_s/\sqrt{2}$ in Eq. (2.4.13) and solving accordingly for v_s.

2.4.2 Scalar Mass Spectrum

Let us now study the scalar mass spectrum for both vacuum structures V^- and V^+. To that end, we express the diagonal components of the S after spontaneous symmetry breaking as

$$S_{ii} = \frac{1}{\sqrt{2}}(s_i + i s_i^c + v_s)\,, \tag{2.4.14}$$

where s_i now denotes the $\mathcal{CP}$-even part of the quantum field S_{ii}, with s_i^c its $\mathcal{CP}$-odd component. Then, in the vacuum V^- aligned along the flavor k the mass terms in the potential (2.4.1) are obtained from

$$\begin{aligned} \left.\frac{\partial^2 V}{\partial h \partial h}\right|_{S,H=0} &= m_h^2 = -\mu^2 + 3v_h^2\lambda + \frac{1}{2}\delta v_s^2 = \frac{2(u+v)\mu^2 - \delta\mu_s^2}{(u+v) - \delta^2/4\lambda}\,, \\ \left.\frac{\partial^2 V}{\partial s_k \partial s_k}\right|_{S,H=0} &= m_s^2 = -\mu_s^2 + 3v_s^2(u+v) + \frac{1}{2}\delta v_h^2 = \frac{2\lambda\,\mu_s^2 - \delta\mu^2}{\lambda - \delta^2/4(u+v)}\,, \\ \left.\frac{\partial^2 V}{\partial h \partial s_k}\right|_{S,H=0} &= m_{sh} = \delta\, v_s v_h = \frac{\delta}{2\sqrt{\lambda(u+v)}}\; m_s m_h\,, \\ \left.\frac{\partial^2 V}{\partial (S_{ij}^2)}\right|_{S,H=0} &= \overline{m}_s^2 = -\mu_s^2 + v_s^2\, v + \frac{1}{2}\delta v_h^2 = -\frac{u}{2(u+v)} m_s^2 \quad \text{for } i,j \neq k\,, \end{aligned} \tag{2.4.15}$$

while all other second derivatives vanish at the minimum. Hence, the scalars with $i, j \neq k$ acquire a mass $\overline{m}_s^2$. Note that $\overline{m}_s^2$ is a positive quantity, since for V^- one requires $u < 0$ and $u + v = 0$. Moreover, Eq. (2.4.15) shows that mixing terms arise between the Higgs scalar and the $\mathcal{CP}$-even part s_k of the component of S which acquires a VEV. Then, h and s_k mix according to the mass potential

$$V^{\text{mass}}(s_k, h) = \frac{1}{2}\begin{pmatrix} s_k \,, & h \end{pmatrix} \begin{pmatrix} m_s^2 & m_{sh} \\ m_{sh} & m_h^2 \end{pmatrix} \begin{pmatrix} s_k \\ h \end{pmatrix} , \tag{2.4.16}$$

which yields the eigenvalues

$$m_{\frac{1}{2}} = \frac{1}{2}\left[m_s^2 + m_h^2 \pm \sqrt{\left(m_s^2 - m_h^2\right)^2 + 4m_{sh}^2} \,\right] . \tag{2.4.17}$$

The mass eigenstates h_1, h_2 can be expressed as

$$\begin{pmatrix} h_1 \\ h_2 \end{pmatrix} = \begin{pmatrix} \cos\beta & \sin\beta \\ -\sin\beta & \cos\beta \end{pmatrix} \begin{pmatrix} s_k \\ h \end{pmatrix} , \tag{2.4.18}$$

in terms of the rotation angle β given by

$$\tan 2\beta = \frac{2m_{sh}}{m_s^2 - m_h^2} = \frac{2\delta v_h v_s}{m_s^2 - m_h^2} , \tag{2.4.19}$$

see Appendix A.2 for details. For BSM models where the S scalars are much heavier than the Higgs, one can approximate

$$\tan 2\beta = \frac{\delta}{\sqrt{\lambda(u+v)}} \frac{m_h}{m_s} \left(1 + \mathcal{O}(m_h^2/m_s^2) \right) . \tag{2.4.20}$$

In V^+, where all diagonal components of S acquire a VEV, the $N_F = 3$ case yields

$$\begin{aligned}
\left.\frac{\partial^2 V}{\partial h \partial h}\right|_{S,H=0} &= {m'_h}^2 = -\mu^2 + 3v_h^2\lambda + \frac{3}{2}\delta v_s^2 \,, \\
\left.\frac{\partial^2 V}{\partial s_i \partial s_i}\right|_{S,H=0} &= {m'_s}^2 = -\mu_s^2 + v_s^2(3u + 5v) + \frac{1}{2}\delta v_h^2 \,, \\
\left.\frac{\partial^2 V}{\partial s_i \partial s_j}\right|_{S,H=0} &= m_{ss} = 2vv_s^2 \quad (i \neq j), \\
\left.\frac{\partial^2 V}{\partial h \partial s_i}\right|_{S,H=0} &= m_{sh} = \delta\, v_s v_h \,, \\
\left.\frac{\partial^2 V}{\partial S_{ij} \partial S^*_{ji}}\right|_{S,H=0} &= 2uv_s^2 \quad \text{for } i \neq j \,,
\end{aligned} \tag{2.4.21}$$

where there are no implicit sums[3]. Thus, in this case the $\mathcal{CP}$-even part s_i of each diagonal component of the S presents mixing with the Higgs scalar. The normalized mass eigenstates

[3]Including the determinant term (2.4.2) yields an extra term $-\mu_{\text{det}} \frac{v_s}{\sqrt{2}}$ in the right-hand side of $\partial^2 V/\partial s_i \partial s_j$ in Eq. (2.4.21).

in the basis (s_1, s_2, s_3, h) read

$$\begin{aligned} h'_1 &= \frac{1}{\sqrt{3}}\left(\cos\beta',\ \cos\beta',\ \cos\beta',\ \sqrt{3}\sin\beta'\right), \qquad h'_3 = \frac{1}{\sqrt{2}}(-1,0,1,0)\,, \\ h'_2 &= -\frac{1}{\sqrt{3}}\left(\sin\beta',\ \sin\beta',\ \sin\beta',\ -\sqrt{3}\cos\beta'\right), \quad h'_4 = \frac{1}{\sqrt{2}}(-1,1,0,0)\,, \end{aligned} \tag{2.4.22}$$

where the corresponding eigenvalues obey

$$\begin{aligned} m'^{\,2}_{1,2} &= \frac{1}{2}\left[m'^{\,2}_s + m'^{\,2}_h + 2m_{ss} \quad \pm \sqrt{\left(m'^{\,2}_s - m'^{\,2}_h + 2m_{ss}\right)^2 + 12\, m_{sh}} \right], \\ m'^{\,2}_3 &= m'^{\,2}_4 = m'^{\,2}_s - m_{ss}\,. \end{aligned} \tag{2.4.23}$$

Note that, due to the degeneracy in the eigenvalues m'_3 and m'_4, any linear combination of the states $h'_{3,4}$ is an eigenvector as well. In the limit $v \to 0$, $\mu_{\rm det} \to 0$ the angle β' can be expressed as

$$\tan 2\beta' = \frac{2\sqrt{3}\, m_{sh}}{m'^2_s - m'^2_h} = \frac{2\sqrt{3}\,\delta v_h v_s}{m'^2_s - m'^2_h}\,. \tag{2.4.24}$$

Inspection of the eigenvectors (2.4.22) shows that the eigenstates $h'_{3,4}$ are purely linear combinations of the gauge eigenstates of the S, while mixing with the Higgs occurs only for the states $h'_{1,2}$, and is universal. This entails that terms in the interaction basis Lagrangian containing the S fields will acquire $\sin\beta'$-suppressed couplings with the Higgs for all flavors involved, in contrast to the case of V^- where only one of the flavors acquires additional Higgs couplings. Both in V^+ and V^+, all mixing-induced interactions are flavor-conserving, since they stem only from diagonal components of the S or the Higgs.

Furthermore, in V^+ the S_{ij} with $i \neq j$ present mixed mass terms, as seen from Eq. (2.4.21). These yield six eigenstates $h^\pm_{ij}$ obeying

$$h^\pm_{ij} = \frac{1}{\sqrt{2}}(S_{ij} \pm S_{ji})\,, \tag{2.4.25}$$

where the h^-_{ij} are massless while h^+_{ij} display masses

$$m_{ij} = 2v_s\sqrt{u}\,. \tag{2.4.26}$$

Let us summarize the scalar mass spectrum. In V^-, the neutral, $\mathcal{CP}$-even component h of the Higgs and the $\mathcal{CP}$-even part s_k of the flavor-aligned scalar S_{kk} mix, and the corresponding eigenstates $h_{1,2}$ acquire masses $m_{1,2}$. The two diagonal components of the S which do not acquire a VEV as well as the off-diagonal components S_{ij} with $i,j \neq k$ acquire a mass $\overline{m}^2_s$. The masses obey

$$\begin{aligned} h_1, h_2 \qquad &\to \qquad m^2_{1,2} = \frac{1}{2}\left[m^2_s + m^2_h \pm \sqrt{\left(m^2_s - m^2_h\right)^2 + 4m^2_{sh}} \right], \\ S_{ij}(i,j\neq k) \quad &\to \qquad \overline{m}^2_s = -\frac{u}{2(u+v)} m^2_s\,, \end{aligned} \tag{2.4.27}$$

with $m_{s,h,sh}$ defined in Eq. (2.4.15). The four remaining S_{ij} (with $i = k$ or $j = k$, and $i \neq j$) and the $\mathcal{CP}$-odd part of S_{kk}, which do not acquire masses, constitute the 9 Goldstone modes.

In V^+, the $\mathcal{CP}$-even parts s_i of the diagonal components of the S mix with h, yielding two eigenstates $h'_{1,2}$ which contain s_k and h, plus two eigenstates $h'_{3,4}$ mixing the s_i amongst themselves. The off-diagonal components of the S_{ij} mix among themselves, yielding 3 massless eigenstates and 3 eigenstates h^+_{ij} with masses m_{ij}. The masses obey

$$\begin{aligned} h'_1, h'_2 \quad &\rightarrow \quad m'^{\,2}_{\frac{1}{2}} = \frac{1}{2}\left[m'^{\,2}_s + m'^{\,2}_h + 2m_{ss} \pm \sqrt{\left(m'^{\,2}_s - m'^{\,2}_h + 2m_{ss}\right)^2 + 12\, m_{sh}} \right], \\ h'_3, h'_4 \quad &\rightarrow \quad m'_3 = m'_4 = m'^{\,2}_s - m_{ss}\,, \\ h^+_{ij} \quad &\rightarrow \quad m_{ij} = 2v_s\sqrt{u}\,, \end{aligned} \tag{2.4.28}$$

with $m'_{s,h}$ and m_{ss} given in Eq. (2.4.21). The three massless eigenstates h^-_{ij} of Eq. (2.4.25), which are complex scalars, together with the three $\mathcal{CP}$-odd components s^c_i of the S_{ii}, constitute the 9 Goldstone modes of V^+.

3 Vector-Like Fermions as Flavor Portals

Vector-like fermions play a crucial role in models featuring asymptotic safety [27, 28]. In Sec. 2.2, we saw explicitly that the model (2.2.1) containing N_F generations of vector-like fermions and $N_F \times N_F$ complex scalars S_{ij} can present asymptotic safety under strict perturbative control. The key ingredient is the Yukawa interaction

$$\mathcal{L}_y = -y \operatorname{Tr}\left[\overline{\psi}_L S \psi_R + \text{h.c.}\right], \tag{3.0.1}$$

which provides a contribution of the correct sign in the β-functions of the gauge couplings so that UV gauge-Yukawa fixed points can potentially arise. Moreover, this BSM particle content can be used as a UV completion of the SM which can successfully render it asymptotically safe [29]. In this chapter, we study whether the Yukawa interactions needed to deliver an asymptotically safe SM may go beyond (3.0.1). In particular, we will be interested in interactions which act as portals between the SM and the sector beyond, in contrast to purely BSM couplings like (3.0.1). The motivation for this is twofold: firstly, Yukawa interactions involving SM fields present a potentially rich phenomenology, testable at current experiments. Secondly, the Yukawa sector constitutes the source of flavor in the SM, and any interplay between SM and BSM fields through Yukawa interactions will have an impact on flavor observables, masses and mixing patterns. Therefore, such interactions might shed light on possible connections between flavor and UV completions of the SM.

In this chapter, based on the findings of [24–26], we study a set of models with Yukawa portals to the lepton sector of the SM and their implications for flavor physics and asymptotic safety. In Sec. 3.1 we describe the models and their flavor symmetries, and in Sec. 3.2 we discuss their fixed point structure and matching both in the 210 and 222 schemes. Phenomenological implications for the different models are worked out in Sec. 3.3, with a special emphasis on lepton anomalous magnetic moments. Finally, we summarize our results in Sec. 3.4.

3.1 The Models

We begin by extending the SM with additional vector-like fermions and scalars. In order to interface with the flavor structure of the SM, we choose $N_F = 3$ generations of vector-like fermions ψ and 3×3 generations of scalars S_{ij}. The BSM fermions are colorless but charged under the $SU(2)_L \times U(1)_Y$ symmetries of the SM, while the scalars remain gauge singlets. Note that introducing a $U(1)_Y$-charged BSM sector will lead to a modifications in the β-function of the hypercharge coupling, and thus allow us to address the Landau pole

problem in its running.

Model	$(R_3,\, R_2,\, Y)$	Yukawa interactions in $\mathcal{L}_{\rm mix}$	Q_F
A	$(\mathbf{1}, \mathbf{1}, -1)$	$\kappa\, \overline{L} H \psi_R + \kappa'\, \overline{E} S^\dagger \psi_L$	-1
B	$(\mathbf{1}, \mathbf{3}, -1)$	$\kappa\, \overline{L} H \psi_R$	$0, -1, -2$
C	$(\mathbf{1}, \mathbf{2}, -\frac{1}{2})$	$\kappa\, \overline{E} H^\dagger \psi_L + \kappa'\, \overline{L} S \psi_R$	$0, -1$
D	$(\mathbf{1}, \mathbf{2}, -\frac{3}{2})$	$\kappa\, \overline{E} \tilde{H}^\dagger \psi_L$	$-1, -2$
E	$(\mathbf{1}, \mathbf{1}, 0)$	$\kappa\, \overline{L} \tilde{H} \psi_R$	0
F	$(\mathbf{1}, \mathbf{3}, 0)$	$\kappa\, \overline{L} \tilde{H} \psi_R$	$+1, 0, -1$

Table 3.1. Gauge representations R_3, R_2 and hypercharges Y of the BSM fermions ψ with respect to the SM gauge group $SU(3)_C \times SU(2)_L \times U(1)_Y$ for the different models A–F. We also indicate the mixed Yukawa terms involving SM leptons, BSM fermions and either singlet BSM scalars S or the SM Higgs. Yukawa couplings with SM scalars (BSM scalars) are denoted by κ (κ'), respectively. The last column denotes the electric charge $Q_F = T_3 + Y$ of the ψ states.

Imposing that at least one Yukawa interaction between the lepton fields L, E and the vector-like fermions be present yields only a few options for the representations the ψ can take. We find that 6 different models, named A – F, allow for such new Yukawa terms. The representations of the ψ in each model together with their portal interactions $\mathcal{L}_{\rm mix}$ are collected in Tab. 3.1. The new Yukawa couplings in $\mathcal{L}_{\rm mix}$ can involve either the SM Higgs or the S, and are denoted κ and κ' in each case, respectively. The models are distinguished solely by the electroweak charges of the vector-like fermions. These are either singlets, doublets or triplets of $SU(2)_L$, and their components carry non-fractional electric charges ranging from -2 to $+1$. For each model, the BSM Yukawa sector $\mathcal{L}_{\rm Y}$ is then given by

$$\mathcal{L}_{\rm Y} = \mathcal{L}_y + \mathcal{L}_{\rm mix}\,, \tag{3.1.1}$$

according to Eq. (3.0.1) and the interactions in Tab. 3.1. A study of portal couplings with the quark sector, however interesting, lies beyond the scope of this work. The full Lagrangian of the models studied here obeys $\mathcal{L} = \mathcal{L}_{\rm SM} + \mathcal{L}_{\rm BSM}$, with

$$\mathcal{L}_{\rm BSM} = \mathrm{Tr}\, \overline{\psi} i \not{D} \psi + \mathrm{Tr}\big[(\partial_\mu S)^\dagger (\partial^\mu S)\big] + \mathcal{L}_{\rm Y} - V(H, S)\,, \tag{3.1.2}$$

where the scalar potential reads

$$\begin{aligned} V(H,S) = &- \mu^2 H^\dagger H - \mu_s^2\, \mathrm{Tr}\Big[S^\dagger S\Big] + \lambda (H^\dagger H)^2 + \delta H^\dagger H\, \mathrm{Tr}\Big[S^\dagger S\Big] \\ &+ u\, \mathrm{Tr}\Big[S^\dagger S S^\dagger S\Big] + v\, \Big(\mathrm{Tr}\Big[S^\dagger S\Big]\Big)^2 - \mu_{\rm det}\Big(\det S + \det S^\dagger\Big)\,. \end{aligned} \tag{3.1.3}$$

Note that V contains a quartic coupling δ, which connects the BSM scalars with the Higgs, acting as a portal to the SM. The potential is invariant under $U(3)_{\psi_L} \times U(3)_{\psi_R}$ rotations of the S, which allows to write the BSM quartics u and v, as well as δ and the dimensionful parameters μ_s and $\mu_{\rm det}$, in scalar rather than tensor form (see Sec. 2.4 for further details

and properties of the potential (3.1.3)). Furthermore, the extended Yukawa sector of our models also contains a priori a large number of parameters, which can be reduced employing symmetry arguments. We start by noting that, in the absence of Yukawa interactions, the flavor symmetry of the Lagrangian is that of the SM plus the symmetries (2.2.4) for $N_F = 3$. More explicitly, for $\mathcal{L}_{\rm Y} = 0$ the BSM Lagrangian (3.1.2) is invariant under global rotations

$$\mathcal{G}_F = U(3)_q^3 \otimes U(3)_\ell^2 \otimes U(3)_\psi^2 \otimes U(3)_S^2 \,, \tag{3.1.4}$$

with

$$\begin{aligned} U(3)_q^3 &= U(3)_Q \otimes U(3)_U \otimes U(3)_D \,, & U(3)_\ell^2 &= U(3)_L \otimes U(3)_E \,, \\ U(3)_\psi^2 &= U(3)_{\psi_L} \otimes U(3)_{\psi_R} \,, & U(3)_S^2 &= U(3)_{S_L} \otimes U(3)_{S_R} \,. \end{aligned} \tag{3.1.5}$$

As we already saw in Sec. 2.2, identifying $U(3)_S^2$ with $U(3)_\psi^2$ allows to write the Yukawa coupling y in its scalar form (3.0.1), an approach we embrace here. Furthermore, in models A and C the mixed Yukawas in $\mathcal{L}_{\rm mix}$ contain interactions with the S_{ij}. In principle, the associated coupling κ' in its most general form is a tensor carrying four flavor indices, as we argued in the case of y. However, identifying $U(3)_E$ with $U(3)_{\psi_R}$ (model A) or $U(3)_L$ with $U(3)_{\psi_L}$ (model C) naturally leads to a scalar form of κ', so that these interactions can be written as

$$\kappa' \ \mathrm{Tr}\Big[\overline{E}\, S^\dagger \psi_L + \text{h.c.}\Big] \ \ \text{(model A)}\,, \qquad \kappa' \ \mathrm{Tr}\big[\overline{L}\, S\, \psi_R + \text{h.c.}\big] \ \ \text{(model C)}\,. \tag{3.1.6}$$

On the other hand, the couplings in $\mathcal{L}_{\rm mix}$ involving the Higgs can take a general form κ_{ij}. Such terms are present in all models (see Tab. 3.1). For models A, B, E and F we identify $U(3)_L$ with $U(3)_{\psi_R}$, while in models C and D we identify $U(3)_E$ with $U(3)_{\psi_L}$, yielding diagonal and universal Yukawa couplings

$$\kappa_{ij} = \kappa\, \delta_{ij} \quad \text{(models A}-\text{F)}\,. \tag{3.1.7}$$

For models A and C this entails $U(3)_L \sim U(3)_E \sim U(3)_{\psi_R}$ and $U(3)_L \sim U(3)_E \sim U(3)_{\psi_L}$, respectively, which leads to $\kappa \sim Y_\ell \sim \mathbf{1}$, implying that the SM lepton Yukawas are universal. Nonetheless, since in the SM the size of the latter is significantly small compared to the rest of parameters, including the observed values of the lepton Yukawas only breaks the flavor symmetry (very) softly.

Alternatively, we could identify $U(3)_E \sim U(3)_{\psi_R}$ (models B, E, and F), and $U(3)_L \sim U(3)_{\psi_L}$ (model D). This in turn would yield hierarchical Yukawas fulfilling

$$\kappa \sim Y_\ell \quad \text{(models B, D, E, F)}\,, \tag{3.1.8}$$

instead of (3.1.7). Here, we shall adhere to the setup where κ takes its diagonal form (3.1.7), and neglect SM lepton Yukawas unless stated otherwise. To conclude with our analysis of flavor symmetries, note that the mass term $\overline{\psi}_L M_F \psi_R$ of the vector-like fermions only respects the symmetry for $U(3)_{\psi_L} \sim U(3)_{\psi_R}$, which in turn yields universal and diagonal M_F in all models. We will stick to this very assumption throughout this work. Note that all

symmetries and couplings assumed here are in line with the criterion of Minimal Flavor Violation, since the flavor structure of higher-dimensional operators of SM fields can be expressed as in terms of products of SM Yukawa matrices.

Under the discussed assumptions on the structure of couplings, the BSM Yukawa Lagrangian $\mathcal{L}_{\rm Y}$ of the models containing κ' interactions can be written as

$$\begin{aligned} -\mathcal{L}_{\rm Y}^{\rm A} &= \kappa\, \overline{L} H \psi_R \ + \kappa'\, \overline{E} S^\dagger \psi_L + y\, \overline{\psi}_L S \psi_R + \text{h.c.}\,, \\ -\mathcal{L}_{\rm Y}^{\rm C} &= \kappa\, \overline{E} H^\dagger \psi_L + \kappa'\, \overline{L} S \psi_R \ + y\, \overline{\psi}_L S \psi_R + \text{h.c.}\,, \end{aligned} \tag{3.1.9}$$

where flavor and gauge indices are implicitly contracted. Note that in models A and C the representations of the vector-like fermions exactly coincide with the representations of the SM lepton singlet and doublet respectively (and are therefore models of vector-like leptons), which precisely allows for Yukawa interactions with a singlet scalar. The BSM Yukawa Lagrangians of the remaining models only contain the couplings y and κ, and obey

$$\begin{aligned} -\mathcal{L}_{\rm Y}^{\rm B} &= \kappa \overline{L} H \psi_R + y\, \overline{\psi}_L S \psi_R + \text{h.c.}\,, \quad & -\mathcal{L}_{\rm Y}^{\rm D} &= \kappa \bar{E} \tilde{H}^\dagger \psi_L + y\, \overline{\psi}_L S \psi_R + \text{h.c.}\,, \\ -\mathcal{L}_{\rm Y}^{\rm E} &= \kappa\, \bar{L} \tilde{H} \psi_R + y\, \overline{\psi}_L S \psi_R + \text{h.c.}\,, \quad & -\mathcal{L}_{\rm Y}^{\rm F} &= \kappa\, \bar{L} \tilde{H} \psi_R + y\, \overline{\psi}_L S \psi_R + \text{h.c.}\,, \end{aligned} \tag{3.1.10}$$

where again index contractions are implicit.

3.2 RGE Analysis

Having specified our set of models, we now set out to investigate their potential to UV-complete the SM by rendering it asymptotically safe. In order to do so, we look for fixed points of the β-functions and explore whether matching to the SM is possible. Our analysis involves the $SU(3)_C \times SU(2)_L \times U(1)_Y$ couplings of the SM,

$$\alpha_1 = \frac{g_1^2}{(4\pi)^2}\,, \quad \alpha_2 = \frac{g_2^2}{(4\pi)^2}\,, \quad \alpha_3 = \frac{g_3^2}{(4\pi)^2}\,, \tag{3.2.1}$$

as well as the top and bottom Yukawas and the Higgs quartic, normalized as

$$\alpha_t = \frac{y_t^2}{(4\pi)^2}\,, \quad \alpha_b = \frac{y_b^2}{(4\pi)^2}\,, \quad \alpha_\lambda = \frac{\lambda}{(4\pi)^2}\,. \tag{3.2.2}$$

The set of BSM couplings in our RGE analysis involves the new Yukawa interactions y, κ, κ' together with the scalar quartics δ, u, v of the potential (3.1.3). Altogether, the considered BSM couplings normalized according to Eq. (1.2.1) read

$$\begin{aligned} \alpha_y &= \frac{y^2}{(4\pi)^2}\,, \quad \alpha_\kappa = \frac{\kappa^2}{(4\pi)^2}\,, \quad \alpha_{\kappa'} = \frac{(\kappa')^2}{(4\pi)^2}\,, \\ \alpha_\delta &= \frac{\delta}{(4\pi)^2}\,, \quad \alpha_u = \frac{u}{(4\pi)^2}\,, \quad \alpha_v = \frac{v}{(4\pi)^2}\,. \end{aligned} \tag{3.2.3}$$

When fixed points are found, we check for RG trajectories which can be matched onto the SM at low energies. We assume that effects of the BSM fields kick in at M_F and are

completely decoupled for $\mu < M_F$, while SM couplings are taken to coincide with their SM values at M_F. Therefore, we identify M_F with the matching scale, which we refer to as

$$\mu = M_F \,. \tag{3.2.4}$$

The SM running, shown in Fig. (1.3), completely determines the values of the SM couplings at the matching scale, while BSM couplings can a priori take any real value at M_F. Demanding that the RG evolution of the full system reach a weakly interacting fixed point in the UV reduces this freedom, which is then determined by the dimensionality of the critical surface, or equivalently by the number of relevant directions of a given fixed point.

In the remainder of this section, we study the β-functions of models A – F, collected in Appendix. B.1, and their fixed points in the `210` and `222` approximations, providing examples of viable matching scenarios. We perform the matching at tree-level only, and do not implement decoupling relations at the new physics threshold. Note that, when using 2-loop running for couplings above the matching scale in the $\overline{\text{MS}}$ scheme, decoupling effects should be considered at 1-loop, see for instance [82]. This lies, however, beyond the scope of this work, given the complexity of our BSM setup. Nonetheless, we expect decoupling effects to leave the fixed-point structure and qualitative RG behavior of our models unchanged, since matching turns out to be possible for sizable regions of BSM parameters and matching scales, as we shall see shortly. Moreover, the phenomenological implications discussed in Sec. 3.3, based on leading-order processes, should also be largely unaffected. Our insistence in employing the BSM running up to 2-loop stems from the wish to capture the leading effects of the Yukawa and scalar sectors in the β-functions. Indeed, in the `210` scheme, 2-loop contributions in the β-functions of gauge couplings encode the leading effects of Yukawa interactions, which are crucial for the existence of UV fixed points. In the `222` approximation, where all β-functions are computed at 2-loop, the RGEs of Yukawa couplings contain the leading contributions from scalar quartic interactions, and the scalar quartic β-functions pick up contributions from all the possible Yukawas in our models.

3.2.1 Benchmark Models and Fixed Points

We now turn to the analysis of the β-functions in the `210` or leading order approximation, where RGEs of gauge and Yukawa couplings are considered at 2-loop and 1-loop, respectively. This scheme does not involve the scalar sector; hence, the BSM couplings we consider consist of the Yukawas α_κ and α_y, and additionally $\alpha_{\kappa'}$ in models A and C. On the SM side, we shall only take into account the $SU(2)_L \times U(1)_Y$ couplings. Since at 2-loop the β-function of α_3 is not modified by BSM physics, we assume that the coupling remains asymptotically free and its running SM-like. For the purposes of the `210` analysis, we do not take α_3 effects into account in the running of the remaining couplings. We also neglect contributions from the SM Yukawa sector. Note that, at 1-loop, SM Yukawas of the quarks are not modified by BSM physics, while lepton Yukawas are parametrically small with respect to gauge couplings.

Our first step is to search for fixed points of the β-functions. Within the `210` approximation one can already encounter up to $(2^{n_G}-1)$ different Banks-Zaks fixed points and a maximum of $(2^{n_G}-1)\times(2^{n_Y}-1)$ different gauge-Yukawa fixed points [28, 59], with n_G, n_Y being the number of gauge groups under which the BSM fields are charged and the number of BSM Yukawa interactions, respectively. In our models, these can take values $n_G = 2, 1, 0$ and $n_Y = 3, 2$. Moreover, the composition of the models contains additional information on which fixed points might be possible. Since only charged fermionic fields are added to the SM, the 1-loop coefficients B_i are shifted by a negative contribution (see Eq. (2.2.5)). Therefore, we will always find $B_1 < 0$, while B_2 can take either sign. Moreover, the matter fields give a positive contribution to the C_{ij} coefficients, in the notation of Eq. (2.1.20). Hence, the C_{ij} are always positive. This game of signs plays a central role in the presence and typology of fixed points in the different models. For instance, Banks-Zaks fixed points only arise in models for which at least one of the B_i is positive. Hence, Banks-Zaks fixed points with $\alpha_1^* \neq 0$ will be absent in all of our models.

In order to classify the fixed points, we use the abbreviation BZ_i to denote a Bank-Zaks fixed point where the gauge coupling α_i does not vanish, and $\mathrm{GY}_{in...m}$ for a gauge-Yukawa fixed point where α_i and the Yukawas denoted by $n...m$ are nonzero. In addition, for couplings which vanish at a fixed point, we indicate that they are marginally relevant or marginally irrelevant by writing their fixed point values as $0^{(-)}$ or $0^{(+)}$, respectively. We use this notation for couplings which display a logarithmic running near the fixed point, as is always the case for asymptotically free gauge interactions. Conversely, if the coupling vanishes at the fixed point but presents a power-law running in its vicinity, it is marked as 0^- (0^+) if it is marginally relevant (marginally irrelevant). This possibility only arises in the case of Yukawa interactions (see Sec. 2.1 for details). In the following, we describe our findings for each of the studied models, focusing on their gauge-Yukawa fixed points. In general, we include results from fixed points which present couplings up to $\mathcal{O}(1)$, allowing for small deviations from strict perturbativity ($\alpha < 1$), which may be alleviated at higher-loop orders.

Model A

The fixed points for model A are collected in Tab. 3.2. In the case of the Gaussian fixed point (FP_1), we find that α_1 and α_2 correspond to marginally irrelevant and marginally relevant directions, respectively. Thus, the Gaussian corresponds to a *saddle* point. We find as well a Banks-Zaks fixed point with interacting α_2 (FP_2). The gauge-Yukawa fixed point FP_3, with $\alpha_2^* \neq 0$, presents no relevant directions and a marginally irrelevant α_1. Hence, one cannot attempt to match it to the SM at low energies. Furthermore, the symmetry between the 1-loop β-functions of α_y and $\alpha_{\kappa'}$ allows for the line of fixed points FP_4. Indeed, since the fields involved in the Yukawa interactions of y and κ' present the same gauge charges, β_y and $\beta_{\kappa'}$ are equivalent for $\alpha_\kappa = 0$. As we shall see, this also happens in model C. Higher order corrections break this degeneracy and consequently the line structure of the fixed points.

Model A	α_1^*	α_2^*	α_κ^*	$\alpha_{\kappa'}^*$	α_y^*	rel.	irrel.	Info	Matching
FP_1	$0^{(+)}$	$0^{(-)}$	$0^{(+)}$	$0^{(+)}$	$0^{(+)}$	1	4	saddle	
FP_2	$0^{(+)}$	0.543	0^-	$0^{(+)}$	$0^{(+)}$	1	4	BZ_2	
FP_3	$0^{(+)}$	0.623	0.311	$0^{(+)}$	0^+	0	5	$\mathrm{GY}_{2\kappa}$	
FP_4	2.746	$0^{(+)}$	0^-	$4.120 - \alpha_y^*$	α_y^*	2	2	line	
FP_5 (A_1)	1.063	$0^{(-)}$	0.886	1.594	0^+	2	3	$\mathrm{GY}_{1\kappa\kappa'}$	✓
FP_6 (A_2)	1.105	0.569	1.205	1.657	0^+	1	4	$\mathrm{GY}_{12\kappa\kappa'}$	✗
FP_7 (A_3)	2.151	$0^{(-)}$	0.782	0^-	3.032	3	2	$\mathrm{GY}_{1y\kappa}$	✓
FP_8 (A_4)	2.267	0.200	0.933	0^-	3.165	2	3	$\mathrm{GY}_{12y\kappa}$	✗

Table 3.2. Fixed points of model A in the 210 approximation. We indicate the number of relevant (rel.) and irrelevant (irrel.) directions, whether the fixed point is Bank-Zaks (BZ) or gauge-Yukawa (GY), with indices specifying the non-zero couplings, and whether matching is possible. Free couplings with power-law running are marked with a superscript $\pm$ if they are irrelevant/relevant, and an additional parenthesis $(\pm)$ indicates that the flow is logarithmic. $\mathrm{FP}_{1,2,3}$ are IR or crossover fixed points, FP_4 is a line of fixed points, and $\mathrm{FP}_{5,6,7,8}$ (also denoted $A_{1,2,3,4}$) are potential UV fixed points. For the latter, we indicate whether matching onto the SM is possible. In Fig. 3.1 (left) we show the phase diagram for the latter, while Fig. 3.2 shows sample trajectories emanating from A_1 and A_2.

In addition, model A presents four gauge-Yukawa fixed points FP_5 – FP_8, also denoted as A_1 – A_4, all featuring a non-vanishing α_1^*. In Fig. 3.1 we show their schematic flow projected in the α_2 – $\alpha_{\kappa'}$ plane, with arrows pointing towards the IR. In this projection, A_3 is a UV fixed point in both directions, while A_2 lies in the IR. Fig. 3.1 also shows the various separatrices connecting the fixed points, which correspond to $\alpha_2 = 0$, $\alpha_{\kappa'} = 0$ and $\alpha_y = 0$ lines. For fixed points A_2 and A_4, we find that the RG flow cannot be matched onto the SM. This is due to trajectories being attracted by the gauge-Yukawa fixed point FP_3 in the infrared, which yields too large values of α_2 at low energies, as shown in Fig. 3.2 (left) for the case of A_2. In contrast, for fixed points A_1 and A_3, which exhibit $\alpha_2^* = 0$, a sufficiently small α_2 allows the trajectories to escape the dominion of attraction of FP_3, and can then be matched onto the SM at any scale. An example of matching at $\mu = 1$ TeV is shown in Fig. 3.2 for an RG flow emanating from A_1. In this case, the BSM couplings can be predicted at the matching scale; we obtain $\alpha_\kappa(M_F = 1\ \mathrm{TeV}) \simeq 2.7 \cdot 10^{-3}$ and $\alpha_{\kappa'}(M_F = 1\ \mathrm{TeV}) \simeq 3.5 \cdot 10^{-3}$. Another feature of fixed points A_1 and A_3 is that the coupling α_y vanishes and is marginally irrelevant. Hence, we find that gauge-Yukawa fixed points are not only present but also can be matched onto the SM in the absence of the BSM Yukawa y required in previous settings [29, 83] if other (mixed) Yukawas are present.

Model B

In Tab. 3.3 we show the 210 fixed points found for model B. In this model, both 1-loop coefficients B_1 and B_2 are negative, so that no Banks-Zaks fixed points arise and the Gaussian (FP_1) corresponds to a total IR fixed point, presenting no relevant directions. The

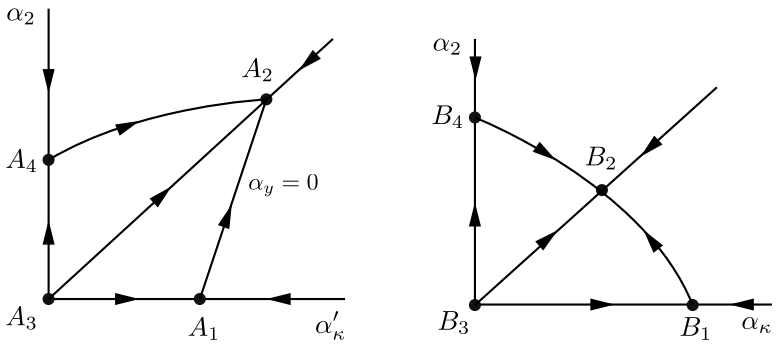

Figure 3.1. Schematic phase diagrams and gauge-Yukawa UV fixed points of model A (left) and B (right) the 210 approximation, see Tabs. 3.2 and 3.3. Arrows indicate the flow into the IR. The fixed points of model A are projected onto the $(\alpha_2, \alpha_{\kappa'})$ plane, while fixed points of model B (Tab. 3.3) are projected onto the $(\alpha_2, \alpha_\kappa)$ plane. Results for model D (see Tab. 3.5 for fixed point details) are equivalent to those of model B. Note in all models the projected RG flows present the same topology.

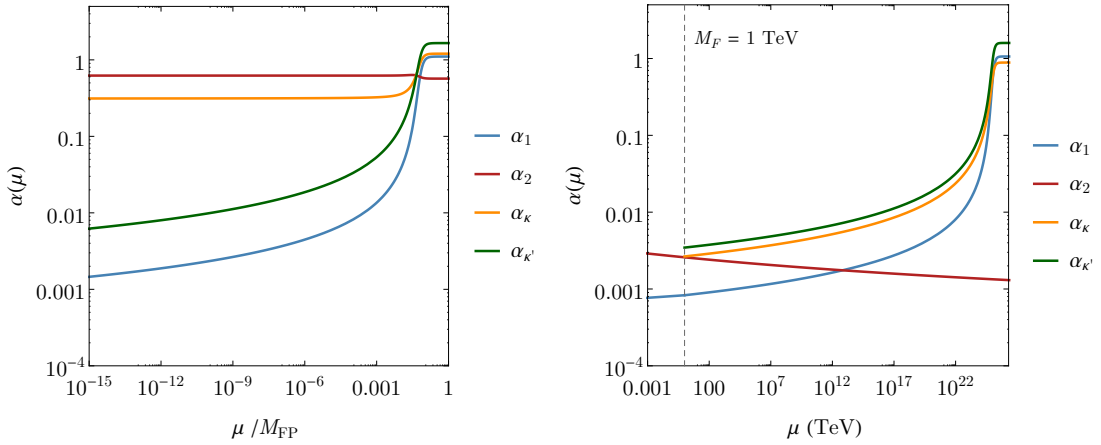

Figure 3.2. Running of couplings of model A in the 210 approximation from fixed point A_2 (left) and A_1 (right), see Tab. 3.2. For A_2, trajectories are invariably attracted by FP_3 in the infrared, and α_2 comes out too large compared to SM values. For A_1 we show matching to the SM at $\mu = 1$ TeV.

remaining fixed points FP_2 – FP_5 are of the gauge-Yukawa type, and all feature $\alpha_y^* \neq 0$. A schematic view of the RG flow around them in the α_2 – α_κ plane is shown in Fig. 3.1 (right). There, one can observe that B_2 is the least ultraviolet fixed point, with α_1 as its only relevant coupling, while B_3 presents three relevant directions.

We find that all gauge-Yukawa fixed points $B_{1,2,3,4}$ can be matched onto the SM at low energies. The main difference with respect to model A is that no Banks-Zaks fixed points featuring $\alpha_2^* \neq 0$ and $\alpha_1^* = 0$ exist, which in model A could attract α_2 towards large values in the IR. For fixed points B_2 and B_4, which feature $\alpha_2^* \neq 0$, we find that matching is

Model B	α_1^*	α_2^*	α_κ^*	α_y^*	rel.	irrel.	Info	Matching
FP_1	$0^{(+)}$	$0^{(+)}$	$0^{(+)}$	$0^{(+)}$	0	4	G	
FP_2 (B_1)	1.953	$0^{(-)}$	1.562	1.888	2	2	$\mathrm{GY}_{1\kappa y}$	✓
FP_3 (B_2)	1.224	0.186	1.326	1.541	1	3	$\mathrm{GY}_{12\kappa y}$	✓
FP_4 (B_3)	2.712	$0^{(-)}$	0^-	2.712	3	1	GY_{1y}	✓
FP_5 (B_4)	1.732	0.216	0^-	2.164	2	2	GY_{12y}	✓

Table 3.3. Fixed points of model B in the `210` approximation, with notation as in Tab. 3.2. All interacting fixed points we encounter are potential UV gauge-Yukawa fixed points ($\mathrm{FP}_{2,3,4,5}$, also referred to as $B_{1,2,3,4}$); for all of these we find that matching onto the SM is possible. See Fig. 3.1 (right) and Fig. 3.3 for the phase diagram and sample trajectories, respectively.

only possible at a given scale, due to the values of the gauge couplings being determined by the flow along a single relevant direction.[1] This is shown in Fig. 3.3 for the case of B_2, where one obtains a matching scale $M_F \simeq 25$ GeV. In the case of B_4 we find as well possible matching scenarios with $M_F \sim \mathcal{O}(10^{-2})$ TeV. Hence, we are presented with a setup where asymptotic safety is able to predict the scale of new physics. However, this scale is phenomenologically disfavored by Drell-Yann constraints, which pose a lower bound on M_F at the order of 10^{-1} TeV, as we spell out in Sec. 3.3.4. Finally, the solutions B_1 and B_3, which exhibit $\alpha_2^* = 0$, can in principle be matched onto the SM. The effective 1-loop coefficient B_2^{eff} remains positive, allowing α_2 to grow towards the IR. Nonetheless, as the flow evolves the contributions of the Yukawas α_κ and α_y may become small enough to flip the sign of B_2^{eff}, driving α_2 to lower values. We postpone the discussion of further matching scenarios to the higher-loop analysis of Sec. 3.2.2.

Model C

Tab. 3.4 shows the physical fixed points of model C in the `210` approximation. Note that all fixed point values are well within the perturbative domain. We encounter the Gaussian (FP_1), a Banks-Zaks fixed point (FP_2) and the gauge-Yukawa fixed points $\mathrm{FP}_{3,4,5,6}$. FP_6 is in fact a line of fixed points which arises due to the symmetry between β_y and $\beta_{\kappa'}$ in the limit of vanishing α_κ, a phenomenon which we already observed in model A. The symmetry is a consequence of the vector-like fermions carrying the same charges as the SM lepton doublets, and disappears when including higher loop corrections. All of the fixed points present an irrelevant α_1, which impedes matching onto the SM. Therefore, in model C we find no UV-completing fixed points in the `210` approximation.

Model D

The fixed points found for model D are listed in Tab. 3.5. Apart from the Gaussian (FP_1) and a Banks-Zaks fixed point (FP_2), we find three gauge-Yukawa solutions with $\alpha_1^* = 0$ ($\mathrm{FP}_{3,4,5}$), which suffer from a marginally irrelevant $U(1)_Y$ coupling and thus cannot be

[1] Fixed point B_4 presents two relevant directions. However, one of them corresponds to the coupling α_κ, which vanishes at the fixed point, and has small effects on the high-energy running.

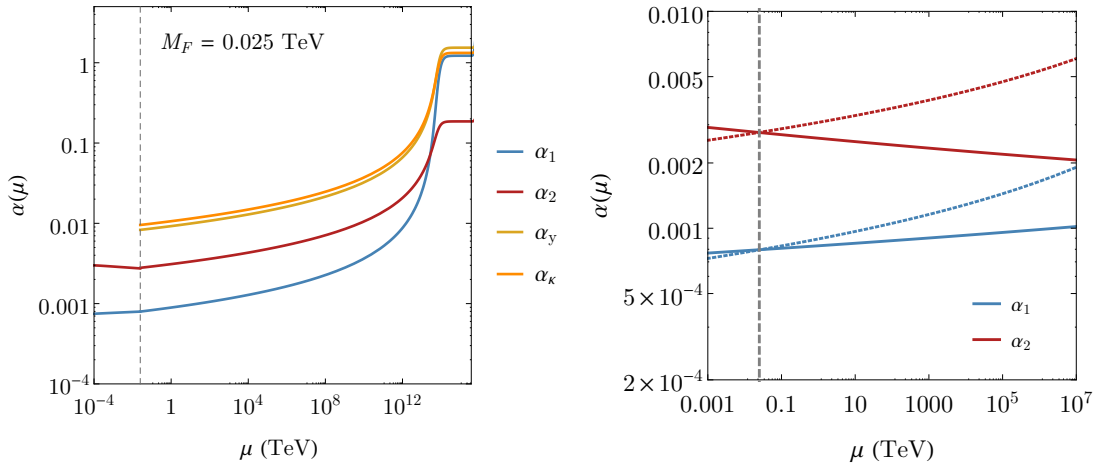

Figure 3.3. Matching at $M_F = 0.025$ TeV for the fully-interacting fixed point B_2. We show the BSM running of the couplings into the fixed point (left) and the zoomed-in running of the gauge couplings (right) near the matching scale, indicated by the dashed vertical line, with the BSM (SM) running of $\alpha_{1,2}$ depicted with dotted (full) lines.

Model C	α_1^*	α_2^*	α_κ^*	$\alpha_{\kappa'}^*$	α_y^*	rel.	ir.	Info
FP_1	$0^{(+)}$	$0^{(-)}$	$0^{(+)}$	$0^{(+)}$	$0^{(+)}$	1	4	G
FP_2	$0^{(+)}$	0.038	0^-	0^-	0^-	3	2	BZ_2
FP_3	$0^{(+)}$	0.039	0.020	0^-	0^-	2	3	$\mathrm{GY}_{2\kappa}$
FP_4	$0^{(+)}$	0.054	0.027	0.049	0^+	0	5	$\mathrm{GY}_{2\kappa\kappa'}$
FP_5	$0^{(+)}$	0.053	0.011	0^-	0.046	1	4	$\mathrm{GY}_{2\kappa y}$
FP_6	$0^{(+)}$	0.052	0^-	$0.047 - \alpha_y^*$	α_y^*	1	3	$\mathrm{GY}_{2\kappa' y}$

Table 3.4. Fixed points of model C in the `210` approximation, with notation as in Tab. 3.2. At this loop order, no viable candidates for UV fixed points exist.

matched onto the SM. The remaining fixed points ($\mathrm{FP}_{6,7,8,9}$, also denoted $D_{1,2,3,4}$) are as well gauge-Yukawa but display $\alpha_1^* \neq 0$. Their schematic flow in the $\alpha_2 - \alpha_\kappa$ plane is analogous to that of model B (shown in Fig. 3.1), with D_3 being the UV-most fixed point, and D_2 the most IR. Moreover, as we already found in model A the Banks-Zaks fixed point FP_2 of model D acts as an IR sink, drawing α_2 to its fixed point value $\alpha_2^* \simeq 0.038$ and impeding SM matching for fixed points D_2 and D_4, which exhibit $\alpha_2^* \neq 0$. This is depicted in Fig. 3.4 (left) for a running emanating from D_2. In the case of the fixed points with $\alpha_2^* = 0$ (D_1 and D_3), α_2 can remain small enough and be matched onto the SM in a range of scales, as shown for D_1 and $M_F = 1$ TeV in Fig. 3.4 (right). In this case, the BSM couplings at the matching scale are predicted to be $\alpha_\kappa(M_F = 1\ \mathrm{TeV}) = 4.2 \cdot 10^{-3}, \alpha_y(M_F = 1\ \mathrm{TeV}) = 5.8 \cdot 10^{-3}$. Fixed point D_3 was previously studied in [61], and discarded due to instability under higher-order corrections. Here, however, we choose to retain it and discuss higher loop-order effects in Sec. 3.2.2.

Model D	α_1^*	α_2^*	α_κ^*	α_y^*	rel.	irrel.	Info	Matching
FP_1	$0^{(+)}$	$0^{(-)}$	$0^{(+)}$	$0^{(+)}$	1	3	G	
FP_2	$0^{(+)}$	0.038	0^-	0^-	2	2	BZ_2	
FP_3	$0^{(+)}$	0.039	0.020	0^-	1	3	$\mathrm{GY}_{2\kappa}$	
FP_4	$0^{(+)}$	0.052	0^-	0.047	1	3	GY_{2y}	
FP_5	$0^{(+)}$	0.053	0.011	0.046	0	4	$\mathrm{GY}_{2\kappa y}$	
FP_6 (D_1)	0.246	$0^{(-)}$	0.322	0.631	2	2	$\mathrm{GY}_{1\kappa y}$	✓
FP_7 (D_2)	0.202	0.145	0.295	0.647	1	3	$\mathrm{GY}_{12\kappa y}$	✗
FP_8 (D_3)	0.288	$0^{(-)}$	0^-	0.778	3	1	GY_{1y}	✓
FP_9 (D_4)	0.239	0.152	0^-	0.782	2	2	GY_{12y}	✗

Table 3.5. Fixed points of model D in the 210 approximation, with notation as in Tab. 3.2. For gauge-Yukawa fixed points with $\alpha_1^* \neq 0$ ($\mathrm{FP}_{6,7,8,9}$, also referred to as $D_{1,2,3,4}$) we indicate whether matching onto the SM is possible. In Fig. 3.1 and Fig. 3.4 we show the phase diagram and sample trajectories, respectively.

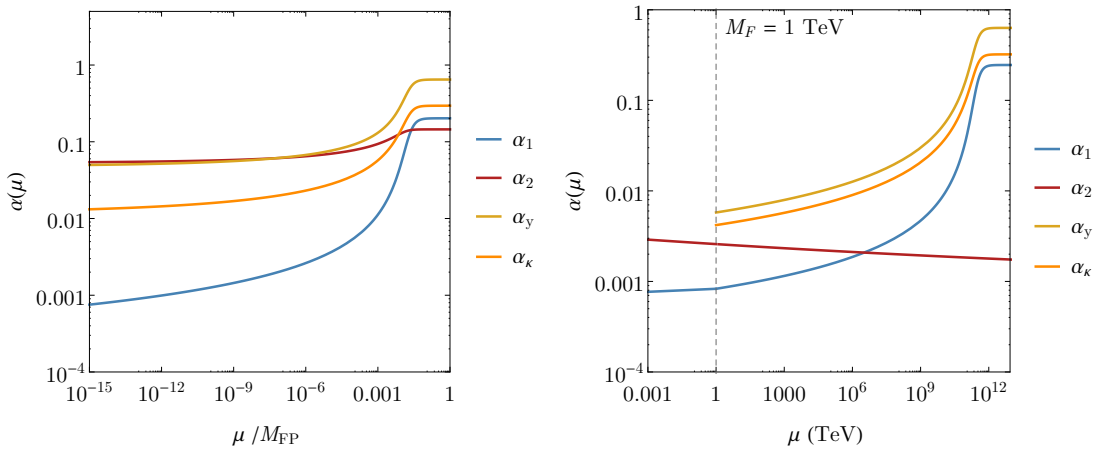

Figure 3.4. Renormalization group running in model D. Left: RG flow emanating from fixed point D_2, where matching is not possible due to the trajectories being attracted by the Banks-Zaks fixed point FP_2 (see Tab. 3.5). Right: running emanating from fixed point D_1 and matching at $\mu = 1$ TeV (dashed vertical line). After matching, values of the BSM couplings at the matching scale are predicted by the running.

Model E

In model E the vector-like fermions are total singlets, and thus only modify the β-functions of the SM gauge couplings through κ. On the other hand, β_y receives no contributions from gauge couplings and can only vanish if $\alpha_y = 0$. This leads to model E displaying only the gaussian, a Banks-Zaks fixed point BZ_2 and a gauge-Yukawa fixed point with vanishing and marginally irrelevant α_1, of the type $\mathrm{GY}_{2\kappa}$. Therefore, we find no viable UV fixed points

in model E within the 210 approximation.

Model F

In model F no viable UV fixed points are found either. Since in this model the vector-like fermions carry no hypercharge, the coupling α_y is absent in β_1 and β_y is independent of α_1. As in model E, the mixed Yukawa α_κ represents the only negative contribution both in β_1 and β_2, and turns out to be insufficient for any gauge-Yukawa fixed points to arise. No Banks-Zaks arise in this model either, since B_2 is negative due to the vector-like fermions being in the triplet representation of $SU(2)_L$, similarly to model B.

Summary

In this section we have performed a top-down study of the β-functions of models A – F in the leading order approximation, looking for UV fixed points and viable matching scenarios. We have found that models A, B and D indeed present gauge-Yukawa fixed points (see Tabs. 3.2, 3.3 and 3.5) which can in some instances be matched onto the SM, while such viable solutions are absent in models C, E and F. In the next section, we study the β-functions at higher loop orders in order to investigate whether patterns beyond those found at 210 arise.

3.2.2 Running beyond Leading Order

In this section we study the RG flow of our couplings beyond the leading order approximation considered in the previous section. In particular, we consider the β-functions at the complete two-loop order (222 approximation), with all couplings being treated on equal footing, including those of the scalar sector. In our analysis we then include the full set of BSM couplings (3.2.3) plus the SM gauge couplings and the top and bottom Yukawas. Note that third-generation Yukawas become especially important at 222, given their significant influence on the running of the Higgs quartic. Overall, we consider the RG evolution of a total of 11 couplings (12 for models A and C).

Due to the increased complexity of the β-functions and their fixed-point solutions at 2-loop we employ a bottom-up strategy, exploring different regions of the parameter space of BSM couplings and their UV fate. In what follows, we refer as *BSM critical surface* to the values of the BSM couplings (3.2.3) at the matching scale whose associated RG trajectories are safe at least until the Planck scale. Opposed to our approach in the 210 analysis carried out in the previous section, here we study RG flows emanating from the IR into the UV, and choose to set the matching scale

$$\mu_0 = 1\,\text{TeV}\,. \tag{3.2.5}$$

Moreover, we use the SM running at 3-loop order (shown in Fig. 1.3) to compute initial conditions. Using $m_t \simeq 172.9$ GeV we obtain [34, 37]

$$\begin{aligned} \alpha_1(\mu_0) &\simeq 8.30 \cdot 10^{-4}, \quad \alpha_\lambda(\mu_0) \simeq 6.09 \cdot 10^{-4}, \\ \alpha_2(\mu_0) &\simeq 2.58 \cdot 10^{-3}, \quad \alpha_t(\mu_0) \simeq 4.61 \cdot 10^{-3}, \\ \alpha_3(\mu_0) &\simeq 7.08 \cdot 10^{-3}, \quad \alpha_b(\mu_0) \simeq 1.22 \cdot 10^{-6}. \end{aligned} \tag{3.2.6}$$

Initial conditions for the BSM couplings are a priori free parameters, and in what follows we explore how the running depends on their values. In particular, we discuss whether the RG flow evolves up to the Planck scale without developing poles (which we refer to as *Planck safety*), if it presents asymptotic safety and the stability of the vacuum. We focus on scenarios where the BSM couplings at the matching scale are of the same order of magnitude as the SM couplings of Eq. (3.2.6), which we refer to as *weak* BSM couplings (within the range $\mathcal{O}(10^{-6} - 10^{-2})$). We shall also refer to couplings as *feeble* when they lie below these orders of magnitude ($\alpha \sim 10^{-7}$ or smaller). For feeble BSM interactions at the matching scale, we find that the new sector decouples and the running of the models resembles that of the SM extended with additional vector-like fermions. Trajectories either reach Planck safety or Landau poles below the Planck scale, see [25] for details. For weak matching-scale values of the couplings trajectories present richer implications. Let us study in more detail the running for two different configurations of the BSM couplings at the matching scale:

i) Weak α_y, with $\alpha_\kappa, \alpha_{\kappa'} \sim 0$ (for all models)

ii) Weak $\alpha_\kappa, \alpha_{\kappa'}$, with $\alpha_y \sim 0$ (models A and C).

Benchmark results for the case *i*) are shown in Fig. 3.5, where trajectories remain safe at least up to the Planck scale thanks to the Yukawa α_y. In Fig. 3.5 we have taken a weak initial value of the portal coupling $|\alpha_\delta| \simeq 10^{-5}$ in all models except for model E, where α_δ is chosen to be very feeble at the matching scale. We find that BSM interactions enhance the portal coupling, which becomes more sizable through its running. In models A and E, this stabilizes the Higgs quartic coupling, which remains positive throughout its running. For models B and F, α_λ switches sign twice, while in models C and D it changes sign only once, yielding a negative α_λ at the Planck scale. Hence, attaining absolute stability of the electroweak vacuum is possible but not guaranteed. In general, we also find that feeble values of α_κ and $\alpha_{\kappa'}$ allow for at least Planck safety in all models.

For the case *ii*), where both α_κ and $\alpha_{\kappa'}$ are weak and α_y is negligible, we choose $\alpha_\kappa \sim 10^{-5}$ at the matching scale, which is compatible with Z data bounds on α_κ studied in Sec. 3.3.1, see Eq. (3.3.9). Results for models A and C are shown in Fig. 3.6, where we have chosen weak matching-scale values of α_δ. A synergy between α_κ and α_δ stabilizes the Higgs quartic, rendering it positive throughout its flow into the deep UV. In both models we observe that the running slows down into a *walking* regime around the Planck scale. This effect is due to the couplings approaching approximate fixed points, which in both cases involve the portal coupling. Moreover, the gauge couplings vanish at the intermediate fixed points, so that their evolution is minimally affected. For model A, the running then abandons its walking

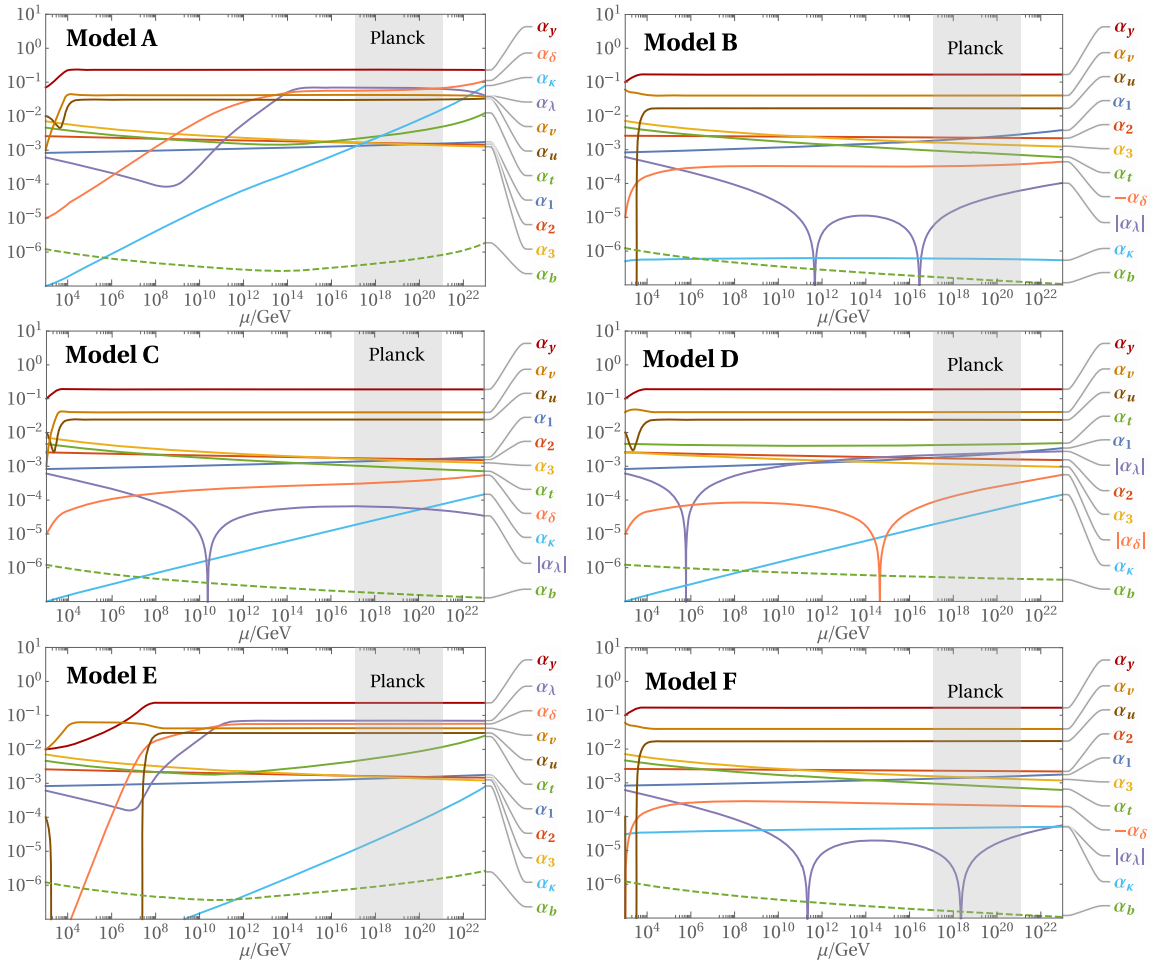

Figure 3.5. Renormalization group running of models A – F and $\alpha_\kappa \approx 0$, $|\alpha_\delta| = 10^{-5}$ (except for model E, where $|\alpha_\delta|$ is very feeble), as well as $\alpha_{\kappa'} = 0$ for models A and C. In model A, C, D and E, small initial values of α_κ (light blue) run into poles in the UV, while for B and F the trajectories remain more stable. The Higgs potential (purple) is not stabilized by Yukawa interactions (model B-C,F), but for sufficiently large initial values of α_δ (orange) in the singlet models (model A and E).

regime to flow into a UV fixed point at

$$\begin{aligned} \alpha_1^* &\simeq 1.93 \cdot 10^{-1}\,, & \alpha_\kappa^* &\simeq 3.05 \cdot 10^{-1}\,, \\ \alpha_3^* = \alpha_2^* = \alpha_y^* &= 0\,, & \alpha_{\kappa'}^* &\simeq 6.25 \cdot 10^{-1}\,, \\ \alpha_\lambda^* &\simeq 1.27 \cdot 10^{-1}\,, & \alpha_\delta^* &\simeq -1.55 \cdot 10^{-2}\,, \\ \alpha_t^* &\simeq 4.78 \cdot 10^{-1}\,, & \alpha_u^* &\simeq 1.19 \cdot 10^{-1}\,, \\ \alpha_b^* &\simeq 4.53 \cdot 10^{-1}\,, & \alpha_v^* &\simeq 4.03 \cdot 10^{-2}\,, \end{aligned} \tag{3.2.7}$$

displaying asymptotic safety. In model C, we find instead that poles arise in the deep UV, with the running being only Planck safe. Larger matching-scale values of α_κ, although phenomenologically disfavored, can help drive the running into a UV fixed point, see [25]

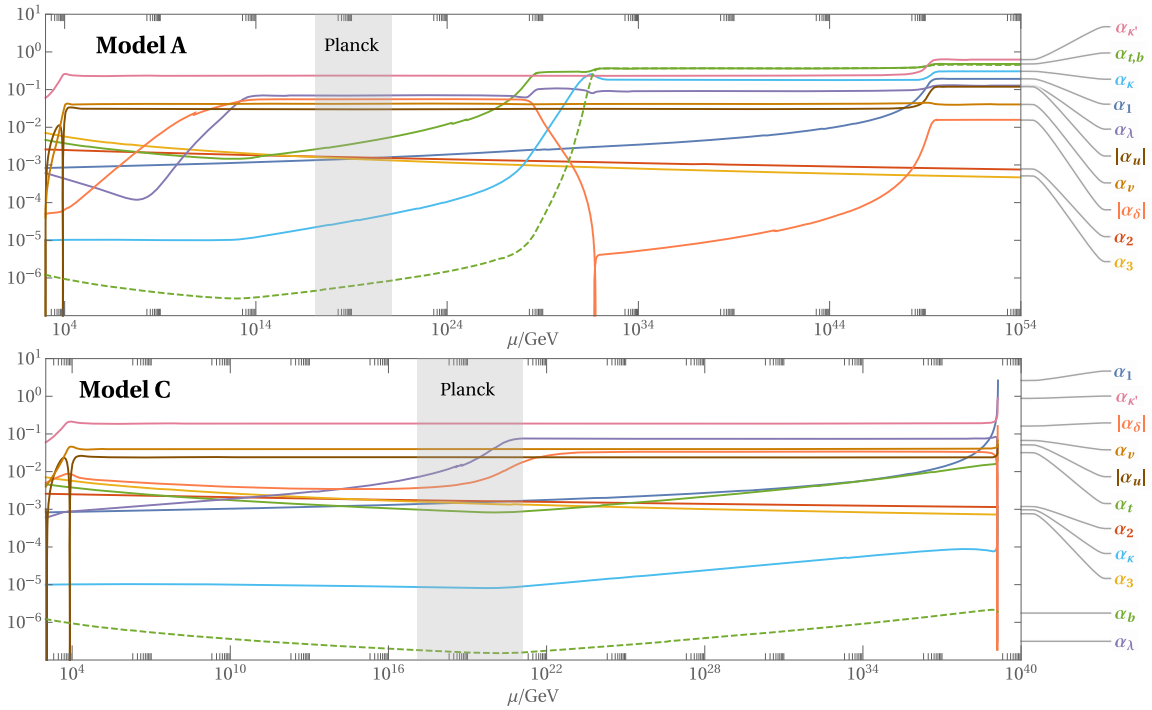

Figure 3.6. Renormalization group running of models A and C for weak matching-scale values of α_κ (light blue), $\alpha_{\kappa'}$ (pink) and $|\alpha_\delta|$ (orange), with $\alpha_y \sim 0$. Flows are stabilized around the Planck scale due to cross-over fixed points involving α_δ, which slows down couplings into a walking regime. In model A, the flow goes on to reach the fixed point (3.2.7) in the far UV, while in model C it runs into poles. The quartic coupling α_u (brown) changes sign below $M_{\rm Pl}$, marking a transition between vacuum structures V^+ and V^-.

for details. In both cases, the coupling α_u changes sign below $M_{\rm Pl}$, leading to a transition between the stable vacuum ground states V^+ and V^-.

In summary, we have found that for certain benchmark values of the BSM couplings at the matching scale our models display in some cases Planck safety, while in others asymptotic safety is realized thanks to the couplings reaching interacting fixed points in the deep UV. We observed that Yukawa interactions are essential both to influence the running of gauge couplings, moving Landau poles past the Planck scale, and to stabilize the Higgs and BSM potential. Moreover, we have found that transitions between the BSM vacua V^+ and V^- can also be realized owing to a change of sign in α_u throughout the running. Implications for the BSM critical surface for a range of values of the Yukawas α_y, α_κ and $\alpha_{\kappa'}$ beyond the benchmark initial conditions studied here are outlined in Appendix B.2 (see Figs. B.2.1 and B.2.2), while explicit computations of the running for further benchmarks can be found in [25].

3.3 Phenomenological Analysis

In the previous sections we have studied the RG flows of our set of models containing portal Yukawa interactions between vector-like fermions and SM leptons. We have seen that a `210` analysis of the flows from UV fixed points drastically reduces the parameter space of the BSM sector after requiring that models be matched onto the SM around the TeV scale. Nevertheless, the `222` analysis involving all couplings revealed a much wider range of fixed point possibilities and matching scenarios, which considerably opens up the parameter space.

In this section we provide a detailed study of the phenomenological implications of our six vector-like fermion models without imposing any previous assumptions on BSM couplings. We study production and decay of BSM states at proton and lepton colliders, Drell-Yann constraints and implications for anomalous magnetic moments, electric dipole moments (EDM) and charged lepton flavor violation (cLFV). A central ingredient for the phenomenological analysis is given by mixing, both in the fermion and scalar sector, which we also discuss in detail. In particular, we shall see that Z data places strong constraints on fermion couplings involved in the mixing angles. Furthermore, we discuss how scalar mixing can provide enhanced 1-loop contributions to anomalous magnetic moments which have the potential to explain current experimental results in tension with SM predictions. The same mechanism, which relies on the portal coupling δ, induces lepton EDMs already at 1-loop once $\mathcal{CP}$-violating phases in the BSM Yukawas κ and κ' are allowed.

3.3.1 Fermion Mixing

The scalar potential $V(H,S)$ of the models in study presents distinct vacuum patterns, described in detail in Sec. 2.4. Indeed, spontaneous symmetry breaking in the BSM sector can yield to two stable vacua, V^+ and V^-, according to the conditions (2.4.12). In V^+, all diagonal components of the S acquire a VEV, while in V^- only one of them does. Therefore, the Yukawa interactions κ' involving the S field, present in models A and C, yield mixing mass terms between the SM leptons and the vector-like fermions which depend on the vacuum ground state. Furthermore, interactions of vector-like fermions with the Higgs yield additional mixed mass terms in all models, in this case proportional to κ. In this section we detail patterns of fermion mixing for both vacuum structures and study implications for electroweak interactions and Higgs couplings.

In order to illustrate how mixing arises, we take the case of model A where the vacuum V^- is aligned in the muon direction. After spontaneous symmetry breaking, the mass Lagrangian of the leptons and vector-like fermions obeys

$$\begin{aligned}\overline{f}_L \mathcal{M}_f f_R = \; & \frac{v_h}{\sqrt{2}}\,\overline{e}_L\, Y_\ell e_R + \frac{v_h}{\sqrt{2}}\,\kappa\,\overline{e}_L\,\psi_R \\ & + \frac{v_s}{\sqrt{2}}\,\kappa'\,\overline{\psi}_{L2}\,\mu_R + \frac{v_s}{\sqrt{2}}\,y\,\overline{\psi}_{L2}\,\psi_{R2} + M_F\,\overline{\psi}_L\,\psi_R\,,\end{aligned} \tag{3.3.1}$$

Vacuum	θ_L^A	θ_R^A	θ_L^B	θ_R^B	$\theta_L^{0,B}$	$\theta_L^{0,C}$
V^+	$\frac{\kappa v_h}{\sqrt{2}\, m_2}$	$\frac{\kappa' v_s}{\sqrt{2}\, m_2}$	$\frac{\kappa v_h}{2\, m_2}$	$\frac{\kappa v_h^2 y_\ell}{2\sqrt{2}\, m_2^2}$	$\frac{\kappa v_h}{\sqrt{2}\, m_2}$	$\frac{\kappa' v_s}{\sqrt{2}\, m_2}$
$V^-(\psi_2 - \ell_2)$	$\frac{\kappa v_h}{\sqrt{2}\, M_F}$	$\frac{\kappa' v_s}{\sqrt{2}\, m_2}$	$\frac{\kappa v_h}{2\, M_F}$	$\frac{\kappa v_h^2 y_\ell}{2\sqrt{2}\, M_F^2}$	$\frac{\kappa v_h}{\sqrt{2}\, M_F}$	$\frac{\kappa' v_s}{\sqrt{2}\, m_2}$
$V^-(\psi_{1,3} - \ell_{1,3})$	$\frac{\kappa v_h}{\sqrt{2}\, M_F}$	$\frac{\kappa v_h^2 y_\ell}{2\, M_F^2}$	$\frac{\kappa v_h}{2\, M_F}$	$\frac{\kappa v_h^2 y_\ell}{2\sqrt{2}\, M_F^2}$	$\frac{\kappa v_h}{\sqrt{2}\, M_F}$	0

Table 3.6. Mixing angles of the $Q_F = -1$ fermions (θ^M) and the $Q_F = 0$ fermions ($\theta^{0,M}$) (see Tab. 3.1), with $m_2 = M_F + y v_s/\sqrt{2}$. Angles are given for both vacuum structures $V^\pm$ in the case where V^- takes a VEV in the second generation. The angles not shown in the table fulfill $\theta^C_{L,R} = \theta^A_{R,L}$ for model C, and $\theta^D_{L,R} = \sqrt{2}\theta^B_{R,L}$ for model D. We also find $\theta^{0,E}_L = \sqrt{2}\theta^{0,F}_L = \theta^{0,B}_L$ and $\theta^F_{L,R} = \sqrt{2}\theta^B_{L,R}$ in models E and F. The additional factor of $1/\sqrt{2}$ in θ^B and $\theta^{0,F}$ originates from Clebsch-Gordan coefficients of the triplet representation (see for instance Eq. (2.3.6)).

where $f_X = (e_X, \mu_X, \tau_X, \psi_{X1}, \psi_{X2}, \psi_{X3})^T$ with $X = L, R$. Then, diagonalizing $\mathcal{M}_f \mathcal{M}_f^\dagger$ and $\mathcal{M}_f^\dagger \mathcal{M}_f$ allows to compute the rotations to the mass basis for f_L and f_R, respectively (see Appendix A.2 for details). The resulting mass eigenstates can be obtained from the rotations (2.3.8) with mixing angles fulfilling

$$\theta_L^A \simeq \frac{\kappa v_h}{\sqrt{2} M_F}, \qquad \theta_R^A \simeq \frac{\kappa' v_s}{\sqrt{2} m_2}\,, \tag{3.3.2}$$

in the small-angle approximation, for $\ell_{Li} - \psi_{Li}$ and $\mu_R - \psi_{R2}$ respectively. We have also defined $m_2 = M_F + \frac{v_s}{\sqrt{2}} y$, and used the diagonal form of the SM lepton Yukawa matrix

$$\frac{v_h}{\sqrt{2}} Y_\ell = \frac{v_h}{\sqrt{2}} \mathrm{diag}(y_e, y_\mu, y_\tau)\,. \tag{3.3.3}$$

For the flavors which are not aligned in the V^- direction, the right-handed rotation angles read instead

$$\theta_R^A = \frac{\kappa\, v_h^2\, y_\ell}{2 M_F^2} \quad (\ell = e, \tau)\,, \tag{3.3.4}$$

again in the small-angle approximation. Hence, in V^- the right-handed rotation angles are parametrically smaller for the non-aligned flavors than for the aligned flavor. Moving on to the case of V^+, we take again model A as an example and find rotation angles fulfilling

$$\theta_L^A \simeq \frac{\kappa v_h}{\sqrt{2} m_2}, \qquad \theta_R^A \simeq \frac{\kappa' v_s}{\sqrt{2} m_2}\,, \tag{3.3.5}$$

for ℓ_{Li}- ψ_{Li}, and ℓ_{iR}- ψ_{Ri}, respectively. Thus, in V^+ rotation angles are the same for all flavors, as should be expected from a flavor-universal vacuum structure. The mixing angles θ_X^M at leading order for all models, indicated by the superscript M, and both vacuum structures are collected in Tab. 3.6. In models B,C, E and F, which contain $Q_F = 0$ states, left-handed rotations $\theta_L^{0,M}$ are introduced between the ψ_L^0 and neutrinos. The rotation angles for the electrically neutral states are also shown in Tab. 3.6.

As described in Sec. 2.3, mixing of colorless vector-like fermions with SM leptons gives rise to tree-level effects in their chiral interactions. This affects couplings to the Z and W bosons as well as to the Higgs. A most important effect for weak-boson interactions is the appearance of vertices involving a vector-like fermion, an SM lepton and either the W or the Z. This is especially relevant for the production and decay of vector-like fermions, as we detail in Sec. 3.3.2.

In the case of the Z, its vector and axial couplings $g_{V,A}$ to any representation of vector-like fermions can be obtained from Tab. 2.1, according to the normalization of the Lagrangian (1.1.31). It is especially relevant that the $Z\ell^+\ell^-$ vertex acquires couplings

$$g_{\substack{V\\A}}^{\ell} = g_{\substack{V\\A}}^{\ell,\,\mathrm{SM}} + \Delta g_{\substack{V\\A}} = g_{\substack{V\\A}}^{\ell,\,\mathrm{SM}} + s_{\theta_L}^2 (T_{\psi^{-1}}^3 + 1/2) \pm s_{\theta_R}^2 T_{\psi^{-1}}^3 \,, \tag{3.3.6}$$

which can deviate from the SM values $g_V^{\ell,\,\mathrm{SM}} = -1/2 + 2s_w^2$ and $g_A^{\ell,\,\mathrm{SM}} = -1/2$. In Eq. (3.3.6), the rotation angles $\theta_{L,R}$ should be taken from Tab. 3.6, and $T_{\psi^{-1}}^3$ denotes the isospin of the $Q_F = -1$ component of the vector-like fermions in each model. For model A (C), the isospin of the negatively charged vector-like fermions leads Δg to depend only on right-handed (left-handed) rotation angles, yielding

$$\Delta g \propto \left(\kappa \frac{v_h}{M_F}\right)^2 \tag{3.3.7}$$

in both cases. For models B and F (model D) one finds in turn $\theta_L \gg \theta_R$ ($\theta_R \gg \theta_L$), which leads to the same parametric dependence of Δg.

Furthermore, the $Z\overline{\nu}\nu$ vertex is modified as well in models containing $Q_F = 0$ states, with its coupling being shifted according to

$$g^{\nu} = g^{\nu,\,\mathrm{SM}} + \Delta g^{\nu} = g^{\nu,\,\mathrm{SM}} + s_{\theta_L^0}^2 \left[T_{\psi^0}^3 - 1/2\right] \,, \tag{3.3.8}$$

with $g^{\nu,\,\mathrm{SM}} = 1/2$ and $T_{\psi^0}^3$ the isospin component of the electrically neutral vector-like fermion. In model C, where the ψ^0 fields carry $T_{\psi^0}^3 = -1/2$, the neutrino coupling g^{ν} remains unaffected. For models B, E and F, one always finds $\Delta g_{\nu} \propto (\kappa v_h/M_F)^2$ according to the angles of Tab. 3.6. Therefore, modifications of the Z couplings to charged leptons and neutrinos, if present, display the dependence (3.3.7) in all models. Since Z couplings to charged leptons and electron-flavored neutrinos demand $\Delta g \lesssim 10^{-3}$ or smaller [37], one obtains the constraint

$$\alpha_{\kappa} \lesssim 4 \cdot 10^{-4} \ (M_F/[\mathrm{TeV}])^2 \,. \tag{3.3.9}$$

Modifications of W vertices can be read off Tab. 2.3, following the notation of Eqs. (2.3.10) and (2.3.11). For our set of models, the non-vanishing Clebsch-Gordan coefficients C_i read

$$C_0^B = -C_{-1}^B = \sqrt{2}, \quad C_0^C = C_{-1}^D = 1, \quad C_1^F = -C_0^F = \sqrt{2} \,, \tag{3.3.10}$$

and angles should be again taken from Tab. 3.6. Note that the $\overline{\nu}\ell^- W^+$ vertex is modified by a factor

$$C^W = c_{\theta_L} c_{\theta_L^0} + C_0 s_{\theta_L} s_{\theta_L^0} \,, \tag{3.3.11}$$

with $C^W = 1$ in the SM. For all models, one obtains at most $C^W \propto \cos(\kappa v_h/M_F)$, up to order one factors. Note that for model C one finds $\theta_L^C = \theta_L^{0,C}$ for V^+ and the vacuum-aligned flavor of V^-, which yields $C^W = 1$, while for the non-aligned flavors $\theta_L^{0,C}$ vanishes and θ_L^C is parametrically small. This entails that, if the requirement (3.3.9) from Z couplings is fulfilled, W data constraints are also avoided.

Finally, let us discuss the effects of mixing in Higgs couplings. Since leptons receive masses from several terms in the Lagrangian, diagonal lepton Yukawas y_ℓ of the $\mathcal{L}_{h\ell\ell} = \frac{y_\ell}{\sqrt{2}}\overline{\ell}\ell h$ interaction are modified. Taking again model A as an example, the couplings are shifted according to

$$y_\ell = y_\ell^{\rm SM} + \sin\theta_L^\ell \left(\kappa' \frac{v_s}{v_h} \cos\theta_R^\ell - \sqrt{2} \frac{M_F}{v_h} \sin\theta_R^\ell \right), \tag{3.3.12}$$

where the $y_\ell^{\rm SM}$ obey the SM relation (1.1.38). Results for model C are obtained by replacing $L \leftrightarrow R$, while in all other models the κ' term is absent. We find that, for angles fulfilling the Z vertex constraint (3.3.9), Higgs signal strength bounds are avoidable for all leptons [37, 40].

3.3.2 BSM Sector Production

We turn now to studying how the BSM sector can be produced at pp and $\ell^+\ell^-$ colliders. Production channels for both the ψ and the S are depicted in Fig. 3.7. Let us first discuss the production of vector-like fermions. Since these are colorless, pair production in hadron colliders occurs solely via quark-antiquark fusion, shown in diagrams (a) and (b). At least one of these channels is present in all models except for model E, where the ψ are electroweak singlets. Single production in pp colliders can occur through s-channel Higgs thanks to the Yukawa interactions κ, shown in diagram (c). Note that ψ^0 production in association with a neutrino only occurs for models B, E and F. Additional channels open up in $\ell\ell$ colliders thanks to the BSM Yukawa interactions. There, pair production can take place through Higgs or S exchange (diagram d) and single production through t-channel Higgs (diagram e).

The contribution to ψ pair production from s-channel Z or photon is especially relevant, since it arises in all models (except for model E) and in both pp and $\ell\ell$ collisions. Furthermore, all $N_F = 3$ flavors of the ψ are produced. The contribution to pair production via photon exchange at center of mass energy squared s reads

$$\sigma_\gamma(\overline{f}f \to \overline{\psi}\psi) = N_F \frac{4\pi}{3} \frac{\alpha_e^2 Q_f^2}{s} \sum_{SU(2)_L} Q_F^2 \sqrt{1 - \frac{4M_F^2}{s}} \left(1 + \frac{2M_F^2}{s}\right) \quad \text{for} \quad s > 4M_F^2\,, \tag{3.3.13}$$

in the limit $M_F \gg m_f$, where f is a quark or a lepton, and we summed over the ψ's flavors and $SU(2)_L$ components. This results in cross sections of the order $N_F Q_f^2 \sum Q_F^2 90\,\text{fb}/(s[\text{TeV}])$ [84]. In models B and D, which contain fermions with $|Q_F| = 2$, the sum over charged states in (3.3.13) enhances the cross section by effective charge-squares of $\sum Q_F^2 = 5$. A more detailed study of pair production at pp colliders in the case of models A and C can be found

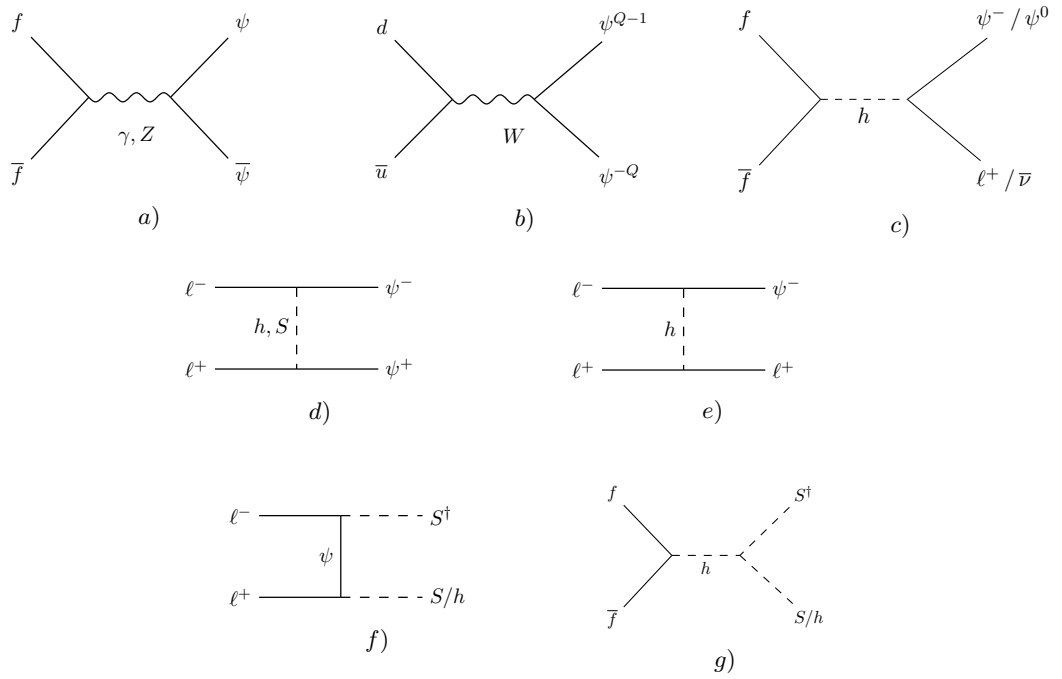

Figure 3.7. Production channels of the BSM particles at pp and $\ell\ell$ colliders, with $f = \ell, q$. In diagram f) the S and $S^\dagger$ labels are schematic for model A, see text for details.

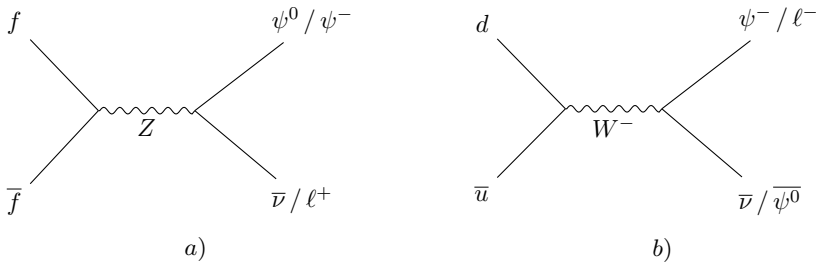

Figure 3.8. Single-production channels via weak bosons of the $Q_F = -1$ and $Q_F = 0$ vector-like fermions at pp and $\ell\ell$ colliders, with $f = \ell, q$. Both diagrams arise from mass mixing between the ψ and SM leptons.

in Chapter 4.

Additionally, mixing between vector-like fermions and leptons allows for further single-production channels of the ψ^{-1} and the ψ^0 through electroweak interactions, see Sec. 3.3.1 for details. In Fig. 3.8 we show how mixing-driven single production can occur via s-channel Z (diagram a) or W (diagram b).

We now focus on the production of BSM scalars. In the following, we denote by Re[S] and Im[S] their real, $\mathcal{CP}$-even and $\mathcal{CP}$-odd physical degrees of freedom, respectively. Note that, since the BSM scalars are SM singlets, their tree-level production through gauge bosons is prohibited. In models A and C, the Yukawa interactions κ' permit their pair production

via ψ exchange at lepton colliders, as shown in Fig. 3.7 (diagram f). The pair-production cross section for a center-of-mass energy $s > 4M_S^2$ reads

$$\sigma(\ell^+\ell^- \to SS^\dagger) = \frac{N_F}{32\pi}\frac{\kappa'^4}{s}\left(1-\frac{4M_S^2}{s}\right)^{5/2} \times \\ \times \int_{-1}^{1} \mathrm{d}x\; x^2(1-x^2)\left[\left(\frac{2(M_F^2-M_S^2)}{s}+1\right)^2 - (1-\frac{4M_S^2}{s})x^2\right]^{-2} . \tag{3.3.14}$$

Additionally, the Yukawa interactions κ and κ' permit single-production of either Re[S] or Im[S] in association with the Higgs, also shown in diagram (f). Furthermore, after spontaneous symmetry breaking in the Higgs and BSM sector the portal coupling δ gives rise to trilinear couplings hRe[S]Re[S], hIm[S]Im[S] and hhRe[S]. This allows the S to be pair- or singly-produced via s-channel Higgs both in pp and $\ell\ell$ colliders (diagram g), a contribution which arises in all models. Hence, S-production occurs through few channels and is driven by either Yukawa or scalar quartic couplings. However, for the appropriate BSM mass hierarchies the S take an important role in the decay of the ψ, and could therefore have a strong presence in processes occurring at colliders, as we study in detail in Chapter 4.

3.3.3 BSM Sector Decay

We now discuss decays of the BSM sector. We first study decays of the vector-like fermions, including as well decay channels induced by mixing, and go on to discuss the decays of the BSM scalars.

Vector-like Fermions

Let us first discuss how the vector-like fermions decay in the absence of mixing. The Yukawa interactions κ allow for decays of the $Q_F = -1$ and $Q_F = 0$ states to $h\nu$ and $h\ell^-$, respectively.[2] The latter occurs at a rate

$$\Gamma(\psi \to \ell h) = \frac{\pi}{4} C_{\psi\ell}^2\, \alpha_\kappa M_F \left(1-\frac{m_h^2}{M_F^2}\right)^2 , \tag{3.3.15}$$

where we have neglected the lepton mass, and the Clebsch-Gordan coefficient reads $C_{\psi\ell} = 1/\sqrt{2}$ for the $T_3 = 0$ states in models B and F and $C_{\psi\ell} = 1$ otherwise. For $\alpha_\kappa \gtrsim 10^{-14}$ and M_F at the TeV scale or above, one obtains a lifetime $\Gamma^{-1} \lesssim \mathcal{O}(10^{-13})$ s, which leads to a prompt decay.

Additionally, in models A (C), the decays $\psi_i \to \ell_j S_{ji}^\dagger$ ($\psi_i \to \ell_j S_{ji}$) are also allowed if the BSM scalars are lighter than the vector-like fermions. The corresponding decay rate obeys

$$\Gamma(\psi \to \ell S) = \frac{\pi}{2} C_{\psi\ell}^2\, \alpha_{\kappa'} M_F \left(1-\frac{M_S^2}{M_F^2}\right)^2 . \tag{3.3.16}$$

[2] With the exception of model C, for which only the $Q_F = -1$ states can decay to Higgs plus lepton due to the $SU(2)_L$ structure of the interaction.

In model C, the decay $\psi_i^0 \to \nu_j S_{ji}$ occurs as well with the same rate. For large values of κ', the decays through S become the main decay channel of the ψ when kinematically allowed, as we shall see explicitly in Chapter 4.

Furthermore, models B and D contain $Q_F = -2$ fermions while model F contains $Q_F = +1$ fermions, which cannot decay through BSM Yukawa interactions. However, $SU(2)_L$ mass splitting leads to mass differences Δm within the multiplets, which are induced at 1-loop via weak interactions. This allows the $Q_F = -2$ and $Q_F = +1$ states to decay to the $Q_F = -1$ or $Q_F = 0$ components within their corresponding multiplet, respectively. The $Q_F = -1$ and $Q_F = 0$ states subsequently decay to leptons and scalars through Yukawa interactions. The mass splitting in the limit $M_F \gg m_W, m_Z$ in models B and D reads [85]

$$\Delta m_{B,D} = M_{\psi^{-2}} - M_{\psi^{-1}} \simeq \frac{\alpha_2^{\rm PDG}}{2}\left(3\sin\theta_w^2 m_Z + k\right) , \tag{3.3.17}$$

with $k = m_W - m_Z$ (model B), $k = 0$ (model D), which is of order GeV for both models, and $\alpha_2^{\rm PDG} = g_2^2/4\pi \simeq 0.034$. Note that in the limit of heavy vector-like fermions the mass splitting (3.3.17) is not proportional to M_F, but scales with the weak boson masses and depends on the $SU(2)_L$ charges of the multiplet. The decay rate then reads

$$\Gamma(\psi^{-2} \to \psi^{-1}\ell\nu) \sim G_F^2 \frac{\Delta m^5}{15\pi^3} \simeq 3\cdot 10^{-13}\text{GeV}\left(\frac{\Delta m}{[\text{GeV}]}\right)^5 , \tag{3.3.18}$$

which has a strong dependence on the value of the mass splitting. We find that the rate (3.3.18) results in picosecond lifetimes for the ψ^{-2}, which give a small but macroscopic displacement $c\tau \simeq 0.3$ mm and a displaced vertex signature which can be searched for at the LHC [86]. For model F, the ψ^{+1} acquire mass splitting

$$\Delta m_F = M_{\psi^{+1}} - M_{\psi^0} = \alpha_2^{\rm PDG} M_W \sin^2\frac{\theta_w}{2} \simeq 166\ \text{MeV} , \tag{3.3.19}$$

which is about one order of magnitude smaller than the splitting in models B and D. The corresponding decay rate, which can be approximated as (3.3.18), is therefore heavily suppressed with respect to the case of the ψ^{-2}. This allows for remarkable long-lived charged particle signatures in the case of model F. However, the presence of fermion mixing induces faster decays unless there is a strong suppression from mixing angles, as we discuss shortly. It is worth noting that the ρ-parameter poses limits on general $SU(2)_L$ mass splittings δM, which imply [84]

$$N_F S(R_2)\,\delta M^2 \lesssim (40\,\text{GeV})^2 , \tag{3.3.20}$$

where $S_2(R_2)$ is the Dynkin index of the representation R_2 of $SU(2)_L$ (see Appendix B for details). For $N_F = 3$ and $S_2 = 2$ ($S_2 = 1/2$) for models B and F (model D), the mass splittings given by Eqs. (3.3.17) and (3.3.19) are well within constraints.

Finally, let us discuss the decays induced by fermion mixing. After rotating to the mass basis, vector-like fermions can decay to weak bosons and fermions with rates

$$\begin{aligned}\Gamma(\psi_i^{Q_e} \to Z f_i^{Q_e}) &= \frac{M_F}{64\pi}\frac{g_2^2}{\cos^2\theta_w}\left(g_V^2+g_A^2\right)(1-r_Z)^2(2+1/r_Z)\,,\\ \Gamma(\psi_i^{Q_e} \to W^- f_i^{Q_e+1}) &= \frac{M_F}{64\pi}g_2^2\,\left[c_L^2+c_R^2\right](1-r_W)^2(2+1/r_W)\,,\end{aligned} \tag{3.3.21}$$

where Q_e denotes the electric charge of a fermion, $r_i = m_i^2/M_F^2$ and $f^{-1} = \ell$, $f^0 = \nu$. The Z couplings $g_{V,A}$ can be read off Tabs. 2.1 and 2.2 for all models, while the W coefficients $c_{L,R}$ are collected in Tab. 2.3 with Clebsch-Gordan coefficients given by Eq. (3.3.10). Electroweak decays through mixing are especially relevant for the ψ^0 states of model C. These can decay via $\psi^0 \to S\nu$ through κ' if kinematically allowed, and for $M_S > M_F$ they can only decay through weak interactions, with different mechanisms for each type of vacuum alignment. First, note that for V^+ and the vacuum-aligned flavor of V^- rotation angles in model C fulfill $\theta_L^C > \theta_R^C$, and at tree level one finds $\theta_L^C = \theta_L^{0,C}$. Therefore, from the W interaction coefficients of Tab. 2.3 one can see that the decay $\psi^0 \to \ell^- W^{+*}$ happens at order $\sin^2\theta_R^C$. Alternatively, if θ_R^C is very small, mass splitting plays again a role in the decay. Note that in model C the ψ^0 is the lightest state in the $SU(2)_L$ doublet, with the mass splitting fulfilling

$$\Delta m_C = M_{\psi^{-1}} - M_{\psi^0} = \frac{\alpha_2^{\rm PDG}}{2}\sin\theta_w^2 m_Z \simeq 0.4\ \text{GeV}. \tag{3.3.22}$$

Then, mixing angles acquire a small difference $\theta_L^{0,C} - \theta_L^C \simeq \theta_L^C(\Delta m_C/M_F)$, and the decay $\psi^0 \to \ell^- W^{+*}$ can take place through left-handed mixing angles. On the other hand, for the non-aligned flavors k of V^-, one finds $\theta_L^{0,C} = 0$, and the angles of the negatively charged rotations have the opposite hierarchy $\theta_L^C \ll \theta_R^C$. Then, the ψ_k^0 decay as $\psi_k^0 \to W^+\ell_k^-$ with coefficient $|c_R| = \sin\theta_R^C \simeq \kappa v_h/\sqrt{2}M_F$.

To summarize, we have found that vector-like fermions can decay through their Yukawa interactions κ to Higgs plus lepton, and additionally in models A and C through κ' to S plus lepton if the BSM mass hierarchy allows it. The $Q_F = -2$ states of models B and D and the $Q_F = +1$ states of model F must first cascade within their multiplet through W exchange driven by $SU(2)_L$ mass splitting, leading to displaced vertices and long-lived signatures, respectively. Electroweak decays to W or Z plus lepton are additionally allowed by mass mixing. In the case of the $Q_F = 0$ states of model C, where decays to Higgs plus neutrino are prohibited, for $M_F < M_S$ decays depend on the vacuum structure and are driven by both mass splitting and mixing.

Scalars

The BSM scalars can decay via four different channels. Schematically, these are:

i) $S \to \overline{\psi}\psi$ through the Yukawa y (for $M_F > 2M_S$, in all models and for all S_{ij} flavors)

ii) $S \to GG'$, where G are gauge bosons, through a ψ loop (only for the diagonal components S_{ii}, and absent in model E)

iii) $S \to \psi\ell, \psi\nu$, either through κ' (models A and C) or through mixing in the y interaction (all models, at order θy)

iv) $S \to \ell\ell'$, which occurs thanks to mixing either at order $\kappa'\theta$ (models A and C) or $y\theta^2$ (all models)

Let us first discuss the decays which do not require mixing. For $M_F > 2M_S$, $S \to \overline{\psi}\psi$ occurs in all models via the y interaction, while in models A and C the decay $S \to \psi\ell, \psi\nu$ takes place for $M_F \gtrsim M_S + m_\ell$, $M_F \gtrsim M_S$ respectively through κ'. These channels are available for all flavors S_{ij}. Neglecting lepton masses, their corresponding decay rates obey

$$\begin{aligned}
\Gamma(S_{ij} \to \overline{\psi}_i\, \ell_j) + \Gamma(S_{ij} \to \overline{\ell_j}\, \psi_i) &= 2\pi\alpha_{\kappa'} M_S \left(1 - \frac{M_F^2}{M_S^2}\right)^2 , \\
\Gamma(S_{ij} \to \overline{\psi}_i\, \psi_j) + \Gamma(S_{ij} \to \overline{\psi_j}\, \psi_i) &= 2\pi\alpha_y M_S \left(1 - \frac{4M_F^2}{M_S^2}\right)^{1/2+\xi} ,
\end{aligned} \tag{3.3.23}$$

where $\xi = 1$ and $\xi = 0$ correspond to the scalar and pseudoscalar parts of S, respectively. Note that for $i = j$ the right-hand side of Eq. (3.3.23) picks up a factor 2, while for $i \neq j$ the second term on the the left-hand side vanishes due to flavor conservation. Model-dependent $SU(2)_L$ multiplicities in the final states are not explicitly shown in Eq. (3.3.23). For example, in model B the S_{ij} decay to $\overline{\psi}_i^{-2}\psi_j^{-2} + \overline{\psi}_i^{-1}\psi_j^{-1} + \overline{\psi}_i^{0}\psi_j^{0}$ plus $\mathcal{CP}$-conjugate final states.

The diagonal components S_{ii} of the BSM scalars can decay through a ψ triangle loop to a pair of electroweak bosons thanks to the Yukawa coupling y. The off-diagonal S_{ij} (with $i \neq j$) do not present this decay, as the y interaction is strictly flavor-conserving in our setup. For the S_{ii}, decays to dibosons take place in all models with the exception of model E, where the ψ are total gauge singlets. The corresponding decay rates to two gauge bosons G and G' read

$$\Gamma(S_{ii} \to GG') = \frac{\alpha_e^2 \alpha_y}{16\pi} \frac{M_S^3}{M_F^2} \left| C_{GG'} A_{1/2}(\tau) \right|^2 . \tag{3.3.24}$$

The coefficients $C_{GG'}$ depend on the representation of ψ and in the limit $M_S \gg M_W$ can be written as

$$\begin{aligned}
C_{\gamma\gamma} &= S_2(R_2) + d(R_2)Y^2 , \quad & C_{ZZ} &= S_2(R_2) \tan^{-2}\theta_w + d(R_2)Y^2 \tan^2\theta_w , \\
C_{WW} &= \frac{\sqrt{2}}{\cos^2\theta_w} S_2(R_2) , & C_{Z\gamma} &= \sqrt{2}\left(S_2(R_2)\tan^{-1}\theta_w - d(R_2)Y^2 \tan\theta_w\right) ,
\end{aligned} \tag{3.3.25}$$

and the loop function reads $A_{1/2}(\tau) = \frac{2}{\tau^2}\left(\xi\tau + (\tau - \xi) f(\tau)\right)$ with

$$f(\tau) = \begin{cases} \arcsin^2(\sqrt{\tau}) & \text{for } \tau \leq 1 , \\ -\frac{1}{4}\left(\ln\frac{1+\sqrt{1-\tau^{-1}}}{1-\sqrt{1-\tau^{-1}}} - i\pi\right)^2 & \text{for } \tau > 1 , \end{cases} \tag{3.3.26}$$

and $\tau = M_S^2/4M_F^2$ [87]. For model A, the reduced rates $\Gamma/(M_S\alpha_y)$ for the different channels as a function of τ are shown in Fig. 3.9 (left) for $\alpha_y = \alpha_{\kappa'}$. One can see that the decay channels $\overline{\psi}\psi$ and $\psi\ell$ dominate, followed by the decay to photons. Since in model A the

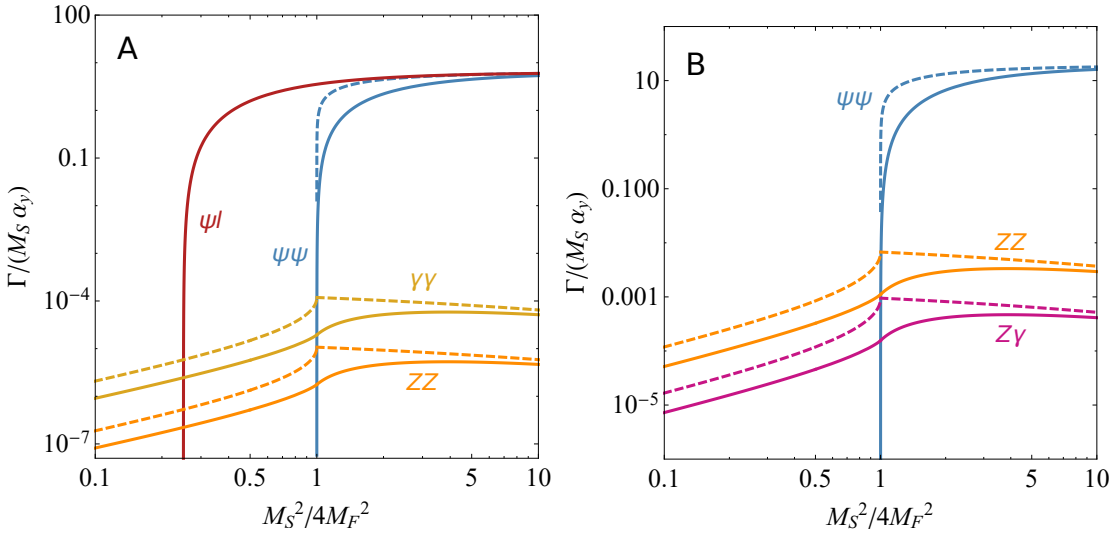

Figure 3.9. Reduced decay rates $\Gamma/(M_S\alpha_y)$ of the flavor-specific components of the BSM scalars S in model A (left) and model B (right) for $\alpha_y = \alpha_{\kappa'}$, see Eqs. (3.3.23) and (3.3.24). Decays to dibosons occur only for the diagonal components S_{ii}. Solid (dashed) lines correspond to the scalar (pseudoscalar) decays; for $S \to \psi\ell$ they coincide. In model A, the decay rate into $Z\gamma$ lies between the ZZ and $\gamma\gamma$ curves, while decay rates in model B into WW and $\gamma\gamma$ satisfy $\Gamma^{\rm B}_{ZZ} > \Gamma^{\rm B}_{\gamma\gamma} > \Gamma^{\rm B}_{WW} > \Gamma^{\rm B}_{Z\gamma}$. If kinematically allowed, decays to fermions dominate.

ψ are $SU(2)_L$ singlets, di-W decays are forbidden, while the coefficients of the remaining gauge boson modes obey $1 > (C_{Z\gamma})^2 = 2\tan\theta_w^2 > (C_{ZZ})^2 = \tan\theta_w^4$.

Similarly, in models B, C, D and F, the decays $S \to \overline{\psi}\psi$ (and additionally $S \to \psi\ell, \psi\nu$ in model C) dominate if kinematically allowed. Furthermore, the decays to W^+W^- are also permitted, as the vector-like fermions carry $SU(2)_L$ charges. In Fig. 3.9 (right) we show the corresponding reduced rates $\Gamma/M_S\alpha_y$ for the case of model B. The hierarchies of the diboson modes for the $SU(2)_L$-charged models read

$$\begin{aligned} &\Gamma^{\rm B}_{ZZ} > \Gamma^{\rm B}_{\gamma\gamma} > \Gamma^{\rm B}_{WW} > \Gamma^{\rm B}_{Z\gamma}\,, \qquad &&\Gamma^{\rm C}_{ZZ} > \Gamma^{\rm C}_{\gamma\gamma} > \Gamma^{\rm C}_{Z\gamma} \approx \Gamma^{\rm C}_{WW}\,, \\ &\Gamma^{\rm D}_{\gamma\gamma} > \Gamma^{\rm D}_{ZZ} > \Gamma^{\rm D}_{Z\gamma} > \Gamma^{\rm D}_{WW}\,, \qquad &&\Gamma^{\rm F}_{ZZ} > \Gamma^{\rm F}_{Z\gamma} > \Gamma^{\rm F}_{WW} > \Gamma^{\rm F}_{\gamma\gamma}\,. \end{aligned} \tag{3.3.27}$$

In addition, if one of the S_{ij} presents mixing with the Higgs with angle β, its real part can decay through scalar mixing at a rate $\Gamma_{\rm mix} = \sin^2\beta\,\Gamma_h^{\rm SM}$, where $\Gamma_h^{\rm SM}$ is the decay rate of the Higgs in the SM. This concludes our discussion of S decays in the absence of fermion mixing. Therefore, for $M_S < M_F$ and within a parameter space where α_y and β are negligible the S could potentially be a stable particle. However, the additional channels arising from fermion mixing may lead to fast decays, as we discuss next.

Models A and C contain κ' interactions. After rotations to the mass basis, tree-level decays $S_{ij} \to \ell_i^\pm \ell_j^\mp$ are allowed with couplings $\kappa'\theta_L^A, \kappa'\theta_R^C \simeq \kappa' \frac{\kappa v_h}{\sqrt{2}M_F}$, using the angles in Tab. 3.6. These decays can be competitive with the diboson modes. For instance, in model A and for $\kappa' \sim y$, they dominate over $S \to \gamma\gamma$ as long as θ_L^A is of order 10^{-3} or larger. The S lifetime

is then below picoseconds, and therefore too fast to yield displaced vertex signatures unless fermion mixing is strongly suppressed, at least by $\kappa' \theta_L^A, \kappa' \theta_R^C \lesssim 10^{-7}$ for M_S at the TeV scale.

For models B, D and F, mixing yields effects for S decays in the Yukawa interaction y: decays of the type $S \to \overline{\psi}\ell$ and $S \to \ell^- \ell'^+$ arise at order $y\theta$ and $y\theta^2$, respectively. More precisely, in models B and F (model D) rotations of the negatively charged states induce $S_{ij} \to \psi_j \ell_i$ ($S_{ij} \to \psi_i \ell_j$) for $M_F > M_S$. Additionally, the decays $S_{ij} \to \ell_i^\pm \ell_j^\mp$ arise at order

$$y\, \theta_L^M \theta_R^M \simeq y \left(\frac{\kappa v_h}{\sqrt{2} M_F} \right)^2 \frac{y_\ell v_h}{\sqrt{2} M_F} \,, \tag{3.3.28}$$

and they can constitute the leading decay channel for $M_S < M_F$. Unless mixing yields a suppression of $y\, \theta_L^M \theta_R^M \sim 10^{-7}$ or smaller, using Eq. (3.3.23) one obtains below-picosecond lifetimes of the S. Furthermore, the coupling (3.3.28) of the dilepton mode is flavor-dependent, with tau-less final states presenting a stronger suppression. Therefore, scenarios are possible where decays into dielectrons, dimuons and $e^\pm \mu^\mp$ are slower and present displaced vertex signatures, while those into ditaus, $e^\pm \tau^\mp$ and $\mu^\pm \tau^\mp$ could remain prompt. Moreover, an important feature of the dilepton decay modes of the S_{ij} is that they can yield different-flavor and opposite-charge leptons, giving rise to LFV-like signatures, even though lepton flavor is strictly conserved by our interactions. We shall exploit this in Chapter 4 when building observables to look for our models at colliders.

Finally, in models with electrically neutral vector-like fermions the decays $S \to \overline{\psi}^0_j \nu_i$ are allowed for $M_S > M_F$. These decays occur at order $y\, \theta_L^{0,M}$ for models B, E and F and at order κ' for model C. For model E they represent the only decay mode of the S_{ij}, apart from $S \to \overline{\psi}\psi$ if kinematically allowed.

3.3.4 Drell-Yan

New particles charged under the SM lead to new physics corrections to the gauge boson propagators, which in the case of electroweak interactions can be quantified in terms of the parameters W and Y. These are defined as [88]

$$Y = \alpha_1 \frac{3}{50} \frac{M_W^2}{\Lambda^2} \left(B_1^{\rm SM} - B_1 \right) , \quad W = \alpha_2 \frac{1}{10} \frac{M_W^2}{\Lambda^2} \left(B_2^{\rm SM} - B_2 \right) , \tag{3.3.29}$$

where $B_{1,2}$ ($B_{1,2}^{\rm SM}$) are the 1-loop coefficients of β_1 and β_2 in a given model (in the SM). Measurements of Drell-Yan processes [89] allow then to constrain the scale of new physics $\Lambda \sim M_F$ in all our models except for model E, for which the vector-like fermions do not couple to the weak bosons. For the remaining models, we find

$$\begin{gathered} M_F \gtrsim 0.1 \text{ TeV (model A)} \,, \; M_F \gtrsim 0.2 \text{ TeV (models C, D)} \,, \\ M_F \gtrsim 0.3 \text{ TeV (models B, F)} \,. \end{gathered} \tag{3.3.30}$$

Constraints for models A, B and D are shown in Fig. 3.10, where we also indicate projected limits. In model B, the bound (3.3.30) excludes matching scenarios of fixed points B_2

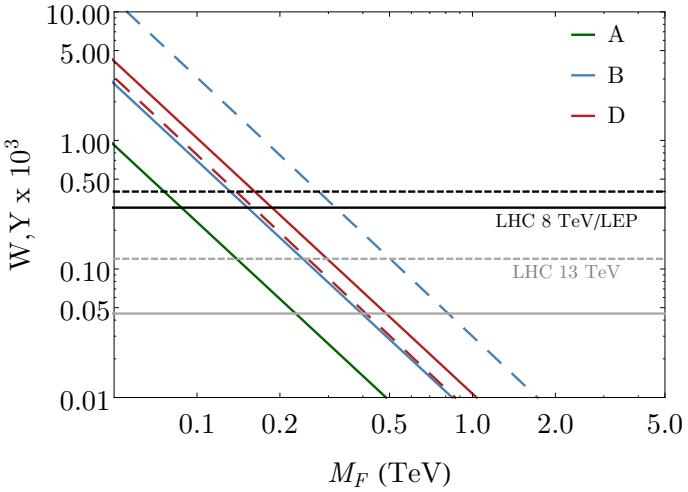

Figure 3.10. Electroweak parameters Y (solid lines) and W (dashed lines) for models A, B and D as functions of the BSM fermion mass. We show as well constraints from either LHC 8 TeV or LEP (black), and the projected sensitivity of LHC 13 TeV (gray) [89].

and B_4, which can only be matched at $M_F \simeq 0.02$ TeV, while fixed points displaying an asymptotically free α_2 remain viable. Effects from two-loop corrections in W, Y can be estimated by employing the effective coefficients B_i^{eff} instead of $B_{2,1}$ in Eq. (3.3.29). For feeble BSM Yukawa couplings, this typically induces relative changes of order 1% or less in W, Y, which do not flip their sign.

3.3.5 Anomalous Magnetic Moments

Our BSM Yukwawa interactions contribute to anomalous magnetic moments of leptons at 1-loop. This constitutes an especially interesting feature for new physics models, since experimental determinations are in tension with SM predictions both in case of the muon and the electron. In this section, we briefly review the theoretical and experimental status of lepton AMMs and explore the parameter space for which our models can explain the current anomalies.

From a quantum field theory point of view, anomalous magnetic moments constitute a certain contribution to loop corrections of the photon coupling to fermions, depicted schematically in Fig. 3.11 for a given lepton ℓ. Contributions to the vertex of Fig. 3.11 can be parametrized through the matrix element [38, 90]

$$\bar{u}(p')\left[e\gamma^\mu F_1(q^2) + ie\frac{\sigma^{\mu\nu}q_\nu}{2m_\ell}F_2(q^2) + ie\,\epsilon^{\mu\nu\sigma\rho}\sigma_{\rho\sigma}q_\nu F_3(q^2)\right]u(p)\,, \tag{3.3.31}$$

where m_ℓ is the lepton mass and F_i are form factors depending on the transfered momentum $q = p - p'$, with $\sigma^{\mu\nu} = \frac{i}{2}[\gamma^\mu, \gamma^\nu]$. At tree level in QED one obtains $F_1(0) = 1$ and $F_2(0) = F_3(0) = 0$. Loop corrections then give rise to scale-dependence effects of α_e through F_1, and can yield nonzero values for F_2 and F_3. The Lorentz structure accompanied by F_2

yields corrections to the magnetic moment of the given fermion, which are precisely what we call its *anomalous magnetic moment*, in the sense that they arise purely from quantum fluctuations. It is worth noting that the AMM is the coefficient of a chirality-flipping operator, as can be gathered from the Lorentz structure containing $\sigma^{\mu\nu}$. The form factor F_3 accompanies a similar Lorentz structure, with the crucial difference that it can only be nonzero if the couplings present a source of $\mathcal{CP}$-violation. It is connected to electric dipole moments, which we discuss in the next section.

The classical value of the magnetic moment, $g^{\rm cl} = 2$, is already contained in the tree-level QED vertex. Then, it is usual to define the anomalous part $(g-2)_\ell$ of the magnetic moment of a lepton ℓ through the relation

$$a_\ell = \frac{(g-2)_\ell}{2} = F_2(0)\,, \tag{3.3.32}$$

which reads $a_\ell = \alpha_e/2\pi$ at 1-loop in QED [91]. From the experimental side, in the case of the muon measurements at BNL report an AMM of [15]

$$a_\mu^{\rm exp} = 11659208.9(6.3)\cdot 10^{-10}\,, \tag{3.3.33}$$

where statistical and systematic uncertainties have been added in quadrature [3]. This entails a discrepancy with SM predictions of [37]

$$\Delta a_\mu = a_\mu^{\rm exp} - a_\mu^{\rm SM} = 268(63)(43)\cdot 10^{-11}\,, \tag{3.3.34}$$

where uncertainties are experimental and theoretical, respectively. Adding them in quadrature, the deviation from the SM adds up to 3.5σ, while certain theory predictions find up to $4.1\,\sigma$ [92, 93]. On the other hand, recent lattice determinations of the hadronic vacuum polarization suggest that the the anomaly could not be present [94]. This is however in tension with electroweak data and earlier lattice studies, and therefore requires further scrutiny [95–97]. In this work we shall use the anomaly (3.3.34) as a guideline, and explore the parameter space in our models which is able to accommodate it. Note that, since the AMM is determined by a matrix element rather than an amplitude, the sign of each contribution is crucial in evaluating whether it alleviates or enhances the discrepancy.

In the case of the electron, direct measurements indicate [98]

$$a_e^{\rm exp} = 1001159652180.73(28)\cdot 10^{-12}\,. \tag{3.3.35}$$

Comparison with SM predictions have recently become in tension with experiment, thanks to a recent determination of the fine structure constant using cesium atoms [14]. This yields a difference between theory and experiment of

$$\Delta a_e = a_e^{\rm exp} - a_e^{\rm SM} = -88(28)(23)\cdot 10^{-14}\,, \tag{3.3.36}$$

[3] This value has been rescaled using the muon and the proton magnetic moment ratio, see [37] for details.

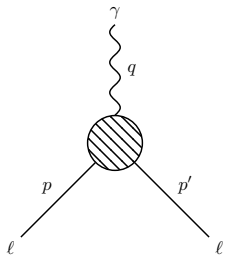

Figure 3.11. Quantum corrections to charged lepton couplings to photons, with incoming and outgoing momenta p and p', respectively.

where we again show experimental and theory uncertainties. The pull from the SM prediction corresponds in this case to -2.4σ, and the discrepancy carries opposite sign with respect to the muon anomaly. Furthermore, a new measurement of the fine structure constant using rubidium atoms has been published very recently. A determination of the electron AMM using the rubidium data yields $\Delta a_e^{\text{Rub}} = (48 \pm 30) \cdot 10^{-14}$, which represents a deviation of 1.6σ from the SM, and a 5.4σ tension with the cesium measurement [99]. Note that the results of both experiments yield values of Δa_e which are comparable in size and error but deviate from the SM in different directions. The origin of the discrepancy between the two measurements remains unclear, and will require further experimental efforts [100]. In what follows, we employ the cesium data [14] unless otherwise specified, and indicate implications of the rubidium measurement in the case of simultaneous explanations of the electron and the muon AMMs.

Significant effort has been invested by the theory community in order to explain the lepton AMM anomalies simultaneously. Models have been put forward which feature new light scalar fields [101–106], leptoquarks [107, 108], extended Higgs sectors [109, 110], supersymmetry [111–114] or other BSM physics [115–123]. Effective field theory methods have also been used to shed light on the subject with a bottom up-approach [124, 125]. In general, these explanations introduce a source of violation of lepton flavor universality (LFU) which allows for the different sizes and signs of the corrections to both anomalies. However, here we shall argue that the electron and muon data can also be explained without an explicit breaking of LFU, provided that a mechanism is in place which allows for different scaling of the corrections to each AMM.

Contributions from General Yukawa Interactions

In our models, contributions to lepton AMMs arise mainly through new Yukawa couplings. For a general Yukawa interaction between a lepton, a fermion ψ with $Q_F = -1$ and a neutral scalar H described by the Lagrangian

$$\mathcal{L}_{\text{Y, gen}} = \overline{\psi}\,(c_L P_L + c_R P_R)\,\ell H + \text{h.c.}\,, \tag{3.3.37}$$

the contribution through a fermion-scalar loop amounts to

$$a_\ell^{\rm NP} = \frac{m_\ell^2}{16\pi^2 m_H^2}\left[\frac{1}{2}(c_L^2+c_R^2)\, I_1(M_F^2/m_H^2) + \frac{M_F}{m_\ell} c_L c_R\, I_2(M_F^2/m_H^2)\right], \tag{3.3.38}$$

where the couplings $c_{L,R}$ are assumed to be real, and the loop integrals in the limit $m_\ell \to 0$ read

$$I_1(t) = \frac{t^3-6t^2+3t+6t\ln(t)+2}{3(t-1)^4}, \qquad I_2(t) = \frac{t^2-4t+2\ln(t)+3}{(t-1)^3}. \tag{3.3.39}$$

These are well defined for $t \to 1$, yielding, $I_1(1) = 1/6$ and $I_2(1) = 2/3$. A crucial feature to note about the new physics contribution (3.3.38) is its dependence on the chiral couplings. The first term in its right-hand side is present for any Yukawa interaction, and always carries a suppression of m_ℓ^2. Except for model E, which is the only model that does not contain $Q_F = -1$ vector-like fermions, such a contribution arises in all of our models via Higgs exchange through the Yukawa interaction κ and additionally via S exchange and κ' in models A and C, as shown in Fig. 3.12. There, the chirality flip necessary for any contribution to the AMM is depicted to occur in an external fermion line. From Eq. (3.3.38) one finds that in the heavy-fermion limit, which yields $I_1(M_F^2/m_H^2) \simeq m_H^2/3M_F^2$, this new physics contribution to the AMM of a lepton can be approximated as

$$a_\ell^{\rm NP} \simeq \frac{1}{6}\,\frac{m_\ell^2}{M_F^2}\,\frac{c_L^2+c_R^2}{16\pi^2}, \tag{3.3.40}$$

where $c_{L,R}$ can be identified with either κ or κ' in our models. For real couplings, the contribution (3.3.40) is always positive, and therefore ill-equipped to alleviate the tension of the electron AMM in Eq. (3.3.36). For models A and C and for $\kappa \sim \kappa'$, the dominant contribution comes from the exchange of the lightest scalar. However, note that for κ' the three flavors of the ψ_i can propagate in the loop (see again Fig. 3.12), which after summing over all flavors leads to an additional factor of $N_F = 3$ in the total new physics contribution with respect to κ-driven loops.

Going back to the general new physics contribution of (3.3.38), we now focus on the second term on its right-hand side, which presents an M_F/m_ℓ enhancement. Such a contribution is often depicted as a Feynman diagram with a chirality flip in an internal fermion line, as shown in Fig. 3.13. For this term to be switched on, one requires $c_L \neq 0$ and $c_R \neq 0$ simultaneously. The contribution ultimately carries a suppression by only one power of the lepton mass. Taking again the limit of heavy vector-like fermions, for which $I_2(M_F^2/m_H^2) \simeq m_H^2/M_F^2$, Eq. (3.3.38) yields a chirally enhanced contribution of

$$a_\ell^{\rm NP*} \simeq \frac{m_\ell}{M_F}\,\frac{c_L c_R}{16\pi^2}, \tag{3.3.41}$$

which can be either positive or negative, depending on the signs of the $c_{L,R}$. As we shall spell out shortly, such chirally enhanced terms only arise in models A and C and in the

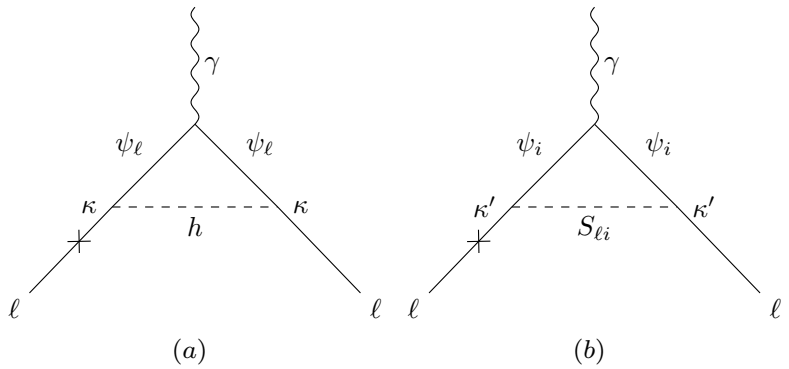

Figure 3.12. Contributions to Δa_ℓ ($\ell = e, \mu, \tau$) with a lepton chiral flip (cross on solid line) via h (a) or $S_{\ell i}$ exchange, with $i = 1, 2, 3$, only present in models A, C (b).

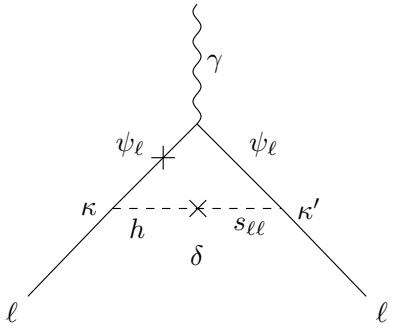

Figure 3.13. Chirally enhanced contribution to the anomalous magnetic moment of a lepton ℓ through scalar mixing (cross on dashed line) and a ψ_ℓ chiral flip (cross on solid line).

presence of scalar mixing. For this reason these models are the only ones which can accommodate both anomalies. The key observation is that, with BSM contributions displaying universal scaling (either linear or quadratic in the lepton mass) both anomalies cannot be explained, as depicted in Fig. 3.14. However, if BSM models present both types of contributions fitting the data is indeed possible, as we detail below.

Furthermore, one might wonder about contributions to the AMMs from gauge boson exchange. Such contributions only arise as a consequence of fermion mixing, which enables couplings between the ψ, SM leptons and weak bosons. The θ^2 suppression in terms of the mixing angle and a quadratic dependence on the lepton mass results in gauge boson exchange yielding parametrically smaller contributions compared to scalar exchange, and we shall neglect it here.

Accommodating Experimental Results

Let us now discuss the parameter space of our Yukawa couplings κ, κ' which are able to accommodate the anomalies (3.3.34) and (3.3.36). We begin with contributions of the type (3.3.40) which, as we have seen, are always positive and thus cannot possi-

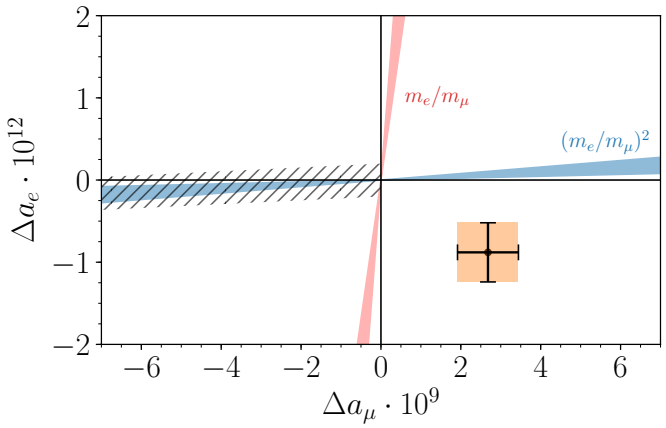

Figure 3.14. Leading contributions to $\Delta a_{e,\mu}$ from Fig. 3.13a (blue) and Fig. 3.13b (red). Band widths represent a 20% mass splitting between BSM fermion flavors from leading loops; the hatched region is inaccessible due to quadratic contributions being positive. The data (3.3.34) and (3.3.36) within their 1σ uncertainties is shown as well (yellow). With a universal scaling for both flavors, simultaneous explanations of the anomalies are not possible.

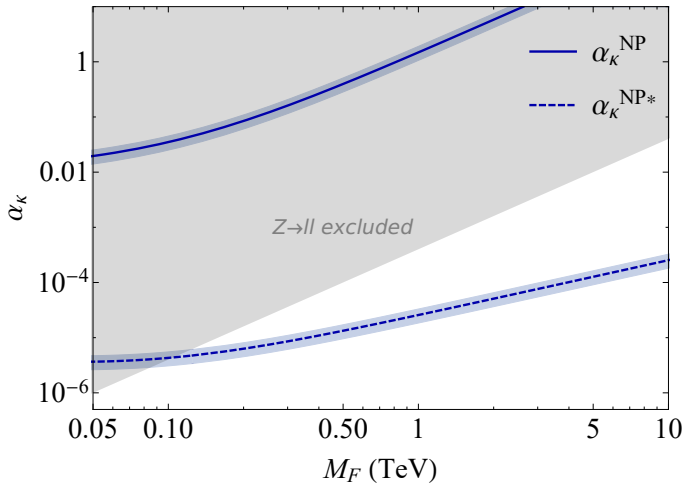

Figure 3.15. Values of α_κ and vector-like fermion masses that account for the $(g-2)_\mu$ anomaly (3.3.34) for new physics contributions scaling as $a_\mu^{\rm NP} \sim \alpha_\kappa m_\mu^2/M_F^2$ (solid line) and as $a_\mu^{\rm NP*} \sim \alpha_\kappa m_\mu/M_F$ (dotted line), see Eqs. (3.3.40) and (3.3.41). The shaded region is excluded by Z-data according to the bound (3.3.9). Contributions scaling quadratically with the muon mass are generally excluded.

bly account for Δa_e. Explaining Δa_μ with κ-mediated Higgs exchange would require $\alpha_\kappa\, M_F^{-2} \approx (1.4 \pm 0.4)\,\text{TeV}^{-2}$ in models A, C and D, and $\alpha_\kappa\, M_F^{-2} \approx (4.2 \pm 1.2)\,\text{TeV}^{-2}$ for models B and F. Nevertheless, Z data heavily constrains the $\alpha_\kappa\,, M_F$ parameter space through fermion mixing. In fact, the bound (3.3.9) rules out any explanation of Δa_μ through the Yukawa coupling κ with scaling (3.3.40) in all of our models, as shown in Fig. 3.15 (solid line), while κ-driven contributions scaling as (3.3.41) are allowed (dotted line). In models

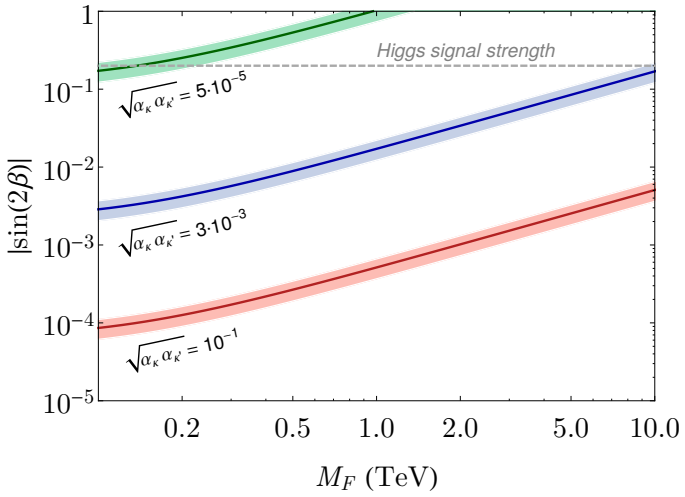

Figure 3.16. Scalar mixing angle $|\sin 2\beta|$ as a function of M_F that explains Δa_μ within its 1σ uncertainty for a muon-aligned vacuum V^-, which yields the chirally enhanced contribution (3.3.46), and for different values of $\sqrt{\alpha_\kappa \alpha_{\kappa'}}$. We show as well the upper bound on β from Higgs signal strength measurements [14]. For V^+ the corresponding, requisite value of $|\sin 2\beta'|$ is a factor of $\sqrt{3}$ larger (see Eq. (3.3.49)).

A and C, however, κ'-mediated interactions remain unconstrained by Z data. In order to follow the conventions of [24], let us rewrite this particular new physics contribution as

$$a_\ell^{\kappa'} = \frac{N_F\, \kappa'^2}{96\pi^2}\, \frac{m_\ell^2}{M_F^2}\, f_1\left(\frac{M_S^2}{M_F^2}\right), \tag{3.3.42}$$

with loop function

$$f_1(t) = \frac{3}{t} I_1(1/t)\,, \tag{3.3.43}$$

in terms of Eq. (3.3.39), and $f_1(0) = 1$. In the limit $M_S^2/M_F^2 \ll 1$, we find that the muon anomaly can be accommodated for a Yukawa coupling

$$\alpha_{\kappa'} \simeq (0.48 \pm 0.15) \left(\frac{M_F}{[\text{TeV}]}\right)^2, \tag{3.3.44}$$

which demands a rather large yet perturbative coupling $\alpha_{\kappa'}$ for M_F at the TeV scale. The contribution (3.3.42) is however universal and positive, so one might wonder if it increases the tension in a_e. Still, the suppression by m_e^2 in the case of the electron AMM yields only $a_e^{\kappa'} \simeq 6 \cdot 10^{-14}$, which represents only about 7% of Δa_e and is smaller than both its theoretical and experimental errors. Thus, we conclude that models A and C can explain the anomaly in the muon AMM through Eqs. (3.3.42) and (3.3.44) without aggravating the status of the electron AMM. It is also worth noting that this is possible regardless of the pattern of spontaneous symmetry breaking in the scalar sector.

Moreover, models A and C contain the necessary ingredients to present a chirally enhanced contribution to the AMMs, of the form (3.3.41). Such a contribution also emerges in other

NP scenarios, such as supersymmetric ones. In our models it arises through mixing in the scalar sector, giving rise to the diagram depicted in Fig. 3.13, which presents a chiral flip in an internal fermion line. As studied in Sec. 2.4, scalar mixing depends on the patterns $V^{\pm}$ of spontaneous symmetry breaking in the potential $V(H,S)$. In the case of V^{-}, where only one of the diagonal components S_{kk} acquires a VEV, scalar mixing only has an effect on the κ' terms involving a lepton and vector-like fermion of flavor k. Then, after rotations to the mass basis the Lagrangian involving the $Q_F=-1$ states of models A and C becomes

$$\begin{aligned}\mathcal{L}_{\beta}^{-} = -\overline{\psi}_j\Big[&\big(\kappa\sin\beta\,\delta_{ji}P_L+\kappa'\cos\beta\,\delta_{ik}\,\delta_{jk}P_R\big)h_1\\ &+\big(\kappa\cos\beta\,\delta_{ij}P_L-\kappa'\sin\beta\,\delta_{ik}\delta_{jk}P_R\big)h_2\Big]\ell_i+\text{h.c.}\,,\end{aligned} \tag{3.3.45}$$

where β is the scalar mixing angle (2.4.19) and h_1, h_2 are the heavy and light mass eigenstates, respectively.[4] Hence, comparing $\mathcal{L}_{\beta}^{-}$ with the general Yukawa Lagrangian (3.3.37) we can already see that for the vacuum-aligned flavor k it fulfills the requirement $c_{L,R}\neq 0$ necessary to obtain enhanced contributions of the type (3.3.41). Then, neglecting the contribution from the heavy scalar mass eigenstate h_1 and in the limit $M_F \gg m_{h_2}$, the new physics contribution to the AMM of the lepton of flavor k reads

$$a_{\ell}^{V^-} \simeq -\frac{m_{\ell}}{2M_F}\,\frac{\kappa\kappa'}{16\pi^2}\,\sin 2\beta\,, \tag{3.3.46}$$

which presents an enhancement factor $\frac{M_F}{m_\ell}(\frac{\alpha_{\kappa'}}{\alpha_\kappa})^{1/2}|\sin 2\beta|$ with respect to new physics contributions such as (3.3.40), and can take either sign. Accommodating Δa_e and Δa_μ with Eq. (3.3.46) requires

$$|\sqrt{\alpha_\kappa\alpha_{\kappa'}}\sin 2\beta|_{\Delta a_e}\simeq 3.4\cdot 10^{-6}\,\frac{M_F}{[\text{TeV}]}\,,\quad |\sqrt{\alpha_\kappa\alpha_{\kappa'}}\sin 2\beta|_{\Delta a_\mu}\simeq 5.1\cdot 10^{-5}\,\frac{M_F}{[\text{TeV}]}\,, \tag{3.3.47}$$

which falls within the bound (3.3.9) for α_κ. Therefore, in V^{-} either the electron or the muon anomalies can be explained via the chirally enhanced contribution. The scalar mixing angle β is constrained by Higgs signal strength measurements, which impose $\sin 2\beta < 0.2$ [84]. The parameter space $\sin 2\beta$, M_F which allows to explain the muon anomaly is shown in Fig. 3.16 for several values of $\sqrt{\alpha_\kappa\alpha_{\kappa'}}$. A crucial feature of the electron-aligned V^{-} is that Δa_e can be explained by fixing $\sqrt{\alpha_\kappa\alpha_{\kappa'}}\sin 2\beta$ according to (3.3.47), while one is still free to choose $\alpha_{\kappa'}$ as in (3.3.44) to explain Δa_μ. Thus, we conclude that models A and C can simultaneously explain both anomalies if the vacuum ground state V^{-} is aligned in the electron direction.

For the vacuum ground state V^{+}, one finds that all diagonal components of the S_{ij} acquire a VEV, which leads to mixing between the three generations of scalars and the Higgs. Two of the four mass eigenstates, which we denote h_1, h_2, mix the Higgs and the three s_i, while the remaining two mix only the s_i amongst themselves (see Sec. 2.4 for details). Then, the

[4] For the sake of this discussion, we neglect effects from fermion mixing.

BSM Yukawa terms of the $Q_F = -1$ fermions of models A and C in the scalar mass basis read

$$\mathcal{L}^{+}_{\beta'} = -\sum_i \overline{\psi}_i \Big[\big(\kappa \sin\beta'\, P_L + \kappa' \cos\beta'\; P_R\big) h_1 + \big(\kappa \cos\beta'\, P_L - \kappa' \sin\beta'\, P_R\big) h_2 \Big] \ell_i + \text{h.c.}\,, \tag{3.3.48}$$

with angle β' given by Eq. (2.4.24). Therefore, the chirally enhanced contribution to the anomalous magnetic moments affects all lepton flavors. Employing again the large-M_F limit, it obeys

$$a_\ell^{V^+} = -\frac{m_\ell}{2\sqrt{3}M_F}\,\frac{\kappa\kappa'}{16\pi^2}\,\sin 2\beta'\,, \tag{3.3.49}$$

which again can take either sign. The parameter space required to explain Δa_μ is the same as depicted in Fig. 3.16 for V^- up to a factor $\sqrt{3}$, which however cancels with the factor in the angle β' (see again Eq. (2.4.24)). However, fixing the combination of couplings $\sqrt{\alpha_\kappa \alpha_{\kappa'}}\sin 2\beta$ in order to explain the $(g-2)_\mu$ anomaly automatically yields electron and tau AMMs

$$a_e^{V^+} = (m_e/m_\mu) a_\mu^{V^+} \simeq 1.4 \cdot 10^{-11}\,, \qquad a_\tau^{V^+} = (m_\tau/m_\mu) a_\mu^{V^+} \simeq 4.5 \cdot 10^{-8}\,. \tag{3.3.50}$$

In the case of the tau, the contribution is four orders of magnitude away from present limits on $\Delta a_\tau \equiv a_\tau^{\text{exp}} - a_\tau^{\text{SM}}$ [37]. On the other hand, $a_e^{V^+}$ comes out of opposite sign and about one order of magnitude larger than Δa_e, and is thus in conflict with data. Nonetheless, if one fixes the contribution (3.3.49) to accommodate Δa_e the corresponding contribution to the muon AMM is roughly $a_\mu^{V^+} \simeq -3.6 \cdot 10^{-10}$, which is of the order of magnitude of both the theoretical and experimental error of Δa_μ. Hence, we find that the vacuum structure V^+ can also accommodate both anomalies. This is a remarkable feature, since V^+ is flavor universal, and entails that models A and C are able to explain both anomalies without relying on any sources of lepton-flavor-universality violation.

Explaining Δa_e and Δa_μ Simultaneously

Having seen that our vector-like lepton models can successfully explain both AMM anomalies, let us explore the parameter space of these solutions in more detail. Firstly, for the combined explanation we saw that Δa_μ needs to be explained via the quadratic contribution (3.3.42) through the Yukawa coupling κ', which must be set approximately according to (3.3.44). Furthermore, the electron AMM receives contributions both with quadratic and linear scaling, and can be expressed as

$$\Delta a_e^{\text{NP}} = \frac{m_e}{M_F}\,\frac{\kappa\,\kappa'\,\sin 2\beta}{32\pi^2}\left[f_2\left(\frac{m_s^2}{M_F^2}\right) - f_2\left(\frac{m_h^2}{M_F^2}\right)\right] + \frac{m_e^2}{m_\mu^2}\Delta a_\mu\,, \tag{3.3.51}$$

where we have assumed that the lightest mass eigenstate h_2 is the 125 GeV Higgs boson, while $m_{h_1} = m_s$ is the mass of the BSM scalar mixing with the Higgs. The loop function

$$f_2(t) = \frac{1}{t} I_2(1/t) \tag{3.3.52}$$

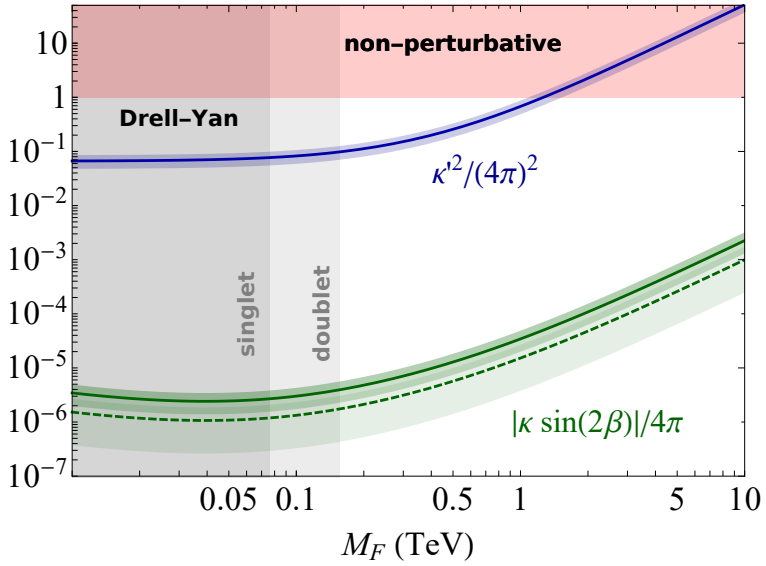

Figure 3.17. Yukawa and portal couplings which simultaneously explain the muon (blue curve) and electron (green curves) anomalous magnetic moment anomalies within their 1σ uncertainties as functions of the vector-like fermion mass, and for $M_S = 500$ GeV. In the case of the electron, we show the values of $|\kappa \sin 2\beta| /(4\pi)$ which accommodate the data (3.3.36) from [14] (solid green line) and from the rubidium measurement [99] (dashed line). Grey-shaded areas are excluded by Drell-Yan searches, the red-shaded area indicates strong coupling. All results refer to V^-, very similar ones are found for V^+ (not shown). A window with vector-like fermion masses up to ~ 1 TeV and large but perturbative κ' exists for which both anomalies are explained.

is positive for any t and fulfills $f_2(0) = 1$ (see Eq. (3.3.39)). Eq. (3.3.51), holds for both vacua $V^\pm$, as long as V^- is electron-aligned. The first term in its right-hand side is the dominant one, as it scales only linearly with m_e, and includes contributions from both scalars propagating in the loop. Note that for $m_s \sim m_h$ the loop functions exert a GIM-like suppression on the chirally enhanced term, which vanishes in the limit of equal scalar masses. The second term in the right-hand side of $\Delta a_e^{\rm NP}$ accounts for the contribution of the κ'-loop, which scales quadratically with the electron mass, and is completely fixed by demanding that the muon anomaly be explained.

The parameter space which simultaneously explains both anomalies is shown in Fig. 3.17 for a benchmark scalar mass of $M_S = 500$ GeV. We also shown Drell-Yann bounds on the vector-like fermion masses, already computed in Sec. 3.3.4, and perturbativity limits. In Fig. 3.17 we show as well the values of $|\kappa \sin 2\beta| /(4\pi)$ needed to explain the electron AMM computed from the rubidium measurement [99] (dashed green curve), which demands mildly smaller couplings. Note that although the rubidium data requires $\Delta a_e > 0$ it can still be accommodated by our models, since $\kappa \sin 2\beta$ can take either sign. In any case, a window where the models can explain both AMMs exists, which demands vector-like fermion masses of at most ~ 1 TeV. Additionally, the mechanism predicts BSM contributions to

the anomalous magnetic moment of the tau of

$$\Delta a_\tau^{\rm NP} \simeq (7.5 \pm 2.1) \cdot 10^{-7}\ (V^+)\,, \qquad \Delta a_\tau^{\rm NP} \simeq (8.1 \pm 2.2) \cdot 10^{-7}\ (V^+)\,. \tag{3.3.53}$$

Finally, it is also worth noting that the BSM parameter space compatible with simultaneous explanations of the anomalies allows for RG trajectories which display either asymptotic safety (singlet model) or Planck safety (doublet model) [24]. This is explicitly shown in Appendix B.2, where we present benchmark trajectories and the BSM critical surface for a range of α_κ and $\alpha_{\kappa'}$ (see Fig. B.2.3).

3.3.6 EDMs

As we have seen in Sec. 3.3.5, BSM Yukawa interactions contribute at 1-loop to lepton AMMs, with scalar mixing enabling chirally enhanced contributions in models A and C. Here, we explore implications for lepton electric dipole moments. These correspond as well to quantum corrections of the photon coupling to fermions, with the crucial difference that a source of $\mathcal{CP}$ violation is required. According to Eq. (3.3.31), the electric dipole moment d_ℓ of a lepton is proportional to the form factor $F_3(0)$, which has dimensions of inverse mass. The effective Lagrangian describing the EDM can be written as the dimension-five operator

$$\mathcal{L}_{\rm EDM} = -\frac{i}{2} d_\ell \bar{\ell} \sigma_{\mu\nu} \gamma_5 F^{\mu\nu} \ell\,, \tag{3.3.54}$$

where $F^{\mu\nu}$ is the electromagnetic field strength tensor. In the SM, EDMs can arise from the two possible sources of $\mathcal{CP}$ violation: the phase in the CKM matrix and the strong $\mathcal{CP}$ phase $\theta_{\rm QCD}$. Leptons do not couple at tree level to any of these, which results in SM contributions to their EDMs being heavily loop-suppressed; in fact, these arise only at 4-loop. Upper bounds on SM contributions to lepton EDMs are found to be [126]

$$d_e^{\rm SM} < 10^{-38}\, e \cdot {\rm cm}\,, \quad d_\mu^{\rm SM} < 1.8 \cdot 10^{-35}\, e \cdot {\rm cm}\,, \quad d_\tau^{\rm SM} < 3.1 \cdot 10^{-34}\, e \cdot {\rm cm}\,. \tag{3.3.55}$$

From the experimental side, measurements have improved immensely in the past years. Current upper bounds on the electron and the muon EDM read

$$|d_e^{\rm exp}| < 1.1 \cdot 10^{-29}\, e \cdot {\rm cm}\,, \qquad |d_\mu^{\rm exp}| < 1.8 \cdot 10^{-19}\, e \cdot {\rm cm}\,, \tag{3.3.56}$$

according to the results of the ACME collaboration @90 % C.L. [127] and the Muon g-2 collaboration @95 % C.L. [128], respectively, while for taus measurements indicate $|d_\tau^{\rm exp}| \lesssim 10^{-17}$ [37]. Therefore, both the smallness of the SM predictions and the increasing precision of the measurements put forward lepton EDMs as unique probes to constrain $\mathcal{CP}$-violating new physics.

Remarkably, for the general Yukawa interaction (3.3.46), lepton EDMs arise already at 1-loop if at least one of the Yukawa couplings presents an imaginary part. The contribution obeys [129]

$$\frac{d_\ell}{e} = -\frac{Q_F}{2M_F}\, \frac{{\rm Im}[c_R^* c_L]}{16\pi^2} f_2(m_H^2/M_F^2)\,, \tag{3.3.57}$$

according to the loop function in (3.3.52). As we saw in the previous section, models A and C contain simultaneously non-vanishing coefficients $c_{L,R}$ thanks to scalar mixing. Unlike in the rest of this chapter, we now allow for small imaginary phases of the couplings κ and κ', which leads to contributions to the EDMs. In model A and for the V^- vacuum ground state, the 1-loop contribution emerges only for the vacuum-aligned flavor, and in the large-M_F limit reads

$$\frac{d_\ell^{V^-}}{e} = -\frac{\sin 2\beta}{4M_F}\,\frac{\mathrm{Im}[\kappa^*\kappa']}{16\pi^2}\,. \tag{3.3.58}$$

Conversely, for the vacuum V^+ EDMs are induced for all flavors. Provided that the $\mathcal{CP}$-violating phases are lepton-universal, we find instead

$$\frac{d_\ell^{V^+}}{e} = -\frac{\sin 2\beta'}{4\sqrt{3}M_F}\,\frac{\mathrm{Im}[\kappa^*\kappa']}{16\pi^2}\,, \tag{3.3.59}$$

which yields the same contribution to all flavors, predicting universal lepton EDMs. Expressions for model C can be obtained by exchanging $\kappa^*\kappa' \to \kappa\kappa'^*$ in Eqs. (3.3.58) and (3.3.59). The electron data (3.3.56) poses the most stringent bound on BSM couplings, which must fulfill

$$\frac{1}{16\pi^2}\big|\sin 2\beta\,\mathrm{Im}[\kappa^*\kappa']\big| < 2.2\cdot 10^{-12}\frac{M_F}{[\mathrm{TeV}]}\,, \tag{3.3.60}$$

for V^+ or electron-aligned V^-. These are precisely the cases for which in the previous section we found that the muon and electron magnetic moment anomalies can be explained, with Δa_e being accommodated via the real counterpart of (3.3.60). Therefore, the scenarios of simultaneous explanations of the AMM anomalies can yield an electron EDM as large as the current experimental bound. $\mathcal{CP}$-violating phases, however, must yield a suppression of at least $\mathcal{O}(10^{-6})$ in order to fulfill the electron EDM bound (3.3.56). Accommodating the $(g-2)_\mu$ anomaly via chirally enhanced contributions within a V^+ ground state demands as well suppressed phases, of $\mathcal{O}(10^{-7})$ or smaller, to avoid the electron EDM bound. Conversely, for a V^- pointing in the muon direction, or if $\mathcal{CP}$ phases are flavor-dependent, the electron bound no longer applies. Instead, the muon measurement yields a bound weaker than (3.3.60) by 10 orders of magnitude . If the muon-specific, chirally-enhanced contribution is set to accommodate Δa_μ with the couplings (3.3.47), the muon EDM could then be as large as $d_\mu \sim 2.5\cdot 10^{-22}\,e\,\mathrm{cm}$, with order one phases. This is interestingly in reach of future experiments expecting to attain a sensitivity of $|d_\mu| \sim 5\cdot 10^{-23}\,e\cdot\mathrm{cm}$ [124].

3.3.7 Charged LFV Processes

Following flavor symmetry arguments we have so far considered only diagonal, universal forms of our BSM Yukawa couplings κ and κ'. This has resulted in a setup which strictly conserves flavor. The y interaction, although it contains a less trivial flavor structure, is also flavor-conserving. We now consider the effects of breaking lepton-flavor conservation, in order to see how these variants of our models can be probed by LFV processes. For the sake of this discussion, we only allow for non-diagonal flavor patterns in the coupling κ. We then study $\ell_i \to \ell_j\gamma$ and $\mu \to 3e$ decays, as well as $\mu \to e$ conversion in nuclei. All these processes, which feature charged lepton flavor violation, are entirely absent in the

SM. However, evidence of neutrino masses and oscillations indicates that cLFV must occur at some scale, with branching ratios of the different processes depending on the particular neutrino model. Nonetheless, neutrino-mediated cLFV may also be very suppressed. For instance, in minimal SM extensions featuring three additional generations of right-handed neutrinos the branching ratio for $\mu \to e\gamma$ is found to be smaller than 10^{-50}, as it depends on the ratio of the neutrino mass differences with respect to the W mass [130, 131]. Therefore, cLFV processes can also be excellent probes of lepton-flavor-violating new physics outside the neutrino sector.

Let us first discuss $\ell_i \to \ell_j\gamma$ decays. Measurements by the MEG experiment [130] and the BABAR collaboration [132] indicate that branching ratios fulfill

$$\begin{aligned} &\mathcal{B}(\mu \to e\gamma) < 4.2 \cdot 10^{-13}\,, \\ &\mathcal{B}(\tau \to e\gamma) < 3.3 \cdot 10^{-8}\,, \\ &\mathcal{B}(\tau \to \mu\gamma) < 4.4 \cdot 10^{-8}\,, \end{aligned} \tag{3.3.61}$$

at 90% C.L., while the MEG-II experiment expects future bounds to constrain $\mathcal{B}(\mu \to e\gamma) \lesssim 2 \cdot 10^{-15}$ [133]. We now consider contributions of the general Yukawa interaction (3.3.37) to these processes, which in our models occur at 1-loop via the diagrams depicted in Fig. 3.18. Firstly, if either the left- or right-handed coefficients c_{iL}, c_{iR} associated to a lepton ℓ_i vanish, one obtains a decay rate [134]

$$\Gamma(\ell_i \to \ell_j\gamma) = \frac{\alpha_e}{576\, m_i^3 M_F^4} \left(m_i^2 - m_j^2\right)^3 \left(m_i^2 + m_j^2\right) \left(\frac{c_{jX}^* c_{iX}}{16\pi^2}\right)^2 |f_1(m_H^2/M_F^2)|^2\,, \tag{3.3.62}$$

where $X = L, R$ and the loop function f_1 in the limit of vanishing lepton masses is given by (3.3.43). Taking the limit $M_F \gg m_H$ and $m_i \gg m_j$ we find

$$\Gamma(\ell_i \to \ell_j\gamma) \simeq \frac{\alpha_e}{576} \left(\frac{c_{jX}^* c_{iX}}{16\pi^2}\right)^2 \frac{m_i^5}{M_F^4}\,. \tag{3.3.63}$$

Except in model E, such a contribution arises in all of our models through h exchange and κ, as shown in Fig. 3.18 (diagram a). The decay rate is then given by Eq. (3.3.63), with couplings

$$\frac{c_{jX}^* c_{iX}}{16\pi^2} = \alpha_\kappa^{ij} = \frac{1}{(4\pi)^2} \sum_m \kappa_{im}\kappa_{jm}\,, \tag{3.3.64}$$

where m runs over the flavors of vector-like fermions in the loop, and $m_H = m_h$ is the mass of the Higgs boson. For model B, Clebsch-Gordan coefficients of the $Q_F = -1$ states yield an additional factor $1/2$ in α_κ^{ij}. The measurements (3.3.61) then constrain the α_κ^{ij} for $i \neq j$ in terms of the vector-like fermion masses. Bounds on $\alpha_\kappa^{\mu e}$ and $\alpha_\kappa^{\tau\mu}$ are shown in Fig. 3.19, together with projected MEG-II limits. For comparison we also show the Z-data bound (3.3.9), which affects the diagonal components of κ. As seen in Fig. 3.19, $\mu \to e\gamma$ constraints (blue) are comparable to the ones from $Z \to \ell\ell$, while $\tau \to \mu\gamma$ (red) is less constraining.[5] Therefore, $\ell_i \to \ell_j\gamma$ constraints do not require the off-diagonal elements

[5]Bounds from $\tau \to e\gamma$ on $\alpha_\kappa^{\tau e}$ are comparable to $\tau \to \mu\gamma$ bounds shown in Fig. 3.19, see Eq. (3.3.61).

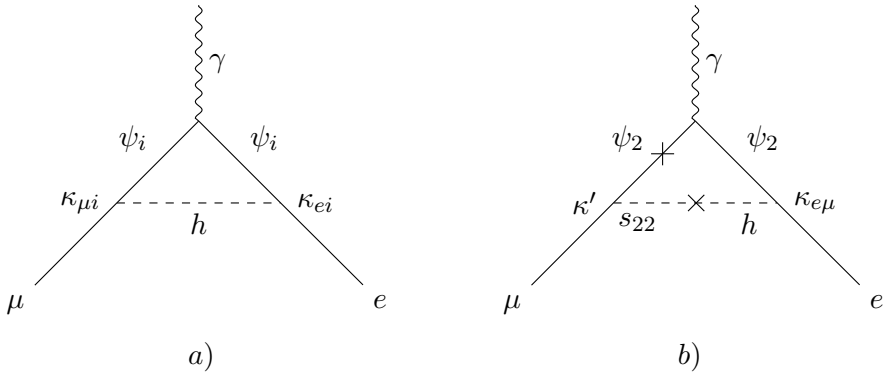

Figure 3.18. Contributions to $\mu \to e\gamma$ via h exchange (a), present in all models except for model E, and chirally enhanced contribution in the case of $h - s_{22}$ mixing (b), only present in models A and C.

of κ to be significantly suppressed with respect to the κ_{ii}, potentially allowing for a non-hierarchical coupling structure.

Furthermore, in models A and C chirally enhanced contributions arise through κ' and scalar mixing, as we have already seen for AMMs and EDMs in the previous sections. In diagram b) of Fig. 3.18 we show how such a contribution arises for $\mu \to e\gamma$ in the case of a muon-aligned V^-. For the general Yukawa interaction (3.3.46), the corresponding decay rate reads

$$\Gamma^*(\ell_i \to \ell_j \gamma) = \frac{\alpha_e}{16} \frac{\left(m_i^2 - m_j^2\right)^3}{m_i^3 M_F^2} |f_2(m_H^2/M_F^2)|^2 \left[\left(\frac{c_{jR}^* c_{iL}}{16\pi^2} \right)^2 + \left(\frac{c_{jL}^* c_{iR}}{16\pi^2} \right)^2 \right] , \tag{3.3.65}$$

where f_2 in the limit of negligible lepton masses is given by (3.3.52), and we have neglected terms proportional to c_L^2, c_R^2. Note that, since $f_2(0) = 1$, in the large-M_F limit the decay rate (3.3.65) scales as $\sim m_i^3/M_F^2$, which represents an M_F/m_i enhancement with respect to the purely left- or right-handed contributions (3.3.62). In this limit, and neglecting the electron mass, chirally enhanced contributions to $\mu \to e\gamma$ in our models A and C then read

$$\Gamma(\mu \to e\gamma) \simeq \frac{\alpha_e}{64} \left(\frac{\kappa_{e\mu} \kappa' \sin 2\beta}{16\pi^2} \right)^2 \frac{m_\mu^3}{M_F^2} , \tag{3.3.66}$$

for the vacuum V^- pointing in the muon direction. For an electron-aligned V^-, a similar contribution arises, with decay rate given by (3.3.65) after replacing $\kappa_{e\mu} \to \kappa_{\mu e}$. Constraints on the coupling $\alpha^{\mu e}_{\kappa\kappa'\delta} = \kappa_{e\mu}\kappa' \sin 2\beta/(16\pi^2)$ from the chirally enhanced rate are therefore stronger than those shown in Fig. 3.19 for $\alpha_\kappa^{\mu e}$ by a factor $m_\mu/3M_F$.

In addition, cLFV decays into three-lepton final states occur as well in our models, receiving contributions from both penguin and box diagrams with κ and κ'. From the experimental side, measurements of $\mu \to ee\bar{e}$ by the SINDRUM collaboration have set the bound [135]

$$\mathcal{B}(\mu \to ee\bar{e}) < 10^{-12} , \tag{3.3.67}$$

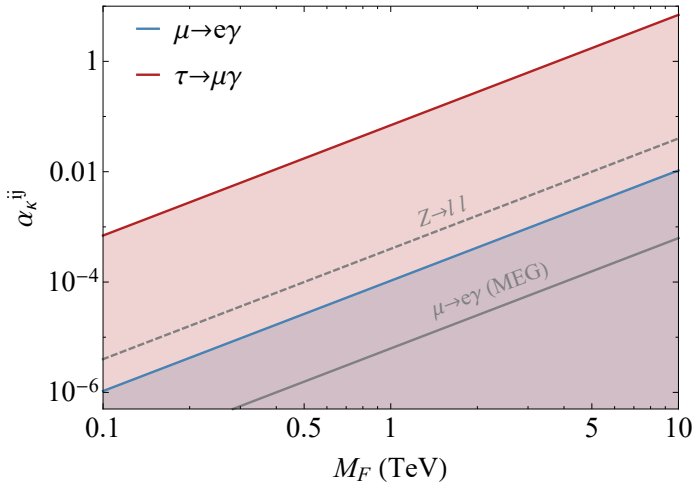

Figure 3.19. Allowed regions (shaded) for $\alpha_\kappa^{\mu e}, \alpha_\kappa^{\tau\mu}$ and M_F from LFV decays (3.3.61). Due to the proximity of upper limits on $\mathcal{B}(\tau \to e\gamma)$ and $\mathcal{B}(\tau \to \mu\gamma)$ only the latter is shown. The projected sensitivity of the MEG-II experiment [133] is shown by the solid gray line. The dashed gray line denotes the $Z \to \ell\ell$-constraint (3.3.9). In the case of chirally enhanced rates such as (3.3.66), bounds from a decay of a lepton ℓ are stronger by a factor $m_\ell/3M_F$

.

at 90% C.L., while future measurements at the Mu3e experiment expect a reach of $\mathcal{B}(\mu \to ee\bar{e}) < 10^{-16}$ [136]. For our models, we estimate [137]

$$\mathcal{B}(\mu \to ee\bar{e}) \sim \frac{3(4\pi)^2\alpha_e^2}{8G_F^2}\frac{(\alpha_\kappa^{\mu e})^2}{M_F^4}\mathcal{B}(\mu \to e\bar{\nu}_e\nu_\mu)\,, \tag{3.3.68}$$

which presents the same $(\alpha_\kappa^{\mu e})^2$ suppression as the κ-mediated $\mu \to e\gamma$ rate (3.3.63). The bound (3.3.67) then yields $\alpha_\kappa^{\mu e}/(M_F[\text{TeV}])^2 < (2-3)\cdot 10^{-4}$, which is comparable to $\mu \to e\gamma$ bounds in Fig. 3.19, yet not more excluding. In the case of τ decays into three charged leptons, present bounds are less constraining, with measurements setting upper limits on the branching ratios at order 10^{-8} [37]. This poses a looser constraint on off-diagonal couplings involving taus, $\alpha_\kappa^{\tau\ell}/(M_F[\text{TeV}])^2 \lesssim 0.1$.

Finally, $\mu \to e$ conversion in nuclei also poses constraints on our models. The SINDRUM II collaboration has set a 90% C.L. limit for the conversion rate (CR) in gold nuclei of [138]

$$\text{CR}(\mu - e, \text{Au}) \lesssim 7 \cdot 10^{-13}\,, \tag{3.3.69}$$

In our models, Z and γ penguin diagrams, which are again $(\alpha_\kappa^{\mu e})^2$-suppressed, contribute to the conversion process. We estimate [139]

$$\text{CR}(\mu - e, \text{Au}) \sim \mathcal{O}(10^{-12})\left(\frac{\alpha_\kappa^{\mu e}}{10^{-4}}\right)^2\left(\frac{[\text{TeV}]}{M_F}\right)^4\,, \tag{3.3.70}$$

in close competition with $\mu \to e\gamma$ bounds. The future Mu2e experiment [140], with expected sensitivity $\text{CR}(\mu - e, \text{Au}) < 6.7 \cdot 10^{-17}$, can improve the bound from SINDRUM II

on $\alpha_\kappa^{\mu e}$ by about two orders of magnitude.

In conclusion, the strongest bounds on the κ_{ij} stem from $\mu \to e\gamma$ measurements, while other processes are competitive yet not more excluding at present. cLFV data cannot, however, constrain the off-diagonal entries of κ to be significantly suppressed with respect to the diagonal components κ_{ii}, limited by Z-coupling measurements. Therefore, a non-hierarchical form of the BSM Yukawa κ remains allowed, and can yield signatures in cLFV observables within reach of future experiments.

3.4 Summary

In this chapter we have studied six models of vector-like fermions with new scalars S_{ij}, each presenting an extended Yukawa sector with BSM interactions κ between the new fermions, SM leptons and the Higgs. Additionally, models A and C feature Yukawa couplings κ' of the vector-like fermions with SM leptons and the new scalars (see Tab. 3.1), and all models admit the purely BSM Yukawa y. The leading order (`210`) RG analysis revealed interacting fixed point solutions which can, in some cases, be matched onto the SM at low scales, resolving the $U(1)_Y$ Landau pole problem. Moreover, matching scenarios exist in the absence of the BSM Yukawa y, distinguishing our models from previous model building efforts [29]. Beyond the `210` approximation, the models exhibit a complex pattern of fixed point solutions, which we have analyzed from a bottom-up approach. Using full 2-loop results (`222` approximation), we found that all models present regions in the parameter space of low-scale BSM couplings which are either Planck safe or display asymptotic safety. In some cases, BSM trajectories are able to completely stabilize the electroweak vacuum.

Phenomenologically, Drell-Yan processes constrain vector-like fermion masses to be at least a few hundred GeV. Thanks to their gauge or Yukawa interactions, both vector-like fermions and BSM scalars can be produced at pp and $\ell\ell$ colliders. Decays of the vector-like fermions occur via their Yukawa interactions or to weak bosons through mixing with the SM leptons, and for sufficiently suppressed couplings can give rise to displaced vertex signatures or long lived states. Additionally, fermion mixing allows the BSM scalars to decay to two leptons of different charge and opposite flavor, giving a distinct LFV-like signature which can be used to probe the models at colliders.

Furthermore, the models offer distinct implications for 1-loop observables, in particular for lepton anomalous magnetic moments. We find that for the models of vector-like leptons (models A and C) both the electron and the muon $g-2$ anomalies can be simultaneously accommodated. The explanation relies on a chirally enhanced contribution to the AMM of the electron, which requires the presence of both Yukawas κ and κ' and a portal coupling in the scalar sector. The parameter space favored by data is depicted in Fig. 3.17, and requires vector-like fermion masses to be ~ 1 TeV or below. Remarkably, the mechanism does not require any explicit breaking of flavor universality, and yields predictions for the tau AMM. Furthermore, allowing for a soft breaking of the flavor or $\mathcal{CP}$ symmetry of the

models allows for 1-loop contributions to cLFV observables and electric dipole moments, respectively. If the vacuum is aligned in the muon direction, we find that electron EDM bounds can be bypassed and the muon EDM can be as large as $\sim 10^{-22}\, e \cdot \text{cm}$. Therefore, we conclude that models connecting the SM with heavy new physics through a mixed Yukawa sector can constitute UV completions of the SM, and at the same time give rise to relevant phenomenological signatures in flavor observables which can be probed at current and future experiments.

4 Vector-Like Leptons at Colliders

In the previous chapter we saw that vector-like fermions are not only a crucial ingredient to build asymptotically safe models but can also present relevant phenomenological implications. In particular, in Sec. 3.3.5 we showed how models of vector-like leptons (VLLs) with additional Yukawa interactions (referred to as models A and C in Chapter 3) are able to simultaneously explain the observed discrepancies between measurements and SM predictions in the anomalous magnetic moments of the electron and the muon. Phenomenologically, Drell-Yan processes constrain vector-like leptons to have masses of at least a few hundred GeV (see Fig. 3.10). However, dedicated searches at colliders might constrain the parameter space further. VLL models are especially suited for such searches as their decay products are mostly leptonic, yielding clean signals and opportunities to look for resonances. Using these features, the CMS collaboration has recently ruled out vector-like lepton doublets in the range of 120 – 790 GeV at 95%C.L. in a particular tau-philic model [141, 142]. This represents a significant improvement with respect to previous searches at LEP, which were able to exclude heavy leptons lighter than ~ 100 GeV [143], and by the ATLAS collaboration, which ruled out singlet VLLs mixing with first-generation leptons in the 114 – 176 GeV range at 95%C.L. [144]. Future LHC searches have the potential to greatly improve current limits on VLL models, already by including the full run 2 dataset.

In this chapter we perform a dedicated collider study for the models of singlet and doublet vector-like leptons described in Chapter 3, focusing on the parameter space which permits simultaneous explanations of the electron and the muon $g-2$ anomalies. Our aim is to ascertain how current analyses can constrain the parameter space of our models and to develop targeted search strategies at colliders. The chapter, which is based on the findings of [145], is organized as follows: in Sec. 4.1 we review the decay and production modes of vector-like leptons at the LHC, placing an emphasis on the effects of fermion mixing. In Sec. 4.2, we recast constraints from the present data [141] using the transverse momenta of the multi-lepton final states. We build dedicated observables which take advantage of the specific features of our models, in particular the LFV-like decays of the BSM scalars S_{ij}, in Sec. 4.3. We exploit the fact that, when pair produced, the VLLs present dominant decays into 6-lepton final states which can be used to look for heavy resonances. In Sec. 4.4 we explore scenarios beyond the $g-2$ parameter space of our models, and we summarize our results in Sec. 4.5.

4.1 Vector-like Lepton Models

We start out with the theories of vector-like leptons ψ described in Chapter 3, corresponding to models A and C in Tab. 3.1. In what follows, we refer to them as *singlet* and *doublet* model, respectively, according to the $SU(2)_L$ representations of the VLLs. We denote the weak isospin components of the doublet VLLs by

$$\psi_{L,R} = (\psi^0_{L,R},\ \psi^-_{L,R})^T\,, \tag{4.1.1}$$

and employ $L = (\nu,\ \ell_L)^T$ and $E = \ell_R$ for the SM leptons. The models also contain the complex scalar singlets S_{ij}, with $i,j = 1,2,3$. The BSM Yukawa Lagrangian of the models in the interaction basis is given by

$$\begin{aligned}\mathcal{L}_{\rm Y}^{\rm singlet} &= -\kappa\overline{L}_i H\psi_{Ri} - \kappa'\overline{E}_i(S^\dagger)_{ij}\psi_{Lj} - y\,\overline{\psi}_{Li}S_{ij}\psi_{Rj} + \text{h.c.}\,,\\ \mathcal{L}_{\rm Y}^{\rm doublet} &= -\kappa\overline{E}_i H^\dagger\psi_{Li} - \kappa'\,\overline{L}_i S_{ij}\psi_{Rj} - y\,\overline{\psi}_{Li}S_{ij}\psi_{Rj} + \text{h.c.}\,,\end{aligned} \tag{4.1.2}$$

where we have spelled out contractions of flavor indices. Here we put aside discussions of the purely BSM Yukawa y, as its effects for collider phenomenology are subleading with respect to the couplings κ and κ', which directly connect the SM with new states. After spontaneous symmetry breaking in the Higgs and S sectors, VLLs acquire mixing with SM leptons, which affects all chiral interactions. Measurements of the Z couplings to leptons constrain left-handed (right-handed) mixing angles in the singlet (doublet) model to fulfill

$$\theta \simeq \frac{\kappa v_h}{\sqrt{2}M_F} \lesssim \mathcal{O}(10^{-2})\,, \tag{4.1.3}$$

see Sec. 3.3.1 for details, and [146] for recent electroweak fits. Therefore, Z data places constraints on κ, while κ', the Yukawa coupling of the new scalars, remains unbounded. At first order in κ, electroweak and Yukawa interactions of the VLLs can be written as

$$\begin{aligned}\mathcal{L}_{\rm int}^{\rm singlet} =& -e\,\overline{\psi}\gamma^\mu\psi A_\mu + \frac{g_2}{\cos\theta_w}\,\overline{\psi}\gamma^\mu\psi Z_\mu + \Bigg(-\frac{\kappa}{\sqrt{2}}\,\bar{\ell}_L\psi_R\,h - \kappa'\bar{\ell}_R S^\dagger\psi_L\\ &+ g_S\,\bar{\ell}_R S^\dagger\ell_L + g_Z\,\bar{\ell}_L\gamma^\mu\psi_L\,Z_\mu + g_W\,\overline{\nu}\gamma^\mu\psi_L\,W^+_\mu + \text{h.c.}\Bigg)\,,\end{aligned} \tag{4.1.4}$$

in the mass basis of the singlet model, where h is the physical Higgs boson with mass $m_h = 125$ GeV. The couplings in the Lagrangian (4.1.4) fulfill

$$g_S = \frac{\kappa'\kappa}{\sqrt{2}}\frac{v_h}{M_F}\,,\quad g_Z = -\frac{\kappa}{\sqrt{2}}\frac{m_Z}{M_F}\,,\qquad g_W = \kappa\frac{m_W}{M_F}\,, \tag{4.1.5}$$

where we have assumed that all flavor and $SU(2)_L$ components of the VLLs have approximately the same mass M_F. For the doublet model we find instead

$$\begin{aligned}\mathcal{L}_{\rm int}^{\rm doublet} =& -e\,\overline{\psi^-}\gamma^\mu\psi^- A_\mu + \frac{g_2}{2\cos\theta_w}\left[(2\sin^2\theta_w - 1)\overline{\psi^-}\gamma^\mu\psi^- + \overline{\psi^0}\gamma^\mu\psi^0\right]Z_\mu\\ &+\Bigg(\frac{g_2}{\sqrt{2}}\,\overline{\psi^-}\gamma^\mu\psi^0 W^-_\mu - \frac{\kappa}{\sqrt{2}}\,\bar{\ell}_R\psi^-_L\,h - \kappa'\bar{\ell}_L S\psi^-_R - \kappa'\bar{\nu}S\psi^0_R + g_S\,\bar{\ell}_L S\,\ell_R\\ &+ g_Z\,\bar{\ell}_R\gamma^\mu\psi^-_R\,Z_\mu + g_W\,\bar{\ell}_R\gamma^\mu\psi^0_R\,W^-_\mu + \text{h.c.}\Bigg)\,,\end{aligned} \tag{4.1.6}$$

where the couplings obey

$$g_S = \frac{\kappa'\kappa}{\sqrt{2}}\frac{v_h}{M_F}\,, \quad g_Z = \frac{\kappa}{\sqrt{2}}\frac{m_Z}{M_F}\,, \qquad g_W = -\kappa\frac{m_W}{M_F}\,. \tag{4.1.7}$$

Note that the vertex $\overline{\nu}\gamma^\mu\psi_L^- W_\mu^+$ is subleading, as it arises only at order κy_ℓ (see Sec. 3.3.1 and the angles in Tab. 3.6 for details).

In order to successfully explain the muon magnetic moment anomaly, the parameters κ', M_F and M_S must allow for the contribution to $(g-2)_\mu$ in Eq. (3.3.42) to accommodate the data (3.3.34), which leads to the condition

$$\Delta a_\mu = \frac{\kappa'^2}{32\pi^2}\,\frac{m_\mu^2}{M_F^2}\,f_1\left(\frac{M_S^2}{M_F^2}\right)\,, \tag{4.1.8}$$

with f_1 given by Eqs. (3.3.43) and (3.3.39). Unless otherwise specified, throughout this work we use the above condition to fix κ' in terms of benchmark masses M_F and M_S. For instance, setting $M_S = 500$ GeV and $M_F = \{100, 500, 1000\}$ GeV requires $\kappa' \simeq \{3.6, 6.5, 10.4\}$, respectively. Furthermore, the coupling κ allows to explain Δa_e by enforcing that the chirally enhanced contribution (3.3.51) coincide with the data (3.3.36). This contribution, however, involves couplings of the scalar sector as well, providing more freedom in the choice of κ. In this chapter, we fix the ratio between couplings as $\kappa = \epsilon\kappa'$ and choose $\epsilon = 10^{-2}$, which for the considered parameter space allows to fulfill the Z-data bound (3.3.9). Moreover, once the hierarchy between BSM Yukawas is set all branching ratios are independent of κ and κ'.

Production of the VLLs at pp colliders occurs via quark fusion and s-channel electroweak bosons or Higgs (Fig. 3.7, diagrams a, b and c). Additional single-production channels arise through mixing, with a VLL being produced alongside a lepton of its same generation (see Fig. 3.8). Note that W-mediated channels are only possible for the doublet model. Together with larger particle multiplicities, this leads to higher production cross sections in the case of the doublet model. Single- and pair-production cross sections for the VLLs at the LHC for a center-of-mass energy $\sqrt{s} = 13$ can be found in Fig. C.3.1 in Appendix C. For VLLs around the TeV scale, we find pair-production cross sections at the order 10^{-4} pb, while single-production is mixing-suppressed and occurs only at order 10^{-7} pb.

After production, the VLLs decay promptly to a scalar and a lepton through their Yukawa interactions or to a weak boson and a lepton through mixing. The rates of all possible decays in the singlet model read

$$\begin{aligned}
\Gamma(\psi_i \to h\ell_i^-) &= \kappa^2\frac{M_F}{64\pi}(1-r_h^2)^2\,,\\
\Gamma(\psi_i \to S_{ij}^*\,\ell_j^-) &= \kappa'^2\frac{M_F}{32\pi}(1-r_S^2)^2\,,\\
\Gamma(\psi_i \to W^-\nu_i) &= g_W^2\frac{M_F}{32\pi}(1-r_W^2)^2(2+1/r_W^2)\,,\\
\Gamma(\psi_i \to Z\ell_i^-) &= g_Z^2\frac{M_F}{32\pi}(1-r_Z^2)^2(2+1/r_Z^2)\,,
\end{aligned} \tag{4.1.9}$$

where $r_X = m_X/M_F$. Corresponding branching ratios are shown in Fig. 4.1 (left) for a range of VLL masses M_F and for $M_S = 500$ GeV. As soon as the S can be produced on shell, and for large κ', the decay $\psi_i \to S_{ij}^* \ell_j^-$ dominates over the rest of channels, which are κ-suppressed. Quantitatively, for large M_F the decays through the S_{ij} dominate over Higgs-mediated decays (decays through weak bosons) as soon as $\kappa' \gtrsim \kappa/\sqrt{6}$ ($\kappa' \gtrsim \kappa/\sqrt{3}$). For the doublet model we find decay rates

$$\begin{aligned}
\Gamma(\psi_i^- \to h\ell_i^-) &= \kappa^2 \frac{M_F}{64\pi}(1-r_h^2)^2\,, \\
\Gamma(\psi_i^- \to S_{ji}\,\ell_j^-) &= \kappa'^2 \frac{M_F}{32\pi}(1-r_S^2)^2\,, \\
\Gamma(\psi_i^0 \to S_{ji}\,\nu_j) &= \kappa'^2 \frac{M_F}{32\pi}(1-r_S^2)^2\,, \\
\Gamma(\psi_i^- \to Z\ell_i^-) &= g_Z^2\,\frac{M_F}{32\pi}(1-r_Z^2)^2(2+1/r_Z^2)\,, \\
\Gamma(\psi_i^0 \to W^+\ell_i^-) &= g_W^2 \frac{M_F}{32\pi}(1-r_W^2)^2(2+1/r_W^2)\,.
\end{aligned} \tag{4.1.10}$$

Branching ratios for the decays of the ψ^- and the ψ^0, displayed in Fig. 4.1 (right), show again a dominance of the decays to S plus lepton for both $SU(2)_L$ components as soon as $M_F > M_S$. In both models, the S_{ij} can decay to ψ plus lepton (for $M_F < M_S$), to a diboson pair (only in the case of the diagonal components S_{ii}), to a VLL pair (for $2M_F < M_S$ through y) and to a dilepton pair via mixing (with coupling g_S), as discussed in detail in Sec. 3.3.3. The dilepton channel is available for all BSM mass hierarchies, and dominant over decays to dibosons unless mixing is very suppressed. In what follows, we assume that the BSM scalars decay entirely to dileptons, while other modes are negligible. Then, the dominant decays of the VLLs through the S_{ij} read

$$\begin{aligned}
&\psi_i \to S_{ij}^*\,\ell_j^- \to \ell_i^-\,\ell_j^+\,\ell_j^-\,, \quad \text{(singlet)} \\
&\psi_i^- \to S_{ji}\,\ell_j^- \to \ell_i^-\,\ell_j^+\,\ell_j^-\,, \quad \psi_i^0 \to S_{ji}\,\nu_j \to \ell_i^-\,\ell_j^+\,\nu_j\,. \quad \text{(doublet)}
\end{aligned} \tag{4.1.11}$$

Note that the decay chains (4.1.11) are strictly flavor-conserving, since the S_{ij} carry flavor. Nonetheless, for $i \neq j$ they can decay to two leptons of opposite charge and different flavor (OCDF), yielding an LFV-like signature. Hence, if the VLLs are heavy enough to decay to on-shell BSM scalars, one can use dilepton invariant masses of OCDF leptons to look for resonances around the S mass. This provides a unique opportunity to specifically target the features of our models, and distinguish them from other theories of vector-like leptons such as [124, 142, 147–149].

Decays via (4.1.11) result in purely leptonic final states, while decays to weak bosons or Higgs can produce either leptons or jets. In the rest of this work, we focus on final states with at least four light leptons (4L), where a light lepton is a muon or an electron, as has also been studied in the CMS analysis [141]. In the case where the VLLs are pair produced and decay through (4.1.11), only certain flavor configurations can give rise to a 4L final state, which we have collected in Tab. 4.1. Note that, in the doublet model, if pair production involves a ψ_3^0 flavor conservation entails that the final state cannot contain four or more light leptons.

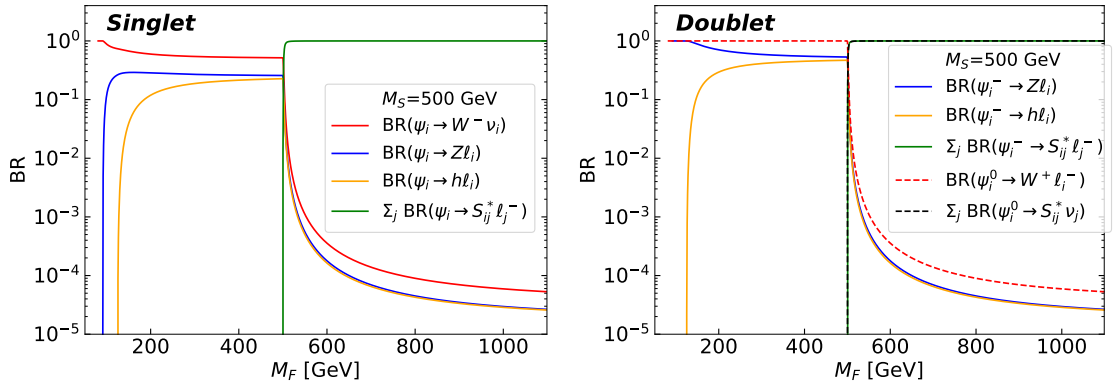

Figure 4.1. Branching ratios of on-shell decays of the VLLs as a function of their mass in the singlet model (left) and the doublet model (right), with scalar mass $M_S = 500$ GeV. For $M_F < M_S$, only electroweak and Higgs-mediated decays are possible, and the rates are independent of κ, κ'. We fix $\kappa = 10^{-2}\,\kappa'$, and therefore the branching ratios at leading order do not depend on κ' either, even in the $M_F > M_S$ range. For the BSM mass hierarchy $M_F > M_S$, decays of the VLLs through the S_{ij} are dominant in both models; increasing the ratio κ/κ' would enhance the branching ratios of electroweak decays.

State	Decay modes
$\psi_1^{(-)}$	$e^-e^+e^-,\ e^-\mu^+\mu^-,\ e^-\tau^+\tau^-$
$\psi_2^{(-)}$	$\mu^-\mu^+\mu^-,\ \mu^-e^+e^-,\ \mu^-\tau^+\tau^-$
$\psi_3^{(-)}$	$\tau^-e^+e^-,\ \tau^-\mu^+\mu^-$
ψ_1^0	$e^-e^+\nu_e\,,\ e^-\mu^+\nu_\mu$
ψ_2^0	$\mu^-\mu^+\nu_\mu\,,\ \mu^-e^+\nu_e$

Table 4.1. Flavor configurations of the decay products of VLL decays through the S scalars (see Eq. (4.1.11)) which can give rise to a final state with at least four light leptons.

4.2 Constraints from CMS Data

In order to study the production of VLLs at the LHC and their subsequent decays into 4L final states, we use FeynRules [150] to compute tree-level Feynman rules for our models. We then create UFO models [151], and use these as input for the Monte Carlo generator MadGraph5_aMC@NLO [152] to generate samples of 5×10^4 events. In the event generation we include all processes which yield a 4L final state (see Appendix C.1 for technical details). We obtain event samples for a set of benchmark masses M_F and M_S, with the coupling κ' fixed according to Eq. (4.1.8), and again fixing $\kappa = \epsilon\kappa'$ with $\epsilon = 10^{-2}$. In order to compare our results with experimental bounds from the CMS search [141], we then compute the scalar sum of the transverse momenta the four light leptons with the largest transverse momenta, L_T, for an integrated luminosity of 77.4 fb^{-1}. In the rest of this section, we review the decay chains yielding 4L final states and go on to present the constraints on the BSM masses M_F and M_S stemming from L_T distributions.

4.2.1 4L Multiplicities

We now explore which decay chains can give rise to final states with at least four light leptons. Such final states can arise both from single and pair production of the VLLs, since the former occurs in association with a lepton. For the decays through the S_{ij}, the different flavor configurations contributing to the 4L final state were already collected in Tab. 4.1. Taking into account all possible decays of the VLLs, the decay chains which yield a 4L final state in the singlet model are

$$\begin{aligned}
&pp \to \psi_i \bar{\psi}_i \to \ell_i^- \ell_i^+ \ell_j^+ \ell_j^- \ell_k^+ \ell_k^- \quad \text{for } i,j,k = 1,2,3\,, \ (20)\\
&pp \to \psi_i \bar{\psi}_i \to \ell_i^- \ell_i^+ q_j \bar{q}_j \ell_k^+ \ell_k^- \quad \text{for } i,k = 1,2\,, \ (15\times 4)\\
&pp \to \psi_i \bar{\psi}_i \to \ell_i^- \ell_i^+ \ell_j^+ \ell_j^- \nu_k \bar{\nu}_k \quad \text{for } i,j = 1,2,\ k = 1,2,3\,, \ (12)\\
&pp \to \psi_i \bar{\psi}_i \to \nu_i \ell_i^+ \ell_j^+ \ell_j^- \ell_k^- \bar{\nu}_k \quad \text{for } i,j,k = 1,2\,, \ (8)\\
&pp \to \psi_i \bar{\psi}_i \to \ell_i^- \bar{\nu}_i \ell_j^+ \ell_j^- \ell_k^+ \nu_k \quad \text{for } i,j,k = 1,2\,, \ (8)\\
&pp \to \psi_i \ell_i^+ \to \ell_i^- \ell_j^+ \ell_j^- \ell_i^+ \quad \text{for } i,j = 1,2\,, \ (4)\\
&pp \to \bar{\psi}_i \ell_i^- \to \ell_i^+ \ell_j^+ \ell_j^- \ell_i^- \quad \text{for } i,j = 1,2\,, \ (4)
\end{aligned} \tag{4.2.1}$$

where we have indicated the multiplicity of each decay chain between parentheses. The allowed values of the lepton flavor indices $i\,, j\,, k$ are also indicated, and for quarks these can take values $q_j = u, d, c, s, b$. The first decay chain in (4.2.1) is especially relevant, since it represents the only channel yielding a 6-lepton final state. Only in this case two taus can be produced alongside four light leptons. Hence, ψ_3 production only contributes to the 4L channel via this decay chain. In the doublet model, single and pair production of the negatively charged component lead to 4L final states following (4.2.1), with the exception of the W-mediated decays $\psi_i^- \to \nu_i \ell_j^- \bar{\nu}_j$, which in the doublet model are subleading and not taken into account for our study. Moreover, when the ψ^0 are produced additional 4L final states arise through

$$\begin{aligned}
&pp \to \psi_i^0 \overline{\psi}_i^0 \to \nu_j \overline{\nu}_k \ell_j^+ \ell_i^- \ell_i^+ \ell_k^- \quad \text{for } i,j,k = 1,2\,, \ (8)\\
&pp \to \psi_i^- \overline{\psi}_i^0 \to \ell_i^- \ell_i^+ \overline{\nu}_j \ell_j^- \ell_k^+ \ell_k^- \quad \text{for } i,j,k = 1,2\,, \ (8)\\
&pp \to \psi_i^0 \psi_i^+ \to \ell_i^- \ell_i^+ \ell_j^+ \nu_j \ell_k^+ \ell_k^- \quad \text{for } i,j,k = 1,2\,, \ (8)\\
&pp \to \psi_i^- \overline{\psi}_i^0 \to \ell_i^- \ell_i^+ \overline{q}_j q_j \ell_k^+ \ell_k^- \quad \text{for } i,k = 1,2\,, \ (15\times 4)\\
&pp \to \psi_i^0 \psi_i^+ \to \ell_i^- \ell_i^+ \overline{q}_j q_j \ell_k^+ \ell_k^- \quad \text{for } i,k = 1,2\,. \ (15\times 4)
\end{aligned} \tag{4.2.2}$$

Production cross sections of the 4L final states through the channels (4.2.1) and (4.2.2) are shown in Fig. 4.2 for both our models (red curves) and third-generation VLL models such as [142] (blue curves). Cross sections are larger by roughly two orders of magnitude in our models due to a higher multiplicity of 4L final states, and are further enhanced when the VLLs are heavy enough to decay to on-shell S_{ij}. As studied in the previous section, these decays are dominant when kinematically allowed and yield purely leptonic final states,

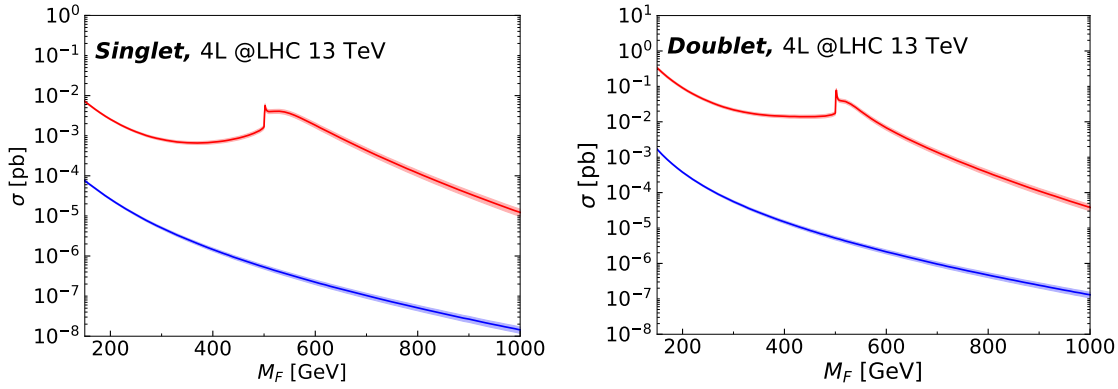

Figure 4.2. Production cross section of 4L final states at a pp collider with $\sqrt{s} = 13$ TeV in the singlet (left) and doublet model (right) in terms of of the VLL mass, with $M_S = 500$ GeV. The red curves correspond to the VLL models (4.1.4) and (4.1.6), while the blue curves correspond to third-generation VLL models such as [142]. In general, cross sections are larger in our models due to higher multiplicities of the 4L final states. Moreover, for $M_F > M_S$ the additional S-mediated decay channels of the VLLs further enhance the cross sections.

populating the 4L channel. This can be observed in Fig. 4.2 through the peak around the benchmark scalar mass $M_S = 500$ GeV. In general, 4L production cross sections are higher in doublet models by at least one order of magnitude, due to additional W-mediated production channels and higher 4L multiplicities.

4.2.2 L_T Distributions and CMS Constraints

The analysis of the transverse momenta distributions in the CMS study [141] allowed to exclude doublet VLL masses in the $120-790$ GeV range at 95%C.L. We now compute these distributions for the 4L channel in our VLL models, scanning over a range of BSM masses M_S and M_F, and after performing a fast detector simulation we compare our results to the limits set by CMS (see [145] and Appendix C.1 for details). Our findings are summarized in Fig. 4.3, where we show the points in our parameter space which are allowed by data together with schematic regions of exclusion. For the doublet model, we find that masses above ~ 800 GeV are excluded, in line with CMS limits. Due to smaller cross sections, no hard lower limit on the VLL masses is found for the singlet model. In both cases, we find that regions around the $M_S \sim M_F$ line are excluded, owing to the enhancement of cross sections around the S resonance. In Fig. 4.3, the green dotted line shows the perturbativity limit of the coupling κ', which is fixed according to Eq. (4.1.8) to explain the $g-2$ anomalies and becomes large for heavy BSM particles. Note that, even though both models allow explanations of the AMM anomalies through the same parameter space of Yukawa and scalar couplings [24], doublet VLL masses are significantly more constrained by present data.

From amongst the scanned masses which avoid present bounds we have selected three representative benchmarks for each model, marked in yellow in Fig. 4.3, which we use in

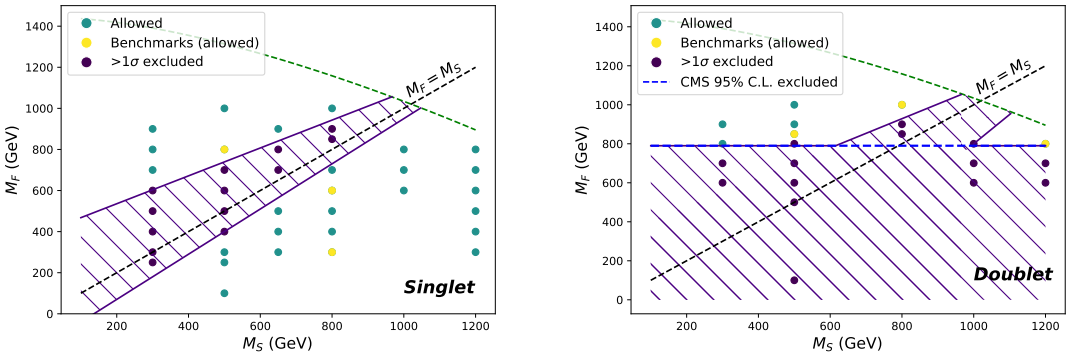

Figure 4.3. Excluded and allowed values of the VLL mass M_F and the BSM scalar mass M_S for the singlet (left) and doublet model (right). The coupling κ' is fixed for each point to explain the $(g-2)_\mu$ anomaly using Eq. (4.1.8); the onset of non-perturbative κ' values is indicated by the green dotted line. For the points marked as allowed, all bins in the distribution of L_T (the scalar sum of the transverse momenta of the four light leptons with the largest transverse momenta) fall within 1σ of the central values measured by CMS [141]. Allowed points marked in yellow are used as benchmarks to study the observables described in Sec. 4.3, and their L_T distributions are displayed in Fig. 4.4.

the following sections to exemplify our analysis strategy. For each model, the benchmarks include at least one case where $M_F > M_S$ and another with $M_S > M_F$. The corresponding L_T distributions after hadronization and detector simulation are shown together with CMS constraints in Fig. 4.4, where we observe that for each bin VLL contributions do not surpass the experimental 1σ limits. Fig. 4.4 also shows the L_T distribution of the dominant SM background processes of ZZ, triboson and $t\bar{t}Z$ production. In the ZZ channel we include contributions from $pp \to \gamma^*\gamma^*, \gamma^*Z$ and ZZj, as well as $gg \to ZZ$. The latter is induced at lowest order at 1-loop, but represents $\sim 15\%$ of the SM ZZ background [153]. Final states with a jet are included via multijet merging in PYTHIA8 [154]. We find that our background simulation is in reasonable agreement with that of CMS in all the bins of the L_T distributions, even though small differences are present. These are, however, expected: we perform leading order computations and employ the publicly available fast detector simulations, in contrast to the more involved analysis performed by CMS in which background distributions are fitted to control region data.

4.3 Observables and Null Tests

So far the study of transverse momenta distributions allowed us to constrain the parameter space of BSM masses through experimental constraints from [141]. In this section, we present observables beyond L_T which specifically target the features of our models and allow to reconstruct masses of the VLLs and the S scalars. The new observables consist of the dilepton invariant masses $m_{2\ell}$ and $m_{2\ell}$_diff, which allow to search for BSM scalar resonances, and the three-lepton invariant masses $m_{3\ell}$ and $m_{3\ell}$_diff, which target the VLL

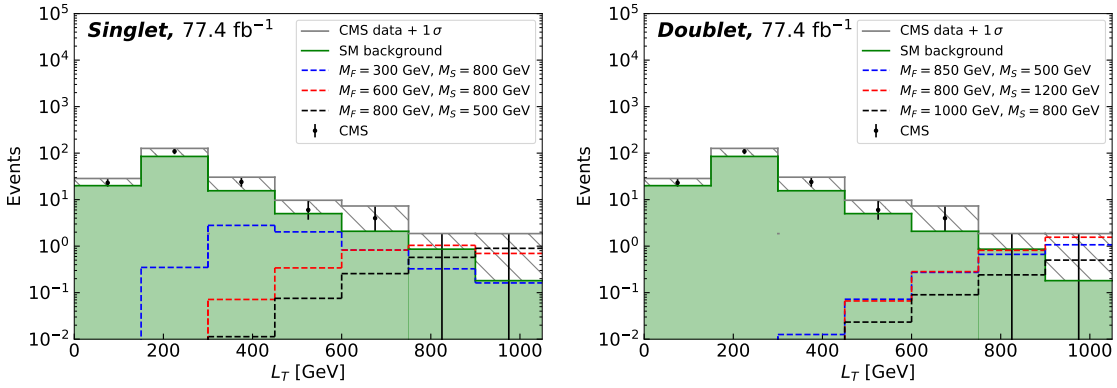

Figure 4.4. Scalar sum of transverse momenta L_T in the singlet (left) and doublet model (right) after detector simulation. Distributions are shown for several benchmark masses of vector-like fermions and BSM scalars (dashed curves), and for SM background processes (solid green area). An integrated luminosity of 77.4 fb^{-1} and a bin width of 150 GeV have been chosen in order to match CMS data from [141], also displayed at 1σ (black points and hatched region). We have included as well the control region veto of two dilepton pairs with invariant masses 76 GeV $< m_{2\ell} <$ 106 GeV. For both models, the displayed benchmarks fall within 1σ CMS constraints, and correspond to the highlighted yellow points of Fig. 4.3. The observed small differences between our simulation of the SM background and the CMS data are expected, as CMS uses a data-driven background estimation not publicly available.

mass. The '_diff' observables contain at least one invariant mass built out of two OCDF leptons, which in our models arise from LFV-like decays of the S_{ij}. Therefore, they are designed to hunt for resonances of the BSM scalars (in the case of $m_{2\ell}$_diff) or the VLLs ($m_{3\ell}$_diff) while suppressing contributions from SM background[1]. Schematically, the four observables we propose are computed as follows (see Appendix C.2 for a detailed account of the algorithms):

$m_{2\ell}$: for each 4L final state, two invariant masses are added to $m_{2\ell}$. These can come from two leptons of opposite charge and same flavor (OCSF) which reconstruct to a Z boson or Higgs, or from two jets or two taus which reconstruct to Z or Higgs. Additionally, we add to $m_{2\ell}$ pairs of dilepton invariant masses either of OCSF or OCDF leptons which do not reconstruct to SM particles but coincide. This last step allows to reconstruct the S scalars without prior knowledge of their mass, and requires VLLs to be pair produced and decay through the BSM scalars.

$m_{2\ell}$_diff: a pair of dilepton invariant masses, where at least one of the invariant masses is constructed out of two OCDF leptons, are added to the observable if they coincide. Therefore, the $m_{2\ell}$_diff targets decays of the type $S_{ij} \to \ell_i^- \ell_j^+$ for $i \neq j$.

[1]The '_diff' observables can in principle be used to search for general models with heavy particles decaying to leptons of different flavors, as long as the BSM states can be pair produced at the LHC.

$m_{3\ell}$: for each 4L final state we start from the dilepton invariant masses added to $m_{2\ell}$, and pair each of them with another lepton in the final state. If a dilepton invariant mass contains OCSF leptons, we require that the paired lepton also be of that same flavor. If the dilepton invariant mass was computed out of two OCDF leptons, we require that the paired lepton be OCSF with respect to one of the leptons in the dilepton invariant mass. We add the subsequent three-lepton invariant masses to $m_{3\ell}$ if they coincide. This allows to reconstruct the masses of the VLLs.

$m_{3\ell}$_diff: similar to $m_{3\ell}$, but in this case we start out from the dilepton invariant masses added to $m_{2\ell}$_diff. Hence, $m_{3\ell}$_diff allows to reconstruct VLL masses in the case where both VLLs decay through the S_{ij} and at least one of these undergoes an LFV-like decay. Only 6-lepton final states contribute to $m_{3\ell}$_diff, and imposing flavor conservation within the hypothesis of our models always allows to group the final-state leptons correctly to reconstruct VLL masses.

We compute the above observables for the benchmarks highlighted in Fig. 4.3 for an integrated luminosity of 150 fb^{-1}, corresponding to the full dataset of run 2 at the LHC [155]. Results are shown in Figs. 4.5 and 4.6 for the singlet and doublet model, respectively. In the case of $m_{2\ell}$ and $m_{2\ell}$_diff, we observe that in benchmarks where on-shell S production is possible peaks around M_S with $\mathcal{O}(10)$ events arise, giving clear signals of the presence of the BSM scalars. For the benchmarks where the VLLs are lighter than the BSM scalars, distributions peak around the electroweak boson resonances but do not rise above the SM background. However, bins where the SM background is absent receive contributions as well. Higher luminosities would benefit these scenarios, making the tails of the distributions more visible. Note that the observable $m_{2\ell}$_diff is in principle a null test of the SM, since it requires at least one LFV-like decay to take place. Nevertheless, a large SM background in the low-mass region can give rise to pairs of coincident dilepton invariant masses which are incorrectly reconstructed as two BSM scalars. Therefore, the SM background is suppressed with respect to $m_{2\ell}$ but not completely absent, as can be seen in Figs. 4.5 and 4.6.

Furthermore, the three-lepton invariant masses $m_{3\ell}$ and $m_{3\ell}$_diff clearly peak around the VLL mass in benchmarks where $M_F < M_S$. This effect arises due to lower VLL masses requiring a smaller κ' coupling to accommodate the $g-2$ explanations, which leads to narrow resonances of the VLLs. However, in these benchmarks the VLL peaks in $m_{3\ell}$_diff are fairly suppressed, since on-shell S production is forbidden. For higher values of κ' the VLLs present faster decays, leading to broad resonances which can however reach $\mathcal{O}(1)$ events in some bins. This can be seen for the $m_{3\ell}$ and $m_{3\ell}$_diff distributions of the benchmarks with $M_F > M_S$ (black curves in Fig. 4.5 and blue and black curves in Fig. 4.6).

Finally, the $m_{3\ell}$_diff distribution presents the advantage of being completely background-free, thanks to strict flavor-conservation conditions imposed on the 4L final state together with the requirement that an LFV-like decay take place. Therefore, the observable is an excellent null test of the SM. The trade-off is however a depletion of both broad distributions and peaks around the VLL masses. Hence, the observables would again greatly benefit from

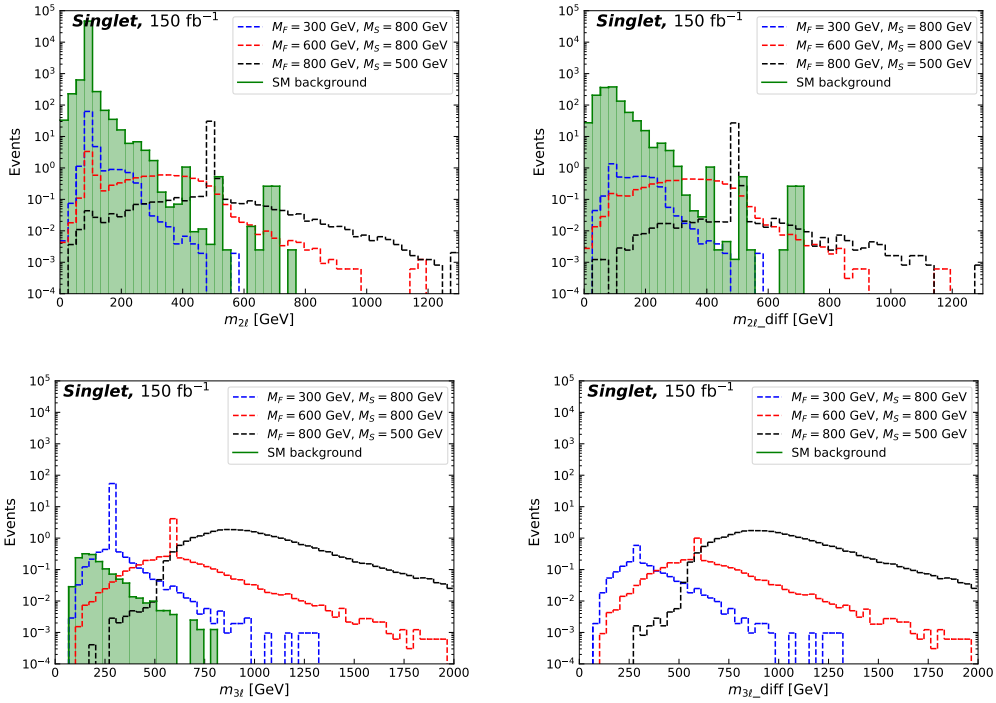

Figure 4.5. Dilepton invariant masses $m_{2\ell}$, $m_{2\ell}$_diff, $m_{3\ell}$, and $m_{3\ell}$_diff (see Sec. 4.3 for details) for the singlet model and for different benchmark masses of the VLLs and the BSM scalars. The distributions are shown for $\sqrt{s} = 13$ TeV and a luminosity of 150 fb^{-1}. For the benchmarks with $M_F < M_S$ (blue and red), VLLs decay mostly to electroweak bosons or Higgs and no peaks around the S mass arise in the dilepton masses, while VLL resonances are clearly visible in the three-lepton invariant masses. For the benchmark with $M_F > M_S$ (black), decays through the S scalars are dominant, yielding clear peaks at the scalar mass in $m_{2\ell}$ and $m_{2\ell}$_diff, while a large value of κ' yields a broad VLL resonance in $m_{3\ell}$ and $m_{3\ell}$_diff. The latter presents a complete suppression of the background, resulting in a null test of the SM.

higher luminosities. To exemplify this, we have computed our set of observables for the studied benchmarks at $\sqrt{s} = 14$ TeV and future HL-LHC luminosities of 3000 fb^{-1} [155], which we present in Fig. C.3.2 in Appendix C. We observe that the enhanced luminosity yields peaks with up to $\mathcal{O}(10^3)$ events, improving the opportunities of discovery.

4.4 Benchmarks beyond $g-2$

In Sec. 4.3 we developed novel observables targeting the features of our models, and computed their distributions for several benchmark BSM parameters compatible with lepton AMM data. In this section, we focus on the singlet model to explore scenarios beyond the $g-2$ explanations, no longer fixing κ' according to Eq. (4.1.8). Since the $g-2$ benchmarks already present a rather large κ', we choose instead the lower value $\kappa' = 1$. The coupling κ, restricted by Z-data, is fixed to $\kappa = 10^{-2}$ as in the rest of this chapter. Note that, for vanishing κ' but $y \neq 0$, the decays $\psi \to S\ell$ and $S \to \ell\ell'$ can still occur, arising at order $y\theta$

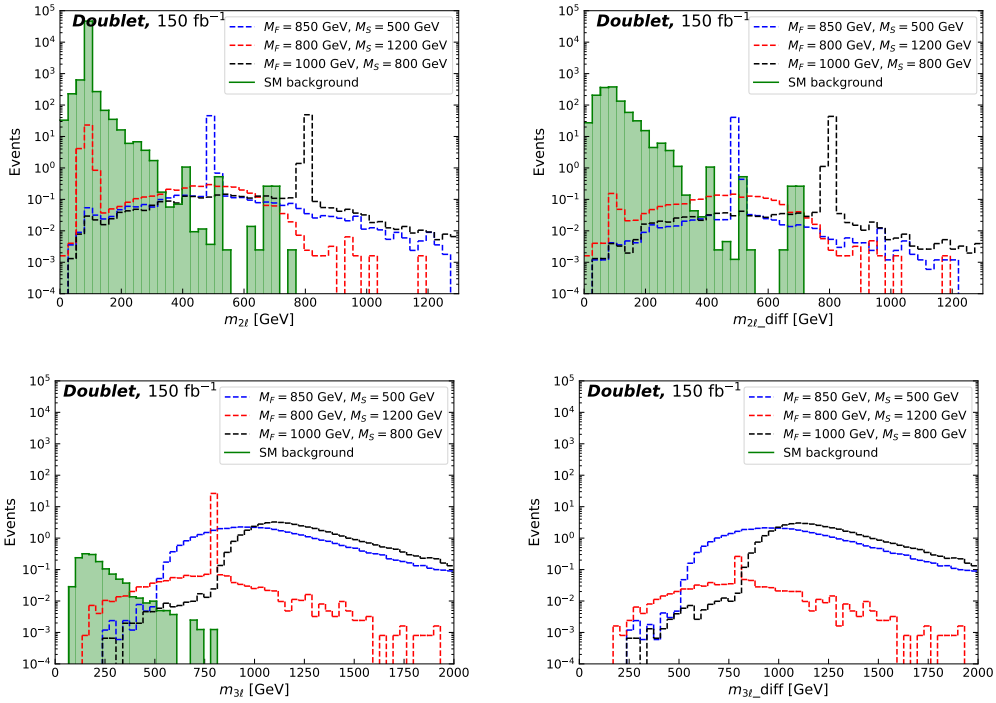

Figure 4.6. Dilepton invariant masses $m_{2\ell}$, $m_{2\ell}$_diff, $m_{3\ell}$, and $m_{3\ell}$_diff (see Sec. 4.3 for details), for the doublet model and for different benchmark masses of the VLLs and the BSM scalars. The distributions are shown for $\sqrt{s} = 13$ TeV and a luminosity of 150 fb^{-1}. Features depending on the BSM mass hierarchy identified in Fig. 4.5 apply.

and $y\theta^2 v_h/M_F y_\ell$, respectively, where y_ℓ is the lepton Yukawa. This holds as well for other models of vector-like fermions considered in Chapter 3, where κ' interactions are absent. In this case, however, the constraint (4.1.3) on the mixing angle θ severely suppresses contributions to the 'diff' observables.

Having fixed the BSM Yukawas to $\kappa' = 1, \kappa = 10^{-2}$, we study the benchmark BSM masses already employed in Sec. 4.3. Results for the corresponding L_T distributions after hadronization and detector simulation are shown in Fig. 4.7 together with limits from CMS [141]. We observe that, for the two benchmarks with lower VLL masses, all L_T bins still lie within experimental bounds, while for the $M_F = 800$ GeV benchmark high-L_T bins are in tension with data. This is due to the lower value of κ' yielding a narrower VLL resonance, which leads to more events in the high-L_T region. For this reason, we have chosen another benchmark, with $M_F = 900$ GeV, which is in agreement with CMS bounds (pink curve in Fig. 4.7). The higher VLL mass yields in this case a lower cross section, which compensates for the resonance effect. We therefore choose the $M_F = 900$ GeV benchmark, together with the $M_F = 300, 600$ GeV benchmarks, to compute the set of new observables described in Sec. 4.3.

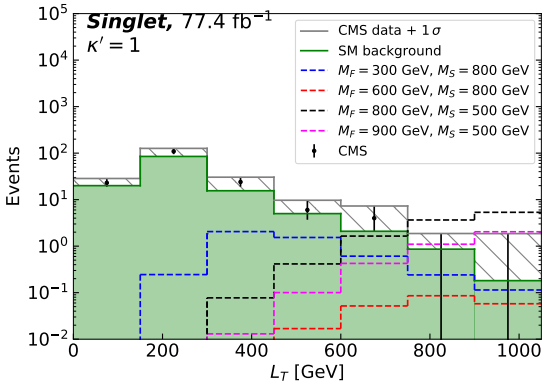

Figure 4.7. Scalar sum of transverse momenta L_T after detector simulation in the singlet model, for different masses of vector-like fermions and BSM scalars and for SM background processes, with $\kappa' = 1$. Results are shown for an integrated luminosity of 77.4 fb^{-1} and a bin width of 150 GeV together with CMS data from [141] at 1σ (black dots). For $\kappa' = 1$, the $M_F = 800$ GeV, $M_S = 500$ GeV benchmark (black curve) is excluded at 1σ, in contrast to the allowed benchmark with the same masses and larger κ' shown in Fig. 4.5. A benchmark with higher $M_F = 900$ GeV is allowed for $\kappa' = 1$ (pink curve).

Results for the new observables are shown in Fig. 4.4. In the case of the dilepton invariant masses $m_{2\ell}$ and $m_{2\ell}$_diff, we observe a similar pattern with respect to the $g-2$ benchmarks studied in Sec. 4.3: when the scalars can be produced on shell, peaks around the S mass are clearly visible (in this case with $\mathcal{O}(10)$ events), while for for $M_F < M_S$ resonances remain below SM background contributions. Furthermore, in the three-lepton invariant masses $m_{3\ell}$ and $m_{3\ell}$_diff the effects of narrower VLL resonances due to smaller κ' are clearly visible, with all benchmarks peaking at the VLL mass. In the cases where $M_F < M_S$, the observable $m_{3\ell}$ is the optimal one, since peaks rise well above SM background. For $M_F > M_S$, $m_{3\ell}$_diff presents the advantage of the SM background being entirely suppressed, while the VLL resonance is nearly as populated as in $m_{3\ell}$_diff . This results from the fact that in this case the VLLs decay almost entirely through the BSM scalars, populating both three-lepton invariant masses similarly.

4.5 Summary

In this chapter we have explored LHC signatures of asymptotically safe models of vector-like leptons with an extended scalar sector. We have focused on the parameter space which allows the models to accommodate the muon and electron anomalous magnetic moment anomalies simultaneously through new Yukawa interactions. For each model, we have generated samples of events in which VLLs are produced and decay to at least four light leptons (electrons or muons). This allowed us to study the transverse momenta L_T of the final state and compare it to current CMS data [141], identifying regions in the parameter space of BSM masses and couplings which are already in tension with data. These results are summarized in Fig. 4.3, which shows that for the doublet model masses below ~ 800 GeV are

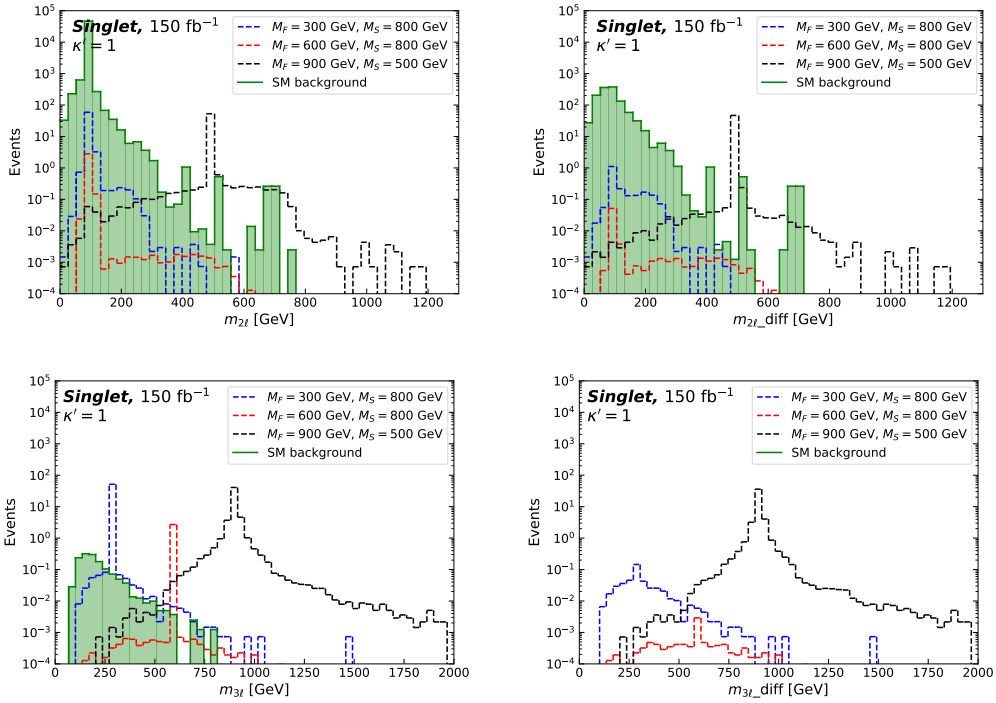

Figure 4.8. Dilepton invariant masses $m_{2\ell}$, $m_{2\ell}$_diff, $m_{3\ell}$, and $m_{3\ell}$_diff (see Sec. 4.3 for details) for the singlet model with fixed $\kappa' = 1$ and for several benchmark masses of the VLLs and the BSM scalars, at a luminosity of 150 fb^{-1} and $\sqrt{s} = 13$ TeV. Lower values of κ' in comparison to the $g-2$ benchmarks shown in Fig. 4.5 lead to narrower VLL resonances, which become visible for all BSM masses in $m_{3\ell}$ and $m_{3\ell}$_diff.

excluded, but lower masses (at least as low as ~ 300 GeV) are still allowed for the singlet model. In both cases the regions with similar BSM scalar and VLL masses are ruled out as well.

Next, we have built novel observables which target the features of our models, in particular the LFV-like decays of the VLLs through the scalars S_{ij}. The observables consist of the dilepton invariant masses $m_{2\ell}$ and $m_{2\ell}$_diff and the three-lepton invariant masses $m_{3\ell}$ and $m_{3\ell}$_diff. Using our event samples and a luminosity of 150 fb^{-1}, we have computed their distributions for several benchmark BSM masses which were found to be allowed in the L_T analysis. As seen in Figs. 4.5 and 4.6, the dilepton invariant masses clearly show peaks around the BSM scalar mass, with $m_{2\ell}$_diff presenting a more suppressed SM background, while the three-lepton invariant masses $m_{3\ell}$ and $m_{3\ell}$_diff allow to reconstruct the VLL masses. In the case of $m_{3\ell}$_diff, the requirement that at least one scalar S_{ij} undergo an LVF-like decay entirely suppresses the background, making it a null test of the SM. A higher luminosity would greatly benefit the observables, with peaks potentially reaching $\mathcal{O}(10^3)$ events at HL-LHC luminosities, as seen in Fig. C.3.2. Lastly, we have explored benchmarks with smaller BSM Yukawa couplings, going beyond the $g-2$ parameter space. We found

that in these cases the VLL resonances can be narrower, yielding higher peaks in the $m_{3\ell}$ and $m_{3\ell}$_diff distributions.

In conclusion, we have shown that our class of VLL models is already constrained by present data, while targeted observables provide unique opportunities to detect BSM particles and distinguish mass hierarchies. Moreover, the LFV-like signature specific to our models allows to build null tests of the SM, where the background is completely absent.

5 Flavor from Running in $U(1)_X$ Models

The evolution of gauge and Yukawa couplings typically presents logarithmic dependence on the energy scale, making it difficult for large hierarchies to arise as a consequence of the renormalization group flow. However, in certain scenarios the running can abandon its logarithmic behavior and present a steeper evolution, making significant RG-induced changes in the couplings possible. It is then natural to wonder whether these effects can induce large hierarchies amongst the couplings of a theory, in particular within the flavor sector. The idea of using RG effects to explain flavor patterns is an early one [12], and it generally requires a mechanism to steer Yukawa couplings away from the logarithmic regime. Examples have been put forward in the context of a nearly scale-invariant gauge coupling [156] and in supersymmetric theories through the coupling of the SM to a conformal field theory [9, 10]. Recent works propose the generation of RG-induced hierarchies between the up and the down sector thanks to hypercharge differences and universal shifts in the β-functions of gauge and Yukawa couplings, with a possible origin in asymptotically safe gravity [11]. Further studies also employing quantum gravity assumptions can accommodate flavor parameters, but fail to generate large ratios between couplings through the running [23].

In the case of asymptotically safe gauge-Yukawa theories a steep running emerges from the UV fixed point, with couplings abandoning their logarithmic flow. In particular, for asymptotically free Yukawa couplings the evolution follows the pure power-law behavior (2.1.26). Then, if the exponents of this flow are different for each fermion species and generation, Yukawa couplings can acquire large hierarchies throughout their running. To this end, a local symmetry with non-universal charges is paramount. Here we explore a simple realization of such a scenario, where the SM is extended with a non-universal $U(1)$ gauge interaction. This chapter, which is based in ongoing works [74], is organized as follows: in Sec. 5.1 we show how ratios of Yukawa couplings can become sizable throughout the running, thanks to the presence of a UV fixed point and generation-dependent charges. In Sec. 5.2 we propose a concrete model which contains the necessary ingredients for RG-induced hierarchies in Yukawa couplings to arise, and discuss possible scenarios of quark mixing. Benchmarks which can reproduce the values of physical parameters of the flavor sector of the SM at the order of magnitude are discussed in Sec. 5.4. Phenomenological implications are worked out in Sec. 5.5, and in Sec. 5.6 we summarize.

5.1 Hierarchies from Running in $U(1)$ Extensions

Let us start by considering a minimal scenario where the SM is extended by a new $U(1)_X$ gauge symmetry. Generally, we would like the SM fermions to be charged under the new

gauge group, in particular with non-universal charges. This will allow $U(1)_X$ interactions to contribute differently to the anomalous dimensions of Yukawa couplings of each generation. An important constraint on the charges that fermionic fields can carry under the new symmetry is encoded in triangle diagrams with three gauge bosons as external legs, where charged fermions propagate in the loop. If the matrix element of a given triangle diagram does not vanish, gauge symmetries are not conserved at a quantum level, yielding *gauge anomalies*. In the SM all gauge anomalies cancel, with a notorious case being the $U(1)_Y^3$ anomaly, which vanishes in a non-trivial manner. Note that any G^3 anomaly of a non-chiral group G always vanishes, owing to contributions of right- and left-handed fermions yielding an opposite sign.

In $U(1)_X$ extensions without any additional matter content gauge anomalies are directly canceled if the new charges of the SM fermions coincide with the values of their hypercharges (see for instance [38] for details). Further scenarios become possible when new charged particles are added to the SM. To this end, we choose to extend the SM with three right-handed fields, denoted by N_i, which we take to be total SM singlets and carry charges under the new symmetry. Then, the anomaly cancellation conditions which are not automatically fulfilled can be written in terms of the fermionic $U(1)_X$ charges X_f as [157]

$$U(1)_X^3 \;:\; \sum \left[2(X_L^3 + 3X_Q^3) - (X_E^3 + X_N^3 + 3X_U^3 + 3X_D^3)\right] = 0\,, \tag{5.1.1a}$$

$$U(1)_X^2 \times U(1)_Y \;:\; \sum \left[- X_L^2 + X_Q^2 + X_E^2 - 2X_U^2 + X_D^2\right] = 0\,, \tag{5.1.1b}$$

$$U(1)_X \times U(1)_Y^2 \;:\; \sum \left[\frac{1}{2}X_L + \frac{1}{6}X_Q - X_E - \frac{4}{3}X_U - \frac{1}{3}X_D\right] = 0\,, \tag{5.1.1c}$$

$$SU(2)_L^2 \times U(1)_X \;:\; \sum \left[X_L + 3X_Q\right] = 0\,, \tag{5.1.1d}$$

$$SU(3)_C^2 \times U(1)_X \;:\; \sum \left[2X_Q - X_U - X_D\right] = 0\,, \tag{5.1.1e}$$

$$\text{grav}^2 \times U(1)_X \;:\; \sum \left[2(X_L + 3X_Q) - (X_E + X_N + 3X_U + 3X_D)\right] = 0\,, \tag{5.1.1f}$$

where the sums run over all flavors, and we have substituted the SM hypercharges according to their values in Tab. 1.1. Let us now consider a few simple solutions of Eq. (5.1.1). First, assume that the anomalies cancel per generation, as is the case in the SM. In that case, Eq. (5.1.1d) immediately requires $X_L = -3X_Q$. Additionally, the conditions

$$X_L^i = X_E^i = X_N^i\,, \quad X_Q^i = X_U^i = X_D^i\,, \tag{5.1.2}$$

that is, all quark and all lepton fields carry the same $U(1)_X$ charges, allow to cancel all remaining equations in (5.1.1)[1]. However, the requirement $X_L = -3X_Q$ invariably leads to larger $U(1)_X$ charges (in absolute value) in the lepton sector. As we shall argue in Sec. 5.4, this can pose challenges when building models with RG-induced hierarchies, as the running of the $U(1)_X$ coupling will enhance the Yukawas of the leptons with respect to those of

[1]The case where charges of quarks and leptons are universal, with $X_Q = 1/3$ and $X_L = -1$, corresponds to $U(1)_{B-L}$ solutions.

the quarks. Abandoning the restriction of anomaly cancellation per generations leads to another set of solutions obeying

$$\sum_i X_f^i = 0\,, \tag{5.1.3}$$

which together with (5.1.2) allows to fulfill all the conditions (5.1.1). In the limit of degenerate fermion masses, Eq. (5.1.3) ensures that no kinetic mixing between $U(1)$ gauge bosons is induced at 1-loop [158]. Finally, note that the presence of additional fermions with vector-like charges would not spoil anomaly cancellation, since right- and left-handed fields contribute terms with opposite signs.

In the remainder of this chapter, we assume that SM fields follow the vector-like charge assignment (5.1.2), with each generation carrying different charges which fulfill as well (5.1.3), while the Higgs field is uncharged under the new symmetry. Then, gauge invariance allows only for diagonal terms in the SM Yukawa matrices $Y_{u,d,\ell}$, and the additional Yukawa coupling $\overline{L}Y_\nu N\tilde{H}$ of the neutrino sector must also take a diagonal form. Within this minimal scenario, we now envision a situation where a gauge-Yukawa fixed point exists at which *all* SM Yukawas as well as the Y_ν vanish. We further assume that the gauge-Yukawa fixed point is negotiated by an entirely BSM Yukawa y (of the type contained in the model (2.2.1)), which does not enter the β-functions of the SM Yukawas at 1-loop. The possible non-vanishing coordinates of the fixed point are thus

$$(\alpha_1^*, \alpha_2^*, \alpha_3^*, \alpha_X^*, \alpha_y^*)\,, \tag{5.1.4}$$

where $\alpha_X = g_X^2/(4\pi)^2$ is the coupling of the new interaction. We postpone the discussion of a model where such a fixed point can be realized to the next sections and focus now on the implications for the SM Yukawas. According to Eqs. (2.1.24) and (2.1.26), their evolution close to the fixed point follows

$$\alpha_n(\mu) \simeq \alpha_{n,0} \left(\frac{\mu}{\mu_0}\right)^{-\sum_{i=1,2,3,X} F_{ni}\alpha_i^*}\,, \tag{5.1.5}$$

where $\alpha_{n,0} = \alpha_n(\mu_0)$, α_i denote gauge couplings, and the F_{ni} can be read off the β-function of α_n following the conventions of (2.1.23). Thus, the evolution of the asymptotically free Yukawas near the fixed point is determined by the values of the gauge couplings at the fixed point together with their associated coefficients in the Yukawa β-function. The $F_{n1,n2,n3}$ depend on SM interactions only, and coincide for all generations within the up, down, charged- and neutral-lepton sectors. Leptons further present $F_{n3} = 0$, and since the $SU(2)_L$ structure of the quark and lepton sector extended with the N_i coincides, one finds $F_{n2} = 9/4$ in all cases (see for instance the 1-loop β-function of the top in Eq. (1.2.10)). In our setup, however, the F_{nX} coefficients associated to the $U(1)_X$ coupling are generation-dependent, and fulfill

$$F_{nX} = 12X_n^2\,, \tag{5.1.6}$$

where X_n is the $U(1)_X$ charge of the fermion species n. Thus, from Eqs. (5.1.5) and (5.1.6) one can directly see that non-universal charges X_n will induce differences within Yukawa

couplings throughout the running. It shall also prove useful to define a measure of the RG time that separates the scale μ_c, at which the running is far enough from the fixed point to slow down its power-law behavior, from the scale μ_0, where we take our initial condition $\alpha_{n,0}$. We define this *critical time* as

$$\tau = -\log \frac{\mu_c}{\mu_0} \,. \tag{5.1.7}$$

Hence, the ratio of the Yukawa couplings of two fermions n and m of the same sector (up, down, charged or neutral lepton) but different generation after the power-law phase of the running can be approximated by

$$\log \frac{\alpha_n}{\alpha_m}\bigg|_{\mu_c} \simeq 12\tau\, \alpha_X^* (X_n^2 - X_m^2) \,, \tag{5.1.8}$$

where we have assumed that at the scale μ_0 there is no significant hierarchy between the couplings and $\alpha_{n,0} \sim \alpha_{m,0}$. As soon as the right-hand side of (5.1.8) is of order one, α_n and α_m can differ by several orders of magnitude. Hence, we have shown how the presence of a gauge-Yukawa fixed point together with non-universal charges can create large differences between Yukawa couplings. Note that if the Yukawas had not been free but interacting at the fixed point (following then the evolution (2.1.12)), their ratio would not be governed by a pure exponential law, and it would become much more difficult to obtain successive hierarchies between couplings, posing a fine-tuning problem.[2]

Furthermore, we can assess how our setup relates couplings from different sectors. For instance, the ratios between up and down and charged-leptons and neutrino Yukawas of the same generation at μ_c read

$$\log \frac{\alpha_{u_i}}{\alpha_{d_i}}\bigg|_{\mu_c} \simeq 2\tau\, \alpha_1^* \,, \qquad\qquad \log \frac{\alpha_{e_i}}{\alpha_{\nu_i}}\bigg|_{\mu_c} \simeq 6\tau\, \alpha_1^* \,. \tag{5.1.9}$$

respectively, where the labels $u_i = u, c, t$, $d_i = d, s, b$, $e_i = e, \mu, \tau$ and $\nu_i = \nu_e, \nu_\mu, \nu_\tau$ denote the diagonal Yukawa couplings. Therefore, the differences in the hypercharges within the quark or lepton sectors already encoded in the SM lead to running-induced hierarchies for a non-vanishing α_1^*. Note that the hypercharge is the only SM gauge coupling which presents this effect, as $\alpha_{2,3}$ are factored out of the ratios (5.1.9). Moreover, Eq. (5.1.9) implies that the ratio between same-generation quarks within the up and down sector is fixed. This is however not the case in the SM, where one finds $y_d/y_u \sim 1, y_s/y_c \sim 10^{-1}$ and $y_b/y_t \sim 10^{-2}$. Nevertheless, these differences could be ameliorated by subleading effects, for example in the running after the power-like phase. On the other hand, Yukawa couplings of an up quark and a charged lepton of generations i and j respectively obey

$$\log \frac{\alpha_{u_i}}{\alpha_{e_j}}\bigg|_{\mu_c} \simeq \tau \left(-\frac{14}{3}\alpha_1^* + 16\alpha_3^* + 12\alpha_X^* (X_{q_i}^2 - X_{\ell_i}^2) \right) , \tag{5.1.10}$$

[2]Yukawas which are interacting at the fixed point evolve as $\alpha \sim \alpha^* + C\mu^\theta$. Therefore, if several Yukawas present non-hierarchical fixed point values $\alpha^* \neq 0$, in order for the couplings to evolve towards values separated by several orders of magnitude there must be at least one fine-tuned cancellation between α^* and the exponential term in the evolution. The possibility that only one of the SM Yukawas is not vanishing might however prove interesting, and we reserve it for future works.

α_t	α_c	α_u	α_b	α_s	α_d	α_τ	α_μ	α_e
$6 \cdot 10^{-3}$	$3 \cdot 10^{-7}$	$1 \cdot 10^{-12}$	$4 \cdot 10^{-6}$	$2 \cdot 10^{-9}$	$5 \cdot 10^{-12}$	$7 \cdot 10^{-7}$	$2 \cdot 10^{-9}$	$5 \cdot 10^{-14}$
y_t	y_c	y_u	y_b	y_s	y_d	y_τ	y_μ	y_e
1.0	$7.3 \cdot 10^{-3}$	$1.3 \cdot 10^{-5}$	$2.4 \cdot 10^{-2}$	$5.5 \cdot 10^{-4}$	$2.7 \cdot 10^{-5}$	$1.0 \cdot 10^{-2}$	$6.1 \cdot 10^{-4}$	$2.9 \cdot 10^{-6}$

Table 5.1. Values $\alpha_f = 2(m_f/4\pi v_h)^2$ and $y_f = \sqrt{2}\, m_f/v_h$ of the Yukawa couplings and masses from [37].

where we have used $X_Q^i = X_U^i = X_D^i = X_{q_i}$ and $X_L^i = X_E^i = X_N^i = X_{\ell_i}$. Note that terms proportional to α_2^* drop out as expected and α_1^* (α_3^*) contribute to larger lepton (quark) couplings, while α_X^* enhances quark masses if the X_{q_i} are larger in magnitude than the X_{ℓ_i}.

In summary, we have shown that non-universal $U(1)_X$ charges together with a fixed point involving an interacting α_X^* can generate sizable hierarchies among Yukawa couplings associated to different flavors, while non-zero α_1^* and α_3^* can add differences between sectors.

5.2 Setup and Mixing Scenarios

We now aim to build a model which can explain the observed hierarchies between the SM Yukawa couplings through the mechanism introduced in the Sec. 5.1, which involves the presence of a gauge-Yukawa fixed point in the UV. We will also require that CKM mixing can be accommodated, while a discussion of mixing in the neutrino sector is beyond the scope of this work. Assuming that SM fermions are non-universally charged under the new $U(1)_X$ symmetry, with anomaly cancellation being fulfilled through the conditions (5.1.2) and (5.1.3), only the diagonal terms in the Yukawa matrices are allowed by gauge invariance. These read

$$\begin{aligned} -\mathcal{L}_{y_f} = &\sum_{d_i=d,s,b} y_{d_i}\, \overline{Q}_i H D_i + \sum_{u_i=u,c,t} y_{u_i}\, \overline{Q}_i \tilde{H} U_i \\ &+ \sum_{e_i=e,\mu,\tau} y_{e_i}\, \overline{L}_i H E_i + \sum_{\nu_i=\nu_e,\nu_\mu,\nu_\tau} y_{\nu_i}\, \overline{L}_i \tilde{H} N_i + \text{h.c.}\,. \end{aligned} \tag{5.2.1}$$

This scenario, however, prohibits any mixing in the quark sector. In order to remedy this issue, we introduce additional $SU(2)_L$ scalar doublets η^{ij}, with hypercharge 1/2 and $U(1)_X$ charges set to allow couplings with different-flavor quarks. In particular, we introduce two additional doublets η^{12} and η^{23}, which link either the first and second generation or the second and third generation. This is only possible when the η^{ij} carry charges $X_{q_i} - X_{q_j}$ or $X_{q_j} - X_{q_i}$, which leads to the mixing Yukawa terms

$$\begin{aligned} -\mathcal{L}^d_{\text{mix}} &= y_{ds}\, \overline{Q}_1\, \eta^{12} D_2 + y_{cu}\, \overline{Q}_2\, \tilde{\eta}^{12} U_1 + y_{sb}\, \overline{Q}_2\, \eta^{23} D_3 + y_{tc}\, \overline{Q}_3\, \tilde{\eta}^{23} U_2 + \text{h.c.}\,, \\ -\mathcal{L}^u_{\text{mix}} &= y_{sd}\, \overline{Q}_2\, \eta^{12} D_1 + y_{uc}\, \overline{Q}_1\, \tilde{\eta}^{12} U_2 + y_{bs}\, \overline{Q}_3\, \eta^{23} D_2 + y_{ct}\, \overline{Q}_2\, \tilde{\eta}^{23} U_3 + \text{h.c.}\,, \end{aligned} \tag{5.2.2}$$

respectively. The labeling of the Lagrangian responds to the fact that for scalar charges $X_{q_i} - X_{q_j}$ ($X_{q_j} - X_{q_i}$) the mixing stems mainly from the down (up) sector, as we shall see shortly. Indeed, if the η^{ij} acquire vacuum expectation values $v_{\eta^{ij}}$, non-diagonal contributions to the mass matrices arise from the interactions (5.2.2), giving rise to quark mixing.

Our choice of two additional scalars renders two extra non-vanishing elements in the mass matrices after spontaneous symmetry breaking, allowing to generate a mixing matrix with no vanishing entries.

In our setup, the values of the Yukawa couplings y_{ij} associated to the η^{ij} can be predicted by the RG evolution once we assume SM Yukawas can be matched to their electroweak-scale values. Since the η^{ij} link two different quark flavors i and j, their critical exponent contains a factor $6(X_{q_i}^2 + X_{q_j}^2)\alpha_X^*$, following the arguments of Sec. 5.1 (see as well the β-functions β_{ij} in Appendix B.3). Comparing this to diagonal Yukawas, which grow with a factor $12X_{q_i}^2$, we find that the y_{ij} after the power-law phase of the running can be approximated as

$$y_{ij}|_{\mu_c} \simeq \sqrt{y_i y_j}|_{\mu_c} \,. \tag{5.2.3}$$

Therefore, in models that reproduce the SM values of the diagonal Yukawas the y_{ij} are predicted by the RG flow via (5.2.3), and the VEVs $v_{\eta^{ij}}$ constitute the only free parameters in the quark mass matrices. Let us now study in more detail the form that the mass and mixing matrices can take in this setup. The mass Lagrangian for the quarks in the interaction basis can be written as

$$\mathcal{L}_{\text{mass}} = \overline{u}_L \, \mathcal{M}_u \, u_R + \overline{d}_L \, \mathcal{M}_d \, d_R \,, + \text{h.c.} \,, \tag{5.2.4}$$

where the mass matrices $\mathcal{M}_q$ ($q = u, d$) contain the diagonal terms $\frac{v_h}{\sqrt{2}} y_q$ arising from Eq. (5.2.1) as well as off-diagonal entries stemming from BSM interactions (5.2.2). The mass matrices can be expressed as

$$\mathcal{M}_d = L_d \, \mathbb{M}_d \, R_d^\dagger \,, \qquad \mathcal{M}_u = L_u \mathbb{M}_u R_u^\dagger \tag{5.2.5}$$

in terms of the diagonal matrices $\mathbb{M}_q$ containing the quark masses. The quark-mixing matrix $V = L_u^\dagger L_d$ can be written as [159, 160]

$$V = \begin{pmatrix} 1 & s_{12} + s_{13}^u s_{23} & s_{13} - s_{12}^u s_{23} \\ -s_{12} - s_{13}^d s_{23} & 1 & s_{23} + s_{12}^u s_{13} \\ -s_{13} + s_{12}^d s_{23} & -s_{23} - s_{12}^d s_{23} & 1 \end{pmatrix} \,, \tag{5.2.6}$$

in terms of the angles s_{ij}^q parameterizing the left-handed rotations L_q, and with

$$s_{ij} = s_{ij}^d - s_{ij}^u \,. \tag{5.2.7}$$

In models where the $\mathcal{M}_q$ are completely known, the angles can be calculated directly in terms of their components. We now set to compute the form of V in two different scenarios, where mixing is driven mainly by either the up or the down sector.

5.2.1 Mixing from the Down Sector

We consider first the scenario where the η^{ij} carry charges $X_{q_i} - X_{q_j}$, leading to the Lagrangian $\mathcal{L}_{\text{mix}}^d$ in Eq. (5.2.2). In this case the mass matrices of the down and the up sector

after spontaneous symmetry breaking read

$$\mathcal{M}_d = \frac{v_h}{\sqrt{2}} \begin{pmatrix} y_d & y_{ds}\, t_{\beta_{12}} & 0 \\ 0 & y_s & y_{sb}\, t_{\beta_{23}} \\ 0 & 0 & y_b \end{pmatrix}, \quad \mathcal{M}_u = \frac{v_h}{\sqrt{2}} \begin{pmatrix} y_u & 0 & 0 \\ y_{cu}\, t_{\beta_{12}} & y_c & 0 \\ 0 & y_{tc}\, t_{\beta_{23}} & y_t \end{pmatrix}, \tag{5.2.8}$$

where $t_{\beta_{ij}} = \tan\beta_{ij} = v_{\eta^{ij}}/v$. Then, the mixing matrix $V = L_u^\dagger L_d$ of Eq. (5.2.6) receives its leading contributions from the angles [159, 160]

$$\begin{aligned} s_{12}^d &\simeq \frac{\mathcal{M}_{12}^d}{\mathcal{M}_{22}^d} \simeq t_{\beta_{12}} \sqrt{\frac{y_d}{y_s}}\,, \\ s_{23}^d &\simeq \frac{\mathcal{M}_{23}^d}{\mathcal{M}_{33}^d} \simeq t_{\beta_{23}} \sqrt{\frac{y_s}{y_b}}\,, \\ s_{12}^u &\simeq \frac{\mathcal{M}_{21}^u \mathcal{M}_{11}^u}{(\mathcal{M}_{22}^u)^2} \simeq t_{\beta_{12}} \left(\frac{y_u}{y_c}\right)^{3/2}, \end{aligned} \tag{5.2.9}$$

where we assumed large third-generation entries $\mathcal{M}_{33}^q$, and used the relation Eq. (5.2.3) the off-diagonal Yukawas. From Eq. (5.2.6) we observe that the contributions to V from s_{23}^u are subleading, and s_{12}^u only enters V_{ub}. Thus, the mixing arising from the matrices (5.2.8) stems mainly from rotations of the down sector, and we find that $V \sim L_d$. For $\tan\beta_{ij} \sim \mathcal{O}(1)$ or lower, the singular values of (5.2.8) correspond approximately to the y_i, so that we may take $y_i \simeq \sqrt{2} m_i/v_h$ at low scales. For $\tan\beta_{12} \sim 1$, we obtain the successful prediction $|V_{us}| \simeq 0.22$, while a lower value of $t_{\beta_{23}}$ is needed to accommodate V_{ts} and V_{cb}. Using $\tan_{\beta_{12}} \simeq 1.1$ and $\tan\beta_{23} \simeq 0.3$ we obtain

$$|V| = \begin{pmatrix} 0.974 & 0.225 & 1.8 \cdot 10^{-6} \\ 0.225 & 0.973 & 0.0422 \\ 0.00950 & 0.0411 & 0.999 \end{pmatrix}, \tag{5.2.10}$$

which is in agreement with measurements of the CKM mixing matrix at the percent level for first-second and second-third generation mixing [16], with larger deviations in V_{ub} and V_{td}. The discrepancies in first-third generation mixing could be accounted for by imaginary phases, which we do not include in this work but contribute significantly to V_{ub} and V_{td}.

5.2.2 Mixing from the Up Sector

Let us now consider the case where the η^{12} and η^{23} carry charges $X_{q_j} - X_{q_i}$, leading to the Lagrangian $\mathcal{L}_{\text{mix}}^u$ in Eq. (5.2.2). The quark mass matrices in this scenario obey

$$\mathcal{M}_d = \frac{v_h}{\sqrt{2}} \begin{pmatrix} y_d & 0 & 0 \\ y_{sd}\, t_{\beta_{12}} & y_s & 0 \\ 0 & y_{bs}\, t_{\beta_{23}} & y_b \end{pmatrix}, \quad \mathcal{M}_u = \frac{v_h}{\sqrt{2}} \begin{pmatrix} y_u & y_{uc}\, t_{\beta_{12}} & 0 \\ 0 & y_c & y_{ct}\, t_{\beta_{23}} \\ 0 & 0 & y_t \end{pmatrix}. \tag{5.2.11}$$

Assuming again large third-generation entries $\mathcal{M}^q_{33}$, and employing Eq. (5.2.3), the leading angles contributing to the quark mixing matrix (5.2.6) read [159, 160]

$$\begin{aligned} s^u_{12} &\simeq \frac{\mathcal{M}^u_{12}}{\mathcal{M}^u_{22}} = t_{\beta_{12}}\sqrt{\frac{y_u}{y_c}}\,, \\ s^u_{23} &\simeq \frac{\mathcal{M}^u_{23}}{\mathcal{M}^u_{33}} = t_{\beta_{23}}\sqrt{\frac{y_c}{y_t}}\,, \\ s^d_{12} &\simeq \frac{\mathcal{M}^d_{21}\mathcal{M}^d_{11}}{(\mathcal{M}^d_{22})^2} = t_{\beta_{12}}\left(\frac{y_d}{y_s}\right)^{3/2}\,. \end{aligned} \tag{5.2.12}$$

Hence, in this case the mixing is driven by the angles of the up sector, and we find $V \sim L_u^\dagger$. For a benchmark with $\tan\beta_{12} \simeq 6.1$ and $\tan\beta_{23} \simeq 0.5$, we obtain

$$|V| = \begin{pmatrix} 0.975 & 0.223 & 0.0101 \\ 0.223 & 0.974 & 0.0399 \\ 0.000974 & 0.0411 & 0.999 \end{pmatrix}\,, \tag{5.2.13}$$

giving again a CKM-like pattern with larger deviations in V_{ub} and V_{td}. Since mixing is given mainly by the rotations of $\mathcal{M}_u$, a very similar result is obtained in the case where $\mathcal{M}_d$ is purely diagonal, with $\mathcal{M}_u$ still fulfilling Eq. (5.2.11). This corresponds to a situation where the couplings of the η^{ij} with the down sector in $\mathcal{L}^u_{\text{mix}}$ exactly vanish. In this case, the mixing matrix is described by the angles of the up sector given by (5.2.12), and V_{ub} becomes strongly suppressed. Phenomenologically, the absence of rotations in the down sector entails that it acquires no flavor-changing couplings with the gauge boson of the new symmetry. As detailed in Sec. 5.5, this scenario is favored by meson mixing data, which poses strong constraints on flavor-changing couplings of the down sector.

To summarize the results of Sec. 5.2.1 and Sec. 5.2.2, we have seen how the charges of the η^{ij} under the new symmetry determine the shape of the quark mass matrices and ultimately the origin of the mixing matrix. The case where the new scalars carry charges $X_{q_i} - X_{q_j}$ leads to $V \sim L_d$, while flipping the sign of their $U(1)_X$ charges leads to $V \sim L_u^\dagger$. If all off-diagonal couplings in the down-quark mass matrix vanish one obtains $V \sim L_u^\dagger$ as well, and additionally suppresses FCNCs in the down sector. Note that, while the masses depend only on the $U(1)_X$ charges of the quarks and the SM pattern of electroweak symmetry breaking, the mixing is regulated by the vacuum expectation values of the new scalars through $\tan\beta_{ij}$.

5.2.3 Lepton Masses

We now turn to the mass pattern of the lepton sector in our setup. After electroweak symmetry breaking, the Yukawa interactions (5.2.1) yield diagonal mass terms $v_h y_{e_i}/\sqrt{2}$ for the charged leptons, while neutrinos acquire diagonal Dirac masses $v_h y_{\nu_i}/\sqrt{2}$. In the mechanism described in Sec. 5.1, the y_{e_i} and y_{ν_i} vanish at a UV fixed point and grow steeply towards the IR, thanks to non-vanishing values of the gauge couplings. Since both

the hypercharge and the $U(1)_X$ couplings enhance the running of the neutrino Yukawas, the y_{ν_i} might give rise to Dirac masses surpassing current bounds. Examples of values the y_{ν_i} can acquire through the running are discussed in the context of two different benchmarks in Sec. 5.4. For now, in order to ensure that a mechanism is in place to sufficiently suppress light neutrino masses, we introduce three generations of SM singlet Majoron fields σ_i with $U(1)_X$ charges $-2X_{\ell_i}$, which allow to write the terms

$$-\mathcal{L}_\sigma = \sum_i y_{\sigma i}\, \sigma_i\, \overline{N^C}_i N_i + \text{h.c.}\,. \tag{5.2.14}$$

After spontaneous symmetry breaking, we assume that the σ_i yield Majorana mass terms large enough to suppress the masses of the light neutrinos via the see-saw mechanism.

In order to describe neutrino mixing, one may consider introducing additional scalar doublets coupling to different-generation leptons, and using a mechanism similar to that described in Secs. 5.2.1 and 5.2.2 for the quark sector. Alternatively, mixing could also be introduced by adding further Majorons σ_{ij} with off-diagonal couplings. Since all fields involved in the y_σ couplings are only charged under $U(1)_X$, introducing a number of σ_{ij} would have no influence on the β-functions of the SM gauge couplings. A detailed study of models for neutrino masses and mixing and their scalar potential lies, however, beyond the scope of the present work. In what follows, we assume diagonal Yukawa couplings in the lepton sector, and postpone a modeling of neutrino mixing to future studies.

5.2.4 Asymptotically Safe Setup

Finally, let us discuss how UV fixed points with interacting $U(1)$ couplings can arise in our setup. If all Yukawas giving rise to fermion masses and mixings are assumed to be asymptotically free, there is no Yukawa interaction which can potentially give rise to such a fixed point.[3] Building on the developments of the previous sections, we introduce a flavor-blind BSM sector composed of N_F vector-like fermions ψ_i and N_F^2 singlet scalars S_{ij}, with Lagrangian following (2.2.1), and assume that the vector-like fermions are only charged under the $U(1)_X$ and $U(1)_Y$ symmetries. This assumption is minimal in the sense that both $U(1)$ charges are essential for α_1 and α_X to present an interacting value at the fixed point, which in turn is paramount if we wish to avoid triviality problems. Conversely, the $SU(2)_L$ and $SU(3)_C$ couplings can remain asymptotically free, and their trajectories from fixed points exhibiting $\alpha^*_{2,3} = 0$ can in principle be matched to the SM. Then, in our setup the BSM Yukawa interaction

$$-\mathcal{L}_y = y\text{Tr}[\overline{\psi}_L S \psi_R + \text{h.c.}]\,, \tag{5.2.15}$$

contributes to the β-functions of the $U(1)$ couplings, allowing to generate fixed points with non-vanishing coordinates $(\alpha_1^*, \alpha_X^*, \alpha_y^*)$. The $U(1)_X$ and $U(1)_Y$ charges X_F and Y_F of the

[3]Note that SM Yukawas are in general insufficient to give rise to a perturbative UV fixed point, as already discussed in Chapter 2. Therefore, a BSM sector is necessary independently of the values of the SM Yukawas at the fixed point.

		Generations	$SU(3)_C \times SU(2)_L \times U(1)_Y$	$U(1)_X$
ψ_i	Vector-like fermions	$i = 1, \ldots, N_F$	$(1, 1, Y_F)$	X_F
S_{ij}	Singlet scalars	$i, j = 1, \ldots, N_F$	$(1, 1, 0)$	0
N_i	Right-handed singlets	$i = 1, 2, 3$	$(1, 1, 0)$	X_L
η^{ij}	Quark-mixing scalars	$ij = 12, 23$	$(1, 2, 1/2)$	$X_{q_i} - X_{q_j}$
σ_i	Majorons	$i = 1, 2, 3$	$(1, 1, 0)$	$-2X_{\ell_i}$

Table 5.2. BSM particle content of the model and its gauge charges under the SM and the new symmetry. For the benchmark scenario of Sec. 5.4.1, only the three upper rows are considered, while the full particle content is included in the benchmark of Sec. 5.4.2.

vector-like fermions, as well as their flavor multiplicity N_F, remain free parameters of the model. This completes the description of our setup, for which the BSM particle content and its charges have been collected in Tab. 5.2. The full Yukawa sector of the theory is described by the Lagrangian

$$\mathcal{L}_{\rm Y} = \mathcal{L}_{y_f} + \mathcal{L}_{\rm mix} + \mathcal{L}_\sigma + \mathcal{L}_y, \tag{5.2.16}$$

where $\mathcal{L}_{\rm mix}$ can be either $\mathcal{L}^d_{\rm mix}$ or $\mathcal{L}^u_{\rm mix}$ in Eq. (5.2.2) depending on the BSM scalar doublet charges.

5.3 Fixed-Point Structure

Having set our model and introduced a mechanism to restore quark mixing, we now study the RGEs and their fixed point solutions, in particular those with non-vanishing coordinates $(\alpha_1^*, \alpha_X^*, \alpha_y^*)$. We perform our study in the `210` approximation, where the β-functions of gauge and Yukawa couplings are computed at 2- and 1-loop order, respectively, and the scalar sector is not included. We include the full set of gauge and Yukawa couplings for the $U(1)_X$ extension of the SM with the additional BSM particles of Tab. 5.2 and Yukawa Lagrangian (5.2.16). The corresponding `210` β-functions computed with `ARGES` [45] are collected in Appendix B.3. In the limit where all Yukawas other than the top and the purely BSM Yukawa α_y vanish, and taking as well $\alpha_2, \alpha_3 = 0$, the β-functions of the $U(1)$ gauge couplings read

$$\begin{aligned}
\beta_1 = \alpha_1^2 \Bigg[& \frac{43}{3} + \frac{8}{3} N_F Y_F^2 + \alpha_1 \left(\frac{217}{9} + 8 N_F Y_F^4 \right) + \alpha_X \left(f_1 + 8 N_F X_F^2 Y_F^2 \right) \\
& - 4 \alpha_y N_F^2 Y_F^2 - \frac{17}{3} \alpha_t \Bigg] , \\
\beta_X = \alpha_X^2 \Bigg[& f_2 + \frac{8}{3} N_F X_F^2 + \alpha_X \left(f_3 + 8 N_F X_F^4 \right) + \alpha_1 \left(f_1 + 8 N_F X_F^2 Y_F^2 \right) \\
& - 4 \alpha_y N_F^2 X_F^2 - 24 X_{q_3}^2 \alpha_t \Bigg] ,
\end{aligned} \tag{5.3.1}$$

while for the Yukawa couplings we find

$$\begin{aligned}\beta_y &= \alpha_y \left[\alpha_y(2N_F+2) - 12\alpha_1 Y_F^2 - 12\alpha_X X_F^2 \right] , \\ \beta_t &= \alpha_t \left[9\alpha_t - \frac{17}{6}\alpha_1 - 12\alpha_X X_{q_3}^2 \right] .\end{aligned} \tag{5.3.2}$$

The f_i are functions of the $U(1)_X$ charges which obey

$$\begin{aligned}f_1 &= \sum_k \left(\frac{22}{3} X_{q_k}^2 + 6 X_{\ell_k}^2 \right) + 4(X_{q_1} - X_{q_2})^2 + 4(X_{q_2} - X_{q_3})^2 , \\ f_2 &= \sum_k \left(16 X_{q_k}^2 + 8 X_{q_\ell}^2 \right) + \frac{4}{3}(X_{q_1} - X_{q_2})^2 + \frac{4}{3}(X_{q_2} - X_{q_3})^2 , \\ f_3 &= \sum_k \left(48 X_{q_k}^4 + 144 X_{\ell_k}^4 \right) + 16(X_{q_1} - X_{q_1})^4 + 16(X_{q_2} - X_{q_3})^4 .\end{aligned} \tag{5.3.3}$$

For $\alpha_y^* \neq 0$, we find that fixed point solutions of the system (5.3.1) exist as a function of the model parameters. These solutions become simple in the large-N_F limit, in which β_1 and β_X are equivalent after interchanging $Y_F \to X_F$. This limit also corresponds to the case where the $U(1)_X$ and $U(1)_Y$ charges of all fields except the vector-like fermions vanish. Then, an interacting fixed point of the system $\{\beta_1, \beta_X, \beta_y, \beta_t\}$ exists with coupling values

$$6\left(\alpha_X^* X_F^2 + \alpha_1^* Y_F^2\right) = 1 , \qquad \alpha_y^* = \frac{1}{N_F} , \qquad \alpha_t^* = 0 , \tag{5.3.4}$$

where the symmetry of β_1 and β_X allows to freely choose one of the fixed-point values of the gauge couplings. The fixed point can be perturbative and physical for $N_F \geq 1$ and appropriate choices of X_F, Y_F. Far from the large-N_F limit, the functions f_i and the numerical coefficients in β_1, which stem purely from the hypercharges, break the symmetry between β_1 and β_X as well as the degeneracy of the fixed point solution (5.3.4). For $\mathcal{O}(1)$ charges, especially f_3 can be significantly large. Including only the gauge 1-loop terms $f_3 \neq 0$ and $c = 217/9$ we find that the fixed point becomes

$$\begin{aligned}\alpha_1^* = \frac{8 N_F Y_F^2 f_3}{48(X_F^4 + Y_F^4) N_F - 3 c f_3} , \qquad \alpha_X^* = \frac{c}{f_3}\alpha_1^* , \\ \alpha_y^* = \frac{1}{N_F - c f_3 / \left[16\left(c X_F^4 + f_3 Y_F^4\right)\right]} ,\end{aligned} \tag{5.3.5}$$

which is physical for $N_F > c f_3/[16\left(X_F^4 + Y_F^4\right)]$. Including all terms in the β-functions we find that fixed points for the $(\alpha_1, \alpha_X, \alpha_y)$ system persist; expressions become however cumbersome and we do not reproduce them here.

Furthermore, demanding that fixed points can be matched to SM values at low scales requires that the $SU(2)_L$ and $SU(3)_C$ couplings, which we assume to vanish at the fixed point, can grow towards the IR. Their evolution close to the fixed point follows

$$\frac{d\alpha_i}{d\ln\mu} \simeq \frac{\alpha_i^2}{2} P_{iii} , \tag{5.3.6}$$

see Sec. 2.1.2 for details. Imposing that α_2 and α_3 correspond to UV-attractive directions and can grow from the fixed point sets constraints

$$P_{222} = -\frac{17}{3} + 5\alpha_1^* + \alpha_X^* \left[\sum_k \left(6X_{q_k}^2 + 2X_{\ell_k}^2\right) + 4(X_{q_1} - X_{q_2})^2 + 4(X_{q_2} - X_{q_3})^2 \right] < 0\,,$$
$$P_{333} = -14 + \frac{11}{3}\alpha_1^* + 8\alpha_X^* \sum_k X_{q_k}^2 < 0\,, \tag{5.3.7}$$

where the P_{iii} are computed from the β-functions in Appendix B.3.[4] Thus, the bounds (5.3.7) constrain the fixed point values of α_1 and α_X in terms of the $U(1)_X$ charges of the model. In summary, we have found that fixed points with non-vanishing coordinates $(\alpha_1^*, \alpha_X^*, \alpha_y^*)$ exist in our model, and that requiring asymptotic freedom in the weak and strong sectors poses constraints on the model parameters.

5.4 Benchmarks

In this section, we study two particular setups of our model: we consider first a simple scenario, referred to as *scenario A*, where only the lepton sector is charged under the new symmetry, putting aside the quark sector and the $U(1)_X$-charged BSM scalars. We then examine the case where the SM is extended with the full particle content in Tab. 5.2, including both the lepton and quark sectors (*scenario B*). For each case, we study a particular benchmark where we fix the parameters N_F, X_F, Y_F of the vector-like fermions and the $U(1)_X$ charges X_{ℓ_i} and X_{q_i}, with the latter being nonzero only in the scenario B. In order to choose the benchmark values of N_F and the BSM charges, we enforce the following conditions:

i) The X_{q_i} and X_{ℓ_i} must fulfill the anomaly-cancellation conditions (5.1.3). Moreover, they must allow α_2 and α_3 to remain UV-attractive directions by fulfilling Eq. (5.3.7).

ii) The fixed point must be physical and perturbative, with $0 < \alpha_1^*, \alpha_X^*, \alpha_y^* < 1$. This specially affects N_F, which cannot be arbitrarily low, as illustrated in Sec. 5.3.

iii) After the power-law phase of the running, diagonal Yukawa couplings must approximately take their SM values at order of magnitude. Using Eqs. (5.1.8)-(5.1.10), this condition affects the X_{q_i} and X_{ℓ_i} charges together with the fixed point values α_1^* and α_X^* . Once the quark and lepton $U(1)_X$ charges are fixed, Y_F, X_F and N_F determine the values of α_1^* and α_X^*.

The parameters we have selected for the benchmarks of both scenarios are summarized in Tab. 5.3. We have chosen $U(1)_X$ charges of quarks and leptons to be of $\mathcal{O}(1)$, ensuring that they fulfill the condition (5.1.3). As seen from the β-functions of the $U(1)$ couplings

[4] Note that the 1-loop coefficient of β_2 and its 2-loop coefficient associated to α_1 differ from the SM due to the two additional $SU(2)$ doublets η^{ij}.

Scenario	N_F	Y_F	X_F	X_{ℓ_i}	X_{q_i}
A (lepton-only)	7	0.907	2.05	$1/2,\ 5/2, -3$	-
B (quarks and leptons)	7	7.1	0.826	$1/2,\ 5/2, -3$	$6/5,\ 31/10, -43/10$

Table 5.3. Benchmark parameters of scenarios A and B, see text for details.

in (5.3.1), this leads to large coefficients f_i in β_X (see Eq. (5.3.3)), and demands a sizable vector-like fermion multiplicity N_F to keep α_y^* perturbative; in our benchmarks we set $N_F = 7$. The $U(1)$ charges X_F, Y_F of the vector-like fermions are then chosen to find fixed point coordinates that lead to trajectories approximating the SM values of the Yukawa couplings towards the IR. A more comprehensive scan over the parameter space is the subject of ongoing and future works.

For the RGE analysis we employ the `210` β-functions assembled in Appendix B.3. In numerical solutions of trajectories one must also fix the $\alpha_{n,0}$, the initial conditions for asymptotically free Yukawa couplings close to the fixed point (see Eq. (5.1.5)). Here we take the same values of $\alpha_{n,0}$ for all Yukawa couplings, although these could in principle be a random set of numbers of the same order of magnitude, introducing minor differences in the final result. Furthermore, we do not attempt to perform an accurate matching between the SM and BSM running: this would demand knowledge of all $U(1)_X$ breaking scales and masses of the BSM sector, which we choose not to fix but assume to lie somewhere between μ_c and the scale of EWSB. We find that, even without imposing matching conditions, a study of the running over a wide range of RG scales is sufficient to identify the features of the framework.

5.4.1 Scenario A: Lepton-only

We consider first the simple scenario where only leptons carry $U(1)_X$ charges, and no additional scalars charged under the new symmetry are present. Note that a feature of anomaly cancellation through the condition $\sum X_{f_i} = 0$ together with the vector-like charge assignment (5.1.2) is that the lepton and quark $U(1)_X$ charges are decoupled in the anomaly cancellation equations (5.1.1). Therefore, we may set all X_{q_i} to zero and focus on how the lepton sector can acquire the desired mass hierarchies through the RGE mechanism described in Sec. 5.1.

In the absence of $U(1)_X$-charged scalars, neutrinos acquire only diagonal Dirac masses $m_{\nu_i} = v_h y_{\nu_i}/\sqrt{2}$. Then, measurements indicate that neutrino Yukawas must fulfill $\alpha_{\nu_i} \lesssim 10^{-26}$ around the electroweak scale [37]. If the largest neutrino mass saturates this bound, from the relation (5.1.9) between the charged- and neutral-lepton sector Yukawas one finds

$$\tau\alpha_1^* \simeq \frac{1}{6}\log\frac{\alpha_\tau}{\alpha_{\nu_\tau}}\bigg|_{\mu_c} \simeq 3.3\,. \tag{5.4.1}$$

The above value of $\tau\alpha_1^*$ can be accommodated with τ of order one and α_1^* close to its perturbative limit. Therefore, Eq. (5.4.1) implies that the hierarchy between the charged-

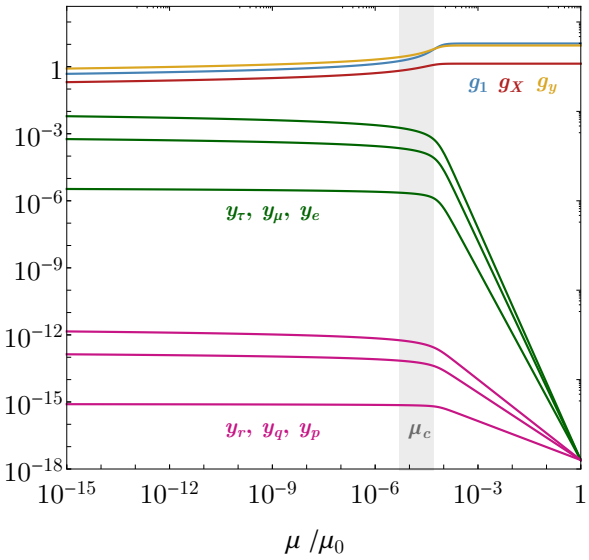

Figure 5.1. RG flow emanating from the fixed point (5.4.2) of the scenario A (lepton-only), with benchmark parameters given in Tab. 5.3, with $p, q, r = \nu_e, \nu_\mu, \nu_\tau$. The gray band indicates the end of the power-like behavior at $\mu_c \sim 10^{-5}$. A large hierarchy between the Yukawa couplings of the charged- and neutral-lepton sector (shown in green and magenta, respectively) arises through differences in SM hypercharges, see Eq. (5.4.1). Values of the charged lepton Yukawas in the IR approximately reproduce observed masses.

and neutral-lepton sectors can actually arise from the different $U(1)_Y$ charges of the right-handed lepton fields. We find that, for the benchmark parameters collected in Tab. 5.3 (scenario A), the condition (5.4.1) is fulfilled, and lepton masses are approximately reproduced. The gauge-Yukawa fixed point is in this case given by the coordinates

$$(\alpha_1^*, \alpha_X^*, \alpha_y^*) = (0.75,\, 0.012,\, 0.50)\,. \tag{5.4.2}$$

Then, for $\tau \sim 5$ one finds $\tau\alpha_1^* \sim 3.4$, which nears the requirement Eq. (5.4.1). A numerical solution of the RG flow is shown in Fig. 5.1. Note that after μ_c the running slows down, abandoning the power-law regime and introducing small changes in the values of the couplings. Indeed, below μ_c charged leptons present Yukawa couplings of the correct order of magnitude ($0.1 < y/y_{\rm SM} < 10$), while the largest neutrino mass is ~ 0.3 eV, a pattern which is not altered as the flow evolves towards the IR. The predicted neutrino mass scheme is compatible in order of magnitude with normal ordering estimates [37]. Therefore, we have shown that differences in hypercharge alone can lead to large hierarchies between lepton sectors, while a non-universal $U(1)_X$ charge assignment is able to approximately reproduce the values of the lepton Yukawas.

5.4.2 Scenario B: Quarks and Leptons

We now consider the both the quark and lepton sectors together with the BSM particle content gathered in Tab. 5.2. This includes the presence of two BSM scalars η^{12} and η^{23}

allowing for quark mixing, which we now assume to take charges $X_{q_i} - X_{q_j}$. In order to generate the appropriate hierarchies in the lepton sector, one may start by assuming that neutrino masses are Dirac, and that the condition (5.4.1) ensures that the lepton sector acquires its correct masses. However, the result (5.1.9) implies that quark Yukawas obey $\log \alpha_{u_i}/\alpha_{d_i} \sim 6.6$, which is too large even for the third-generation ratio. Thus, we abandon any attempts to fulfill (5.4.1) when dealing with the full SM. On the other hand, if $\tau\alpha_1^*$ is smaller than in (5.4.1) the Yukawas of charged and neutral leptons will turn out parametrically closer than in the lepton-only benchmark. This entails that, if the running reproduces charged lepton masses, neutrino masses will become too large. This can however be remedied by the Majoron terms (5.2.14), which allow for large Majorana masses which can potentially suppress light neutrino masses via the see-saw mechanism. Here we assume that the Majoron VEVs v_{σ_i} are sizable enough to generate the appropriate neutrino mass spectrum. The only gauge coupling entering the β-functions of the Majoron couplings $y_{\sigma i}$ is α_X, which leads to the relation

$$\log \frac{\alpha_{\sigma_i}}{\alpha_{\sigma_j}}\bigg|_{\mu_c} \sim 12\tau\alpha_X^* \left[X_{\ell_i}^2 - X_{\ell_j}^2\right]. \tag{5.4.3}$$

between couplings of different generations.

Moreover, equations (5.1.8) – (5.1.10) allow to obtain a bound on the quark $U(1)_X$ charges. From imposing that the charged leptons have a mass approximately equal or less than the down quarks of the same generation one obtains

$$(X_{q_i})^2 \gtrsim (X_{\ell_i})^2 + \frac{5}{9}\frac{\alpha_1^*}{\alpha_X^*} - \frac{4}{3}\frac{\alpha_3^*}{\alpha_X^*}. \tag{5.4.4}$$

Since the up sector carries larger hypercharges than the down sector, the above bound also ensures that up-quark Yukawas will turn out larger than those of charged leptons. It is noteworthy that, in a fixed point where $\alpha_3^* = 0$, the $U(1)_X$ charges of the quarks must always be larger in absolute value than those of the leptons of the same generation.

For a quantitative study of this scenario, we choose benchmark parameters displayed in Tab. 5.3 (scenario B), which give rise to the UV fixed point

$$(\alpha_1^*, \alpha_X^*, \alpha_y^*) = (0.064,\, 0.010,\, 0.41). \tag{5.4.5}$$

A numerical solution of trajectories emanating from the above fixed point is depicted in Fig. 5.2 for the diagonal quark and charged-lepton Yukawas (left) and the off-diagonal quark Yukawas (right), together with the evolution of the $U(1)$ gauge couplings and the BSM Yukawa y. We find that the diagonal couplings are all reproduced at order-of-magnitude level at $\mu \sim 10^{-15}$, while the off-diagonal components follow Eq. (5.2.3) up to order one factors.

Lastly, one may wonder whether the presented benchmarks can be matched to the SM. After the 15 orders of magnitude in RG time shown in Fig. 5.2, one finds $g_1 \sim 0.5$, which is

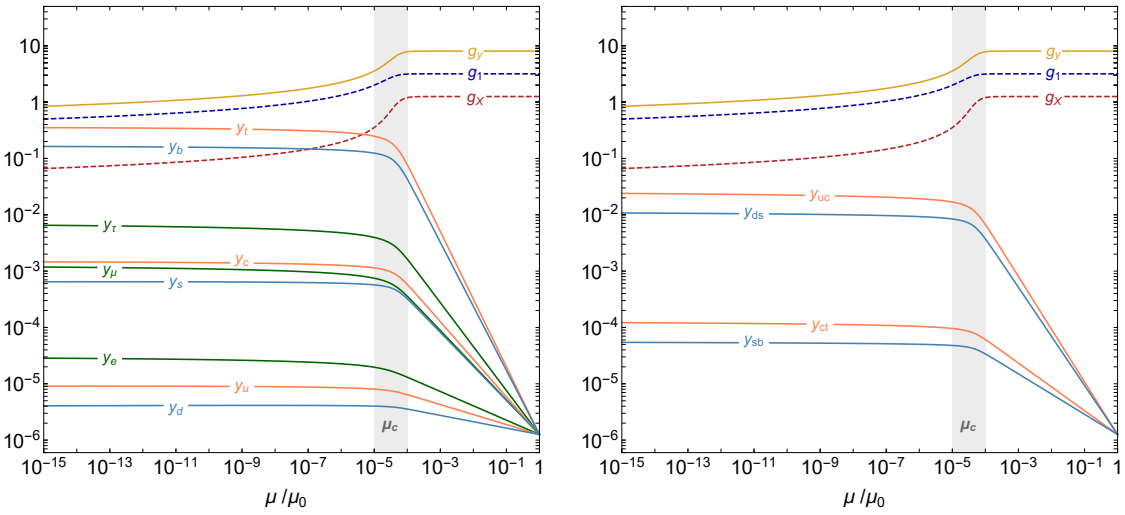

Figure 5.2. RG flow emanating from the fixed point (5.4.5) of the scenario B (quarks and leptons), with benchmark parameters collected in Tab. 5.3. Trajectories are shown for diagonal charged-lepton and quark Yukawas (left) and off-diagonal quark Yukawa couplings (right), together with the running of $U(1)$ gauge couplings and the BSM Yukawa y. The gray band indicates the end of the power-like behavior at $\mu_c \sim 5 \cdot 10^{-5}$. Towards the IR end of the flow, diagonal couplings approximately reproduce SM masses, while off-diagonal Yukawas follow (5.2.3) up to order one factors.

larger but comparable to $g_1^{\rm SM}(1\,\text{TeV}) \simeq 0.36$ (see for instance Eq. (3.2.6)), and well within the range of values g_1 takes through its SM running below the Planck scale. Therefore, we conclude that matching this scenario with the SM could be possible. The $U(1)_X$ coupling is predicted to be smaller, with $g_X \sim 0.07$ at the IR end of our numerical solution.

5.5 Phenomenological Analysis

So far we have shown how the model considered in this chapter presents the correct ingredients to reproduce the flavor patterns of the SM, and we now wish to explore its phenomenological implications. In our framework, additional $U(1)_X$-charged scalar content restores quark mixing and provides neutrino Majorana masses after undergoing spontaneous symmetry breaking. Therefore, the gauge boson of the new interaction becomes massive and mixes with the SM Z boson. The new mass eigenstate Z' presents diagonal couplings with the leptons and tree-level off-diagonal interactions with the quark sector, giving rise to flavor-changing neutral currents (FCNCs). The BSM scalars mediate FCNCs as well, since they couple directly to quarks of different generations. In what follows we consider phenomenological constraints on the model parameters stemming from the ρ-parameter, Z' searches and different flavor-changing processes.

5.5.1 Mass Spectrum and the ρ-parameter

We begin by studying the mass spectrum of the massive neutral bosons in our setup. After spontaneous symmetry breaking the gauge interactions of the Higgs and the BSM scalars lead to a mass matrix

$$\mathcal{M}_{ZX} = \frac{1}{4}\begin{pmatrix} \frac{g_2^2}{c_w^2} v_\phi^2 & -2\frac{g_2}{c_w} g_X v_\phi'^2 \\ -2\frac{g_2}{c_w} g_X v_\phi'^2 & 4 g_X^2 v_\phi''^2 \end{pmatrix} \tag{5.5.1}$$

in the (Z_μ, X_μ) basis, where $Z_\mu = c_w W_\mu^3 - s_w B_\mu$ and X_μ is the gauge boson of the new symmetry in the interaction basis, and we have neglected contributions from kinetic mixing. The third neutral boson $A_\mu = c_w B_\mu + s_w W_\mu^3$, corresponding to the photon, remains massless. The reduced VEVs in (5.5.1) obey

$$\begin{aligned} v_\phi^2 = v_h^2 + \sum_{ij} v_{\eta^{ij}}^2 \,, \qquad v_\phi'^2 = \sum_{ij} (X_Q^i - X_Q^j) v_{\eta^{ij}}^2 \,, \\ v_\phi''^2 = \sum_{ij} (X_Q^i - X_Q^j)^2 v_{\eta^{ij}}^2 + \sum_i (2X_L^i)^2 v_{\sigma_i}^2 \,. \end{aligned} \tag{5.5.2}$$

where $v_{\eta^{ij}}$ and v_{σ_i} are the VEVs of the scalar doublets and Majorons of Tab. 5.2, respectively. The mass matrix $\mathcal{M}_{ZX}$ can be diagonalized with an orthogonal matrix obeying $O^T \mathcal{M}_{ZX} O = \mathrm{diag}(m_Z, m_{Z'})$, with m_Z and $m_{Z'}$ the masses of the physical bosons. The matrix O can be parametrized as

$$O = \begin{pmatrix} \cos\theta & -\sin\theta \\ \sin\theta & \cos\theta \end{pmatrix} \,, \tag{5.5.3}$$

where the mixing angle θ fulfills

$$\sin 2\theta (m_{Z'}^2 - m_Z^2) = \frac{g_2}{c_w} g_X v_\phi'^2 \,. \tag{5.5.4}$$

The masses of the gauge bosons then obey

$$\begin{aligned} m_Z^2 = \frac{1}{4}\frac{g_2^2}{c_w^2} v_\phi^2 (1 - \delta\rho) \,, \qquad m_{Z'}^2 = g_X^2 v_\phi''^2 \left[1 + \left(\frac{g_2}{2 g_X c_w}\right)^2 \frac{v_\phi^2}{v_\phi''^2}\,\delta\rho\right] \,, \\ \delta\rho = \frac{v_\phi'^4 / v_\phi^4}{v_\phi''^2 / v_\phi^2 - (g_2 / 2 c_w\, g_X)^2} \,, \end{aligned} \tag{5.5.5}$$

see Appendix A.2 for details. The mass of the W boson is only altered with respect to its SM tree-level expression by the VEVs of the $SU(2)_L$-charged fields, and reads $m_W^2 = \frac{1}{4} g_2^2 v_\phi^2$. Then, using (5.5.5), we find that the masses of the W and Z boson in our model read

$$\frac{m_W^2}{c_w^2} = \rho m_Z^2 = (1 + \delta\rho) m_Z^2 \,. \tag{5.5.6}$$

Therefore, the ρ-parameter deviates from its SM tree level relation (1.1.25) by $\delta\rho$. In the absence of fine-tuned cancellations, ensuring that $\delta\rho \ll 1$ can be achieved either with large

$v_\phi''^2$ or small g_X. For large $v_\phi''^2$ the shift in the ρ-parameter scales as

$$\delta\rho \sim \frac{v_\phi^2}{v_\phi''^2}\,, \tag{5.5.7}$$

in the approximation $v_\phi'/v_\phi \sim \mathcal{O}(1)$. Note that this contribution is positive, as is favored by measurements [16]. Assuming that the Majoron VEVs constitute the leading contribution to v_ϕ'', the data (1.1.26) yields the constraint

$$v_\phi'' \sim v_{\sigma_i} \gtrsim 42 \text{ TeV} \left(\frac{[\text{TeV}]}{v_\phi}\right), \tag{5.5.8}$$

at 1σ. According to Eq. (5.5.5), for small $\delta\rho$ and large v_ϕ'' one can approximate $m_{Z'} \sim g_X v_\phi''$ [5]. If the bound (5.5.8) is saturated, Z' masses can be at the TeV scale as soon as g_X is of order 10^{-1} or smaller.

5.5.2 Z' Searches

Production of the Z' boson at colliders allows to perform direct searches. Measurements at e^+e^- colliders constrain its coupling to electrons to fulfill [161, 162]

$$\frac{m_{Z'}}{g_X|X_{\ell_1}|} \gtrsim 6.9 \text{ TeV}\,. \tag{5.5.9}$$

The above is valid for $m_{Z'} \lesssim 209$ GeV, which requires $g_X|X_{\ell_1}| \lesssim 0.03$. The bound does not constrain our benchmark of Sec. (5.4.2), but becomes relevant for smaller g_X. Moreover, Z' interactions with quarks allow its production at pp colliders as well, with cross section [37, 163]

$$\sigma(pp \to Z'X \to f\bar{f}X) \simeq \frac{\pi}{48s}\sum_i c_{q_i}^f\, w_{q_i}(s, m_{Z'})\,, \tag{5.5.10}$$

where the sum is over all quarks and $f\overline{f}$ is the difermion decay product of the Z'. The coefficients w_{q_i} include all information of parton distribution functions and QCD corrections, while the dependence on the Z' couplings is completely encoded in the coefficients $c_{q_i}^f$. The w_u and w_d functions are substantially more sizable than the rest of w_{q_i}. In the absence of kinetic mixing and neglecting mass mixing with the Z boson, we find that in our class of models the coefficients $c_{q_i}^{\ell_j}$ for two charged leptons in the final state obey

$$c_{q_i}^{\ell_j} \simeq 2g_X^2\, X_{q_i}^2\, \text{Br}(Z' \to \ell_j\bar{\ell_j}) \simeq g_X^2\, \frac{X_{q_i}^2 X_{\ell_j}^2}{\sum_k \left[3X_{q_k}^2 + X_{\ell_k}^2\right]}\,, \tag{5.5.11}$$

where the sum runs over all fermion final states, and we have assumed that no scalar final states are kinematically allowed. For the benchmark considered in Sec. 5.4.2, we find $c_{u,d}^e \simeq 1.8 \cdot 10^{-5}$ and $c_{u,d}^\mu \simeq 4,4 \cdot 10^{-5}$. Small values of the $c_{q_i}^{\ell_j}$ in our setup stem from leptons carrying lower $U(1)_X$ charges than quarks, according to the constraint (5.4.4), which in turn leads to suppressed branching ratios to leptons. The CMS [164, 165] and

[5] This approximation may not hold if g_X is very feeble, but is valid for the benchmark scenarios considered in Sec. 5.4, which predict $g_X \sim 10^{-1} - 10^{-2}$.

ATLAS [166] collaborations have set bounds on the cross section (5.5.10) for specific Z' models. For our benchmark values of $c^{\ell}_{u,d}$ we estimate $m_{Z'} \gtrsim 2.5$ TeV. A precise recasting of experimental limits is however beyond the scope of this work.

5.5.3 Flavor-changing Processes

Due to the non-universality in the $U(1)_X$ charges of the SM fermions, unitary rotations to the mass basis do not cancel in the kinetic terms involving the new gauge boson. The Z' interactions with the quarks in the mass basis are then described by the Lagrangian

$$-\mathcal{L}_{qZ'} = g_X\ \bar{q}_i \gamma^\mu (B^{q_L}_{ij} P_L + B^{q_R}_{ij} P_R)\, q_j\, Z'_\mu\,, \tag{5.5.12}$$

where the coefficients obey

$$B^{q_L}_{ij} = (L^\dagger_q \mathbb{X}_Q L_q)_{ij}\,, \qquad B^{q_R}_{ij} = (R^\dagger_q \mathbb{X}_Q R_q)_{ij}\,, \tag{5.5.13}$$

with $\mathbb{X}_Q = \mathrm{diag}\{X_{q_i}\}$ and L_q, R_q the matrices diagonalizing the quark masses. From (5.5.13) one can directly see that Z'-mediated FCNCs arise at tree-level thanks to the off-diagonal elements of the B_{ij} matrices. In what follows, we study the Z' contributions to the mixing and decays of neutral mesons, and then consider FCNC constraints on the scalar sector. Since in this chapter we do not attempt to describe lepton mixing, lepton flavor violating observables are not discussed.

Meson Mixing

Z' contributions to the mixing of neutral mesons pose strong constraints on the model parameters. In the limit of small $Z - Z'$ mixing, the Z' exchange contribution to the mass splitting of a meson $P^0 = \bar{q}_j q_i$ reads [167]

$$\Delta m_P = m_P f_P^2 B_P \frac{g_X^2}{m_{Z'}^2} \frac{1}{3} \left[\mathrm{Re}\left[(B^{q_L}_{ij})^2 + (B^{q_R}_{ij})^2 \right] - \left(\frac{3}{2} + \frac{m_P^2}{(m_{q_i} + m_{q_j})^2} \right) \mathrm{Re}\left[B^{q_L}_{ij} B^{q_R}_{ij} \right] \right], \tag{5.5.14}$$

where m_P is the meson mass and f_P its decay constant, and the bag parameters B_P encode deviations from naive factorization, see for instance [168, 169]. From Eq. (5.5.14) and current meson mixing data and predictions we estimate [16, 170–173]

$$\begin{aligned} \frac{g_X}{m_{Z'}} |B^{d_{R,L}}_{12}| &\lesssim 5.7 \cdot 10^{-5}\ \mathrm{TeV}^{-1}\,, & \frac{g_X}{m_{Z'}} |B^{d_{R,L}}_{13}| &\lesssim 6.9 \cdot 10^{-4}\ \mathrm{TeV}^{-1}\,, \\ \frac{g_X}{m_{Z'}} |B^{d_{R,L}}_{23}| &\lesssim 3.4 \cdot 10^{-3}\ \mathrm{TeV}^{-1}\,, & \frac{g_X}{m_{Z'}} |B^{u_{R,L}}_{12}| &\lesssim 7.5 \cdot 10^{-4}\ \mathrm{TeV}^{-1}\,. \end{aligned} \tag{5.5.15}$$

where we have considered one non-vanishing coefficient $B^{q_L}_{ij}, B^{q_R}_{ij}$ at a time.[6] The various mixing scenarios considered in Sec. 5.2 yield different results for the B_{ij} coefficients. In the case where mixing is driven by the down sector (with $V \sim L_d$), we find that the off-diagonal elements of the B^{d_L} matrices fulfill $B^{d_L}_{ij} \simeq |V_{ij}(X_{q_i} - X_{q_j})|$, while the $|B^{d_R}_{ij}|$ are

[6] For Kaon mixing, data points to a negative new physics contribution to Δm_K [173], which requires $\mathcal{CP}$ violating couplings not considered here. The bound in (5.5.15) considers the SM prediction at 2σ, which allows for positive new physics contributions.

parametrically smaller. Then, for the quark $U(1)_X$ charges and the low-scale value of g_X of the benchmark of Sec. 5.4.2, we find that the bound from the Kaon system poses the strong constraint $m_{Z'} \gtrsim \mathcal{O}(500)$ TeV. Similar results are obtained for the scenario where $V \sim L_u^\dagger$, with $B_{ij}^{d_R}$ being the larger coefficients. Instead, in the scenario where the down-type mass matrix is diagonal, rotations are absent in the down sector, and one obtains $B_{ij}^{u_L} \simeq |V_{ij}(X_{q_i} - X_{q_j})|$. Then, charm mixing data poses the strongest bound, which yields

$$m_{Z'} \gtrsim 3 \cdot \left(\frac{g_X}{10^{-2}}\right) \left(\frac{|B_{12}^{u_L}|}{0.22}\right) \text{ TeV}\,, \tag{5.5.16}$$

allowing for lower Z' masses, within the reach of present colliders.

Neutral Meson Decays

The flavor-changing Z' current contributes at 1-loop level to radiative decays of neutral mesons, and at tree level to leptonic and semileptonic decays. Here we follow [167] to obtain bounds on the Z' couplings from experimental data. In the case of radiative decays, for $b \to s\gamma$ one finds

$$\frac{\Gamma(B \to X_s\gamma)}{\Gamma(B \to X_c e\overline{\nu}_e)} = \frac{8\alpha_e}{3\pi} f^{-1}(m_c^2/m_b^2) \frac{g_X^4}{|V_{cb}|^2} \frac{m_W^4}{m_{Z'}^4 m_b^2} \left[|(B^{d_L}\mathbb{M}_d B^{d_R})_{23}|^2 + |(B^{d_R}\mathbb{M}_d B^{d_L})_{23}|^2\right], \tag{5.5.17}$$

with $f(x) = 1 - 8x + 8x^3 - x^4 - 12x^2 \ln x$. The experimental fit of the branching ratio $\mathcal{B}(B \to X_s\gamma) = (3.32 \pm 0.15) \cdot 10^{-4}$ [168] gives constraints on the BSM couplings and $m_{Z'}$ much weaker than meson mixing bounds in Eq. (5.5.15). In the case of leptonic decays of the type $P^0 \to \ell^+\ell^-$, the Z' contribution vanishes in the limit of no lepton mixing, since the Z' interaction with the leptons is purely vectorial. Finally, vectorial couplings can be constrained in the decays of P^0 to another pseudoscalar meson and a lepton pair. Here we shall not consider the $\mathcal{CP}$-violating decay $K_L^0 \to \ell^+\ell^-$, which is proportional to the imaginary parts of the Z' couplings. For the semileptonic decays of B^0 and D^0 we find [167]

$$\begin{aligned}
\Gamma(D^0 \to \ell^+\ell^-\pi^0) &= \Gamma(D^+ \to \ell^+\nu_\ell\pi^0) \frac{4(X_L^\ell)^2}{|V_{cb}|^2} g_X^4 \frac{m_W^4}{m_{Z'}^4} |B_{12}^{u_L} + B_{12}^{u_R}|^2\,, \\
\Gamma(B^0 \to \ell^+\ell^-K^0) &= \Gamma(B^+ \to \ell^+\nu_\ell\overline{D}^0) \frac{f(m_K^2/m_B^2)}{f(m_D^2/m_B^2)} \frac{4(X_L^\ell)^2}{|V_{cb}|^2} g_X^4 \frac{m_W^4}{m_{Z'}^4} |B_{23}^{d_L} + B_{23}^{d_R}|^2\,.
\end{aligned} \tag{5.5.18}$$

In the case of the $D^0 \to \ell^+\ell^-\pi^0$, the resulting bounds are again softer than (5.5.15). Furthermore, the B^0 decay in (5.5.18) is part of the $b \to s\,\ell^+\ell^-$ observables which have been seen to show discrepancies with the SM. Models with a heavy Z' have been put forward as a solution for the B anomalies, see for instance [174–178]. In the conventions of [175], new physics contributions to the relevant weak Hamiltonian coefficients in our models give

$$\begin{aligned}
\delta C_9^{bs\mu\mu} &= -\delta C_{10}^{bs\mu\mu} = -\frac{\pi}{\alpha_e} \frac{v_h^2}{V_{ts}^* V_{tb}} \frac{g_X^2 X_\mu B_{23}^{d_L}}{m_{Z'}^2}\,, \\
\delta C_{9'}^{bs\mu\mu} &= \delta C_{10'}^{bs\mu\mu} = -\frac{\pi}{\alpha_e} \frac{v_h^2}{V_{ts}^* V_{tb}} \frac{g_X^2 X_\mu B_{23}^{d_R}}{m_{Z'}^2}\,.
\end{aligned} \tag{5.5.19}$$

Accommodating $b \to s\,\ell^+\ell^-$ data at 2σ with a $V-A$ structure requires [179]

$$\delta C_9^{bs\mu\mu} = -\delta C_{10}^{bs\mu\mu} \in [-0.69, -0.37] \;\Rightarrow\; \frac{g_X^2 X_\mu B_{23}^{d_L}}{m_{Z'}^2[\mathrm{TeV}^{-2}]} \in [0.59, 1.1]\cdot 10^{-3}, \tag{5.5.20}$$

Assuming that the B_s mixing bound in (5.5.15) is saturated, one obtains $g_X X_\mu / m_{Z'}[\mathrm{TeV}] \in [0.17, 0.32]$. As long as $g_X X_\mu \lesssim \mathcal{O}(0.1)$, as is the case for our benchmark model shown in Fig. 5.2, this demands below-TeV Z' masses, in tension with constraints from direct searches. Benchmarks featuring higher $g_X X_\mu$ values may however allow to accommodate (5.5.20) while fulfilling B_s mixing bounds.

Scalar-mediated FCNCs

Scalar-mediated FCNCs arise as a result of quarks receiving their masses from different $SU(2)_L$ doublets [41, 42]. In the limit where both $U(1)_X$-charged scalars acquire the same VEV v_η, the Yukawa couplings of the quark mass eigenstates can be expressed as

$$\begin{aligned} -\mathcal{L}_{q\phi} = \overline{d}_L \left[\left(\frac{\sqrt{2}}{v_h} \mathbb{M}_d - \epsilon^d \tan\beta \right) H + \epsilon'^d \eta^{12} + \epsilon''^d \eta^{23} \right] d_R \\ + \overline{u}_L \left[\left(\frac{\sqrt{2}}{v_h} \mathbb{M}_u - \epsilon^u \tan\beta \right) H + \epsilon'^u \tilde{\eta}^{12} + \epsilon''^u \tilde{\eta}^{23} \right] u_R + \text{h.c.}\,, \end{aligned} \tag{5.5.21}$$

where flavor-changing processes are governed by the non-holomorphic couplings

$$\begin{aligned} \epsilon^d_{ij} &= (\epsilon'^d + \epsilon''^d)_{ij} = (y_{ds}\,\delta_{i1}\delta_{j2} + y_{sb}\,\delta_{i2}\delta_{j3})(L_d^\dagger)_{ik}(R_d)_{kj}\,, \\ \epsilon^u_{ij} &= (\epsilon'^u + \epsilon''^u)_{ij} = (y_{cu}\,\delta_{i2}\delta_{j1} + y_{tc}\,\delta_{i3}\delta_{j2})(L_u^\dagger)_{ik}(R_u)_{kj}\,. \end{aligned} \tag{5.5.22}$$

A plethora of observables constrain the $\epsilon^{u,d}_{ij}$ together with the scalar masses and $\tan\beta$ [180, 181]. Again, one of the most stringent set of constraints stems from meson mixing. In the Kaon system, $K-\bar{K}$ mixing data sets

$$-1.0\cdot 10^{-10} \leq \mathrm{Re}[\epsilon^d_{12}\epsilon^{d*}_{21}] \left(\frac{\tan\beta}{m_\eta/100\ \mathrm{GeV}} \right)^2 \leq 3.0\cdot 10^{-11}\,, \tag{5.5.23}$$

with weaker bounds from other systems. In our setup, where the ϵ_{ij} arise from the mass matrices of the quarks, the ϵ^d_{ij} and ϵ^u_{ji} with $i<j$ are naturally suppressed (for instance, with $\tan\beta \simeq 1.2$ we find $\mathrm{Re}[\epsilon^d_{12}\epsilon^{d*}_{21}] \simeq 3.7\cdot 10^{-11}$), and meson mixing constraints are generally fulfilled for $m_\eta \gtrsim 130$ GeV.

5.6 Summary

In this chapter we have explored how SM masses and quark mixing can arise from renormalization group effects. The mechanism relies on a new $U(1)_X$ gauge symmetry, under which quarks and leptons must be non-universally charged. The presence of a UV fixed point where the hypercharge and the coupling of the new symmetry are interacting then enables SM Yukawas, assumed asymptotically free, to grow with a power-law scaling and evolve towards significantly diverse values towards the IR. The hierarchy between two Yukawa

couplings of the same sector after the power-law phase of the running depends mainly on the non-universal charges and the value of the new gauge coupling at the fixed point, as shown in Eq. (5.1.8).

In order to model quark mixing, we introduced additional scalar doublets carrying charges under the new symmetry. Their Yukawa couplings, which grow according to Eq. (5.2.3), allow to approximately reproduce CKM mixing for appropriate values of their vacuum expectation values. We studied a particular benchmark of the full model, and saw that quark and charged-lepton masses can be approximately reproduced, as depicted in Fig. 5.2. Phenomenological implications of the model revolve around a massive Z' boson with tree-level FCNCs in the quark sector. Direct searches constrain the new boson to be at the TeV scale, while meson mixing poses the strongest bounds on new physics couplings, with different implications for the three studied mixing scenarios. In the case where mixing is driven by the up sector, the Z' could be as light as a few TeV.

6 Summary and Conclusions

In this thesis we have studied asymptotically safe extensions of the SM with implications for flavor phenomenology. In order for weakly interacting UV fixed points to arise, Yukawa couplings are essential. For this reason, the models we have studied contain vector-like fermions and singlet scalars which allow to write the purely BSM Yukawa interaction (3.0.1), already considered in previous works as an extension of the SM [29, 61]. In Chapter 3, we studied for the first time effects of linking the new sector to SM leptons through mixed Yukawa interactions, finding that these can be sufficient for UV fixed points to arise. Both in the 210 approximation and using full 2-loop results, we found benchmarks which can be matched onto the Standard Model around the TeV scale, as seen in Figs. 3.2 and 3.6. Furthermore, the extended Yukawa sector acts as a portal to the SM, yielding a rich phenomenology. In particular, models where the new fermions transform as vector-like leptons allow to simultaneously explain the observed anomalies in the anomalous magnetic moments of the electron and the muon, thanks to the BSM Yukawa interactions and mixing between the Higgs and the new scalars. As shown in Fig. 3.17, the parameter window which allows for simultaneous explanations of the lepton AMM data demands vector-like lepton masses around the TeV scale or below. Remarkably, the mechanism requires no explicit breaking of lepton-flavor universality and is able to predict the AMM of the tau. The models can yield as well contributions to lepton-flavor-violating observables and EDMs which will be probed in the near future.

With vector-like fermions carrying SM gauge charges, the particles of the BSM sector studied in Chapter 3 can be produced at both pp and $\ell\ell$ colliders. In Chapter 4, we focused on the models of vector-like leptons (models A and C) and studied their potential signatures at the LHC, developing targeted search strategies. After simulating production of vector-like leptons within LHC conditions, we studied decays yielding a final state with at least four light leptons (electrons on muons). Comparing the sum of transverse momenta of the final-state leptons with current CMS data we were able to constrain the allowed range of BSM masses, as summarized in Fig. 4.3. In general, we found that doublet VLLs lighter than ~ 800 GeV are excluded, while singlets can be at least as light as ~ 300 GeV. For the parameter space of BSM Yukawa couplings which allows to explain the AMM anomalies, VLLs decay almost entirely to a lepton and a BSM scalar. The latter can subsequently decay to two leptons of different flavor, yielding an LFV-like signature. We exploited this feature to build novel observables in the form of dilepton and three-lepton invariant masses, which can serve as null tests of the SM and permit to identify the masses of the BSM sector. Their distributions for several $g-2$-favored benchmark scenarios are shown in Figs. 4.5 and 4.6, where clean BSM resonances can be observed. With current LHC data the observables present a limited potential for discovery, while higher luminosities can greatly enhance it.

In Chapter 5 we proposed a model where fermion masses and quark mixing can be explained via RG effects, thanks to a power-law scaling of asymptotically free couplings near UV fixed points. We began by showing that hierarchies between Yukawa interactions can arise through the running if fermions carry non-universal gauge charges. These effects were explored in the context of an extension of the SM with a new $U(1)_X$ symmetry, under which SM fields were assigned vector-like charges. We showed that RG-induced differences among couplings of the same sector depend on their non-universal charges, as described by Eq. (5.1.8). We studied as well benchmark values of the BSM sector parameters which can reproduce SM masses at order of magnitude, as depicted in Fig. 5.2. For each benchmark, the coupling of the new gauge interaction is fixed by the running. Moreover, the setup predicts a Z' boson with tree-level FCNCs. If quark mixing is driven by the up sector, both meson mixing and direct detection bounds allow the Z' to be as light as a few TeV.

In conclusion, we have shown that asymptotically safe extensions of the SM can be strongly connected to the flavor sector and present low-scale signatures which can be measured at current and near-future experiments. Their phenomenology can address both experimental discrepancies with the SM and the more fundamental issue of the flavor puzzle while rendering the running of the Standard Model UV complete. We look forward to further studies and tests of asymptotically safe models.

Appendix

A General Formulae

In this appendix we collect several useful formulae used throughout this thesis. The employed conventions for the SM couplings are

$$\begin{aligned} U(1)_Y &: g_1 = g' , \quad \alpha_1 = \frac{g_1^2}{(4\pi)^2} , \quad \alpha_e = \frac{e^2}{4\pi} = \frac{(g_1 \cos\theta_w)^2}{4\pi} , \\ SU(2)_L &: g_2 = g , \quad \alpha_2 = \frac{g_1^2}{(4\pi)^2} , \quad \alpha_2^{\text{PDG}} = \frac{g_2^2}{4\pi} , \\ SU(3)_C &: g_3, \qquad\quad \alpha_3 = \frac{g_3^2}{(4\pi)^2} , \quad \alpha_s = \frac{g_3^2}{4\pi} . \end{aligned} \tag{A.0.1}$$

A.1 Generators of $SU(2)$

The generators of $SU(2)$ in the doublet representation correspond to $\sigma^i/2$, where the Pauli matrices σ^i are given by

$$\sigma^1 = \begin{pmatrix} 0 & 1 \\ 1 & 0 \end{pmatrix} , \qquad \sigma^2 = \begin{pmatrix} 0 & -i \\ i & 0 \end{pmatrix} , \qquad \sigma^3 = \begin{pmatrix} 1 & 0 \\ 0 & -1 \end{pmatrix} . \tag{A.1.1}$$

Furthermore, the generators in the triplet or adjoint representation read

$$t^1 = \frac{1}{\sqrt{2}} \begin{pmatrix} 0 & 1 & 0 \\ 1 & 0 & -1 \\ 0 & -1 & 0 \end{pmatrix} , \qquad t^2 = \frac{1}{\sqrt{2}} \begin{pmatrix} 0 & -i & 0 \\ i & 0 & i \\ 0 & -i & 0 \end{pmatrix} , \qquad t^3 = \begin{pmatrix} 1 & 0 & 0 \\ 0 & 0 & 0 \\ 0 & 0 & -1 \end{pmatrix} . \tag{A.1.2}$$

A.2 Mass Mixing

In models where gauge eigenstates acquire mixed mass terms the mass matrix must be diagonalized in order to obtain the mass eigenstates. In a general case with two-particle mixing, one is confronted with a mass matrix of the type

$$\mathcal{N} = \begin{pmatrix} A & C \\ C & B \end{pmatrix} . \tag{A.2.1}$$

For fermions, the mass matrix can be generally written as $\mathcal{M} = L\mathbb{M}R^\dagger$, where $\mathbb{M}$ contains the singular values of $\mathcal{M}$. In order to find the left and right rotations one must then diagonalize $\mathcal{M}\mathcal{M}^\dagger$ and $\mathcal{M}^\dagger\mathcal{M}$ respectively, which take the form of $\mathcal{N}$ in Eq. (A.2.1). In the case of two real scalars, one finds $\mathcal{N} = \frac{1}{2}\mathcal{M}$. The eigenvalues of $\mathcal{N}$ fulfill

$$\lambda_\pm = \frac{1}{2}\left[A + B \pm \sqrt{(A-B)^2 + 4C^2}\right] , \tag{A.2.2}$$

$\mathbf{R_2}$	$C_2(R_2)$	$S_2(R_2)$	$\mathbf{R_3}$	$C_2(R_3)$	$S_2(R_3)$
2	3/4	1/2	**3**	4/3	1/2
3	2	2	**8**	3	3

Table B.1. Values of the Casimir operator and the Dynkin index for the fundamental and adjoint representations of $SU(2)$ and $SU(3)$.

and their corresponding normalized eigenvalues can be written as

$$v_+ = (\cos\alpha, \sin\alpha)\,, \qquad v_- = (-\sin\alpha, \cos\alpha)\,, \tag{A.2.3}$$

with

$$\tan 2\alpha = \frac{2\,C}{A-B}\,. \tag{A.2.4}$$

Then, if the mass matrix is written in the interaction basis, the interaction eigenstates (H, L) can be expressed in terms of the mass eigenstates (H^m, L^m) as

$$H = \cos\alpha H^m - \sin\alpha L^m\,, \qquad L = \cos\alpha L^m + \sin\alpha H^m\,. \tag{A.2.5}$$

For $C > 0$, the heaviest eigenstate always carries a minus sign. In the case above, for $A > B$ one finds $\alpha > 0$ and H^m (L^m) correspond to the heavy (light) eigenstates.

B RGE Studies

This appendix contains the RGE equations of several models discussed in this thesis. We denote the Casimir operator and the Dynkin index of a given representation R as $C_2(R)$ and $S_2(R)$, respectively. These are related through

$$S_2(R) = \frac{d(R)}{d(\mathrm{Adj})} C_2(R)\,, \tag{B.0.1}$$

where Adj denotes the adjoint representation, and their values are collected in Tab. B.1 for the fundamental and adjoint representations of $SU(2)$ and $SU(3)$. For $U(1)$ symmetries one finds $C_2(Y) = S_2(Y) = Y^2$ for fields with charge Y.

The β-functions collected in the rest of this section are computed in the $\overline{\mathrm{MS}}$ scheme with the Mathematica package `ARGES` [45] (available at `https://github.com/TomSteu/ARGES`), which builds on [46, 182–186]. Further computational tools to compute RGEs can be found in the `SARAH` package [187], while analytical results can be obtained by using the methods of the structure δ [188], which generalizes the results of [46, 182, 183] to be readily applicable to any model. The β-functions for the SM up to three-loop can be found for instance in [34, 47].

B.1 β-functions for Models of Vector-like Fermions

In this section we reproduce the β-functions for the models A – F studied in Chapter 3 up to 2-loop order for all couplings. For the coefficients of the 2-loop gauge and 1-loop Yukawa RGEs we employ the notation of Eq. (2.1.20) and Eq. (2.1.23), respectively. Model-specific coefficients are listed in Tabs. B.2-B.4, while others are universal or can be easily expressed in terms of the Casimir operator and Dynkin index of the $SU(2)_L \times SU(3)_C$ representations R_2, R_3 and the hypercharge Y of the vector-like fermions [29]. For the hypercharge coupling β-function, the coefficients read

$$\begin{aligned} &B_1 = -\frac{41}{3} - 8\, d(R_2) Y^2\,, && C_{11} = \frac{199}{9} + 24\, d(R_2)\, Y^4\,, \\ &C_{12} = 9 + 24\, C_2(R_2) d(R_2) Y^2\,, && C_{13} = \frac{88}{3}\,, \\ &D_{1t} = \frac{17}{3}\,, && D_{1b} = \frac{5}{3}\,, && D_{1y} = 36\, d(R_2)\, Y^2\,. \end{aligned} \tag{B.1.1}$$

For the β-function of the $SU(2)_L$ coupling, coefficients obey

$$\begin{aligned} &B_2 = \frac{19}{3} - 8\, S_2(R_2)\,, && C_{21} = 3 + 24\, S_2(R_2)\, Y^2\,, \\ &C_{22} = \frac{35}{3} + 12\, S_2(R_2)\,(2C_2(R_2) + 20/3)\,, && C_{23} = 24\,, \\ &D_{2t} = D_{2b} = 3\,, && D_{2y} = 36\, S_2(R_2)\,. \end{aligned} \tag{B.1.2}$$

Finally, in our models the coefficients of the strong coupling β-function are not modified by the BSM sector, and read

$$\begin{aligned} B_3 = 14\,, \quad D_{3t} = 4\,, \quad D_{3b} = 4\,, \\ C_{31} = \frac{11}{3}\,, \quad C_{32} = 9\,, \quad C_{33} = -52\,. \end{aligned} \tag{B.1.3}$$

For the β-functions of Yukawa couplings, model-dependent coefficients are collected in Tab. B.2. The remaining coefficients are given by

$$\begin{aligned} &E_{tt} = E_{bb} = 9\,, && E_{tb} = E_{bt} = 3\,, && F_{t1} = \frac{17}{6}\,, \\ &F_{b1} = \frac{5}{6}\,, && F_{t2} = F_{b2} = \frac{9}{2}\,, && F_{t3} = F_{b3} = 16\,, \\ &E_{yy} = 2\,[3 + d(R_2)]\,, && F_{y1} = 12\, Y^2\,, && F_{y2} = 12\, C_2(R_2)\,, \\ &E_{\kappa t} = E_{\kappa b} = 6\,, && E_{\kappa y} = 3\,, && E_{\kappa\kappa'} = F_{\kappa 3} = 0\,. \end{aligned} \tag{B.1.4}$$

In order to simplify expressions of the β-functions of scalar couplings, it is convenient to use the definition

$$\widetilde{\alpha}_y = \begin{cases} \alpha_{\kappa'} + \alpha_y & \text{model A, C} \\ \alpha_y & \text{model B, D, E, F} \end{cases}\,. \tag{B.1.5}$$

Model	$D_{1\kappa}$	$D_{1\kappa'}$	$D_{2\kappa}$	$D_{2\kappa'}$	$E_{t\kappa}$	$E_{b\kappa}$	$E_{y\kappa}$	$E_{y\kappa'}$	$E_{\kappa\kappa}$	$F_{\kappa 1}$	$F_{\kappa 2}$	$E_{\kappa'\kappa'}$	$E_{\kappa' y}$	$E_{\kappa'\kappa}$	$F_{\kappa' 1}$	$F_{\kappa' 2}$
A	15	36	3	0	6	6	2	8	9	15/2	9/2	8	8	0	12	0
B	45/4	0	33/4	0	6	6	1/2	0	23/4	15/2	33/2					
C	15	18	3	18	9/2	9/2	1	10	9	15/2	9/2	10	10	0	3	9
D	39	0	3	0	6	6	1	0	9	39/2	9/2					
E	3	0	3	0	6	6	2	0	9	3/2	9/2					
F	9/4	0	33/4	0	6	6	1/2	0	23/4	3/2	33/2					

Table B.2. Model-specific loop coefficients for the gauge and Yukawa β-functions of the vector-like fermion models of Chapter 3, following the conventions of (2.1.20) and (2.1.23).

Model	I_κ	$J^\lambda_{\kappa\kappa}$	$K^\lambda_{11\kappa}$	$K^\lambda_{12\kappa}$	$K^\lambda_{22\kappa}$	$H^\lambda_{\kappa\kappa\kappa}$	$H^\delta_{\kappa\kappa y}$	$L^\lambda_{1\kappa}$	$L^\lambda_{2\kappa}$	L^δ_{1y}	L^δ_{2y}
A	12	6	75/4	$-33/2$	9/4	10	14	12	0	12	0
B	9	15/8	225/16	$-51/8$	$-21/16$	47/32	39/8	15/4	15/2	9	18
C	12	6	75/4	$-33/2$	9/4	10	16	12	0	6	6
D	12	6	219/4	39/2	9/4	10	16	36	0	30	6
E	12	6	3/4	3/2	9/4	10	14	0	0	0	0
F	9	15/8	9/16	57/8	-21/16	47/32	39/8	0	15/2	0	18

Table B.3. Model-specific loop coefficients for the quartic and Yukawa β-functions (B.1.6), (B.1.7), (B.1.9) and (B.1.10).

Then, the 1-loop RGEs for the scalar quartic couplings read

$$\begin{aligned}
\beta^{(1)}_\lambda &= \beta^{(1)}_{\lambda,\,\mathrm{SM}} + 9\alpha_\delta^2 + I_\kappa\,\alpha_\kappa\alpha_\lambda - J^\lambda_{\kappa\kappa}\,\alpha_\kappa^2\,,\\
\beta^{(1)}_\delta &= \alpha_\delta\left[4\alpha_\delta + 12\alpha_\lambda + 24\alpha_u + 40\alpha_v + 6\alpha_t + 6\alpha_b + \frac{1}{2}I_\kappa\,\alpha_\kappa + 2\,d(R_2)\,\widetilde{\alpha}_y\right.\\
&\qquad\left.-\frac{3}{2}\alpha_1 - \frac{9}{2}\alpha_2\right] - \frac{1}{3}I_\kappa\,\alpha_\kappa\alpha_y\,,\\
\beta^{(1)}_u &= 24\alpha_u\,(\alpha_u+\alpha_v) + 2\,d(R_2)\widetilde{\alpha}_y\,(2\alpha_u - \widetilde{\alpha}_y)\,,\\
\beta^{(1)}_v &= 52\alpha_v^2 + 12\alpha_u\,(\alpha_u + 4\alpha_v) + 2\alpha_\delta^2 + 4\,d(R_2)\,\widetilde{\alpha}_y\alpha_v\,,
\end{aligned} \tag{B.1.6}$$

where $\beta^{(1)}_{\lambda,\,\mathrm{SM}}$ denotes the 1-loop β-function of the Higgs quartic in the SM, and the 1-loop coefficients I_κ and $J^\lambda_{\kappa\kappa}$ are collected in Tab. B.3.

At 2-loop order, the RGEs of $\alpha_{t,b,\lambda}$ are found to obey

$$
\begin{aligned}
\frac{\beta_t^{(2)}}{\alpha_t} &= \frac{\beta_{t,\,\mathrm{SM}}^{(2)}}{\alpha_t} + 9\alpha_\delta^2 - \frac{9}{4}J_{\kappa\kappa}^{\lambda}\,\alpha_\kappa^2 - \frac{27}{24}I_\kappa\,\alpha_\kappa\left(\alpha_y + \alpha_t - \frac{15}{27}\alpha_b\right) \\
&\quad + \frac{5}{4}\left(D_{1\kappa}\,\alpha_1 + 3D_{2\kappa}\,\alpha_2\right)\alpha_\kappa + 6\,S_2(R_2)\,\alpha_2^2 + \frac{58}{9}Y^2\,d(R_2)\,\alpha_1^2\,, \\
\frac{\beta_b^{(2)}}{\alpha_b} &= \frac{\beta_{b,\,\mathrm{SM}}^{(2)}}{\alpha_b} + 9\alpha_\delta^2 - \frac{9}{4}J_{\kappa\kappa}^{\lambda}\,\alpha_\kappa^2 - \frac{27}{24}I_\kappa\,\alpha_\kappa\left(\alpha_y + \alpha_b - \frac{15}{27}\alpha_t\right) \\
&\quad + \frac{5}{4}\left(D_{1\kappa}\,\alpha_1 + 3D_{2\kappa}\,\alpha_2\right)\alpha_\kappa + 6\,S_2(R_2)\,\alpha_2^2 - \frac{2}{9}Y^2\,d(R_2)\,\alpha_1^2\,, \\
\beta_\lambda^{(2)} &= \beta_{\lambda,\,\mathrm{SM}}^{(2)} - 90\alpha_\delta^2\alpha_\lambda - 36\alpha_\delta^3 - 18\,d(R_2)\,\widetilde{\alpha}_y\alpha_\delta^2 - 12\,I_\kappa\,\alpha_\kappa\alpha_\lambda^2 - \frac{1}{2}J_{\kappa\kappa}^{\lambda}\,\alpha_\kappa^2\alpha_\lambda \\
&\quad - \frac{27}{12}I_\kappa\,\alpha_\kappa\alpha_y\alpha_\lambda + 3\,J_{\kappa\kappa}^{\lambda}\alpha_y\alpha_\kappa^2 + 3\,H_{\kappa\kappa\kappa}^{\lambda}\alpha_\kappa^3 - L_{1\kappa}^{\lambda}\alpha_1\alpha_\kappa^2 - L_{2\kappa}^{\lambda}\alpha_2\alpha_\kappa^2 \\
&\quad + \frac{5}{2}\left(D_{1\kappa}\,\alpha_1 + 3D_{2\kappa}\,\alpha_2\right)\alpha_\kappa\alpha_\lambda - K_{11\kappa}^{\lambda}\alpha_1^2\alpha_\kappa - K_{12\kappa}^{\lambda}\alpha_1\alpha_2\alpha_\kappa - K_{22\kappa}^{\lambda}\alpha_2^2\alpha_\kappa \\
&\quad + 30\,S_2(R_2)\,\alpha_2^2\alpha_\lambda + 10\,d(R_2)Y^2\,\alpha_1^2\alpha_\lambda - 4d(R_2)Y^2\,(\alpha_1 + \alpha_2)\,\alpha_1^2 \\
&\quad - 4\,S_2(R_2)\,(\alpha_1 + 3\alpha_2)\,\alpha_2^2\,,
\end{aligned}
\tag{B.1.7}
$$

where coefficients are given in in Tabs. B.2 and B.3, and $\beta_{t,b,\lambda,\,\mathrm{SM}}^{(2)}$ denote the 2-loop β-

functions of the SM. 2-loop RGEs of the BSM Yukawas $\alpha_{y,\kappa,\kappa'}$ read

$$
\begin{aligned}
\frac{\beta_\kappa^{(2)}}{\alpha_\kappa} =& - P_{\kappa\kappa}^{\kappa}\alpha_\kappa^2 - \frac{9}{4}\left(1+2d(R_2)\right)\widetilde{\alpha}_y\alpha_y - \frac{3}{32}\left[90+d(R_2)\,\left(89-27\,d(R_2)\right)\right]\alpha_y\alpha_\kappa + R_{11}^{\kappa}\,\alpha_1^2 \\
& - \frac{1}{6}\left[49+d(R_2)\,\left(39-19\,d(R_2)\right)\right]\alpha_2^2 + Q_{1y}^{\kappa}\,\alpha_1\alpha_y + Q_{2\kappa}^{\kappa}\,\alpha_2\alpha_\kappa + Q_{12}^{\kappa}\,\alpha_1\alpha_2 + Q_{1\kappa}^{\kappa}\,\alpha_1\alpha_\kappa \\
& + \frac{5}{12}\,\alpha_1\left[17\,\alpha_t+5\,\alpha_b\right] + \frac{45}{4}\,\alpha_2\left[\alpha_t+\alpha_b\right] + 40\,\alpha_3\left[\alpha_t+\alpha_b\right] - 6S_2(R_2)\left[1-2d(R_2)\right]\,\alpha_2\alpha_y \\
& - \frac{27}{2}\left[\alpha_t^2+\alpha_b^2\right] + 3\,\alpha_t\,\alpha_b - J_{\kappa\kappa}^{\lambda}\,I_\kappa^{-1}\,\left(27\,\alpha_t+27\,\alpha_b+48\,\alpha_\lambda\right)\alpha_\kappa - 12\,\alpha_y\alpha_\delta + 9\alpha_\delta^2 + 12\alpha_\lambda^2\,. \\
\frac{\beta_{\kappa'}^{(2)}}{\alpha_{\kappa'}} =& \left[\frac{211}{3}+2\,Y^2\left(20\,d(R_2)-3\right)\right]Y^2\,\alpha_1^2 - \left[\frac{257}{3}+6\,C_2(R_2)-40\,S_2(R_2)\right]C_2(R_2)\,\alpha_2^2 \\
& - 12\,C_2(R_2)Y^2\,\alpha_1\,\alpha_2 + \left[48+10\,d(R_2)\right]\,Y^2\,\alpha_1\,\widetilde{\alpha}_y + \left[48+10\,d(R_2)\right]\,C_2(R_2)\,\alpha_2\widetilde{\alpha}_y \\
& + 8\left[5\,\alpha_u^2+5\,\alpha_v^2+6\,\alpha_u\alpha_v\right] + 2\alpha_\delta^2 - 16\,\left(5\,\alpha_u+3\,\alpha_v\right)\widetilde{\alpha}_y - \left[\frac{1}{2}+18\,d(R_2)\right]\widetilde{\alpha}_y^2 \\
& - P_{\kappa\kappa}^{y}\,\alpha_\kappa^2 + Q_{1\kappa}^{y}\,\alpha_1\alpha_\kappa + Q_{2\kappa}^{y}\,\alpha_2\alpha_\kappa - \frac{3}{2^{d(R_2)}}\left(2\,d(R_2)+1\right)\alpha_y\alpha_\kappa\,, \\
\frac{\beta_y^{(2)}}{\alpha_y} =& \left[\frac{211}{3}+2\,Y^2\left(20\,d(R_2)-3\right)\right]Y^2\,\alpha_1^2 - \left[\frac{257}{3}+6\,C_2(R_2)-40\,S_2(R_2)\right]C_2(R_2)\,\alpha_2^2 \\
& - 12\,C_2(R_2)Y^2\,\alpha_1\,\alpha_2 + \left[48+10\,d(R_2)\right]\,Y^2\,\alpha_1\,\widetilde{\alpha}_y + \left[48+10\,d(R_2)\right]\,C_2(R_2)\,\alpha_2\widetilde{\alpha}_y \\
& + 8\left[5\,\alpha_u^2+5\,\alpha_v^2+6\,\alpha_u\alpha_v\right] + 2\alpha_\delta^2 - 16\,\left(5\,\alpha_u+3\,\alpha_v\right)\widetilde{\alpha}_y - \left[\frac{1}{2}+18\,d(R_2)\right]\widetilde{\alpha}_y^2 \\
& - P_{\kappa\kappa}^{y}\,\alpha_\kappa^2 + Q_{1\kappa}^{y}\,\alpha_1\alpha_\kappa + Q_{2\kappa}^{y}\,\alpha_2\alpha_\kappa \\
& - 2^{-d(R_2)}\left[18\,\alpha_t+18\,\alpha_b+3\left(2\,d(R_2)+1\right)\alpha_y+16\,\alpha_\delta\right]\alpha_\kappa\,,
\end{aligned}
\tag{B.1.8}
$$

using as well the loop coefficients in Tab. B.4. Finally, the 2-loop RGEs of the BSM scalar quartic couplings fulfill

$$
\begin{aligned}
\beta_u^{(2)} =& - 336\,\alpha_u^3 - 1056\,\alpha_u^2\alpha_v - 688\,\alpha_u\alpha_v^2 + \left[Y^2 d(R_2)\alpha_1 + 3\,S_2(R_2)\alpha_2\right]\left[20\alpha_u - 8\widetilde{\alpha}_y\right]\widetilde{\alpha}_y \\
& - 48 d(R_2)\widetilde{\alpha}_y\left(\alpha_u+\alpha_v\right)\alpha_u + 2d(R_2)\,\left[6\widetilde{\alpha}_y - 9\alpha_u + 4\alpha_v\right]\widetilde{\alpha}_y - 20\,\alpha_\delta^2\alpha_u + I_\kappa\,\alpha_\kappa\alpha_y\left[\frac{1}{3}\widetilde{\alpha}_y - \frac{1}{2}\alpha_u\right]\,, \\
\beta_v^{(2)} =& - 288\,\alpha_u^3 - 688\,\alpha_u^2\alpha_v - 1056\,\alpha_u\alpha_v^2 - 816\,\alpha_v^3 + 20\left[Y^2 d(R_2)\,\alpha_1 + 3S_2(R_2)\,\alpha_2\right]\widetilde{\alpha}_y\alpha_v \\
& - 24 d(R_2)\left[\alpha_u^2 + 4\alpha_v\alpha_u + \frac{13}{3}\alpha_v^2\right]\,\widetilde{\alpha}_y + 2d(R_2)\left[4\,\alpha_u - 9\,\alpha_v + 2\,\widetilde{\alpha}_y\right]\widetilde{\alpha}_y^2 - \frac{1}{2}I_\kappa\,\alpha_\kappa\alpha_y\alpha_v \\
& + 4\left[\alpha_1 + 3\,\alpha_2 - 3\,\alpha_t - 3\,\alpha_b - 3\,\alpha_\kappa - 5\,\alpha_v - 2\,\alpha_\delta\right]\alpha_\delta^2\,,
\end{aligned}
\tag{B.1.9}
$$

Model	$P^y_{\kappa\kappa}$	$P^\kappa_{\kappa\kappa}$	$Q^y_{1\kappa}$	$Q^y_{2\kappa}$	Q^κ_{1y}	$Q^\kappa_{2\kappa}$	R^κ_{11}
A	19/2	24	37/4	51/4	6	225/8	721/12
B	57/32	59/8	37/16	−101/16	6	1343/32	1249/12
C	5	24	55/8	33/8	15	225/8	589/12
D	5	24	95/8	33/8	27	225/8	4541/12
E	19/2	24	17/4	51/4	0	225/8	35/12
F	57/32	59/8	17/4	-101/16	0	1343/32	35/12

Table B.4. Model-specific 2-loop coefficients for the BSM Yukawa β-functions (B.1.8).

while for the portal coupling the 2-loop β-function obeys

$$\begin{aligned}
\beta^{(2)}_\delta = &\left[\frac{557}{48} + 5\,Y^2 d(R_2)\right]\alpha_1^2\alpha_\delta + \frac{15}{8}\alpha_1\alpha_2\alpha_\delta + \left[-\frac{145}{16} + 15\,S_2(R_2)\right]\alpha_2^2\alpha_\delta + \left[\frac{85}{12}\alpha_t + \frac{25}{12}\alpha_b\right]\alpha_1\alpha_\delta \\
&+ \frac{45}{4}\left[\alpha_t + \alpha_b\right]\alpha_2\alpha_\delta + 40\,\left[\alpha_t + \alpha_b\right]\alpha_3\alpha_\delta + 10\left[Y^2 d(R_2)\,\alpha_1 + 3\,S_2(R_2)\,\alpha_2\right]\widetilde{\alpha}_y\alpha_\delta \\
&- \frac{27}{2}\left[\alpha_t^2 + \alpha_b^2\right]\alpha_\delta - 21\,\alpha_t\alpha_b\alpha_\delta - d(R_2)\left[48\,\alpha_u + 80\,\alpha_v + 9\widetilde{\alpha}_y\right]\widetilde{\alpha}_y\alpha_\delta - \frac{17}{24}I_\kappa\,\alpha_\kappa\alpha_y\alpha_\delta - \frac{27}{12}J^\lambda_{\kappa\kappa}\alpha_\kappa^2\alpha_\delta \\
&- 200\left[\alpha_u^2 + \frac{6}{5}\alpha_u\alpha_v + \alpha_v^2\right]\alpha_\delta + 12\left[2\,\alpha_1 + 6\,\alpha_2 - 6\,\alpha_t - 6\,\alpha_b - 6\,\alpha_\kappa - 5\alpha_\lambda\right]\alpha_\lambda\alpha_\delta \\
&+ \left[\alpha_1 + 3\alpha_2 - 12\alpha_t - 12\alpha_b - 144\alpha_u - 240\alpha_v - I_\kappa\,\alpha_\kappa - 4\,d(R_2)\,\widetilde{\alpha}_y - 19\alpha_\delta - 72\,\alpha_\lambda\right]\alpha_\delta^2 \\
&+ \frac{15}{4}\left[\frac{1}{3}\,D_{1\kappa}\alpha_1 + D_{2\kappa}\alpha_2\right]\alpha_\kappa\alpha_\delta + \frac{5}{2}I_\kappa\,\alpha_\kappa\alpha_y\widetilde{\alpha}_y + H^\delta_{\kappa\kappa y}\,\alpha_\kappa^2\alpha_y \\
&- 12\,Y^2 d(R_2)\,\alpha_1^2\widetilde{\alpha}_y - 36\left[\frac{5}{3}d(R_2) - 4\right]S_2(R_2)\,\alpha_2^2\widetilde{\alpha}_y - L^\delta_{1y}\,\alpha_1\alpha_y\alpha_\kappa - L^\delta_{2y}\,\alpha_2\alpha_y\alpha_\kappa\,,
\end{aligned} \tag{B.1.10}$$

with further model-specific loop coefficients specified in Tab. B.3.

B.2 BSM Critical Surface

Using the β-functions detailed above, in Chapter 3 we explored the RGE structure of models of colorless vector-like fermions, both with a bottom-up approach in the `210` approximation and from a top-down perspective for some benchmarks of our BSM couplings at a matching scale of 1 TeV, in this case using full 2-loop results. Here, we study the UV fate of the running more comprehensively by scanning over the values of the BSM Yukawas at the matching scale, mapping the *BSM critical surface*. Employing as well 2-loop results, we integrate the RGEs up to the Planck scale and determine if the vacuum is stable (with V^+ or V^- structure), or if vacuum stability is not fulfilled. In the latter case we distinguish between instances where α_u or α_v violate the vacuum stability conditions (2.4.12), regardless of the values of α_λ and α_δ (a situation labeled V *unstable*), and cases where the Higgs quartic is metastable, with $0 > \alpha_\lambda|_{M_{\rm Pl}} > -10^{-4}$ (*Higgs metastable*) or unstable with $\alpha_\lambda|_{M_{\rm Pl}} < -10^{-4}$ (*Higgs unstable*). We also indicate regions where poles arise at or below the Planck scale.

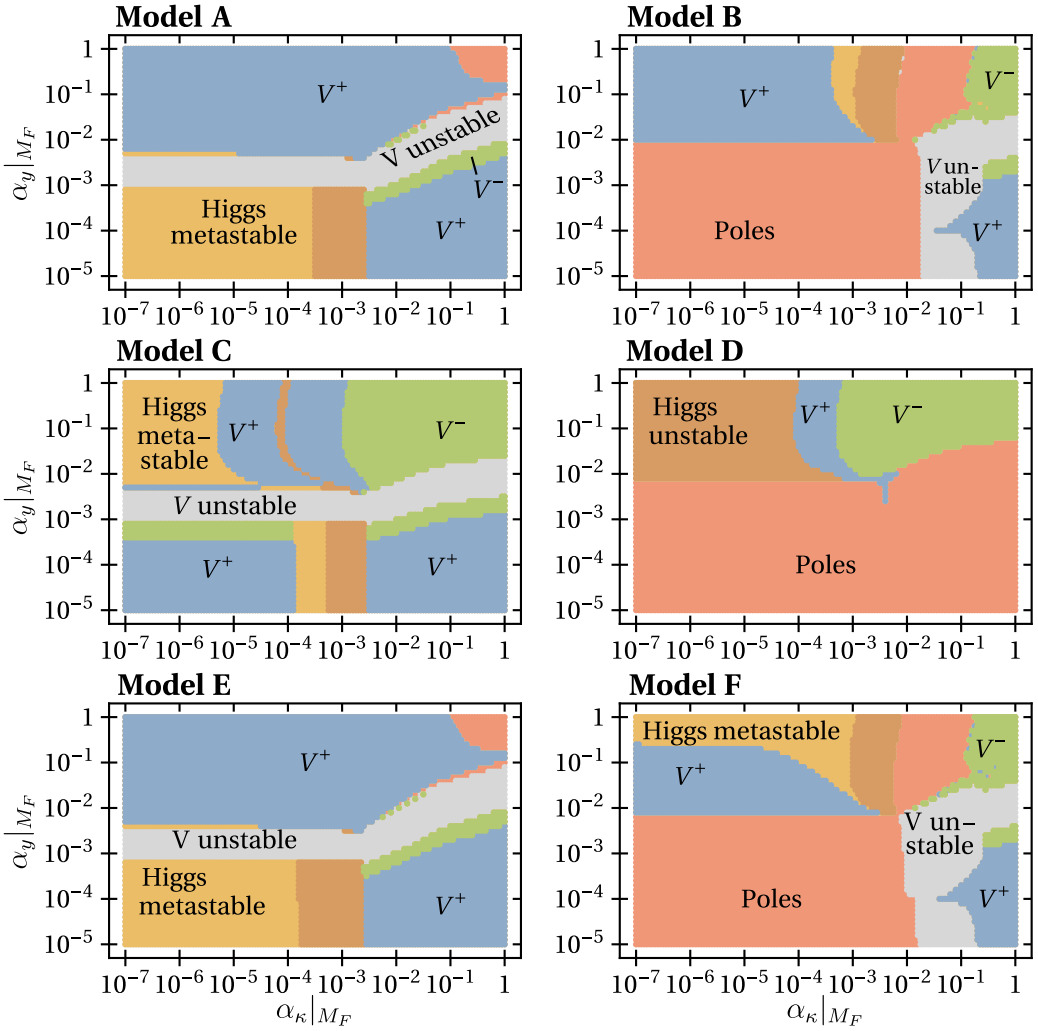

Figure B.2.1. BSM critical surface for models A – F in the $\{\alpha_\kappa, \alpha_y\}|_{M_F}$ plane, from [25]. Initial conditions at the matching scale for the remaining couplings are given by Eq. (B.2.1). We indicate whether the vacuum at the Planck scale $M_{\rm Pl}$ corresponds to a stable V^+ (blue) or V^- (green) according to Eq. (2.4.12), an unstable BSM vacuum (gray), a stable vacuum for $\alpha_{u,v}|_{M_{\rm Pl}}$ but with $\alpha_\lambda|_{M_{\rm Pl}} < 0$ (yellow for $\alpha_\lambda|_{M_{\rm Pl}} > -10^{-4}$, otherwise brown) or if the RG flow runs into poles (red). Resolution is 141×61 points per model. All models allow for regions where the BSM and Higgs vacuum present absolute stability (green and blue areas). These corresponding to the $\mu_0 = 1$ TeV slices of the parameter space we refer to as *BSM critical surface*.

Results for models A – F (see Tab. 3.1) are shown in Fig. B.2.1, where we scan over a range of the couplings α_y and α_κ. The remaining BSM couplings at the matching scale are taken at benchmark values

$$\{\alpha_{\kappa'}, \alpha_\delta, \alpha_u, \alpha_v\}|_{M_F} = \{0, 5, 1, 4\} \cdot 10^{-5} \,. \tag{B.2.1}$$

We observe that, for all models, regions of absolute stability arise ($V^\pm$ regions depicted in green and blue in Fig. B.2.1), while large values of both scanned Yukawas generally lead to

poles below or at the Planck scale.

For models A and C, results for a scan of the couplings α_κ and $\alpha_{\kappa'}$ are shown in Fig. B.2.2, where the remaining BSM couplings are in this case set to

$$\{\alpha_y,\, \alpha_\delta,\, \alpha_u,\, \alpha_v\}\,|_{M_F} = \{0,\, 5,\, 1,\, 4\} \cdot 10^{-5}\,. \tag{B.2.2}$$

at the matching scale. In both cases, large regions with absolute vacuum stability exist, which in the case of model A require at least one of the couplings to be of $\mathcal{O}(10^{-2})$ or larger, while in model C $\alpha_{\kappa'}$ must be weaker. Note, however, that values of α_κ at the order 10^{-3} or larger are disfavored by the Z data constraint (3.3.9).

Finally, in Sec. 3.3.5 we found that for certain values of the BSM couplings models A and C can accommodate both the muon and the electron anomalous magnetic moment anomalies. In Fig. B.2.3 (left) we show the running in these models for benchmark BSM couplings at the matching scale which are able to explain the anomalies. The right panels of Fig. B.2.3 show the BSM critical surface in the α_κ and $\alpha_{\kappa'}$ plane, where red-shaded regions correspond to the values of the couplings preferred by the data (3.3.34) and (3.3.36) at 1σ, and the white dots indicate the benchmarks for which we show the running. Similarly to the results shown in Fig. 3.6, when extending the running shown in Fig. B.2.3 into the deep UV trajectories end in interacting fixed points (for model A) or run into transplanckian poles (model C). The scanning of trajectories for different values of the BSM Yukawas shown in Fig. B.2.3 (right) displays sizable regions with a stable V^+ vacuum (metastable Higgs sector) in model A (model C) at the Planck scale, while poles are found for large, non-perturbative values of $\alpha_{\kappa'}$ in both models.

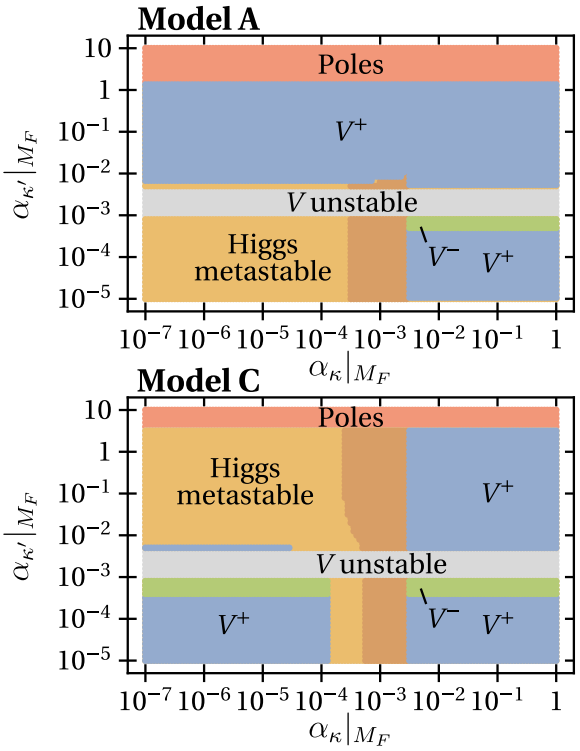

Figure B.2.2. BSM critical surface for models A and C in the $\{\alpha_\kappa, \alpha_{\kappa'}\}|_{M_F}$ plane with matching conditions (B.2.2), from [25]. The color coding of Fig. B.2.1 applies. Resolution is 141×61 points per model. Both models present a large parameter space for which absolute stability is achieved by the SM and BSM vacuum at the Planck scale.

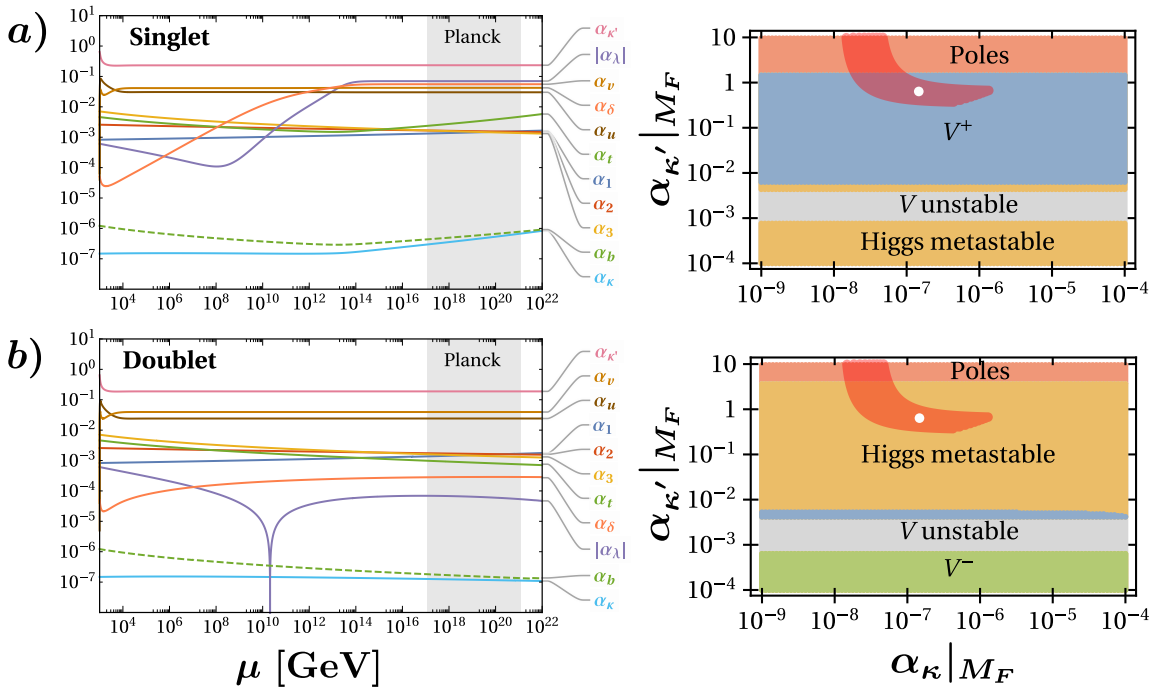

Figure B.2.3. Renormalization group running for $M_F = 2M_S = 1$ TeV between the matching scale M_F and the Planck scale (left), and BSM critical surface at the Planck scale in the $\alpha_\kappa, \alpha'_\kappa$ plane (right) for *a*) the singlet model or model A (top) and *b*) the doublet model or model C (bottom), from [24]. For the surface plots, the color coding of Fig. B.2.1 applies. BSM couplings at the matching scale are set to $(\alpha_\delta, \alpha_u, \alpha_v, \alpha_y)|_{M_F} = (5, -1, 4, 0) \cdot 10^{-5}$. Parameters within the red-shaded areas are compatible with data (3.3.34), and white dots refer to the benchmarks on the left.

B.3 β-functions for $U(1)_X$ Models

Here we present 2-loop gauge and 1-loop Yukawa β-functions for the $U(1)_X$ extensions of the SM studied in Chapter 5, with the particle content shown in Tab. 5.2 and Yukawa sector (5.2.16), with mixing terms $\mathcal{L}^d_{\text{mix}}$ in Eq. (5.2.2). In the following, a sum over $k = 1, 2, 3$ is understood. For the gauge couplings we find

$$
\begin{aligned}
\beta_1 &= \alpha_1^2\bigg[\frac{43}{3} + \frac{8}{3}N_F Y_F^2 + \alpha_1\left(\frac{217}{9} + 8N_F Y_F^4\right) + 15\alpha_2 + \frac{88}{3}\alpha_3 - 4\alpha_y N_F^2 Y_F^2 \\
&\quad + \alpha_X\left(\frac{22}{3}X_{q_k}^2 + 6X_{\ell_k}^2 + 4(X_{q_1} - X_{q_2})^2 + 4(X_{q_2} - X_{q_3})^2 + 8N_F X_F^2 Y_F^2\right) \\
&\quad - \frac{17}{3}(\alpha_{u_k} + \alpha_{u_{12}} + \alpha_{u_{23}}) - \frac{5}{3}(\alpha_{d_k} + \alpha_{d_{12}} + \alpha_{d_{23}}) - 5(\alpha_{e_k} + \alpha_{\nu_k})\bigg], \\
\beta_2 &= \alpha_2^2\bigg[-\frac{17}{3} + 5\alpha_1 + \frac{61}{3}\alpha_2 + 24\alpha_3 \\
&\quad + \alpha_X\big(6X_{q_k}^2 + 2X_{\ell_k}^2 + 4(X_{q_1} - X_{q_2})^2 + 4(X_{q_2} - X_{q_3})^2\big) \\
&\quad - 3(\alpha_{u_k} + \alpha_{u_{12}} + \alpha_{u_{23}}) - 3(\alpha_{d_k} + \alpha_{d_{12}} + \alpha_{d_{23}}) - (\alpha_{e_k} + \alpha_{\nu_k})\bigg], \\
\beta_3 &= \alpha_3^2\bigg[-14 + \frac{11}{3}\alpha_1 + 9\alpha_2 - 52\alpha_3 + 8\alpha_X X_{q_k}^2 \\
&\quad - 4(\alpha_{u_k} + \alpha_{u_{12}} + \alpha_{u_{23}} + \alpha_{d_k} + \alpha_{d_{12}} + \alpha_{d_{23}})\bigg], \\
\beta_X &= \alpha_X^2\bigg[\frac{8}{3}N_F X_F^2 + 8\alpha_1 N_F X_F^2 Y_F^2 - 4\alpha_y N_F^2 X_F^2 \\
&\quad + \alpha_X\big(8N_F X_F^4 + 48X_{q_k}^4 + 144X_{\ell_k}^4 + 16(X_{q_1} - X_{q_2})^4 + 16(X_{q_2} - X_{q_3})^4\big) \\
&\quad + X_{q_k}^2\left(16 + \frac{22}{3}\alpha_1 + 18\alpha_2 + 64\alpha_3 - 24(\alpha_{u_k} + \alpha_{d_k}) - 12(\alpha_{u_{12}} + \alpha_{d_{12}})\right) \\
&\quad + X_{\ell_k}^2(6\alpha_1 + 6\alpha_2 - 8\alpha_{e_k} - 8\alpha_{\sigma_k} + 8) \\
&\quad + \left[(X_{q_1} - X_{q_2})^2 + (X_{q_2} - X_{q_3})^2\right]\left(4\alpha_1 + 3\alpha_2 + \frac{4}{3}\right)\bigg],
\end{aligned}
\tag{B.3.1}
$$

while the BSM Yukawa y obeys

$$
\beta_y = \alpha_y\big[\,\alpha_y(2N_F + 2) - 12\alpha_1 Y_F^2 - 12\alpha_X X_F^2\,\big]\,. \tag{B.3.2}
$$

The Yukawa couplings of the lepton sector fulfill

$$\begin{aligned}
\beta_{e_i} &= \alpha_{e_i}\Bigg[-\frac{15}{2}\alpha_1 - \frac{9}{2}\alpha_2 - 12\alpha_X X_{\ell_i}^2 + 5\alpha_{e_i} - \alpha_{\nu_i} + 2(\alpha_{e_{k\neq i}} + \alpha_{\nu_{k\neq i}}) \\
&\quad +6\left(\alpha_{u_k} + \alpha_{d_k}\right)\Bigg], \\
\beta_{\nu_i} &= \alpha_{e_i}\Bigg[-\frac{3}{2}\alpha_1 - \frac{9}{2}\alpha_2 - 12\alpha_X X_{\ell_i}^2 + 5\alpha_{\nu_i} - \alpha_{e_i} + 4\alpha_{\sigma_i} + 2(\alpha_{e_{k\neq i}} + \alpha_{\nu_{k\neq i}}) \\
&\quad +6\left(\alpha_{u_k} + \alpha_{d_k}\right)\Bigg], \\
\beta_{\sigma_i} &= \alpha_{\sigma_i}\Big[-6\alpha_X X_{\ell_i}^2 + 6\alpha_{\sigma_i} + 2\alpha_{\nu_i}\Big],
\end{aligned} \tag{B.3.3}$$

while the RGEs of the diagonal quark Yukawas read

$$\begin{aligned}
\beta_{u_i} &= \alpha_{u_i}\Big[-\frac{17}{6}\alpha_1 - \frac{9}{2}\alpha_2 - 16\alpha_3 - 12\alpha_X X_{q_i}^2 + 9\alpha_{u_i} + 3\alpha_{d_i} + 6(\alpha_{u_{k\neq i}} + \alpha_{d_{k\neq i}}) \\
&\quad + 2(\alpha_{e_k} + \alpha_{\nu_k}) - 4\big(\alpha_{d_{il}}\alpha_{d_l}\alpha_{u_{il}}\alpha_{u_i}^{-1}\big)^{1/2} + \alpha_{d_{il}} + 2\alpha_{u_{il}}\Big], \\
\beta_{d_i} &= \alpha_{d_i}\Big[-\frac{5}{6}\alpha_1 - \frac{9}{2}\alpha_2 - 16\alpha_3 - 12\alpha_X X_{q_i}^2 + 9\alpha_{d_i} + 3\alpha_{u_i} + 6(\alpha_{u_{k\neq i}} + \alpha_{d_{k\neq i}}) \\
&\quad + 2(\alpha_{e_k} + \alpha_{\nu_k}) - 4\big(\alpha_{d_{il}}\alpha_{d_l}^{-1}\alpha_{u_{il}}\alpha_{u_i}\big)^{1/2} + \alpha_{u_{il}} + 2\alpha_{d_{il}}\Big],
\end{aligned} \tag{B.3.4}$$

with an implicit sum over $l > i$ and $l < i$ for the up and down sector, respectively. Finally, the RGEs of the off-diagonal Yukawa couplings obey

$$\begin{aligned}
\beta_{u_{ij}} &= \alpha_{u_{ij}}\Big[-\frac{17}{6}\alpha_1 - \frac{9}{2}\alpha_2 - 16\alpha_3 - 6\alpha_X(X_{q_i}^2 + X_{q_j}^2) + 9\alpha_{u_{ij}} + 6\alpha_{d_{ij}} \\
&\quad + 2\alpha_{u_i} + \alpha_{u_j} + \alpha_{d_j} - 4(\alpha_{d_{ij}}\alpha_{d_j}\alpha_{u_{ij}}^{-1}\alpha_{u_i})^{1/2} + \alpha_{d_{23}}\delta_{i1}\delta_{j2}\Big], \\
\beta_{d_{ij}} &= \alpha_{d_{ij}}\Big[-\frac{5}{6}\alpha_1 - \frac{9}{2}\alpha_2 - 16\alpha_3 - 6\alpha_X(X_{q_i}^2 + X_{q_j}^2) + 9\alpha_{d_{ij}} + 6\alpha_{u_{ij}} \\
&\quad + 2\alpha_{d_j} + \alpha_{d_i} + \alpha_{u_i} - 4(\alpha_{d_{ij}}^{-1}\alpha_{d_j}\alpha_{u_{ij}}\alpha_{u_i})^{1/2} + \alpha_{u_{12}}\delta_{i2}\delta_{j3}\Big],
\end{aligned} \tag{B.3.5}$$

where all indices are fixed.

C Collider Studies with MadGraph5_aMC@NLO

In this appendix we provide additional information and results regarding the study of vector-like lepton models at colliders presented in Chapter 4.

C.1 Event Simulation

In order to create samples of events of our VLL models in Eqs. (4.1.4) and (4.1.6), we first employ FeynRules [150] to compute tree-level Feynman rules, which are then used to generate UFO models [151]. These are given as an input to the Monte Carlo generator MadGraph5_aMC@NLO [152], with which we generate event samples that can be used to compute observables. For the event generation we use the set of parton distribution functions (PDFs) NNPDF3.0 [189]. In the 4L cross sections of Fig. 4.2 and the single- and pair-production cross sections of Fig. C.3.1, PDF and scale variation uncertainties are shown, see [145] for details.

For the study of the L_T distributions and the new observables, we generate, for each benchmark of BSM masses in Fig. 4.3, a sample of 5×10^4 events with at least four light leptons in the final state. The same number of events is computed for SM background processes contributing at leading order to 4L final states. We include ttZ-, triboson- and ZZ-mediated 4L production (see Sec. 4.2 for a discussion of the ZZ background). Higher-order corrections to SM production cross sections are taken into account by applying k factors to the leading order contributions [190–196]. The SM and VLL distributions for each observable are rescaled to the desired luminosity (77.4, 150 or 3000 fb^{-1}) using cross sections obtained with MadGraph5_aMC@NLO .

The event generation is performed with settings similar to the CMS study [141], with parameters collected in Tab. C.1. The cut on the missing transverse momentum is set to $p_T^{\text{miss}} < 50$ GeV in order to reproduce the signal region considered by CMS and to suppress contributions from final states with neutrinos. Electrons and muons are required to carry a minimum transverse momentum $p_T^{\ell} \geq 20$ GeV. Following CMS settings, and in order to suppress resonances in the low-mass region, we demand a light-lepton invariant mass $m_{\ell\ell} \geq 12$ GeV for all flavor and charge configurations of the final states. In events containing jets, we require as well $p_T^{\text{jet}} \geq 20$ GeV. To perform a simulation of the detector response, which in this thesis is included only in the L_T distributions shown in Figs. 4.4 and 4.7, we shower and hadronize the events with PYTHIA8 [154] and use DELPHES3 [197] for the fast detector simulation, see [145] for further details.

C.2 Algorithms for Null Tests

In Sec. 4.3 we described a set of four observables which allow to look for our VLL models at colliders, targeting their specific LFV-like decay signatures. Here we give a detailed account of the algorithms we use to compute the observables from the generated event samples. The parameters of the reconstruction algorithms are collected in Tab. C.1.

Parameters	Signal selection cuts	Reconstruction
$\alpha_s(m_Z) = 0.118$	$p_T^{\text{miss}} < 50$ GeV	$\Delta m_Z = 15$ GeV
$m_h = 125$ GeV	$p_T^{\ell} \geq 20$ GeV	$\Delta m_h = 5$ GeV
$m_W = 80.379$ GeV	$p_T^{\text{jet}} \geq 20$ GeV	$\Delta M_S = 5$ GeV
$m_t = 172$ GeV	$m_{\ell\ell} \geq 12$	$\Delta M_F = 100$ GeV
$m_b = 4.7$ GeV	-	-

Table C.1. Parameters used in the event generation and the reconstruction algorithm.

$m_{2\ell}$ and $m_{2\ell}$_diff

For each event with at least four light leptons in the final state, we compute all possible sets of two dilepton invariant masses from leptons of opposite charge, where each lepton contributes to only one of the invariant masses in the pair. If present, τ leptons are included in this step. If the event contains jets, we compute as well all possible pairs of invariant masses where one of them is a dilepton invariant mass and the other is the dijet invariant mass. For each event, only one pair of invariant masses is added to the observable $m_{2\ell}$. In order to be added, it must fulfill one of the following requirements:

a) Each invariant mass is equal either to $m_Z \pm \Delta m_Z$ or to $m_h \pm \Delta m_h$, according to the parameters in Tab. C.1, and each dilepton pair contains OCSF leptons. The states used to compute the masses are in this case $(\ell_i^+\ell_i^-)(\ell_j^+\ell_j^-)$, $(\tau^+\tau^-)(\ell_i^+\ell_i^-)$ or $(\ell_i^+\ell_i^-)(jj)$ with $i, j = 1, 2$. This condition reconstructs Z and Higgs bosons.

b) The difference between both invariant masses is less than ΔM_S (see Tab. C.1), while none of the other invariant mass pairs present a smaller difference, and each invariant mass is computed from OCSF leptons. The states used to compute the masses are in this case $(\ell_i^+\ell_i^-)(\ell_j^+\ell_j^-)$ with $i, j = 1, 2$. This condition reconstructs two scalars, S_{ii} and S_{jj}.

c) Both invariant masses differ by less than ΔM_S (see Tab. C.1), while none of the other invariant mass pairs present a smaller difference, and at least one of the invariant masses contains two OCDF leptons. The states used to compute the masses are in this case $(\ell_i^+\ell_j^-)(\ell_k^+\ell_i^-)$ with $i, j, k = 1, 2, 3$ and a maximum of one τ^+ and one τ^-. This condition reconstructs two scalars, S_{ij} and S_{ik}.

We check for these conditions in the above order ($a \to b \to c$) and stop when one of the requirements is fulfilled. We define the observable $m_{2\ell}$_diff as invariant mass pairs that only fulfill condition *c*), where two particles of approximately equal invariant mass are found and at least one of them is reconstructed from OCDF leptons. All SM contributions to $m_{2\ell}$_diff, although they can be sizable due to combinatorics in regions with a large SM background, are purely statistical.

$m_{3\ell}$ and $m_{3\ell}$_diff

These observables are designed to reconstruct the invariant masses of the VLLs via their three-body decays. For each pair of two-particle invariant masses added to $m_{2\ell}$, we look for the additional lepton which comes from the decay of each ψ. We add to $m_{3\ell}$ the pairs of three-particle invariant masses which fulfill one the following conditions:

i) For two-particle invariant masses which reconstruct to a Z or Higgs (condition a in the previous section) each two-particle invariant mass is paired with an additional lepton present in the final state. The resulting three-particle invariant masses are added to $m_{3\ell}$ if their difference is smaller than ΔM_F, and no other combination presents a smaller difference.

ii) For two-lepton invariant masses which reconstruct to S_{ii} and S_{jj} (condition b in the previous section) each two-lepton invariant mass is paired with an additional lepton present in the final state which has the *same* flavor of the two leptons in the two-lepton invariant mass. The resulting three-lepton invariant masses are added to $m_{3\ell}$ if their difference is smaller than ΔM_F, and no other combination presents a smaller difference.

iii) For two-lepton invariant masses which reconstruct to S_{ik} and S_{kj} (condition c in the previous section) if a two-lepton invariant mass contains two same-flavor leptons, it is paired with an additional lepton present in the final state which has the *same* flavor. If it contains two *different*-flavor leptons, it is paired with an additional lepton which has the same flavor but opposite charge of one of the leptons in the two-lepton invariant mass. For each event, we find at most one possible combination that fulfills this condition. The corresponding three-lepton invariant masses are added to $m_{3\ell}$.

In the last two conditions, flavor requirements are designed to reflect flavor conservation in the decays of the S_{ij}. We define the observable $m_{3\ell}$_diff as invariant mass pairs that only fulfill condition *iii*). Remarkably, the selection of the third leptons via flavor rules allows to populate $m_{3\ell}$_diff even when the ψ do not present a narrow width, which is the case for larger masses $M_F > M_S$. Similarly to $m_{2\ell}$_diff, $m_{3\ell}$_diff is a null test of the SM given perfect reconstruction of the events.

C.3 Cross Sections and Observables

Production cross sections: Fig. C.3.1 shows pair- and single- production cross sections of the VLLs at the LHC for $\sqrt{s} = 13$. The BSM scalar mass is taken to be $M_S = 500$ GeV and we fix κ' according to Eq. (4.1.8) and $\kappa = 10^{-2}\kappa'$. Note that the value of M_S has no influence on VLL production per se, but has an impact on the chosen values of κ, κ'. The BSM Yukawas do not affect pair production at leading order, which occurs through s-channel electroweak bosons (see Figs. 3.7 and 3.8) but have an impact on single production, which occurs at order κ and is suppressed by several orders of magnitude with respect to pair production.

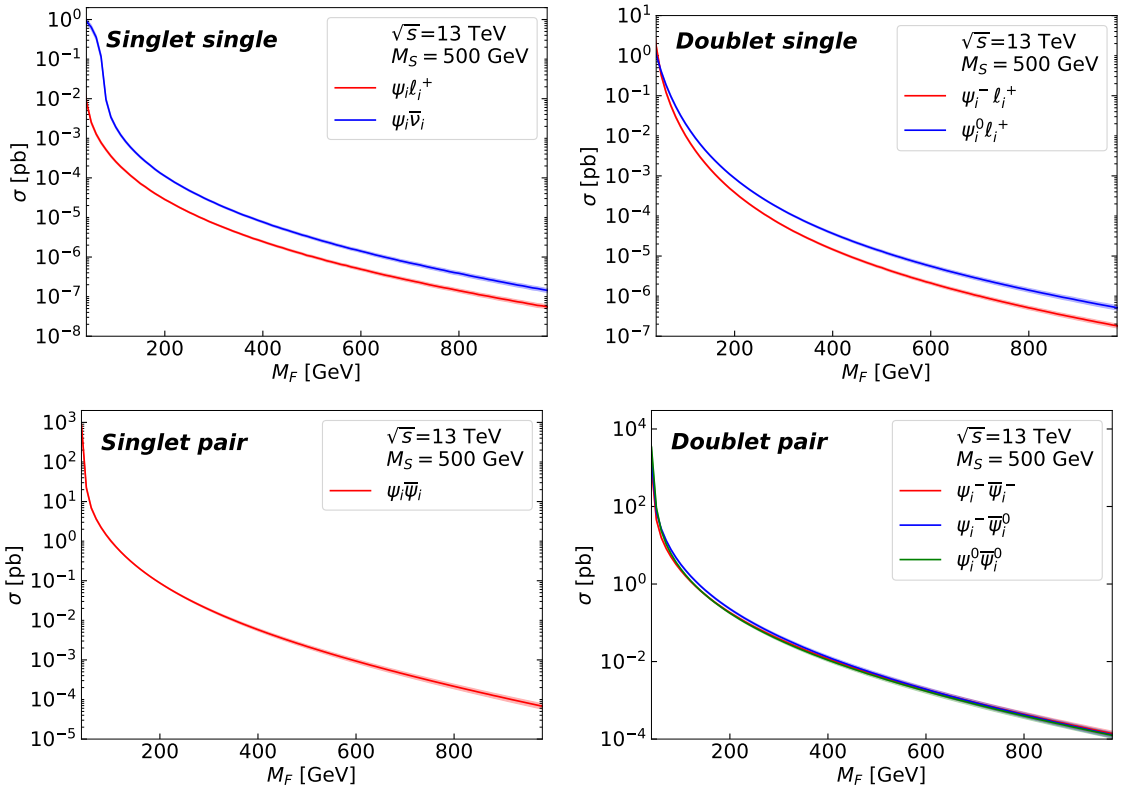

Figure C.3.1. Cross sections for VLL single production (top) and pair production (bottom) at $\sqrt{s} = 13$ TeV for different VLL masses in the singlet (left) and the doublet model (right). Results are shown for production of a single VLL flavor. For the computation we use $\kappa = 10^{-2}\kappa'$, while κ' is computed with Eq. (4.1.8) for each value of M_F and for $M_S = 500$ GeV.

Invariant masses: for the observables described in Sec. 4.3, larger luminosities enhance the number of events present in the distributions, yielding higher chances of detection. In Fig. C.3.2 we display the invariant masses $m_{2\ell}$, $m_{2\ell}$_diff, $m_{3\ell}$ and $m_{3\ell}$_diff for the $\sqrt{s} = 14$ TeV HL-LHC at a luminosity of 3000 fb^{-1}, and for the benchmarks studied in Sec. 4.3. We observe that peaks reach $\mathcal{O}(10^3)$ events in most cases, and distributions show a clear separation between BSM distributions and SM background, which is confined to low invariant mass regions.

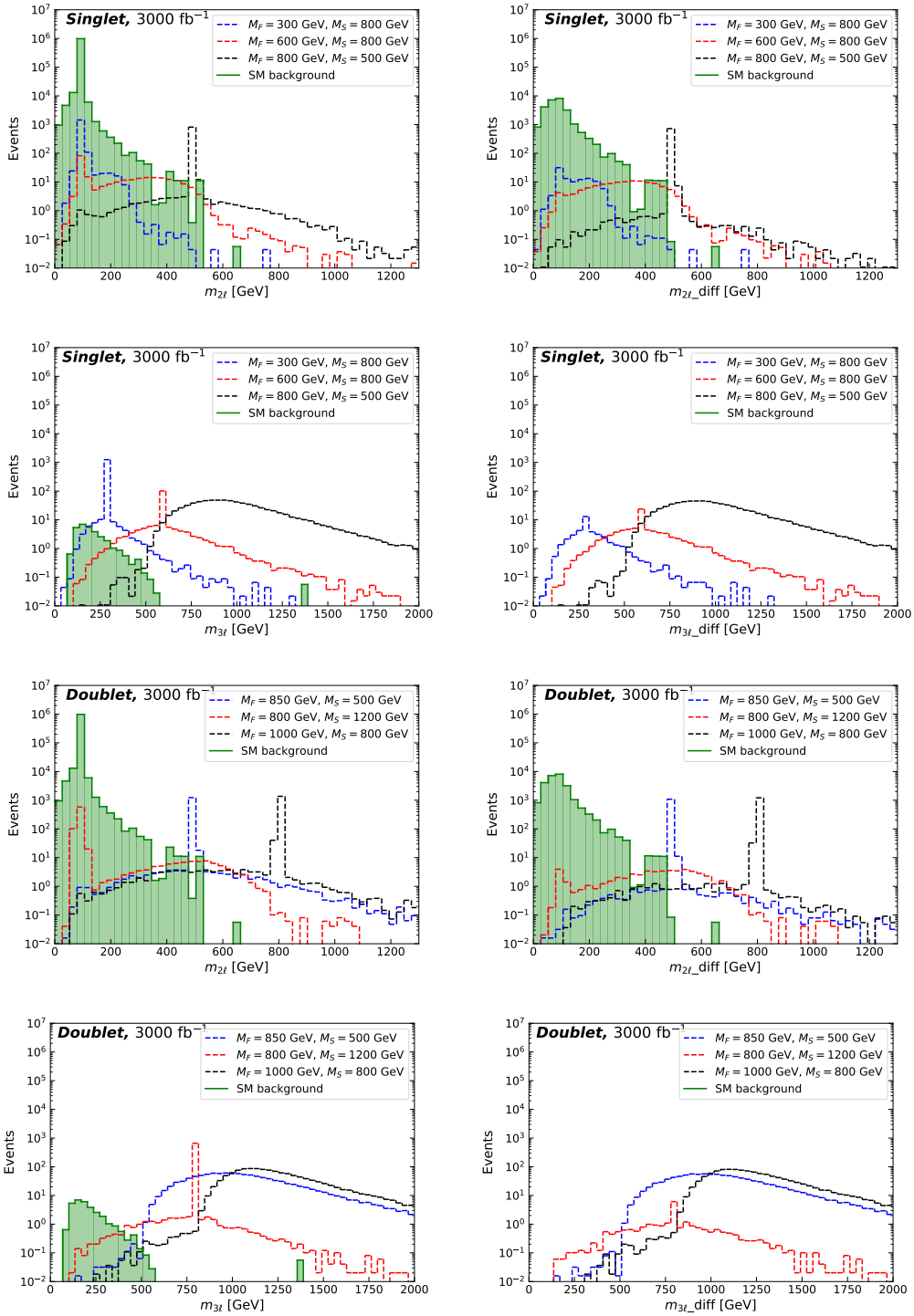

Figure C.3.2. Dilepton invariant masses $m_{2\ell}$, $m_{2\ell}$_diff, $m_{3\ell}$, and $m_{3\ell}$_diff (see Sec. 4.3 for details) for the singlet and doublet model for different benchmark masses of the VLLs and the BSM scalars at a luminosity of 3000 fb^{-1} and $\sqrt{s} = 14$ TeV. The coupling κ' is fixed according to Eq. (4.1.8).

Bibliography

[1] **CMS** Collaboration, S. Chatrchyan et al., *Observation of a New Boson at a Mass of 125 GeV with the CMS Experiment at the LHC*, Phys. Lett. B **716** (2012) 30–61, [arXiv:1207.7235].

[2] **ATLAS** Collaboration, G. Aad et al., *Observation of a new particle in the search for the Standard Model Higgs boson with the ATLAS detector at the LHC*, Phys. Lett. B **716** (2012) 1–29, [arXiv:1207.7214].

[3] Y. Nir, *Probing new physics with flavor physics (and probing flavor physics with new physics)*, in *Prospects in Theoretical Physics (PiTP) summer program on The Standard Model and Beyond IAS, Princeton, NJ, June 16-27, 2007*, 2007. arXiv:0708.1872.

[4] **Super-Kamiokande** Collaboration, Y. Fukuda et al., *Evidence for oscillation of atmospheric neutrinos*, Phys. Rev. Lett. **81** (1998) 1562–1567, [hep-ex/9807003].

[5] **SNO** Collaboration, Q. Ahmad et al., *Direct evidence for neutrino flavor transformation from neutral current interactions in the Sudbury Neutrino Observatory*, Phys. Rev. Lett. **89** (2002) 011301, [nucl-ex/0204008].

[6] N. Arkani-Hamed and M. Schmaltz, *Hierarchies without symmetries from extra dimensions*, Phys. Rev. D **61** (2000) 033005, [hep-ph/9903417].

[7] A. Delgado, A. Pomarol, and M. Quiros, *Electroweak and flavor physics in extensions of the standard model with large extra dimensions*, JHEP **01** (2000) 030, [hep-ph/9911252].

[8] G. F. Giudice and M. McCullough, *A Clockwork Theory*, JHEP **02** (2017) 036, [arXiv:1610.07962].

[9] A. E. Nelson and M. J. Strassler, *Suppressing flavor anarchy*, JHEP **09** (2000) 030, [hep-ph/0006251].

[10] A. E. Nelson and M. J. Strassler, *Exact results for supersymmetric renormalization and the supersymmetric flavor problem*, JHEP **07** (2002) 021, [hep-ph/0104051].

[11] A. Eichhorn and A. Held, *Mass difference for charged quarks from asymptotically safe quantum gravity*, Phys. Rev. Lett. **121** (2018), no. 15 151302, [arXiv:1803.04027].

[12] C. D. Froggatt and H. B. Nielsen, *Hierarchy of Quark Masses, Cabibbo Angles and CP Violation*, Nucl. Phys. **B147** (1979) 277–298.

[13] G. D'Ambrosio, G. F. Giudice, G. Isidori, and A. Strumia, *Minimal flavor violation: An Effective field theory approach*, Nucl. Phys. **B645** (2002) 155–187, [hep-ph/0207036].

[14] R. H. Parker, C. Yu, W. Zhong, B. Estey, and H. Müller, *Measurement of the fine-structure constant as a test of the Standard Model*, Science **360** (2018) 191, [arXiv:1812.04130].

[15] **Muon g-2** Collaboration, G. W. Bennett et al., *Final Report of the Muon E821 Anomalous Magnetic Moment Measurement at BNL*, Phys. Rev. **D73** (2006) 072003, [hep-ex/0602035].

[16] **Particle Data Group** Collaboration, P. Zyla et al., *Review of Particle Physics*, PTEP **2020** (2020), no. 8 083C01.

[17] **LHCb** Collaboration, R. Aaij et al., *Search for lepton-universality violation in $B^+ \to K^+\ell^+\ell^-$ decays*, Phys. Rev. Lett. **122** (2019), no. 19 191801, [arXiv:1903.09252].

[18] **LHCb** Collaboration, R. Aaij et al., *Test of lepton universality with $B^0 \to K^{*0}\ell^+\ell^-$ decays*, JHEP **08** (2017) 055, [arXiv:1705.05802].

[19] **LHCb** Collaboration, R. Aaij et al., *Test of lepton universality using $B^+ \to K^+\ell^+\ell^-$ decays*, Phys. Rev. Lett. **113** (2014) 151601, [arXiv:1406.6482].

[20] **LHCb** Collaboration, R. Aaij et al., *Angular analysis of the $B^0 \to K^{*0}\mu^+\mu^-$ decay using 3 fb^{-1} of integrated luminosity*, JHEP **02** (2016) 104, [arXiv:1512.04442].

[21] **CMS** Collaboration, V. Khachatryan et al., *Angular analysis of the decay $B^0 \to K^{*0}\mu^+\mu^-$ from pp collisions at $\sqrt{s} = 8$ TeV*, Phys. Lett. B **753** (2016) 424–448, [arXiv:1507.08126].

[22] A. Eichhorn and F. Versteegen, *Upper bound on the Abelian gauge coupling from asymptotic safety*, JHEP **01** (2018) 030, [arXiv:1709.07252].

[23] R. Alkofer, A. Eichhorn, A. Held, C. M. Nieto, R. Percacci, and M. Schröfl, *Quark masses and mixings in minimally parameterized UV completions of the Standard Model*, Annals Phys. **421** (2020) 168282, [arXiv:2003.08401].

[24] G. Hiller, C. Hormigos-Feliu, D. F. Litim, and T. Steudtner, *Anomalous magnetic moments from asymptotic safety*, Phys. Rev. D **102** (2020) 071901, [arXiv:1910.14062].

[25] G. Hiller, C. Hormigos-Feliu, D. F. Litim, and T. Steudtner, *Model Building from Asymptotic Safety with Higgs and Flavor Portals*, Phys. Rev. D **102** (2020), no. 9 095023, [arXiv:2008.08606].

[26] G. Hiller, C. Hormigos-Feliu, D. F. Litim, and T. Steudtner, *Asymptotically safe extensions of the Standard Model with flavour phenomenology*, in *54th Rencontres de Moriond on Electroweak Interactions and Unified Theories (Moriond EW 2019) La Thuile, Italy, March 16-23, 2019*, 2019. arXiv:1905.11020.

[27] D. F. Litim and F. Sannino, *Asymptotic safety guaranteed*, JHEP **12** (2014) 178, [arXiv:1406.2337].

[28] A. D. Bond and D. F. Litim, *Theorems for Asymptotic Safety of Gauge Theories*, Eur. Phys. J. **C77** (2017), no. 6 429, [arXiv:1608.00519]. [Editor's Erratum: Eur. Phys. J.C77,no.8,525(2017)].

[29] A. D. Bond, G. Hiller, K. Kowalska, and D. F. Litim, *Directions for model building from asymptotic safety*, JHEP **08** (2017) 004, [arXiv:1702.01727].

[30] M. E. Peskin and D. V. Schroeder, *An Introduction to quantum field theory*. Addison-Wesley, Reading, USA, 1995.

[31] F. Halzen and A. D. Martin, *QUARKS AND LEPTONS: AN INTRODUCTORY COURSE IN MODERN PARTICLE PHYSICS*. 1, 1984.

[32] Y. Grossman, *Introduction to Flavour Physics*, in *69th Scottish Universities Summer School in Physics: LHC Physics*, pp. 35–80, 11, 2014.

[33] R. Peccei, *The Strong CP problem and axions*, Lect. Notes Phys. **741** (2008) 3–17, [hep-ph/0607268].

[34] D. Buttazzo, G. Degrassi, P. P. Giardino, G. F. Giudice, F. Sala, A. Salvio, and A. Strumia, *Investigating the near-criticality of the Higgs boson*, JHEP **12** (2013) 089, [arXiv:1307.3536].

[35] G. Degrassi, S. Di Vita, J. Elias-Miro, J. R. Espinosa, G. F. Giudice, G. Isidori, and A. Strumia, *Higgs mass and vacuum stability in the Standard Model at NNLO*, JHEP **08** (2012) 098, [arXiv:1205.6497].

[36] A. Shkerin and S. Sibiryakov, *On stability of electroweak vacuum during inflation*, Phys. Lett. **B746** (2015) 257–260, [arXiv:1503.02586].

[37] **Particle Data Group** Collaboration, M. Tanabashi et al., *Review of Particle Physics*, Phys. Rev. **D98** (2018), no. 3 030001.

[38] M. D. Schwartz, *Quantum Field Theory and the Standard Model*. Cambridge University Press, 3, 2014.

[39] **ATLAS** Collaboration, G. Aad et al., *Combined measurements of Higgs boson production and decay using up to* 80 fb^{-1} *of proton-proton collision data at* $\sqrt{s} = 13$ *TeV collected with the ATLAS experiment*, Phys. Rev. D **101** (2020), no. 1 012002, [arXiv:1909.02845].

[40] W. Altmannshofer, J. Brod, and M. Schmaltz, *Experimental constraints on the coupling of the Higgs boson to electrons*, JHEP **05** (2015) 125, [arXiv:1503.04830].

[41] E. A. Paschos, *Diagonal Neutral Currents*, Phys. Rev. **D15** (1977) 1966.

[42] S. L. Glashow and S. Weinberg, *Natural Conservation Laws for Neutral Currents*, Phys. Rev. **D15** (1977) 1958.

[43] A. Hook, *TASI Lectures on the Strong CP Problem and Axions*, PoS **TASI2018** (2019) 004, [arXiv:1812.02669].

[44] W. A. Bardeen, A. Buras, D. Duke, and T. Muta, *Deep Inelastic Scattering Beyond the Leading Order in Asymptotically Free Gauge Theories*, Phys. Rev. D **18** (1978) 3998.

[45] D. F. Litim and T. Steudtner, *ARGES – Advanced Renormalisation Group Equation Simplifier*, [arXiv:2012.12955].

[46] M. E. Machacek and M. T. Vaughn, *Two Loop Renormalization Group Equations in a General Quantum Field Theory. 1. Wave Function Renormalization*, Nucl. Phys. **B222** (1983) 83–103.

[47] L. N. Mihaila, J. Salomon, and M. Steinhauser, *Renormalization constants and beta functions for the gauge couplings of the Standard Model to three-loop order*, Phys. Rev. **D86** (2012) 096008, [arXiv:1208.3357].

[48] **L3** Collaboration, P. Achard et al., *Measurement of the running of the electromagnetic coupling at large momentum-transfer at LEP*, Phys. Lett. B **623** (2005) 26–36, [hep-ex/0507078].

[49] **ATLAS** Collaboration, *Determination of the strong coupling constant and test of asymptotic freedom from Transverse Energy-Energy Correlations in multijet events at* $\sqrt{s} = 13$ *TeV with the ATLAS detector*, .

[50] B. Pendleton and G. G. Ross, *Mass and Mixing Angle Predictions from Infrared Fixed Points*, Phys. Lett. B **98** (1981) 291–294.

[51] C. T. Hill, *Quark and Lepton Masses from Renormalization Group Fixed Points*, Phys. Rev. D **24** (1981) 691.

[52] C. Wetterich, *GAUGE HIERARCHY DUE TO STRONG INTERACTIONS?*, Phys. Lett. B **104** (1981) 269–276.

[53] A. Held, *Effective asymptotic safety and its predictive power: Gauge-Yukawa theories*, Front. in Phys. **8** (2020) 341, [arXiv:2003.13642].

[54] S. Weinberg, *Ultraviolet divergences in quantum theories of gravitation*, in: General Relativity: An Einstein centenary survey, Eds. Hawking, S.W., Israel, W; Cambridge University Press (1979) 790–831.

[55] K. G. Wilson, *Renormalization group and critical phenomena. 1. Renormalization group and the Kadanoff scaling picture*, Phys.Rev. **B4** (1971) 3174–3183.

[56] K. G. Wilson, *Renormalization group and critical phenomena. 2. Phase space cell analysis of critical behavior*, Phys. Rev. B **4** (1971) 3184–3205.

[57] A. D. Bond and D. F. Litim, *Price of Asymptotic Safety*, Phys. Rev. Lett. **122** (2019), no. 21 211601, [arXiv:1801.08527].

[58] A. D. Bond, D. F. Litim, and T. Steudtner, *Asymptotic safety with Majorana fermions and new large N equivalences*, Phys. Rev. D **101** (2020), no. 4 045006, [arXiv:1911.11168].

[59] A. D. Bond and D. F. Litim, *More asymptotic safety guaranteed*, Phys. Rev. **D97** (2018), no. 8 085008, [arXiv:1707.04217].

[60] D. F. Litim, M. Mojaza, and F. Sannino, *Vacuum stability of asymptotically safe gauge-Yukawa theories*, JHEP **01** (2016) 081, [arXiv:1501.03061].

[61] D. Barducci, M. Fabbrichesi, C. M. Nieto, R. Percacci, and V. Skrinjar, *In search of a UV completion of the standard model — 378,000 models that don't work*, JHEP **11** (2018) 057, [arXiv:1807.05584].

[62] P. Schuh, *Vacuum Stability of Asymptotically Safe Two Higgs Doublet Models*, Eur. Phys. J. C **79** (2019), no. 11 909, [arXiv:1810.07664].

[63] A. D. Bond and D. F. Litim, *Asymptotic safety guaranteed in supersymmetry*, Phys. Rev. Lett. **119** (2017), no. 21 211601, [arXiv:1709.06953].

[64] K. Moch, *Fixed Points in Supersymmetric Extensions of the Standard Model*. PhD thesis, Tech. U., Dortmund (main), 6, 2020.

[65] A. D. Bond, D. F. Litim, G. Medina Vazquez, and T. Steudtner, *UV conformal window for asymptotic safety*, Phys. Rev. **D97** (2018), no. 3 036019, [arXiv:1710.07615].

[66] G. M. Pelaggi, A. D. Plascencia, A. Salvio, F. Sannino, J. Smirnov, and A. Strumia, *Asymptotically Safe Standard Model Extensions?*, Phys. Rev. **D97** (2018), no. 9 095013, [arXiv:1708.00437].

[67] R. Mann, J. Meffe, F. Sannino, T. Steele, Z.-W. Wang, and C. Zhang, *Asymptotically Safe Standard Model via Vectorlike Fermions*, Phys. Rev. Lett. **119** (2017), no. 26 261802, [arXiv:1707.02942].

[68] K. Kowalska and E. M. Sessolo, *Gauge contribution to the $1/N_F$ expansion of the Yukawa coupling beta function*, JHEP **04** (2018) 027, [arXiv:1712.06859].

[69] O. Antipin, N. A. Dondi, F. Sannino, A. E. Thomsen, and Z.-W. Wang, *Gauge-Yukawa theories: Beta functions at large N_f*, Phys. Rev. D **98** (2018), no. 1 016003, [arXiv:1803.09770].

[70] S. Abel, E. Mølgaard, and F. Sannino, *Complete Asymptotically Safe Embedding of the Standard Model*, Phys. Rev. D **99** (2019), no. 3 035030, [arXiv:1812.04856].

[71] T. Alanne, S. Blasi, and N. A. Dondi, *Critical Look at β -Function Singularities at Large N*, Phys. Rev. Lett. **123** (2019), no. 13 131602, [arXiv:1905.08709].

[72] V. Leino, T. Rindlisbacher, K. Rummukainen, F. Sannino, and K. Tuominen, *Safety Versus Triviality on the Lattice*, Phys. Rev. D **101** (2020), no. 7 074508, [arXiv:1908.04605].

[73] K. Kowalska, E. M. Sessolo, and Y. Yamamoto, *Flavor anomalies from asymptotically safe gravity*, [arXiv:2007.03567].

[74] G. Hiller and C. Hormigos-Feliu, *Flavor from running in $U(1)_X$ models*, (in preparation).

[75] W. E. Caswell, *Asymptotic Behavior of Nonabelian Gauge Theories to Two Loop Order*, Phys. Rev. Lett. **33** (1974) 244.

[76] T. Banks and A. Zaks, *On the Phase Structure of Vector-Like Gauge Theories with Massless Fermions*, Nucl. Phys. **B196** (1982) 189.

[77] G. Veneziano, *Some Aspects of a Unified Approach to Gauge, Dual and Gribov Theories*, Nucl. Phys. B **117** (1976) 519–545.

[78] H. Georgi, *Lie algebras in particle physics*, vol. 54. Perseus Books, Reading, MA, 2nd ed., 1999.

[79] T. M. P. Tait and Z.-H. Yu, *Triplet-Quadruplet Dark Matter*, JHEP **03** (2016) 204, [arXiv:1601.01354].

[80] Y. Bai and B. A. Dobrescu, *Minimal $SU(3) \times SU(3)$ Symmetry Breaking Patterns*, Phys. Rev. **D97** (2018), no. 5 055024, [arXiv:1710.01456].

[81] A. J. Paterson, *Coleman-Weinberg Symmetry Breaking in the Chiral SU(N) X SU(N) Linear Sigma Model*, Nucl. Phys. **B190** (1981) 188–204.

[82] K. Chetyrkin, B. A. Kniehl, and M. Steinhauser, *Decoupling relations to $\mathcal{O}(\alpha_s^3)$ and their connection to low-energy theorems*, Nucl. Phys. B **510** (1998) 61–87, [hep-ph/9708255].

[83] K. Kowalska, A. Bond, G. Hiller, and D. Litim, *Towards an asymptotically safe completion of the Standard Model*, PoS **EPS-HEP2017** (2017) 542.

[84] **Particle Data Group** Collaboration, C. Patrignani et al., *Review of Particle Physics*, Chin. Phys. **C40** (2016), no. 10 100001.

[85] M. Cirelli, N. Fornengo, and A. Strumia, *Minimal dark matter*, Nucl. Phys. **B753** (2006) 178–194, [hep-ph/0512090].

[86] J. A. Evans and J. Shelton, *Long-Lived Staus and Displaced Leptons at the LHC*, JHEP **04** (2016) 056, [arXiv:1601.01326].

[87] J. F. Gunion, H. E. Haber, G. L. Kane, and S. Dawson, *The Higgs Hunter's Guide*, Front. Phys. **80** (2000) 1–404.

[88] D. S. M. Alves, J. Galloway, J. T. Ruderman, and J. R. Walsh, *Running Electroweak Couplings as a Probe of New Physics*, JHEP **02** (2015) 007, [arXiv:1410.6810].

[89] M. Farina, G. Panico, D. Pappadopulo, J. T. Ruderman, R. Torre, and A. Wulzer, *Energy helps accuracy: electroweak precision tests at hadron colliders*, Phys. Lett. **B772** (2017) 210–215, [arXiv:1609.08157].

[90] J. P. Leveille, *The Second Order Weak Correction to (G-2) of the Muon in Arbitrary Gauge Models*, Nucl. Phys. **B137** (1978) 63–76.

[91] J. S. Schwinger, *On Quantum electrodynamics and the magnetic moment of the electron*, Phys. Rev. **73** (1948) 416–417.

[92] F. Jegerlehner, *Muon g – 2 theory: The hadronic part*, EPJ Web Conf. **166** (2018) 00022, [arXiv:1705.00263].

[93] M. Davier, *Update of the Hadronic Vacuum Polarisation Contribution to the muon g-2*, Nucl. Part. Phys. Proc. **287-288** (2017) 70–75, [arXiv:1612.02743].

[94] S. Borsanyi et al., *Leading-order hadronic vacuum polarization contribution to the muon magnetic momentfrom lattice QCD*, [arXiv:2002.12347].

[95] T. Aoyama et al., *The anomalous magnetic moment of the muon in the Standard Model*, Phys. Rept. **887** (2020) 1–166, [arXiv:2006.04822].

[96] A. Crivellin, M. Hoferichter, C. A. Manzari, and M. Montull, *Hadronic vacuum polarization: $(g-2)_\mu$ versus global electroweak fits*, Phys. Rev. Lett. **125** (2020), no. 9 091801, [arXiv:2003.04886].

[97] A. Keshavarzi, W. J. Marciano, M. Passera, and A. Sirlin, *Muon $g-2$ and $\Delta\alpha$ connection*, Phys. Rev. D **102** (2020), no. 3 033002, [arXiv:2006.12666].

[98] D. Hanneke, S. Fogwell, and G. Gabrielse, *New Measurement of the Electron Magnetic Moment and the Fine Structure Constant*, Phys. Rev. Lett. **100** (2008) 120801, [arXiv:0801.1134].

[99] L. Morel, Z. Yao, P. Cladé, and S. Guellati-Khélifa, *Determination of the fine-structure constant with an accuracy of 81 parts per trillion*, Nature **588** (2020), no. 7836 61–65.

[100] H. Müller, *Standard model of particle physics tested by the fine-structure constant*, Nature **588** (2020) 37.

[101] H. Davoudiasl and W. J. Marciano, *Tale of two anomalies*, Phys. Rev. **D98** (2018), no. 7 075011, [arXiv:1806.10252].

[102] J. Liu, C. E. M. Wagner, and X.-P. Wang, *A light complex scalar for the electron and muon anomalous magnetic moments*, JHEP **03** (2019) 008, [arXiv:1810.11028].

[103] S. Gardner and X. Yan, *Light scalars with lepton number to solve the $(g-2)_e$ anomaly*, Phys. Rev. D **102** (2020), no. 7 075016, [arXiv:1907.12571].

[104] C. Cornella, P. Paradisi, and O. Sumensari, *Hunting for Alps with Lepton Flavor Violation*, JHEP **01** (2020) 158, [arXiv:1911.06279].

[105] M. Bauer, M. Neubert, S. Renner, M. Schnubel, and A. Thamm, *Axion-like particles, lepton-flavor violation and a new explanation of a_μ and a_e*, Phys. Rev. Lett. **124** (2020), no. 21 211803, [arXiv:1908.00008].

[106] B. Dutta, S. Ghosh, and T. Li, *Explaining $(g-2)_{\mu,e}$, the KOTO anomaly and the MiniBooNE excess in an extended Higgs model with sterile neutrinos*, Phys. Rev. D **102** (2020), no. 5 055017, [arXiv:2006.01319].

[107] I. Bigaran and R. R. Volkas, *Getting chirality right: single scalar leptoquark solution/s to the $(g-2)_{e,\mu}$ puzzle*, Phys. Rev. D **102** (2020), no. 7 075037, [arXiv:2002.12544].

[108] I. Doršner, S. Fajfer, and S. Saad, *$\mu \to e\gamma$ selecting scalar leptoquark solutions for the $(g-2)_{e,\mu}$ puzzles*, Phys. Rev. D **102** (2020), no. 7 075007, [arXiv:2006.11624].

[109] F. J. Botella, F. Cornet-Gomez, and M. Nebot, *Electron and muon $g-2$ anomalies in general flavour conserving two Higgs doublets models*, Phys. Rev. D **102** (2020), no. 3 035023, [arXiv:2006.01934].

[110] S. Jana, V. P. K., and S. Saad, *Resolving electron and muon $g-2$ within the 2HDM*, Phys. Rev. D **101** (2020), no. 11 115037, [arXiv:2003.03386].

[111] B. Dutta and Y. Mimura, *Electron $g-2$ with flavor violation in MSSM*, Phys. Lett. **B790** (2019) 563–567, [arXiv:1811.10209].

[112] M. Endo and W. Yin, *Explaining electron and muon $g-2$ anomaly in SUSY without lepton-flavor mixings*, JHEP **08** (2019) 122, [arXiv:1906.08768].

[113] M. Badziak and K. Sakurai, *Explanation of electron and muon $g-2$ anomalies in the MSSM*, JHEP **10** (2019) 024, [arXiv:1908.03607].

[114] J.-L. Yang, T.-F. Feng, and H.-B. Zhang, *Electron and muon $(g-2)$ in the B-LSSM*, J. Phys. G **47** (2020), no. 5 055004, [arXiv:2003.09781].

[115] X.-F. Han, T. Li, L. Wang, and Y. Zhang, *Simple Interpretations of Lepton Anomalies in the Lepton-Specific Inert Two-Higgs-Doublet Model*, Phys. Rev. D **99** (2019), no. 9 095034, [arXiv:1812.02449].

[116] M. Abdullah, B. Dutta, S. Ghosh, and T. Li, *$(g-2)_{\mu,e}$ and the ANITA anomalous events in a three-loop neutrino mass model*, Phys. Rev. D **100** (2019), no. 11 115006, [arXiv:1907.08109].

[117] A. Cárcamo Hernández, Y. Hidalgo Velásquez, S. Kovalenko, H. Long, N. A. Pérez-Julve, and V. Vien, *Fermion spectrum and $g-2$ anomalies in a low scale 3-3-1 model*, [arXiv:2002.07347].

[118] N. Haba, Y. Shimizu, and T. Yamada, *Muon and electron $g-2$ and the origin of the fermion mass hierarchy*, PTEP **2020** (2020), no. 9 093B05, [arXiv:2002.10230].

[119] L. Calibbi, M. López-Ibáñez, A. Melis, and O. Vives, *Muon and electron $g-2$ and lepton masses in flavor models*, JHEP **06** (2020) 087, [arXiv:2003.06633].

[120] C. Arbeláez, R. Cepedello, R. M. Fonseca, and M. Hirsch, *$(g-2)$ anomalies and neutrino mass*, Phys. Rev. D **102** (2020), no. 7 075005, [arXiv:2007.11007].

[121] C.-H. Chen and T. Nomura, *Electron and muon $g-2$, radiative neutrino mass, and $\ell' \to \ell\gamma$ in a $U(1)_{e-\mu}$ model*, [arXiv:2003.07638].

[122] C. Hati, J. Kriewald, J. Orloff, and A. Teixeira, *Anomalies in ^{8}Be nuclear transitions and $(g-2)_{e,\mu}$: towards a minimal combined explanation*, JHEP **07** (2020) 235, [arXiv:2005.00028].

[123] S. Jana, P. Vishnu, W. Rodejohann, and S. Saad, *Dark matter assisted lepton anomalous magnetic moments and neutrino masses*, Phys. Rev. D **102** (2020), no. 7 075003, [arXiv:2008.02377].

[124] A. Crivellin, M. Hoferichter, and P. Schmidt-Wellenburg, *Combined explanations of $(g-2)_{\mu,e}$ and implications for a large muon EDM*, Phys. Rev. **D98** (2018), no. 11 113002, [arXiv:1807.11484].

[125] A. Crivellin and M. Hoferichter, *Combined explanations of $(g-2)_\mu$, $(g-2)_e$ and implications for a large muon EDM*, in *33rd Rencontres de Physique de La Vallée d'Aoste (LaThuile 2019) La Thuile, Aosta, Italy, March 10-16, 2019*, 2019. arXiv:1905.03789.

[126] P. Mohanmurthy and J. A. Winger, *Estimation of CP violating EDMs from known mechanisms in the SM*, in *40th International Conference on High Energy Physics*, 9, 2020. arXiv:2009.00852.

[127] **ACME** Collaboration, V. Andreev et al., *Improved limit on the electric dipole moment of the electron*, Nature **562** (2018), no. 7727 355–360.

[128] **Muon (g-2)** Collaboration, G. W. Bennett et al., *An Improved Limit on the Muon Electric Dipole Moment*, Phys. Rev. **D80** (2009) 052008, [arXiv:0811.1207].

[129] C. Cesarotti, Q. Lu, Y. Nakai, A. Parikh, and M. Reece, *Interpreting the Electron EDM Constraint*, JHEP **05** (2019) 059, [arXiv:1810.07736].

[130] **MEG** Collaboration, A. Baldini et al., *Search for the lepton flavour violating decay $\mu^+ \to e^+\gamma$ with the full dataset of the MEG experiment*, Eur. Phys. J. C **76** (2016), no. 8 434, [arXiv:1605.05081].

[131] S. M. Bilenky, S. Petcov, and B. Pontecorvo, *Lepton Mixing, $\mu \to e + \gamma$ Decay and Neutrino Oscillations*, Phys. Lett. B **67** (1977) 309.

[132] **BaBar** Collaboration, B. Aubert et al., *Searches for Lepton Flavor Violation in the Decays $\tau^\pm \to e^\pm\gamma$ and $\tau^\pm \to \mu^\pm\gamma$*, Phys. Rev. Lett. **104** (2010) 021802, [arXiv:0908.2381].

[133] G. Cavoto, A. Papa, F. Renga, E. Ripiccini, and C. Voena, *The quest for $\mu \to e\gamma$ and its experimental limiting factors at future high intensity muon beams*, Eur. Phys. J. **C78** (2018), no. 1 37, [arXiv:1707.01805].

[134] L. Lavoura, *General formulae for $f_1 \to f_2\gamma$*, Eur. Phys. J. **C29** (2003) 191–195, [hep-ph/0302221].

[135] **SINDRUM** Collaboration, U. Bellgardt et al., *Search for the Decay $\mu^+ \to e^+e^+e^-$*, Nucl. Phys. **B299** (1988) 1–6.

[136] **Mu3e** Collaboration, A.-K. Perrevoort, *Searching for Lepton Flavour Violation with the Mu3e Experiment*, PoS **NuFact2017** (2017) 105, [arXiv:1802.09851].

[137] T. A. Chowdhury and S. Nasri, *Charged Lepton Flavor Violation in a class of Radiative Neutrino Mass Generation Models*, Phys. Rev. **D97** (2018), no. 7 075042, [arXiv:1801.07199].

[138] **SINDRUM II** Collaboration, W. H. Bertl et al., *A Search for muon to electron conversion in muonic gold*, Eur. Phys. J. **C47** (2006) 337–346.

[139] R. Kitano, M. Koike, and Y. Okada, *Detailed calculation of lepton flavor violating muon electron conversion rate for various nuclei*, Phys. Rev. **D66** (2002) 096002, [hep-ph/0203110]. [Erratum: Phys. Rev.D76,059902(2007)].

[140] **Mu2e Calorimeter Group** Collaboration, R. Donghia, *The Mu2e experiment at Fermilab*, Nuovo Cim. **C40** (2017), no. 1 48.

[141] **CMS** Collaboration, A. M. Sirunyan et al., *Search for vector-like leptons in multilepton final states in proton-proton collisions at $\sqrt{s}$ = 13 TeV*, Phys. Rev. **D100** (2019), no. 5 052003, [arXiv:1905.10853].

[142] N. Kumar and S. P. Martin, *Vectorlike Leptons at the Large Hadron Collider*, Phys. Rev. **D92** (2015), no. 11 115018, [arXiv:1510.03456].

[143] **L3** Collaboration, P. Achard et al., *Search for heavy neutral and charged leptons in e^+e^- annihilation at LEP*, Phys. Lett. B **517** (2001) 75–85, [hep-ex/0107015].

[144] **ATLAS** Collaboration, G. Aad et al., *Search for heavy lepton resonances decaying to a Z boson and a lepton in pp collisions at $\sqrt{s} = 8$ TeV with the ATLAS detector*, JHEP **09** (2015) 108, [arXiv:1506.01291].

[145] S. Bißmann, G. Hiller, C. Hormigos-Feliu, and D. F. Litim, *Multi-lepton signatures of vector-like leptons with flavor*, Eur. Phys. J. C **81** (2021), no. 2 101, [arXiv:2011.12964].

[146] A. Crivellin, F. Kirk, C. A. Manzari, and M. Montull, *Global Electroweak Fit and Vector-Like Leptons in Light of the Cabibbo Angle Anomaly*, [arXiv:2008.01113].

[147] A. Das and S. Mandal, *Bounds on the triplet fermions in type-III seesaw and implications for collider searches*, [arXiv:2006.04123].

[148] B. Barman, D. Borah, L. Mukherjee, and S. Nandi, *Correlating the anomalous results in $b \to s$ decays with inert Higgs doublet dark matter and muon $(g-2)$*, Phys. Rev. D **100** (2019), no. 11 115010, [arXiv:1808.06639].

[149] D. Sabatta, A. S. Cornell, A. Goyal, M. Kumar, B. Mellado, and X. Ruan, *Connecting muon anomalous magnetic moment and multi-lepton anomalies at LHC*, Chin. Phys. C **44** (2020), no. 6 063103, [arXiv:1909.03969].

[150] A. Alloul, N. D. Christensen, C. Degrande, C. Duhr, and B. Fuks, *FeynRules 2.0 - A complete toolbox for tree-level phenomenology*, Comput. Phys. Commun. **185** (2014) 2250–2300, [arXiv:1310.1921].

[151] C. Degrande, C. Duhr, B. Fuks, D. Grellscheid, O. Mattelaer, and T. Reiter, *UFO - The Universal FeynRules Output*, Comput. Phys. Commun. **183** (2012) 1201–1214, [arXiv:1108.2040].

[152] J. Alwall, R. Frederix, S. Frixione, V. Hirschi, F. Maltoni, O. Mattelaer, H. S. Shao, T. Stelzer, P. Torrielli, and M. Zaro, *The automated computation of tree-level and next-to-leading order differential cross sections, and their matching to parton shower simulations*, JHEP **07** (2014) 079, [arXiv:1405.0301].

[153] S. Richter, *Measurements of ZZ production with the ATLAS detector and simulation of loop-induced processes with the HERWIG event generator*. PhD thesis, U. Coll. London, 2017. arXiv:1806.02697.

[154] T. Sjöstrand, S. Ask, J. R. Christiansen, R. Corke, N. Desai, P. Ilten, S. Mrenna, S. Prestel, C. O. Rasmussen, and P. Z. Skands, *An Introduction to PYTHIA 8.2*, Comput. Phys. Commun. **191** (2015) 159–177, [arXiv:1410.3012].

[155] *High-Luminosity Large Hadron Collider (HL-LHC): Technical Design Report V. 0.1*, CERN Yellow Rep. Monogr. **4** (2017) 1–516.

[156] H. Georgi, A. E. Nelson, and A. Manohar, *On the Proposition That All Fermions Are Created Equal*, Phys. Lett. **126B** (1983) 169–174.

[157] F. Correia and S. Fajfer, *Light mediators in anomaly free U (1)$_X$ models. Part I. Theoretical framework*, JHEP **10** (2019) 278, [arXiv:1905.03867].

[158] B. Holdom, *Two U(1)'s and Epsilon Charge Shifts*, Phys. Lett. B **166** (1986) 196–198.

[159] Y. Nir and G. Raz, *Quark squark alignment revisited*, Phys. Rev. D **66** (2002) 035007, [hep-ph/0206064].

[160] L. J. Hall and A. Rasin, *On the generality of certain predictions for quark mixing*, Phys. Lett. B **315** (1993) 164–169, [hep-ph/9303303].

[161] **ALEPH, DELPHI, L3, OPAL, SLD, LEP Electroweak Working Group, SLD Electroweak Group, SLD Heavy Flavour Group** Collaboration, S. Schael et al., *Precision electroweak measurements on the Z resonance*, Phys. Rept. **427** (2006) 257–454, [hep-ex/0509008].

[162] M. Bauer, S. Diefenbacher, T. Plehn, M. Russell, and D. A. Camargo, *Dark Matter in Anomaly-Free Gauge Extensions*, SciPost Phys. **5** (2018), no. 4 036, [arXiv:1805.01904].

[163] E. Accomando, A. Belyaev, L. Fedeli, S. F. King, and C. Shepherd-Themistocleous, *Z' physics with early LHC data*, Phys. Rev. **D83** (2011) 075012, [arXiv:1010.6058].

[164] **CMS** Collaboration, C. Collaboration, *Search for a high-mass resonance decaying into a dilepton final state in 13 fb^{-1} of pp collisions at $\sqrt{s} = 13$ TeV*, CMS-PAS-EXO-16-031 (2016).

[165] **CMS** Collaboration, A. M. Sirunyan et al., *Search for high-mass resonances in dilepton final states in proton-proton collisions at $\sqrt{s} = 13$ TeV*, JHEP **06** (2018) 120, [arXiv:1803.06292].

[166] **ATLAS** Collaboration, M. Aaboud et al., *Search for new high-mass phenomena in the dilepton final state using 36 fb^{-1} of proton-proton collision data at $\sqrt{s} = 13$ TeV with the ATLAS detector*, JHEP **10** (2017) 182, [arXiv:1707.02424].

[167] P. Langacker and M. Plumacher, *Flavor changing effects in theories with a heavy Z' boson with family nonuniversal couplings*, Phys. Rev. **D62** (2000) 013006, [hep-ph/0001204].

[168] **HFLAV** Collaboration, Y. S. Amhis et al., *Averages of b-hadron, c-hadron, and τ-lepton properties as of 2018*, [arXiv:1909.12524].

[169] **HFLAV** Collaboration, Y. Amhis et al., *Averages of b-hadron, c-hadron, and τ-lepton properties as of summer 2016*, Eur. Phys. J. **C77** (2017), no. 12 895, [arXiv:1612.07233].

[170] R. Bause, M. Golz, G. Hiller, and A. Tayduganov, *The New Physics Reach of Null Tests with $D \to \pi\ell\ell$ and $D_s \to K\ell\ell$ Decays*, Eur. Phys. J. **C80** (2020), no. 1 65, [arXiv:1909.11108].

[171] D. Bečirević, O. Sumensari, and R. Zukanovich Funchal, *Lepton flavor violation in exclusive $b \to s$ decays*, Eur. Phys. J. C **76** (2016), no. 3 134, [arXiv:1602.00881].

[172] T. Jubb, M. Kirk, A. Lenz, and G. Tetlalmatzi-Xolocotzi, *On the ultimate precision of meson mixing observables*, Nucl. Phys. B **915** (2017) 431–453, [arXiv:1603.07770].

[173] J. Aebischer, A. J. Buras, and J. Kumar, *Another SMEFT Story: Z' Facing New Results on ε'/ε, ΔM_K and $K \to \pi\nu\bar{\nu}$*, JHEP **12** (2020) 097, [arXiv:2006.01138].

[174] J. Ellis, M. Fairbairn, and P. Tunney, *Anomaly-Free Models for Flavour Anomalies*, Eur. Phys. J. C **78** (2018), no. 3 238, [arXiv:1705.03447].

[175] A. Celis, W.-Z. Feng, and M. Vollmann, *Dirac dark matter and $b \to s\ell^+\ell^-$ with* U(1) *gauge symmetry*, Phys. Rev. **D95** (2017), no. 3 035018, [arXiv:1608.03894].

[176] A. Vicente, *Anomalies in $b \to s$ transitions and dark matter*, Adv. High Energy Phys. **2018** (2018) 3905848, [arXiv:1803.04703].

[177] B. C. Allanach and J. Davighi, *Third family hypercharge model for $R_{K^{(*)}}$ and aspects of the fermion mass problem*, JHEP **12** (2018) 075, [arXiv:1809.01158].

[178] W. Altmannshofer, J. Davighi, and M. Nardecchia, *Gauging the accidental symmetries of*

the standard model, and implications for the flavor anomalies, Phys. Rev. **D101** (2020), no. 1 015004, [arXiv:1909.02021].

[179] J. Aebischer, W. Altmannshofer, D. Guadagnoli, M. Reboud, P. Stangl, and D. M. Straub, *B-decay discrepancies after Moriond 2019*, Eur. Phys. J. C **80** (2020), no. 3 252, [arXiv:1903.10434].

[180] A. Crivellin, A. Kokulu, and C. Greub, *Flavor-phenomenology of two-Higgs-doublet models with generic Yukawa structure*, Phys. Rev. **D87** (2013), no. 9 094031, [arXiv:1303.5877].

[181] A. J. Buras, M. V. Carlucci, S. Gori, and G. Isidori, *Higgs-mediated FCNCs: Natural Flavour Conservation vs. Minimal Flavour Violation*, JHEP **10** (2010) 009, [arXiv:1005.5310].

[182] M. E. Machacek and M. T. Vaughn, *Two Loop Renormalization Group Equations in a General Quantum Field Theory. 2. Yukawa Couplings*, Nucl. Phys. **B236** (1984) 221–232.

[183] M. E. Machacek and M. T. Vaughn, *Two Loop Renormalization Group Equations in a General Quantum Field Theory. 3. Scalar Quartic Couplings*, Nucl. Phys. **B249** (1985) 70–92.

[184] M.-x. Luo, H.-w. Wang, and Y. Xiao, *Two loop renormalization group equations in general gauge field theories*, Phys. Rev. **D67** (2003) 065019, [hep-ph/0211440].

[185] I. Schienbein, F. Staub, T. Steudtner, and K. Svirina, *Revisiting RGEs for general gauge theories*, Nucl. Phys. **B939** (2019) 1–48, [arXiv:1809.06797].

[186] A. G. M. Pickering, J. A. Gracey, and D. R. T. Jones, *Three loop gauge beta function for the most general single gauge coupling theory*, Phys. Lett. **B510** (2001) 347–354, [hep-ph/0104247]. [Erratum: Phys. Lett.B535,377(2002)].

[187] F. Staub, *SARAH*, [arXiv:0806.0538].

[188] E. Mølgaard, *Decrypting gauge-Yukawa cookbooks*, Eur. Phys. J. Plus **129** (2014) 159, [arXiv:1404.5550].

[189] **NNPDF** Collaboration, R. D. Ball, V. Bertone, S. Carrazza, L. Del Debbio, S. Forte, A. Guffanti, N. P. Hartland, and J. Rojo, *Parton distributions with QED corrections*, Nucl. Phys. **B877** (2013) 290–320, [arXiv:1308.0598].

[190] **LHC Higgs Cross Section Working Group** Collaboration, D. de Florian et al., *Handbook of LHC Higgs Cross Sections: 4. Deciphering the Nature of the Higgs Sector*, [arXiv:1610.07922].

[191] F. Campanario, V. Hankele, C. Oleari, S. Prestel, and D. Zeppenfeld, *QCD corrections to charged triple vector boson production with leptonic decay*, Phys. Rev. D **78** (2008) 094012, [arXiv:0809.0790].

[192] V. Hankele and D. Zeppenfeld, *QCD corrections to hadronic WWZ production with leptonic decays*, Phys. Lett. B **661** (2008) 103–108, [arXiv:0712.3544].

[193] A. Lazopoulos, K. Melnikov, and F. Petriello, *QCD corrections to tri-boson production*, Phys. Rev. D **76** (2007) 014001, [hep-ph/0703273].

[194] T. Binoth, G. Ossola, C. Papadopoulos, and R. Pittau, *NLO QCD corrections to tri-boson production*, JHEP **06** (2008) 082, [arXiv:0804.0350].

[195] F. Cascioli, T. Gehrmann, M. Grazzini, S. Kallweit, P. Maierhöfer, A. von Manteuffel,

S. Pozzorini, D. Rathlev, L. Tancredi, and E. Weihs, *ZZ production at hadron colliders in NNLO QCD*, Phys. Lett. B **735** (2014) 311–313, [arXiv:1405.2219].

[196] S. Frixione, V. Hirschi, D. Pagani, H. S. Shao, and M. Zaro, *Electroweak and QCD corrections to top-pair hadroproduction in association with heavy bosons*, JHEP **06** (2015) 184, [arXiv:1504.03446].

[197] **DELPHES 3** Collaboration, J. de Favereau, C. Delaere, P. Demin, A. Giammanco, V. Lemaître, A. Mertens, and M. Selvaggi, *DELPHES 3, A modular framework for fast simulation of a generic collider experiment*, JHEP **02** (2014) 057, [arXiv:1307.6346].